Cracow University of Technology
Faculty of Civil Engineering
Institute for Computational Civil Engineering

mgr inż. Magdalena German

# Modelling of chloride corrosion and resultant fracture in RC elements

PhD thesis

Supervisor:
dr hab. inż. Jerzy Pamin, prof.PK

October 18, 2016

I would like to express my sincere gratitude to
Professor Jerzy Pamin for his patience, essential
guidance and many fruitful discussions considering
problems of (not only) mechanical world.

I am grateful to Dr Adam Zaborski
for introducing me to the corrosion problem.

I would also like to thank all my colleagues
from the Institute for Computational Civil Engineering.

*Dedicated to all my family,*
*to my parents, grandparents, siblings*
*and especially to my husband and daughters*

# Contents

# Chapter 1

# Introduction

## 1.1 Objective of the thesis

The objective of the dissertation is to perform a numerical analysis of the behavior of reinforced concrete (RC) elements under the destructive actions of corrosion products and external loading. In particular, the thesis considers the chloride corrosion of reinforcement and resultant cracking of concrete. Corrosion products, accumulating around the reinforcement, increase their volume. Therefore internal pressure acting on the surrounding concrete is generated. As a result cracks along reinforcing bars appear.

The analysis considers RC beams with corroded reinforcement subjected to live load and interactions between the corrosion and external loading. The aim of the thesis is to create a reliable model of concrete-rust-steel interface, taking into account the volumetric expansion of corrosion products. Within the dissertation, two- and three-dimensional numerical models, based on the Finite Element Method (FEM), Cellular Automata and Finite Difference Method (FDM) are built. The analysis is performed using Matlab and Abaqus software.

The analysis of fracture caused by chloride corrosion can help one to understand the character of the observed damage. It can bring the answer to the question whether the damage is a result of cracking, spalling, the loss of bond between steel and concrete or a combination of all these actions. The important point of the analysis is building a proper numerical model for concrete-rust and rust-steel interface. This can be treated as a contact problem which makes the analysis more difficult. The problem of a proper representation of pressure generated due to expanding corrosion products is another task that is considered within the thesis. The results of the analysis are compared with the experimental findings of corrosion tests [1, 18, 46, 50].

## 1.2 Motivation of the thesis

The results of the simulations can be helpful in safety and durability predictions. The corrosion of steel reinforcement in concrete structures exposed to the extensive use of de-

icing salts is a worldwide problem which consumes large amounts of money allocated for repairs every year. The model proposed in the thesis could be used when expert opinions are prepared, for repair cost estimation or structure life-time predictions. Any experimental research of corroded constructions should be supported with a correct numerical procedure.

According to [51] the estimated cost of highway bridges corrosion in US is 37% of all corrosion costs in the infrastructure sector. It was reported that in 1998 there were 583 000 bridges in the United States, of which 235 000 were conventional reinforced concrete and 108 000 bridges were prestressed concrete structures. Approximately 15% of the bridges were structurally deficient, primarily due to corrosion of steel or steel reinforcement. The annual direct cost of corrosion for highway bridges was estimated at \$8.3 billion, consisting of \$3.8 billion to replace structurally deficient bridges over the next 10 years, \$2.0 billion for maintenance of concrete bridge decks, \$2.0 billion for maintenance of concrete substructures (excluding decks), and \$0.5 billion for maintenance painting of steel bridges [51].

The corrosion problem becomes even more severe problem when safe storage of nuclear waste is considered. Nuclear waste are generated from spent nuclear fuel, dismantled nuclear weapons, and products such as radio pharmaceuticals. The most important design item for the safe storage of nuclear waste is effective shielding of radiation. The casks used for permanent storage have a design life of several thousand years. In 1998 total life-cycle cost analysis by the U.S. Department of Energy for the permanent disposal of nuclear waste in Yucca Mountain, Nevada, estimated the total repository cost by the construction phase at \$4.9 billion with an average annual cost (from 1999 to 2116) of \$205 million. Of this cost, \$42.2 million is corrosion-related [51]. In the United Kingdom the estimate annual costs of corrosion of reinforced concrete structures is £550 million.

In Poland in 2013 General Director for National Roads and Motorways (GDDKiA) reported that at the beginning of summer 2013 the reparation of the bridge in Biały Dunajec was planned. According to the report the RC bridge was getting deteriorated continuously due to water sorption, chlorides ingress and defrosting cycles. As a result the load carrying capacity and strength of the concrete decreased. For the time of maintenance of 65-m long bridge, being the part of the highly attended Cracow-Zakopane route, the alternating traffic was introduced and speed limited to 30 km/h. GDDKiA reported that direct costs of reparation were estimated to 26 million PLN.

However, it must be emphasized that apart from direct costs, considering maintenance and repair costs, corrosion generates also the indirect costs. The indirect costs are delays in transport, accidents, compensations, losses in local budgets. Life-cycle analysis estimates the indirect costs to the user due to traffic delays and lost productivity at more than 10 times the direct cost of corrosion maintenance, repair, and rehabilitation. In the case of the bridge in Biały Dunajec the estimated reparation time was 1 year and 3 months. The bridge is a facilitation for local residents and for tourists traveling mainly to Zakopane. Annually Zakopane is visited by 3 million tourists. Thus, only 0.5 hour delay for each person can lead to 15 million PLN loss.

Some of the examples of effects of corrosion are presented in Fig. 1.1. Corrosion controls the lifetime of constructions, hence good understanding of the phenomena can help to extend their safe service life and to reduce maintenance expenses. The subject matter of the dissertation considers issues constantly under research. However, there is still a lack of credible numerical models of the behavior of reinforced elements subjected to detrimental actions of corrosion products.

## 1.3 State of the art

Chloride corrosion is one of the most frequent causes of deterioration of reinforced concrete elements. The most exposed are bridges, road infrastructure buildings, marine or industrial structures, and all constructions undergoing deicing programs. The first signs indicating that corrosion may have occurred are rusty stains on the concrete surface. Next, longitudinal cracks appear, concrete spalls from the reinforcement and the loss of bond between steel and concrete occurs, which finally leads to a general failure of the element.

The problem of corrosion of reinforced concrete elements involves many phenomena. The reinforced concrete elements can be chemically damaged by:

- Acids which dissolve calcium hydroxide $Ca(OH)_2$ present in the Portland cement
- Soft water, with pH ranging 5-6.5, which washes $Ca(OH)_2$ out from concrete
- Sea water, containing chlorides, which leads to chloride corrosion, degrading reinforcement and bonding between steel and concrete
- Sulphate corrosion which leads to degradation of chemical bindings in cement and production of ettringite

Leaching of $Ca(OH)_2$ from concrete results in a loss of weight of concrete and weakening of bindings in C-S-H phase. This may also affect the lowering of pH of concrete. Sulphate corrosion is a process, in which chemical reactions between active components of concrete and sulphates may lead to the formation of ettringite crystal. During the crystallization process, ettringite tends to increase its volume. This generates pressure acting on the surroundings, causing micro-cracks in cement paste. As a consequence the value of elasticity modulus decreases and the whole element is impaired [54].

The chloride corrosion is one of the most important destructive effects. The phenomenon may be divided into two steps. The first step is an initiation phase, in which chlorides penetrate the concrete cover and accumulate around the reinforcement. High alkalinity of concrete forms a passive layer on rebar surface. The presence of the passive layer prevents steel from corrosion. Unfortunately as pH of concrete lowers, the passive layer becomes more exposed to detrimental action of chloride ions. Chlorides around the reinforcement take part in the process of decomposition of the passive layer. When the concentration of chlorides around the reinforcement reaches a threshold value the passive

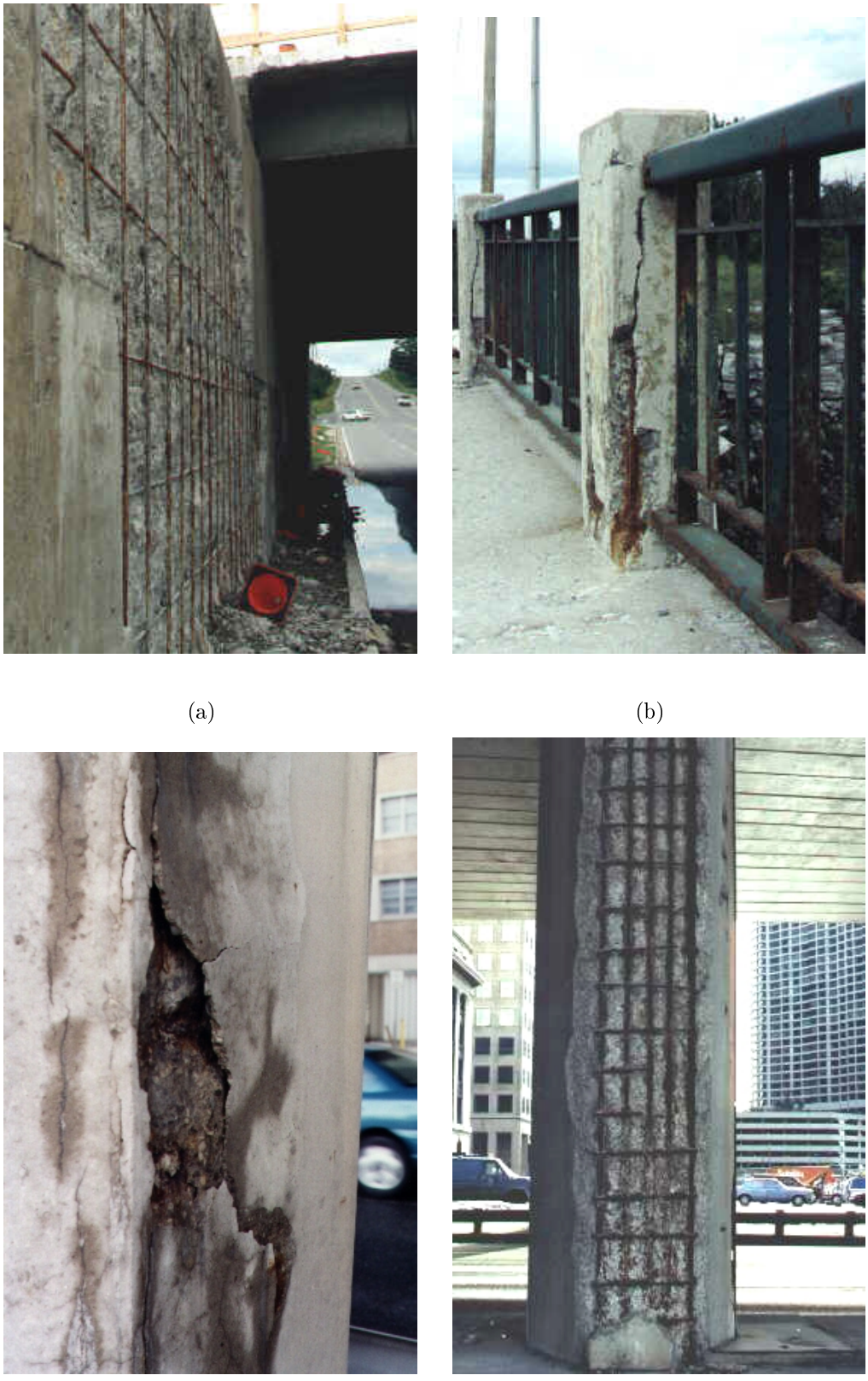

(a) (b)

(c) (d)

Figure 1.1: Effects of corrosion, photos quoted from www.corrosion-club.com

film breaks and a corrosion cell is formed. Then, the second step of corrosion, i.e. the propagation phase, begins. While the propagation phase continues, rust is produced. The composition of corrosion products is difficult to determine, yet it is known that the density of rust is much smaller than the density of steel. This means that the volume occupied by rust is much bigger than the volume of steel consumed in the process of corrosion. Thus, as a result, the volumetric expansion of corrosion products takes place, an internal pressure is generated, and tensile stresses appear in the surrounding concrete. When the hoop stresses exceed the tensile strength, the concrete cracks.

In real structures the failure is caused by a combination of many factors, e.g. sulphate corrosion intensifies damage caused by freezing cycles, carbonation of concrete favors chloride corrosion. In fact, the observation of detrimental action of one specified factor is possible only in laboratory conditions [54].

According to the international standards the reinforced concrete structure should be designed and constructed in a way to fulfill the reliability requirements:

- withstand all external and internal loadings
- complete the tasks demanded by the user with acceptable probability
- present adequate durability with reasonable costs of maintenance

All the requirements and limitations imposed on a structure are defined as two limit states: the ultimate limit state and serviceability limit state. The ultimate limit state is a computational condition that must be fulfilled in order to comply with the engineering demands for strength and stability under design loads. The criteria of the ultimate limit state are considered as the minimum requirement to provide the proper structural safety. They consider the loss of balance of the whole structure or its part, the loss of load-carrying capacity of cross-sections, transformation into a mechanism or loss of stability.

The serviceability limit state defines the performance criterion for exploitation and durability of a structure. Hence, the serviceability limit state means that a structure may fail to meet technical requirements for use even though it may be strong enough to remain standing. A structure that fails serviceability is in a state that has a negative influence on its usefulness. This can be caused by excessive local or global deflections or displacements of the structure, excessive cracking, vibrations, etc.

The corrosion research defines the durability of reinforced concrete structures or the degree of degradation. The research are supposed not only to describe the state of structure, but also the remaining service time. Hence the corrosion is a threat to a structure that results in making the requirements of serviceability limit states more strict. According to Eurocode 2, the main anti-corrosion protection should be provided by concrete cover and crack width limitation. The concrete cover must be thick enough and tight. The tightness can be achieved by controlling maximum $w/c$ (water-to-cement) ratio and minimum cement content. These parameters influence the degree of steel protection and the porosity. Also, they are related to concrete class. For the conventional RC structures the service time is assumed to be equal to 50 years, for special engineering structures,

Table 1.1: Exposure classification

| Class | Corrosion induced by | Examples |
|---|---|---|
| XO | no risk | concrete used for interior structures, very low air humidity |
| XC | carbonation | contact with water, foundations, high air humidity |
| XD | chlorides (excluding seawater) | air or industrial water contaminated by chlorides, swimming-pools, elements of bridges, roads, parking |
| XS | seawater | structures at the seashore |
| XF | freeze/thaw attack | elements of structures exposed to rain, frost and anti-icing |
| XA | chemical attack | natural soils and soil water contaminated by aggressive chemicals |

bridges or monumental structures it is 100 years. According to Eurocode 2 there are 6 types of environmental exposure, presented in Table 1.1.

The environmental conditions need to be assumed by an engineer. Unfortunately, in some cases, e.g. when one part of a structure is exposed to seawater, an other is exposed to air and high temperature, the conditions can endanger the structure more than it would be predicted by Eurocode. In such case the danger needs to be specified individually [59].

The minimum cover thickness should provide safe bonding force distribution, protection barrier against corrosion and guarantee the fire protection. The minimum cover thickness depends on 6 classes of structures (S1 to S6 defined in Eurocode 2) and environmental conditions. The minimum cover thickness for objects exposed to chlorides is ranging from 20 mm to 55 mm, [59]. The minimum value may be increased for additional protection or decreased in case of stainless steel, minding the bond strength distribution. Eurocode 2 also defines the dimension deviation which is related to constructing precision and is equal to 10 mm. However, if the constructing precision is very high the deviation value can be decreased or completely neglected.

Eurocode 2 limits the crack width. For ordinary RC structures it is 0.3 mm. The limit is imposed with respect to external appearance and durability of structure. However, in environment contaminated with chlorides this limit is not sufficient and the admissible crack width can be restricted even to 0.1 mm [28]. Unfortunately, the experimental research has revealed that corrosion develops in cracks with width smaller than 0.1 mm [59].

For a proper description of the initiation phase of chloride corrosion the analysis of the transport of moisture, oxygen and chlorides in concrete needs to be considered. The basic model for transport descriptions is the Fick's diffusion law. In fact, the diffusion is just one of many driving forces describing transport in concrete. However, in the case of water transport in aged concrete, reliable results can be achieved considering diffusion as the only mechanism governing the problem. On the other hand, the capillary water sorption has been analyzed in [19, 26, 34, 38].

Another problem to be analyzed is oxygen transport. Martin-Perez [34] considers oxygen transport as diffusion-driven, while in the papers of Ozbolt et al. [37–40] it is described as a convective-diffusive problem. Other authors seem to neglect the process.

However, in uncracked concrete the convective term can be neglected, since the capillary water sorption which governs the convection is significant when concrete is damaged. Also, in aged concrete oxygen concentration can be assumed as uniformly distributed. For concrete which is most of the time exposed to air, the concentration of oxygen in the body may be taken the same as on the free surface, thus the transport analysis can be neglected.

The main point of the analysis of the initiation phase of chloride corrosion is the chloride transport in concrete. Some authors assume only the diffusion-driven transport, while others use more complex expressions considering also other mechanisms. The diffusive chloride transport has been used e.g. in [10,26,35]. The chloride diffusion models depend on capillary water, temperature, degree of hydration or relative humidity, however, they are limited to just one driving force. In [19,34,36–40] the chloride transport is a result of diffusion and convection. On the other hand, Samson et al. [44] assume the chloride transport to be a result of two driving forces – diffusion and migration. The whole process is expressed by Nernst-Planck equation in a simplified version, neglecting the chemical activity of chlorides. When considering the chloride transport, the rate of chlorides binding also needs to be defined. Ozbolt et al. [38], as well as Oh and Jang [36] proposed a linear relation between bound and free chlorides. On the other hand Martin-Perez [34] assumes linear and non-linear chloride binding relations. Nielsen and Geiker [35] present the results calculated using non-linear Freundlich binding isotherm.

Once the chlorides decompose the rebar passive layer, the corrosion cell is formed. The description of the electrochemical process occurring in the reinforced concrete can be found in [26,34,37,59]. In [34] the corrosion current is calculated as a result of an electrochemical process, considering Butler-Volmers kinetics, however some simplifications are made during the analysis. A more thorough simulation of corrosion current flow is proposed in [37]. On the other hand, Krykowski [26] and Balafas and Burgoyne [3] express the corrosion current as an empirical function of chloride concentration, temperature, concrete resistivity and time, which was proposed for the first time by Liu and Weyers [30].

Due to corrosion current flowing through the pore solution the rust is produced. The most common model used for the calculation of the mass of rust produced in the process is Faraday's law, assuming the linear increase of the mass of rust with time. It was used in [26,34,37,42,43]. However, as the rust layer thickens, the iron ionic diffusion distance increases, so the diffusion rate goes down and the rate of rust production decreases. In the paper of Pantazopoulou and Papoulia [42] an alternative formula, adopted from Liu [31] and assuming a variable rate of rust production with time is considered. Both the formulae, the Faraday's law and Liu's model, have disadvantages. The Faraday model does not include the presence of the gradually thickening protective rust layer. On the other hand, the formula proposed by Liu [31] gives unrealistic corrosion rates for short times. In [3] a combined rule is adopted, where it is assumed that initially the corrosion rate is constant, following Faraday's law, and later the corrosion rate is evaluated using Liu's expression.

Corrosion can be distributed uniformly along the reinforcement or localized in pits.

However, it must be pointed out that due to varying concrete cover carbonation and content of chloride ions around the bar, the reinforcement corrosion does not usually take place uniformly along the circumference of the bar cross section. Since in actual environments chlorides penetrate in one direction, the corrosion starts from the most-outer part of the rebar and thus the reinforcement does not corrode uniformly in a cross section. A broad analysis of non-uniform distribution of corrosion can be found for instance in [12, 22, 40].

Once the rust is produced the propagation phase of chloride corrosion begins. In this phase concrete is damaged due to corrosion products. The simulation of damage is aimed at the analysis of concrete cracking. This behavior has been considered by many authors and therefore a variety of nonlinear models of concrete can be found in the literature. The constitutive models are usually divided into the ones based on the theory of elasticity and the ones based on inelastic theories, in particular the theory of plasticity. The important feature of different constitutive models is an appropriate failure criterion. For biaxial states of stress the Kupfer experiment is widely used.

In fact, while simulating concrete structures under multiaxial loading it is more proper to include inelastic strains in the calculations. The concrete mechanical behavior at the macroscopic level can be modelled with classical plasticity, however micro-cracking also causes elastic stiffness degradation. Modelling the stiffness degradation is difficult to be represented by means of the theory of plasticity and therefore the theory is often coupled with continuum damage mechanics. Some of the damage and fracture models, considering both elastic and plastic theories, are reviewed for instance in [24].

Bazant introduced a model representing rust expansion and its influence on surrounding concrete as a thick-walled cylinder [6]. This approach is limited to the consideration of one corroding rebar surrounded by a concrete cylinder with thickness equal to concrete cover. However, this model does not represent the real structure geometry. The model assumes that the cover fails with the first appearance of the crack on the surface. Using the thick-walled model it is not possible to obtain the pattern of possible failure of the whole element, because the interactions in concrete caused by more than one corroding rebars are neglected. The results of such analysis can only estimate the time to cracking of the concrete cover and confirm that damage is caused by tensile cracking, but they do not give the image of possible failure of the whole element. The thick-walled cylinder model has been used by other researchers, who extended the model with different material descriptions. In the paper of Pantazopulou and Papoulia [42] concrete softening was introduced into the model and the numerical analysis based on the finite difference method was performed. Martin-Perez [34] analyzed a concrete ring with two zones – the cracked zone with some residual strength and uncracked elastic zone. Balafas and Burgoyne [4] focused on rust accumulation and different ways of rust production. The research conducted by Guzman et al. [19] also considers the model where one corroding rebar is analyzed. However, in the next paper [20] the authors expand their model and analyze a fragment of a bridge deck reinforced with six rebars, three of which corrode.

It must be pointed out that apart from cracking of the concrete cover, another im-

portant modelling aspect is the incorporation of adhesive-frictional action at the interface of the corroding rebar and concrete. Concrete and steel should be firmly connected at the contact surfaces to ensure the transfer of forces between two materials. The cooperation between steel and concrete is possible due to similar thermal expansion and bond, which guaranty compatibility of strains in steel and concrete. The bonding forces can be influenced by friction between concrete and steel, type of steel (smooth or deformed), adhesion or chemical bonding of steel and concrete. What is more, the condition of the reinforcement is of great importance. The rough rebar surface with very thin rust coating can in fact increase bonding, while on smooth bars greasy rust stains cause the decrease of the bond forces.

The steel-concrete bond strength can be reduced by concrete cracking, reduction of reinforcement cross-sectional area, and losses in friction between steel ribs and concrete. The loss of bond strength for unconfined reinforcement can be much more critical than the cross-section losses. It is stated that a small decrease of the bar diameter could lead to even 80% bond reduction [13].

The corrosion products accumulated on the bar surface cause cracking of the concrete cover. When the concrete cover is cracked, the remaining concrete still exhibits some residual confining action. Nevertheless, this implies the loss of confinement and a reduction in bond strength in the interfacial zone between the two materials. What is more, the soft layer created by corrosion products that accumulate on the bar surface can effectively reduce the friction component of the bond strength. In addition, the deterioration of the ribs of the deformed bars causes a significant reduction of the interlocking forces between the ribs of the bars and the surrounding concrete keys. This deteriorates the primary mechanisms of bond between the deformed bars and concrete, and hence, the bond strength decreases significantly.

According to Zybura et al. [59] when a rebar is slightly corroded (approx. 4% of steel mass) the adhesion of steel and concrete increases about 15%. This is a consequence of the increase of friction and roughness of steel surface. However, further corrosion results in an abrupt decrease of concrete-steel adhesion, to 15% of the initial value. After reducing to 8% adhesion decreases but insignificantly.

On the other hand studies conducted by Fang [13] revealed the dependence of the bonding on the type of steel and the presence of stirrups in the analyzed samples. According to experimental results of pullout tests presented by Fang et al. [13], the bond strength of deformed reinforcing bars without stirrups confinement is very sensitive to corrosion and generally decreases with the increase of corrosion. For deformed bars with confinement, corrosion has no substantial influence on the bond strength. For smooth bars, however, there is an opposite effect of corrosion on the bond strength. For smooth bars without stirrups confinement corrosion results in a small increase in the bond strength. For smooth bars with confinement, the bond strength considerably increases as corrosion advances.

In the paper by Wang and Liu [53] the bond strength of corroded reinforcement in RC specimens without stirrups is calculated. In the model proposed in [53] corrosion is introduced by equivalent pressure acting on concrete, according to the formulae presented

in [42]. The main emphasis is placed on the confinement that is created by the concrete cover. It is observed that the cover cracking implies the loss of bond between concrete and steel. The corrosion causes cracking of the cover and also affects the friction between steel and concrete. In the paper, the bond strength of corroded deformed bar under splitting failure is mainly studied. The failure of a structural member is treated as the failure of concrete under multiaxial stress state. The model does not consider the possible failure mechanism due to the lubricating effect of corrosion products.

The paper of Berto et al. [8] presents two ways of bond modelling, related to the experiment conducted by Al-Sulaimani [1]. First, the frictional-type law is presented. The model is able to represent the slip between steel and concrete, but cannot reproduce the loss of strength after reaching the strength limit evidenced by experimental studies. The effects of corrosion influence the bond strength value and the initial slope of the curve, but without changing the shape of the bond-slip curve. The second proposal is the damage-type model. The bond-slip relation is initially linear, achieving the maximum bond stress and later descending until reaching the residual bond strength. This approach allows for modifying not only the bond strength but also the shape of the bond-slip curve with respect to the corrosion level.

To sum up, the simulations performed within the thesis will contribute to the discussion of the following scientific issues:

- mechanisms of oxygen and chloride transport,
- corrosion cell analysis,
- mechanisms of fracture due to expanding corrosion products,
- interaction between damaged zones within reinforced concrete cross-section,
- interaction between longitudinal and transversal cracks,
- representation of interfacial action between concrete and corroding steel.

The research included in the project generally considers the response of an RC element to chloride corrosion, however during the analysis a few other issues are also investigated. The main goal is the analysis of the influence of expanding corrosion products on reinforced concrete element. It considers simulation of the corroding reinforcement in element's cross-section, pullout of the single rebar and finally RC beam subjected to live load and corrosion. The mechanical analysis is preceded by simulation of chloride and oxygen transport.

# Chapter 2

# Theoretical foundations of corrosion process

It has been assumed to describe the process of chloride corrosion by the two-stage Tuutti's model which is presented in Fig. 2.1. The stages can be characterized as initiation and propagation phases. During the initiation phase chlorides penetrate the concrete cover and accumulate around reinforcement bars, decomposing the passive layer. As time passes by, chloride concentration in concrete increases until it reaches a chloride threshold value, causing complete depassivation of reinforcement. The moment of reaching the threshold is the moment when the initiation phase ends and the propagation stage begins. During the propagation phase steel has no natural anti-corrosion protection and a corrosion current starts to flow. The electrical current induces the production of rust. A growing amount of corrosion products generates stresses appearing in the element. In the end the corrosion process leads to cracking, splitting, delamination, loss of strength and general failure of the element.

## 2.1 Initiation stage

Highly alkaline pore solution with pH equal to at least 12 or more provides a passive layer on reinforcement surface, which protects steel from corroding. However, with time pH of concrete lowers, mainly due to carbonation of concrete and presence of chloride ions. Carbonation is a process of leaching $Ca(OH)_2$ out of concrete, according to reaction:

$$Ca(OH)_2 + CO_2 \rightarrow CaCO_3 + H_2O \tag{2.1}$$

Reaction (2.1) results in decreasing pH, due to consumption of free $OH^-$ ions and dilution of the pore solution. When pH of pore solution is below 12, the protective function of the passive layer cannot be fulfilled [59].

During the initiation phase chloride ions permeate into concrete, which leads to decomposition of the passive layer. Chlorides accelerate the process of passive layer decomposition, yet the exact mechanism of the phenomenon is still not convincingly described [59].

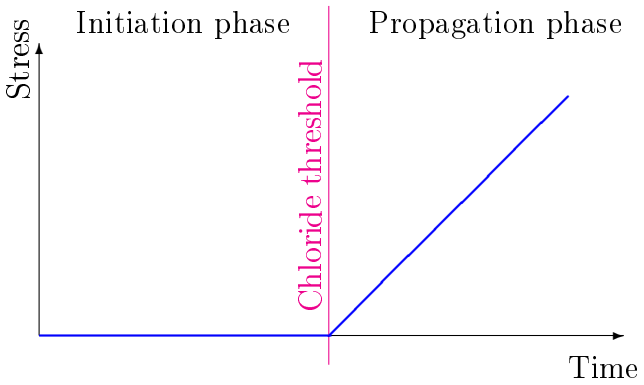


Figure 2.1: Two-stage Tuutti's model

A schematic representation of initiation phase is presented in Fig. 2.2. It is assumed that the initiation phase ends when the chloride concentration around the reinforcement reaches a chloride threshold value. At this moment the steel passive layer is completely decomposed, the rebar becomes electro-chemically active and a corrosion macro-cell is formed.

### 2.1.1 Chlorides transport

For uncracked, unsaturated concrete, in a general case the total ion flux can be caused by diffusion, migration, advection and chemical activity of ionic species in the solution. The diffusion flux is caused by concentration gradient, the migration flux is caused by electrical potential gradient and advection is a result of fluid flow.

Contrary to molecules, ions are charged particles. During the diffusion process, some ions tend to diffuse at higher rate. However, any excess charge transferred by the faster ions builds up a local electric field, which slows down the faster ions, and accelerates the

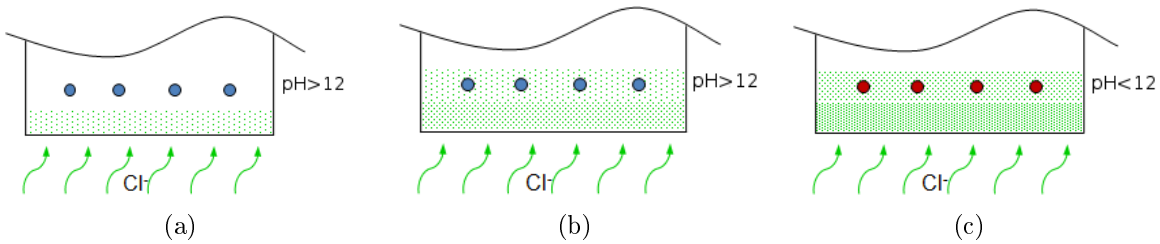


Figure 2.2: Schematic representation of initiation phase of chloride corrosion: (a) high pH of pore solution and low chlorides concentration, steel is passive, (b) high pH of pore solution and medium chlorides concentration, steel is passive, (c) smaller pH of pore solution and high chlorides concentration, steel is depassivated

slower ions [44, 45]. Thus the migration term should not be neglected in the description of ionic transport.

The total chloride ion flux $\mathbf{J}_{cl}$ can be described by the extended Nernst-Planck equation:

$$\mathbf{J}_{cl} = D_{cl}\left(H,T,h\right)\nabla C_{cl}^{f} + \frac{zFD_{cl}\left(H,T,h\right)}{RT}C_{cl}^{f}\nabla E_{cl} + D_{cl}\left(H,T,h\right)C_{cl}^{f}\nabla\left(\ln\gamma_i\right) + C_{cl}^{f}\mathbf{v}_w \tag{2.2}$$

where: $C_{cl}^{f}$ – free chlorides concentration; $D_{cl}\left(H,T,h\right)$ – chloride diffusion coefficient, depending on relative humidity, temperature and hydration; $T$ – absolute temperature; $z$ – valence of the ion; $F$ – Faraday constant; $R$ – universal gas constant; $E_{cl}$ – diffusion potential set up by drifting ions; $\gamma_i$ – chemical activity coefficient; $\mathbf{v}_w$ – velocity of pore liquid.

In eq. (2.2) the terms represent diffusion, migration, chemical activity and advection, respectively.

During the initiation process a part of chlorides reacts with hydration products and cement. Only the free chlorides cause the corrosion of the reinforcement [34, 35, 38, 45]. The total chloride concentration is a sum of free $C_{cl}^{f}$ and bound $C_{cl}^{b}$ chlorides:

$$C_{cl} = C_{cl}^{b} + C_{cl}^{f} \tag{2.3}$$

The relation between free and bound chloride can take the form of linear or non-linear expression. Among the non-linear forms there are two models commonly used: Freundlich isotherm and Langmuir isotherm [34, 35, 45]. The Freundlich isotherm is a power law between bound and free chlorides concentration:

$$C_{cl}^{b} = \alpha\left(C_{cl}^{f}\right)^{\beta} \tag{2.4}$$

where: $\alpha$, $\beta$ – empirical constants.

The linear binding relation can be obtained by assuming $\beta$ equal to 1. The Langmuir isotherm is expressed as:

$$C_{cl}^{b} = \frac{\alpha \cdot C_{cl}^{f}}{1 + \beta \cdot C_{cl}^{f}} \tag{2.5}$$

where: $\alpha$, $\beta$ – empirical constants.

The local electrical potential set up by drifting ions can be determined on the basis of the Poisson equation [44, 45]:

$$\nabla^2 E_{cl} = \frac{zFC_{cl}^{f}}{\varepsilon_m} \tag{2.6}$$

where: $\varepsilon_m$ – dielectric constant of the medium.

When the problem of chloride transport in uncracked concrete is described at the macroscopic scale, some simplifications can be introduced in eq. (2.2). In the case of ionic

transport problems in reactive materials it has been assumed to separate the transport and chemical reaction parts [45]. Thus the chemical activity effects can be neglected, however the chloride binding must be considered as it influences the chloride concentration significantly. Assuming the average concentration of pore water, i.e. with no variation in water content, the advective term in eq. (2.2) can also be neglected.

The diffusion coefficient $D_{cl}\left(H,T,h,t\right)$ is dependent on the degree of cement hydration, cement type, temperature, porosity, pore relative humidity and time. The diffusivity of chlorides also represents the effects of the complex geometry of the porous network of concrete. In general it can be expressed as:

$$D_{cl}\left(H,T,h,t\right) = D_{c,ref} \cdot f_1\left(H\right) \cdot f_2\left(T\right) \cdot f_3\left(h\right) \cdot f_4\left(t\right) \tag{2.7}$$

where: $D_{c,ref}$ – reference value evaluated at standard conditions ($T = 23$℃, $t_e = 28$ days, $H = 1$); $f_1\left(H\right)$, $f_2\left(T\right)$, $f_3\left(h\right)$, $f_4\left(t\right)$ – functions expressing the dependence of the diffusion coefficient on relative pore humidity, temperature, hydration and time, respectively.

Once the hydration process is completed, function $f_3\left(h\right)$ that describes the decrease of chloride diffusion coefficient with time reaches a constant value [38]. The influence of temperature on the macroscopic mechanical properties of concrete becomes important only at relatively high temperatures and for usual temperatures it can be neglected. The humidity is strictly related to pore water content. Due to the assumption of average concentration of pore water, function $f_1\left(H\right)$ is equal to 1. Thus when concrete is analyzed in averaged conditions at macroscale the diffusion coefficient becomes a constant material parameter.

The dependence on time corresponds with the type of cement used in concrete mix and is described by the power expression [50]:

$$f_4\left(t\right) = \left(t_e/t\right)^m \tag{2.8}$$

where: $m$ – empirical parameter.

The cements with addition of fly ash or slag reveal high dependence on time. In comparison, the diffusion coefficient for ordinary Portland cement (OPC) seems to be almost constant in time. The diagrams showing the relationship of $D_{cl}$ and time are presented in Fig. 2.3. Assuming OPC as cementitious material the time dependence can be neglected.

Using the above-mentioned simplifications the equation of mass conservation can be written as:

$$\frac{\partial C_{cl}^f}{\partial t} = \nabla \cdot \left( D_{cl} \nabla C_{cl}^f + \frac{zFD_{cl}}{RT} C_{cl}^f \nabla E_{cl} \right) - \frac{\partial C_{cl}^b}{\partial t} \tag{2.9}$$

with initial and boundary conditions specified as follows (see Fig. 2.4):

$$C_{cl}\left(\bar{x},0\right) = 0, \quad \bar{x} \in \Omega \tag{2.10}$$

$$C_{cl}\left(\bar{x}_0,t\right) = C_0, \quad \bar{x}_0 \in \Gamma \tag{2.11}$$

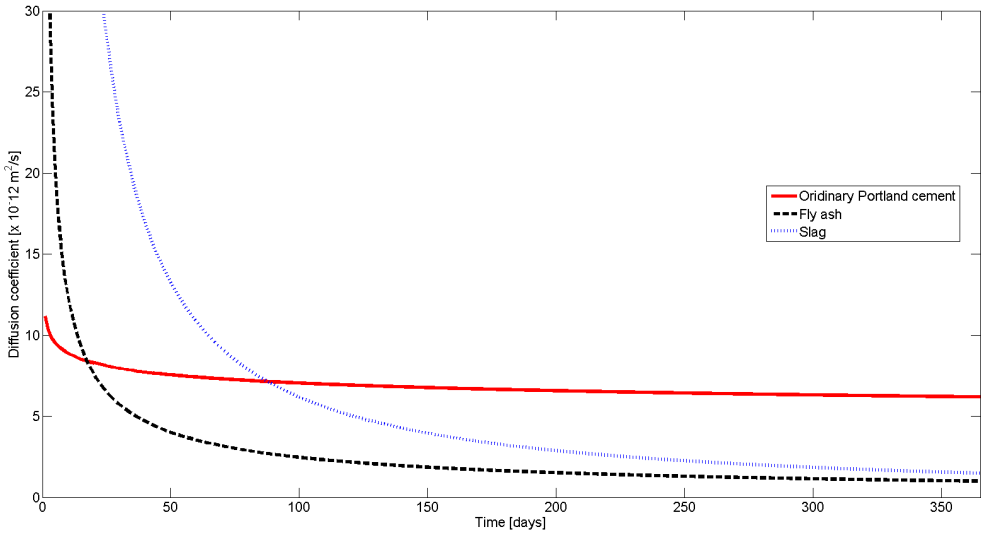


Figure 2.3: Dependence of diffusion coefficient on time [50]

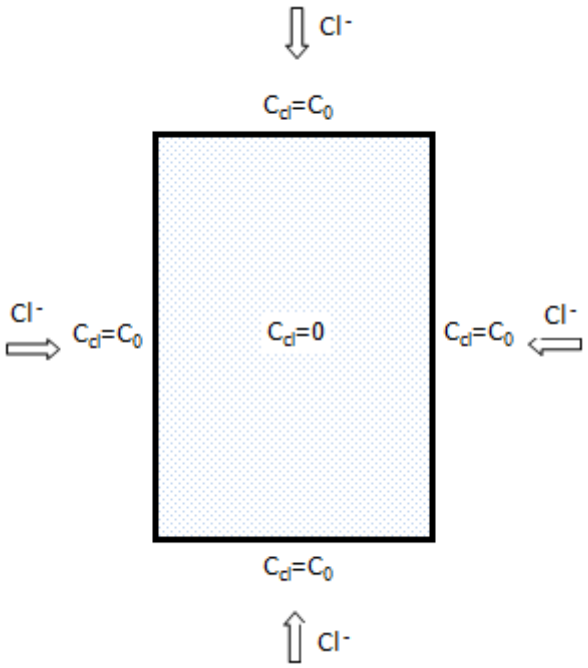


Figure 2.4: Boundary conditions for chloride concentration calculations

This procedure is applicable only in the case of uncracked concrete. The cracked concrete cannot be treated as a homogenous porous material and the rate of diffusion and migration of chloride ions towards the reinforcement is additionally dependent on crack characteristics. Moreover, the capillary sorption in cracked concrete is fast in comparison to diffusion or migration. Hence, the transport of water as well as the advection term must be considered. According to the current knowledge water and free chlorides penetrate the crack immediately after crack opening, hence the depassivation time is significantly shorter and related to the maximum crack width [38].

To determine the time of depassivation it is necessary to establish the threshold chloride concentration. Many service life models assume that the end of service life of a structure happens when the passive layer is decomposed. It must be noticed that a higher chloride content can be tolerated when chlorides are added to the original concrete mix. However, to prevent corrosion due to chlorides already present in the concrete mix, concrete standards have provided guidelines on the allowable amount of chloride ions coming from the original mix ingredients [34]. Definitely the chloride threshold for prestressed concrete is much lower than for plain reinforced concrete. The chloride threshold concentration may depend on several parameters, i.e.:

- the condition of steel/concrete interface
- the properties of concrete, such as its binding capacity and the pH level of the pore solution
- the exposure conditions, such as the source and type of chloride contamination, temperature, and moisture content.

The chloride threshold value is usually expressed as a percentage of cement mass. The reported values range from 0.17 to 2.5% [34], however it has been used to assume that for ordinary reinforced concrete the chloride threshold is 0.4% of cement mass.

### 2.1.2 Oxygen transport

The modelling of corrosion process requires, apart from chlorides, also the oxygen transport considerations, as the cathodic reaction is controlled by oxygen concentration $C_{ox}$. While corrosion proceeds, the initial oxygen supply available in concrete gets exhausted, and oxygen must be transported into a cross-section. Oxygen is transported to the cross-section as a particle, thus the total flux can be expressed by eq. (2.2) without consideration of the migration term. Since concrete is considered at macroscopic scale, the oxygen flux can be expressed just as a diffusion driven process. To describe total oxygen flux $\mathbf{J}_{ox}$ Fick's equation can be used:

$$\mathbf{J}_{ox} = D_{ox}(H)\,\nabla C_{ox} \tag{2.12}$$

where: $C_{ox}$ – oxygen concentration; $D_{ox}(H)$ – oxygen diffusion coefficient

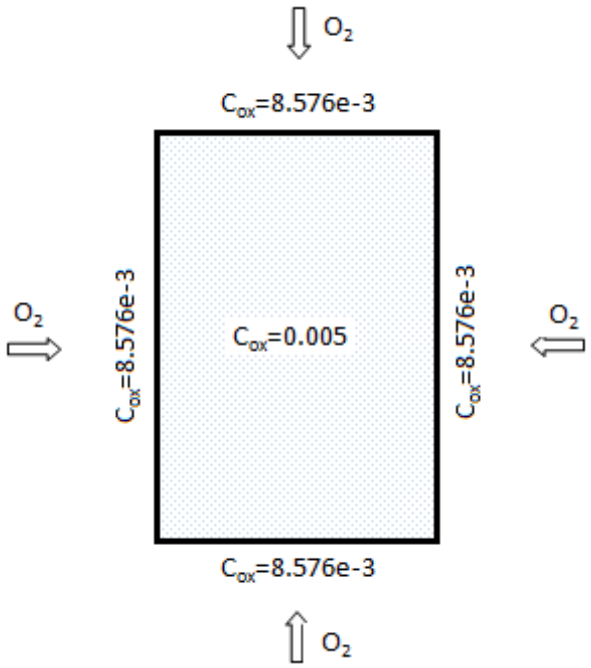


Figure 2.5: Boundary conditions for oxygen concentration calculations

The diffusion coefficient $D_{ox}(H)$ is dependent on the water content of concrete,

$$D_{ox}(H) = 1.92 \cdot 10^{-6} \cdot f_1(H) \tag{2.13}$$

where: $f_1(H)$ – function expressing dependence of diffusion coefficient on relative pore humidity.

In wet concrete, oxygen diffuses in solution, while in partially-saturated concrete, oxygen diffuses partly through the gas phase and partly through the pore solution. To be consumed in the cathodic reaction, oxygen has to be in a dissolved state. The moisture distribution along the concrete cover will certainly affect the amount of oxygen available at the reinforcement level. However, similarly to the case of chlorides, the oxygen diffusion coefficient becomes a constant material parameter due to the assumption of average concentration of pore water.

Thus for oxygen the equation of mass conservation can be written as follows:

$$\frac{\partial C_{ox}}{\partial t} = \nabla \cdot (D_{ox} \nabla C_{ox}) \tag{2.14}$$

with initial and boundary conditions (see Fig. 2.5):

$$C_{ox}(\bar{x}, 0) = 0.005, \quad \bar{x} \in \Omega \tag{2.15}$$

$$C_{ox}(\bar{x}_0, t) = 8.576 \cdot 10^{-3}, \quad \bar{x}_0 \in \Gamma \tag{2.16}$$

The values used in conditions (2.15) and (2.16) correspond to the amount of dissolved oxygen in concrete mixed with typical fresh water and the quantity of dissolved oxygen at the concrete surface.

## 2.2 Corrosion cell

When the chloride threshold value is reached by the free chloride concentration at the reinforcement level, steel becomes depassivated, and corrosion cell is formed. The location of passive layer decomposition is random and depends on the properties of pore solution and mechanical influences. Iron is oxidized to ferrous ions at the anode and the oxygen is reduced releasing hydroxide ions at the cathode. The pore solution is an electrolyte and the steel rebar is a conductor. The macro-cell model is illustrated in Fig. 2.6.

The cathodic half-cell reaction can be described by:

$$O_2 + 2H_2O + 4e^- \rightarrow 4OH^- \tag{2.17}$$

The dissolution of iron at the anodic sites takes place according to:

$$2Fe \rightarrow 2Fe^{2+} + e^- \tag{2.18}$$

The rust is produced according to:

$$Fe^{2+} + 2OH^- \rightarrow Fe(OH)_2 \tag{2.19}$$

$$4Fe(OH)_2 + O_2 + 2H_2O \rightarrow 4Fe(OH)_3 \tag{2.20}$$

The supply of oxygen and water is essential for the progress of steel corrosion. However, water does not directly control the process.

The oxygen molecules are consumed both on the anode and cathode. The number of hydroxide ions produced per unit surface of cathode and per unit time due to oxygen consumption is described by electric current density $i_c$ and can be expressed as [34, 37]:

$$i_c = -F\omega_c Q \tag{2.21}$$

where: $\omega_c$ – number of hydroxide ions produced in the oxygen reduction reaction, $\omega_c = 4$, $Q$ – number of oxygen molecules reduced per unit surface of cathode and per unit time.

The oxygen flux at the cathode or anode surface $j_{c/a}^{ox}$ can be calculated as:

$$j_{c/a}^{ox} = D_{ox}\frac{\partial C_{ox}}{\partial n} \tag{2.22}$$

where: $n$ – outward normal to the cathode/anode surface.

The approaching and reacting oxygen molecules should be in equilibrium, thus the number of oxygen molecules reduced at the cathode can be expressed as:

$$j_c^{ox} = Q \tag{2.23}$$

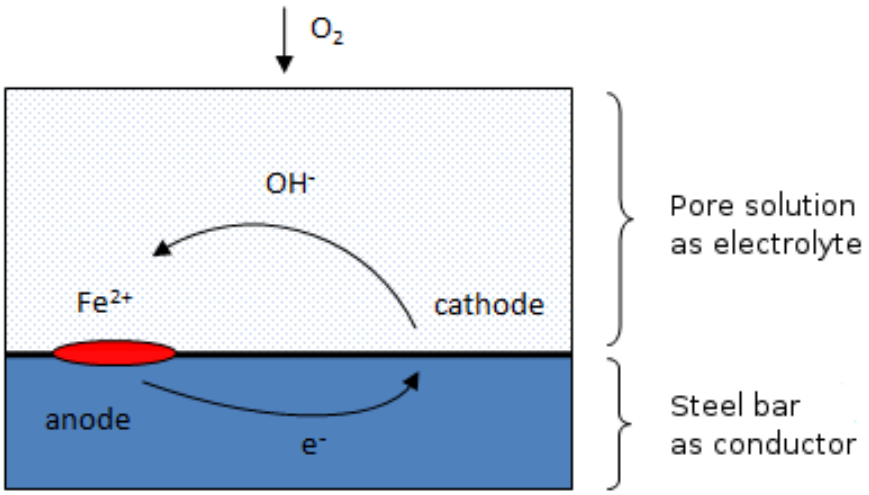


Figure 2.6: Corrosion cell model

or, after substituting eq. (2.21):

$$D_{ox}\frac{\partial C_{ox}}{\partial n}|_{cathode} = -\frac{1}{F\omega_c}i_c \tag{2.24}$$

On the other hand, the hydroxide ions released at the cathode combine with the ferrous ions released at the anode to form ferrous hydroxide. The rate of ferrous hydroxide production at the anode $j_{fh}$ can be evaluated from [34,37]:

$$j_{fh} = \frac{i_a}{F\omega_a} \tag{2.25}$$

where: $i_a$ – current density at the anode surface, $\omega_a = 2$.

According to eq. (2.20) 4 moles of $Fe(OH)_2$ (359.38 g) combine with 1 mol of $O_2$ (32 g/mol) to form 4 moles of $Fe(OH)_3$. Hence, the rate of oxygen consumption at the anode $j_a^{ox}$ is given by [34,37]:

$$j_a^{ox} = -\frac{32}{359.4}j_{fh} \tag{2.26}$$

or, after substituting eq. (2.25):

$$D_{ox}\frac{\partial C_{ox}}{\partial n}|_{anode} = -\frac{1}{F\omega_a}i_a \tag{2.27}$$

When the anodic reaction is in equilibrium, it can be described by reversible potential $E_a^0$ and corresponding exchange current $I_{oa}$ (see Fig. 2.7). The cathodic reaction in equilibrium, is described by reversible potential $E_c^0$ and corresponding exchange current $I_{oc}$. The current flowing causes the polarization of cathode and anode areas, and the difference in potentials is known as overpotential. The relation between half-cell potentials and the

corrosion current flowing through the cell forms the polarization curve of the electrode, known as the Evans diagram (Fig. 2.7) [23, 27, 34].

The polarization can be caused by different types of overpotential. Three types of overpotential can be distinguished: activation, concentration and ohmic overpotential. According to Bulter-Volmer kinetics the anodic reaction is subject to activation polarization, while the reaction at the cathode is subject to activation and concentration polarization. To break the barrier during ion transfer between the electrode and pore solution an external activation energy needs to be supplied. This results in the activation overpotential. The concentration polarization occurs when the reaction is controlled by a slow mass transfer of reactants from solution to the electrode surface.

The kinetics of iron oxidation at the anode and oxygen reduction at the cathode can be expressed by:

$$i_a = i_{oa} e^{\left(2.3 \frac{E_a^0 - E_{corr}}{\beta_a}\right)} \tag{2.28}$$

$$i_c = i_{oc} \frac{C_{ox}}{C_{ox}^s} e^{\left(2.3 \frac{E_{corr} - E_c^0}{\beta_c}\right)} \tag{2.29}$$

where: $i_a$ – current density for iron oxidation reaction, $i_c$ – current density for oxygen reduction reaction, $i_{oa}$ – exchange current density for iron dissolution, $i_{oc}$ – exchange current density for cathodic reaction, $E_a^0$ – standard potential in anodic reaction, $E_c^0$ – standard potential in cathodic reaction, $\beta_a$ – activation Tafel slope for anodic reaction, $\beta_c$ – activation Tafel slope for cathodic reaction, $C_{ox}$ – dissolved oxygen concentration at steel surface, $C_{ox}^s$ – dissolved oxygen concentration at external concrete surface.

Equation (2.29) considers the difference in oxygen concentration at the steel surface and at the external concrete surface. In the case of anodic reaction, the change of concentration of reduced substance can be neglected, due to unlimited iron supply.

As a result of polarization caused by the current flowing between anode and cathode, the potentials of electrode become equal and the reinforcing steel freely corrodes. The new potential, called corrosion potential $E_{corr}$ is a value for which the oxidation and reduction reaction rates are equal. The corrosion potential $E_{corr}$ and corrosion current $I_{corr}$ is a point of intersection of anodic and cathodic branches of the polarization curves in Fig. 2.7. This intersection point represents the conditions in which the anodic and cathodic currents are equal (but opposite in polarity) [23, 34]:

$$I_{corr} = i_{oc} A_c = i_{oa} A_a \tag{2.30}$$

where: $I_{corr}$ – corrosion current, $A_a$ – anode area, $A_c$ – cathode area.

By substituting eqs. (2.28) and (2.29) into eq. (2.30), the corrosion potential can be expressed as:

$$E_{corr} = \frac{1}{\beta_a + \beta_c} \left( \frac{\beta_a \beta_c}{2.3} \ln \left( \frac{i_{oc} C_{ox} A_c}{i_{oa} C_{ox}^s A_a} \right) + \beta_c E_a^0 + \beta_a E_c^0 \right) \tag{2.31}$$

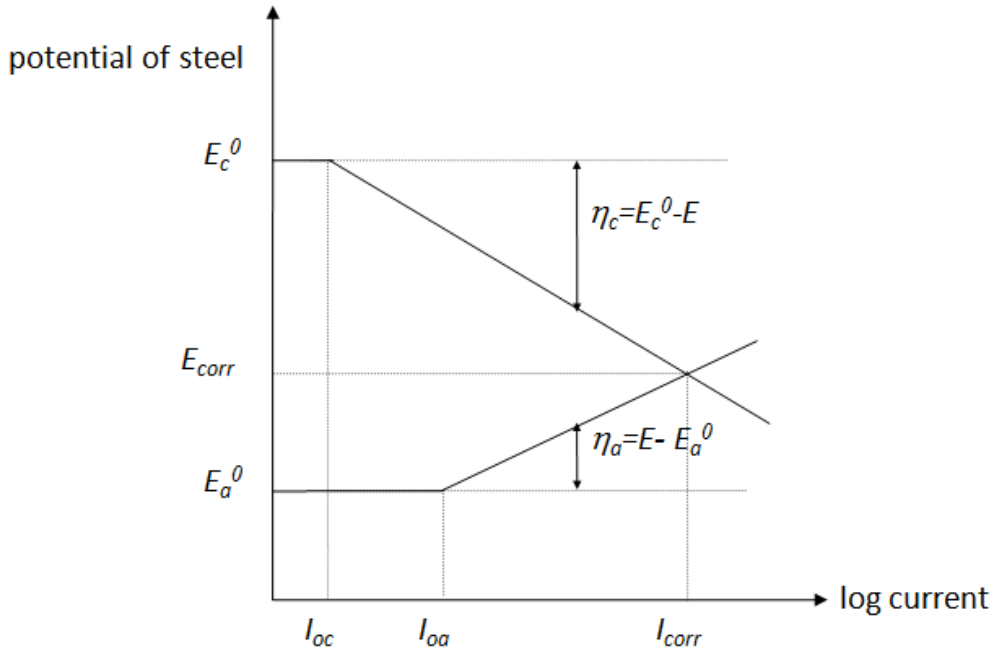


Figure 2.7: Simplified Evans diagram

Equation (2.31) can be used for calculations of the potential in the model based on a cross-section of a reinforced concrete member where the reinforcing steel is considered to be active. However, a better representation of the corrosion process would be obtained by computing the steady-state current flow in the concrete pore solution, where the influence of the concrete electrical resistivity is considered. Such model should be formulated for a longitudinal direction of a reinforced concrete member [34].

Equations (2.28) and (2.29) can be used to define the conditions at the steel/concrete interface. The equation of electrical charge conservation follows from the equation of mass conservation and can be expressed as [34, 37]:

$$\nabla \cdot \mathbf{i} = 0 \tag{2.32}$$

where: $\mathbf{i}$ – current density vector.

The current density vector $\mathbf{i}$ is related to the electrical potential $E$ through Ohm's law:

$$\mathbf{i} = -\sigma \nabla E \tag{2.33}$$

where: $\sigma$ – electrical conductivity of concrete.

The negative sign in eq. (2.33) indicates that the direction of the current is along a voltage drop. Assuming that the electrical conductivity of concrete is constant and uniformly distributed, eq. (2.32) can be written as:

$$\nabla^2 E = 0 \tag{2.34}$$

For given boundary conditions determined using eqs. (2.28) and (2.29), the solution of eq. (2.34) determines the distribution of the electric potential, and the corrosion current can be calculated from eq. (2.33).

The pore structure of concrete, the degree of water saturation, and the total ionic concentration of the pore solution are relevant factors affecting the electrical conductivity of concrete. Since the concrete pore solution acts as an electrolyte with lower resistivity than the cement matrix, the moisture content plays in fact a significant role in determining the electrical properties of concrete. Drying initially water-saturated concrete results in an increase of the resistivity (or decrease of the conductivity).

The concrete electrical resistivity is also affected by the concrete temperature, and is reduced with increasing temperature. At higher temperature, more ions dissolve into the concrete pore solution, facilitating the flow of electrical current [34]. However, it is assumed that the concrete structure is exposed to usual temperature, thus the temperature influence on the concrete properties can be neglected.

Concrete is assumed to be a homogeneous material, thus the electrical conductivity is assumed to be a constant parameter, uniformly distributed throughout the entire material, but depending on the saturation level [37].

## 2.3 Propagation phase

The first sings indicating corrosion are rusty stains on the concrete surface and cracking of the cover. Depending on the oxidation degree the volumetric expansion of corrosion products can vary. Oxides created during the iron oxidation process, can have even 6 times greater volume than iron. Typical oxides produced during corrosion have the following volume ratios in comparison to iron: $FeO = 1.7$, $Fe_3O_4 = 2$, $Fe_2O_3 = 2.1$, $Fe(OH)_2 = 3.6$, $Fe(OH)_3 = 4.0$, and $Fe(OH)_3 \cdot 3H_2O = 6.15$. Considering the fact that 1 mol of Fe is 55.85 g, 1 mol of $O_2$ is 32 g, and 1 mol of $H_2$ is 2 g, the iron-to-rust molecular weight ratio $r_m$ is equal to 0.523 for $Fe(OH)_3$ and 0.622 for $Fe(OH)_2$ [42]. When the volume of all corrosion products takes too much space, hoop stresses exceed the concrete tensile strength and a longitudinal crack is formed. In view of the fact that it is not possible to reliably define the rust structure, it has been assumed that the rust density is a fraction of steel density. Thus the mass and density of rust are respectively expressed as:

$$M_r = \frac{M_s}{r_m} \qquad \rho_r = \frac{\rho_s}{\gamma} \tag{2.35}$$

where: $M_r$ – mass of rust, $M_s$ – mass of steel, $\rho_r$ – rust density, $\rho_s$ – steel density, $\gamma$ – parameter with a value usually ranging 2 – 4.

The loss of rebar diameter caused by corrosion process can be expressed in mm, using an empirical relation (see Fig. 2.8):

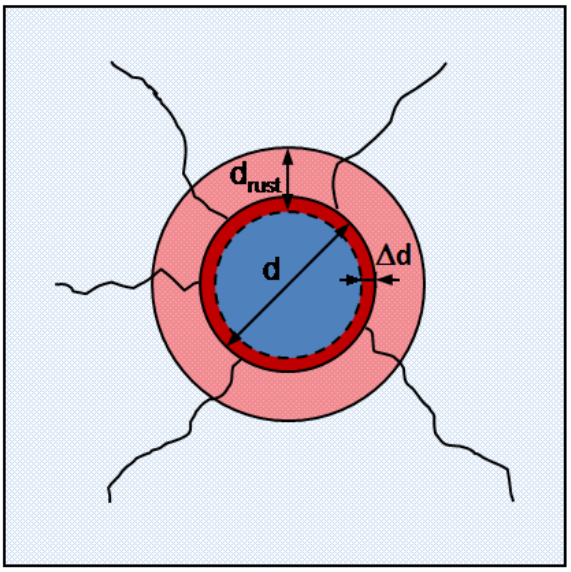


Figure 2.8: Rust volumetric expansion

$$d_{red} = d - \Delta d = d - 0.023 i_{corr} \Delta t \tag{2.36}$$

where: $d_{red}$ – reduced diameter, $d$ – initial diameter in mm, $i_{corr}$ – corrosion current density in $\frac{\mu A}{cm^2}$, $\Delta t$ – time of propagation phase in years. However, one must notice that the diameter reduction is negligible when compared with the initial diameter.

The mass of steel consumed in the process $M_s$ can be expressed by Faraday's law:

$$\frac{dM_s}{dt} = \frac{m_a I_{corr}}{zF} \tag{2.37}$$

where: $m_a$ – atomic weight of dissolved ions (for Fe $m_a$=55.85 g/mol), $z$ – valence of ions, assumed to be equal to 2.

Taking into account eq. (2.35) and expressing the corrosion current in A/m as:

$$I_{corr} = \pi d \, i_{corr} \tag{2.38}$$

the mass of rust produced in the process can be expressed as:

$$M_r = \frac{2.895 \cdot 10^{-7} \pi d \Delta t \, i_{corr}}{r_m} \tag{2.39}$$

The geometry of rust is rather irregular and rarely uniformly distributed around the reinforcement. However, it is now assumed for simplicity that all corrosion products are accumulated uniformly along the rebar perimeter, as illustrated in Fig. 2.8. Hence, the relation between the change of volume and unit volume of reinforcement bar can be expressed as:

Table 2.1: Empirical relationship between corrosion rate and remaining service life [25]

| $i_{corr}$ [A/cm$^2$] | Service life |
|---|---|
| $i_{corr} < 0.5$ | no corrosion damage expected |
| $0.5 \leq i_{corr} < 2.7$ | corrosion damage possible in 10–15 years |
| $2.7 \leq i_{corr} < 27$ | corrosion damage expected in 2–10 years |
| $27 \leq i_{corr}$ | corrosion damage expected in 2 years or less |

$$\epsilon_v = \frac{\Delta V}{V} = \frac{M_r}{\frac{\pi d^2}{4}} \left( \frac{1}{\rho_r} - \frac{0.523}{\rho_s} \right) \tag{2.40}$$

Equation (2.40) represents the radial expansion due to corrosion. The volumetric expansion of corrosion products results in the formation of internal pressure expressed by:

$$p = \frac{E_r}{2\,(1+\nu_r)\,(1-2\nu_r)}\,\epsilon_v \quad \rightarrow \quad p = \psi \cdot i_{corr} \tag{2.41}$$

where: $E_r$ – rust Young modulus, $\nu_r$ – rust Poisson ratio.

The mechanical properties of rust are hard to be determined. It is common to assume that rust behaves like water with bulk modulus $K_r$ equal to 2 GPa and Poisson ratio 0.49 [3, 34], although there were attempts to test rust specimens, cf. [3].

Equation (2.41) is a linear relation between internal pressure acting on the concrete cover and corrosion current density $i_{corr}$. This is an effect of using Faraday's law for the calculations of mass of rust products. The Faraday's law assuming constant rust production is the most common model used in corrosion calculations, however one can find other models assuming variable rate of the process [3, 31, 42, 49].

In [25] one can find also the empirical relation between the corrosion current density and the remaining service life time reported in Table 2.1.

### 2.3.1 Concrete cylinder model

The most popular model used for the analysis of the state of stress in the concrete surrounding a corroding reinforcement bar is a thick-walled cylinder model [5]. The thickness of the ring is defined as the shortest distance from rebar to concrete surface, i.e. the shortest way to crack the concrete cover. The stresses caused by rust expansion are treated as a homogeneous pressure and the problem of an empty thick-walled cylinder with an axisymmetric load is considered in plane strain conditions. The plain strain state corresponds well with the corrosion-induced damage due to the following assumptions: concrete is a homogeneous elastic material and cylinder length to radius ratio is high enough to assume that the longitudinal strain is zero.

The equations for the analysis of the isotropic linear-elastic hollow cylinder, loaded with axisymmetric pressure acting on the internal surface and including appropriate

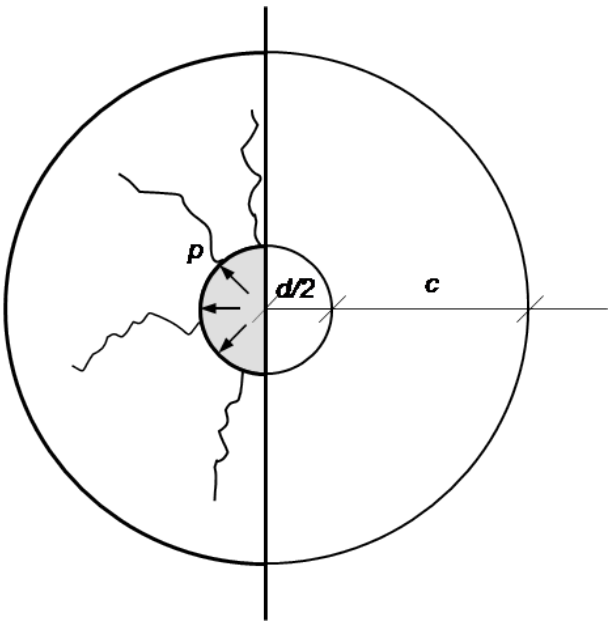


Figure 2.9: Concrete cylinder model

boundary conditions, can be expressed as follows:

- equilibrium equations

$$\sigma_r + \frac{d\sigma_r}{dr} r - \sigma_\theta = 0 \tag{2.42}$$

- geometrical equations

$$\varepsilon_r = \frac{du_r}{dr} \qquad \varepsilon_\theta = \frac{u_r}{r} \tag{2.43}$$

- constitutive equations

$$E_r \varepsilon_r = \sigma_r - \nu_{r\theta}\sigma_\theta - \nu_{rz}\sigma_z \tag{2.44}$$

$$E_\theta \varepsilon_\theta = \sigma_\theta - \nu_{\theta r}\sigma_r - \nu_{\theta z}\sigma_z \tag{2.45}$$

When the tensile stress $\sigma_\theta$ is no longer balanced by the tensile strength of concrete $f_t$, an internal crack starts to form. In this situation two layers can be distinguished in the concrete ring: the inner part, in which the hoop stresses have already reached $f_t$, and the outer part, in which concrete is still a continuous elastic material and the stress values are below $f_t$ (see Fig. 2.9).

When a crack develops, pressure $p$ is carried by the outer layer and its value is reduced together with the expansion of the cracked zone. When cracks penetrate through the whole thickness revealing reinforcement the load carrying capacity of the concrete cylinder under tension is reached. According to [49] the relation between loss of diameter $\Delta d$ and crack width $\Delta w$ can be approximated by a linear function, where the proportionality factor depends on initial diameter $d$ and concrete cover $c$ (see Fig. 2.9), all expressed in mm:

$$\Delta w = \left(\frac{1}{\gamma} - 1\right) \pi d \frac{d/2 + c}{(d + c)\, c} \Delta d \tag{2.46}$$

where: $\Delta d$ – rebar diameter reduction, eq. (2.36).

The thick-walled cylinder model has some limitations, especially due to the simplification in geometry. However, the cylinder model is considered as a foundation for corrosion estimations.

### 2.3.2 Bond reduction

Corrosion of reinforcing bar can greatly influence the bond strength between deformed bars and concrete, leading to relative displacements between steel and concrete. First, the soft layer created by the accumulated corrosion products on the bar surface may effectively reduce the friction component of the bond strength. In addition, the deterioration of the ribs of the deformed bars causes a significant reduction of the interlocking forces between the ribs of the bars and the surrounding concrete keys. Second, the accumulated corrosion products on the bar surface cause cracking of the concrete cover. The loss of concrete cover implies a loss of confinement and a reduction in bond strength. However, it is quite difficult to distinguish the effects of the reduction in bond strength due to the loss of concrete cover and due to the loss of friction.

During the RC element performance the concrete keys become crushed by the reinforcement ribs. This generates microcracking around rebar. Next, diagonal forces act in concrete to balance the force in the reinforcement bar [9]. The angle of the forces is always larger than 45° [48]. The diagonal forces are balanced by longitudinal compression forces and circumferential tensile forces, presented in Fig. 2.10.

When the tensile stresses, forming rings around reinforcement exceed concrete tensile strength the concrete cracks. However, the cover thickness can help to mitigate the damage in concrete. It has been established that cover with thickness of $2.5\phi - 3.0\phi$ is enough to prevent cracking due to pullout [48].

The pullout action generates tangential stresses $\tau$ at concrete-steel interface, expressed as:

$$\tau = \frac{(\sigma_s + d\sigma_s)A_s - \sigma_s A_s}{\Pi\, d\, dx} = \frac{d}{4}\,\frac{d\sigma_s}{dx} \tag{2.47}$$

where: $A_s$ – bar cross-section area, $\sigma_s$ – axial stress in the reinforcement.

Hence, the radial, tensile component of bond stress $p_b$ is given by:

$$p_b = \tau \tan(\phi) \tag{2.48}$$

Initially, for low levels of corrosion the radial stresses increase causing initial small increase of bond strength. Further rust accumulation leads to cracking of the concrete cover, which results in noticeable reduction of bond strength. The confining action can

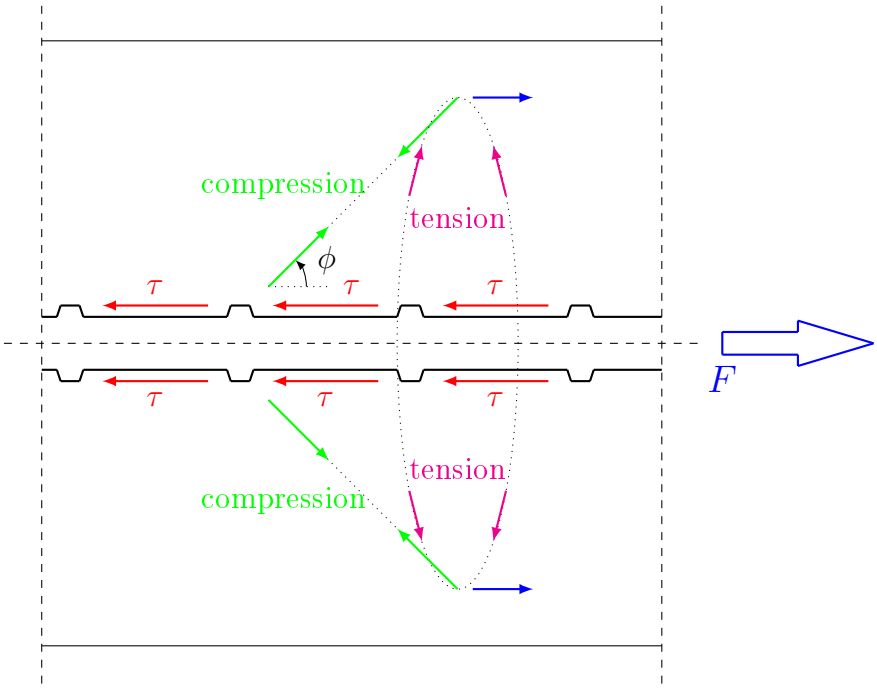


Figure 2.10: Distribution of forces in concrete around rebar during pullout bond reduction

be provided only by the transverse reinforcement, minding that this confinement will decrease too if the transverse reinforcement are affected by corrosion.

The total radial pressure applied at steel-concrete interface is a sum of corrosion pressure $p$ and radial bond component $p_b$:

$$p_{total} = \tau \tan(\phi) + p \tag{2.49}$$

Thus, the reduction of tangential stresses can be expressed as [34]:

$$\tau = \frac{1}{\tan(\phi)} \left(p_{total} - p\right) \tag{2.50}$$

Assuming that the total pressure around reinforcement must be balanced by concrete strength, pressure $p_{total}$ can be treated as a material characteristic, depending on concrete tensile strength, concrete cover thickness and presence of transverse reinforcement.

# Chapter 3

# Calculation models

## 3.1 Analysis scheme

Within the framework of the thesis calculations of the corrosion process are performed considering both the initiation and propagation phases. The scheme of the calculation procedure is presented in Fig. 3.1. The computations are divided into two parts. The first one includes the determination of chloride and oxygen concentrations, as well as of the corrosion current and volumetric expansion of rust. The second part considers the mechanical aspect of corrosion. For the purpose of the first part of calculations a Matlab script is written considering the mathematical model presented in Section 2.1. The loading programme determined as a result of the first part of calculations is implemented in Abaqus, the Finite Element package, used for the second stage. In Abaqus the influence of corrosion on concrete cracking and concrete-steel bond is analyzed.

The research included in the dissertation generally considers the response of an RC element to chloride corrosion, however during the analysis a few minor issues are also investigated. The main goal is the analysis of the influence of expanding corrosion products on reinforced concrete member.

During the initiation phase of corrosion, the key point is to assume the proper chloride threshold value and binding relation. The duration of the initiation phase can in fact be identified as the service life-time of a structure. Once the reinforcement is depassivated, the destruction due to corrosion is very quick. Therefore, the calculations of initiation time should be performed with respect to available experimental data, possibly considering all the phenomena appearing during the phase. However, it must be noticed that in the experimental results available in literature there are discrepancies in many data items, such as diffusion coefficients, binding parameters or chloride threshold values. Hence, in the simulation presented in the thesis, some arbitrary material properties are going to be used. Additionally, parametric studies performed, hoping to bring a reliable model representing the initiation phase of corrosion.

In the second part of calculations the Finite Element models are built to analyze the mechanical processes occurring in the RC members due to reinforcement corrosion.

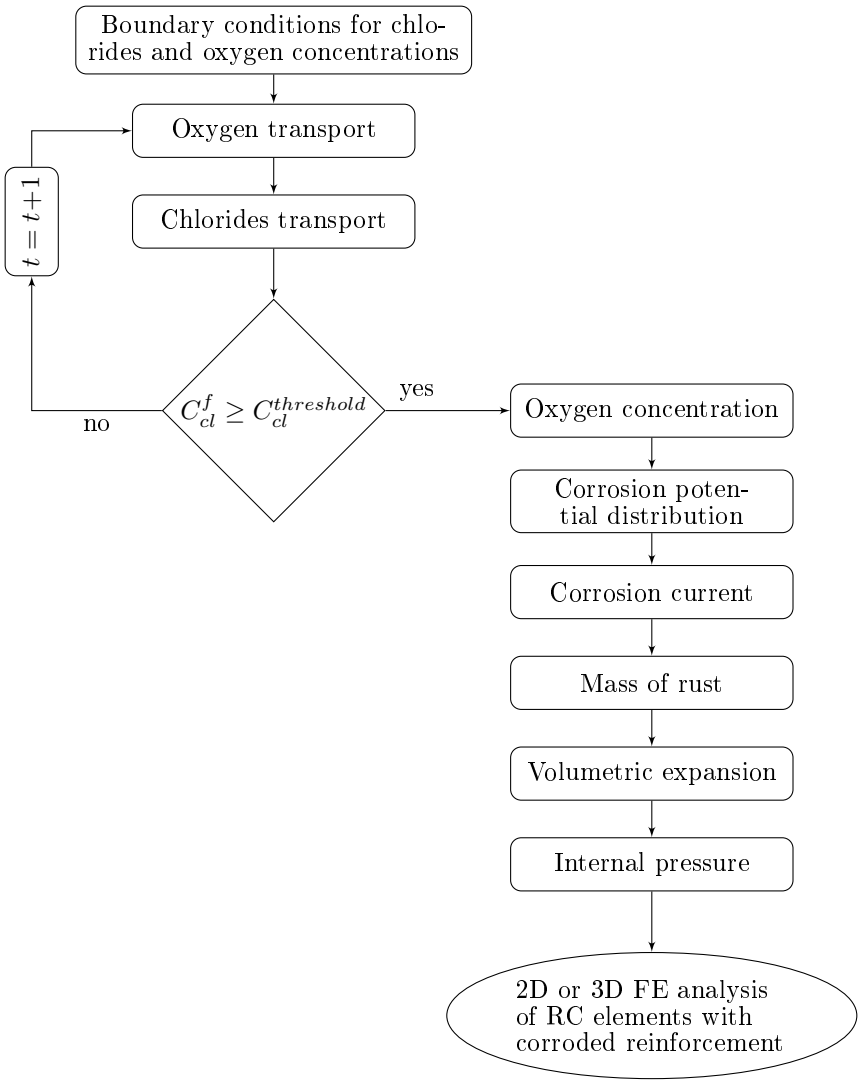


Figure 3.1: Calculation procedure

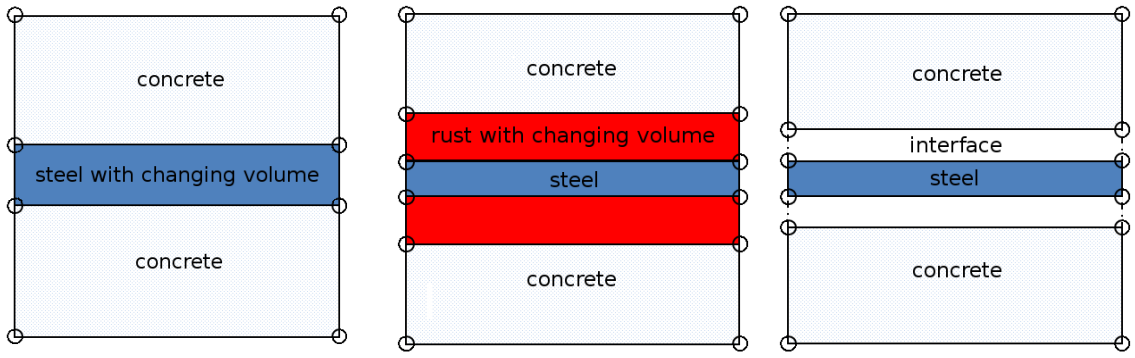


Figure 3.2: Different versions of concrete-rust-steel interface models: (a) – continuum model of steel and concrete, (b) – continuum model composed of three layers, (c) – continuum model of steel and concrete, corrosion introduced as interface elements

The chloride corrosion is a constantly investigated problem, however the composition of corrosion products is not known in advance. The mechanical parameters such as Young modulus or Poisson ratio are arbitrarily selected, moreover the character of the contact between rust and concrete and actions occurring on the contact surface need to be approximated. The concrete-rust-steel interface models can be built in different ways. The first one is a continuum model of steel and concrete, in which corrosion expansion is represented by a change of volume of steel. The alternative representation is a continuum model of three layers – steel, rust and concrete. In the third variant steel and concrete are modeled with continuum elements, while corrosion products are introduced as interface elements. The last model could represent three materials and interfaces between them. Different versions of the concrete-rust-steel interface model are presented in Fig. 3.2.

Another problem to be solved is to create a credible way of applying rust expansion. There are three proposals in this respect. The first one is to apply an equivalent pressure estimated on the basis of the electro-chemical analysis. In this option the uniformly distributed pressure representing the action of expanding corrosion products is applied to the steel-rust-concrete contact surfaces. The second is to create a layer of rust material. During the calculations the thickness of the layer increases, imitating the behavior of volumetric expansion of corrosion products. The last concept is to represent the action of expanding corrosion products by the behavior of interface elements placed between particular materials. As corrosion products increase their volume, the interfaces between concrete and steel open (and possibly slide).

The FE models presented in this thesis are built using two materials – concrete and steel, and rust interface between them. The rust expansion is represented by the opening of the interface.

In a general case, a three-dimensional FE model needs to be constructed to analyze both the action of corrosion products and the external loading applied to the element. The

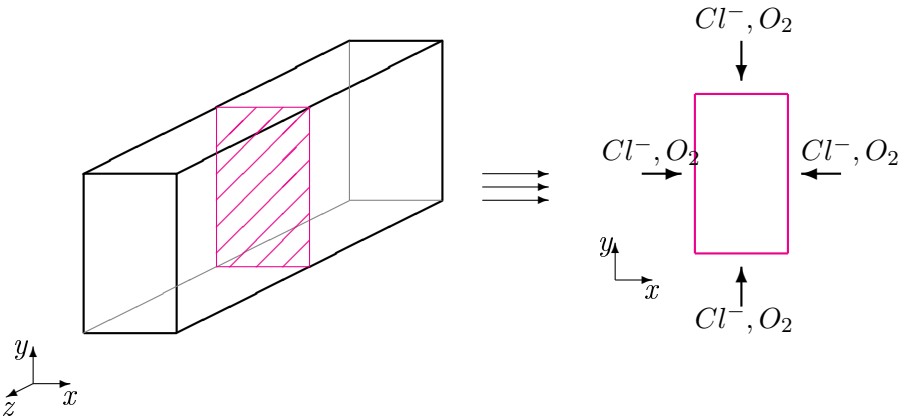


Figure 3.3: Configuration for concentration calculations

research involves two ways of loading. It investigates how the corroded element behaves under the external loading and, on the other hand, how the loaded element behaves when additionally chloride corrosion occurs.

As the component materials are represented as inelastic, Newton-Raphson algorithm is used in the nonlinear computations. Moreover, the FE calculations are performed with two time integration schemes – explicit and implicit.

## 3.2 Numerical model of initiation phase and corrosion current

In the first part of calculations the chloride and oxygen transport are analyzed, as well as the corrosion current and volumetric expansion are estimated. It has been assumed that all the material parameters governing the chloride and oxygen transport problem are constant during the analysis. Concrete is considered at the macroscale as a good quality homogeneous material with a water-to-cement ratio $w/c$ equal to 0.4. Due to the assumption of average saturation of concrete with pore water, the diffusion coefficients for both chlorides and oxygen are constant material parameters, uniformly distributed throughout the whole concrete element( attention is focused on beams). What is more, for simplicity, during the initiation phase concrete is assumed to be solid, without any slots for reinforcement. The degree of water saturation is assumed to be 65% and concrete is uncracked. For the initiation phase calculations concrete is a 3D block with constant material parameters and one 2D cross-section can be analyzed. The concentrations of oxygen and chlorides calculated for one cross-section are assumed to be the same in all other cross-sections along the beam longitudinal axis. The configuration for oxygen and chloride concentration calculations is presented in Fig. 3.3.

The electric conductivity of concrete, which in fact is dependent on the degree of

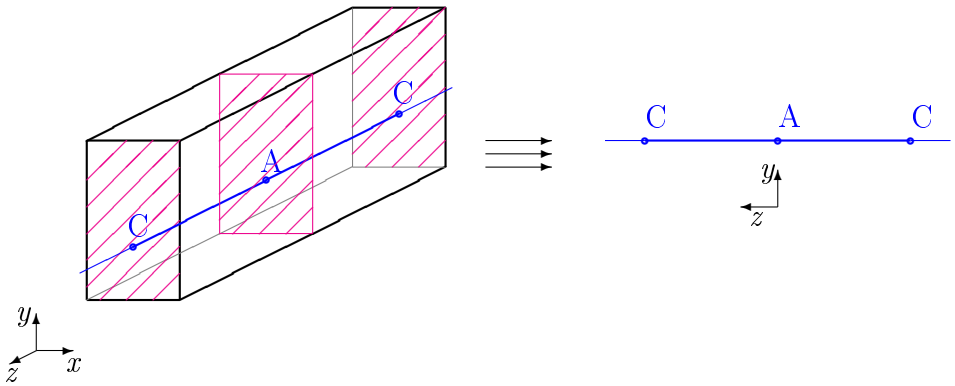


Figure 3.4: Configuration for current calculations (C – cathode, A – anode)

water saturation and porosity, is considered as constant throughout the entire solid. As the electric current flows through the rebar, the current and potential calculations should be performed in a configuration along the reinforcement axis. In the analysis it is assumed that one, specified beam cross-section is related to anode and another one is related to cathode. With this assumption the boundary conditions for the potential distribution can be calculated for specified nodes. The potential distribution and corrosion current are calculated in 1D configuration presented in Fig. 3.4.

The chlorides binding is assumed to run according to Freundlich isotherm, see eq. (2.4). Considering this fact, eq. (2.9) can be rewritten as:

$$\frac{\partial C_{cl}^{f}}{\partial t} = \nabla \cdot \left(\mathbf{J}_{cl}^{f}\right) - \frac{\partial C_{cl}^{b}}{\partial C_{cl}^{f}} \frac{\partial C_{cl}^{f}}{\partial t} \tag{3.1}$$

which leads to:

$$\frac{\partial C_{cl}^{f}}{\partial t} = \frac{1}{1 + \alpha\beta \left(C_{cl}^{f}\right)^{\beta-1}} \nabla \cdot \left(\mathbf{J}_{cl}^{f}\right) \tag{3.2}$$

By assuming the values of $\alpha$ and $\beta$ the binding relation can be controlled. The expression (3.2) allows one to obtain the results for no binding ($\alpha = 0$), linear binding ($\alpha \neq 0$, $\beta = 1$) or nonlinear binding ($\alpha, \beta \neq 0$, $\beta \neq 1$).

For computation of the chloride and oxygen concentrations cellular automata (CA) are used. CA are mathematical idealizations of physical systems in which space and time are discrete and physical quantities are taken from a finite set of discrete values. Any physical system satisfying differential equations may be approximated as a CA by introducing discrete coordinates and variables, as well as discrete time steps. The CA can be understood as an alternative approach to physical modelling rather than an approximation. Due to their simple formulation they are potentially adaptable to a more detailed and complex analysis, giving to the whole system some properties, self-induced only by its local dynamics [10].

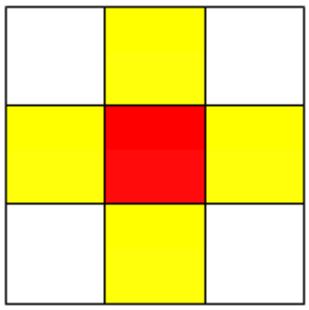

Figure 3.5: Von Neumann neighborhood of the cell: red – the considered cell, yellow – neighbors

The elementary form of CA consist of a regular uniform grid of cells with a discrete variable in each cell taking one of a finite number of states. The set of variables $c_i^k = c_i(t_k)$ at each cell $i$ and time $k$, defines the state of CA. As calculations proceed CA evolves in discrete time steps according to a specified rule. The updated state of CA is defined by "new" values of variables $c_i^{k+1} = c_i(t_{k+1})$ based on the values of variables $c_n^k$ in their neighborhood $n$ and the cell itself at the preceding time $t_k$. Thus, the dynamics of a CA can be formally represented as [10]:

$$c_i^{k+1} = \Phi\left(c_i^k; c_n^k\right) \qquad i - r \leq n \leq i + r \tag{3.3}$$

where: $\Phi$ – evolutionary rule of the automaton, $r$ – radius specifying cell neighborhood.

A proper choice of the neighborhood plays a crucial role in determining the effectiveness of such a rule. One of the possible neighborhoods is von Neumann neighborhood, presented in Fig. 3.5. It consists of cells belonging to a cross, while the center lies in the considered cell. Also attention should be paid to the cells lying at the boundary of the cell grid, where neighbors exist on one side only.

Thus, eq. (3.2), as well as eq. (2.14) can be effectively simulated by adopting a von Neumann neighborhood with radius equal to 1, which means the concentration calculated in the closest neighbors affects the value of concentration in the considered cell. The rule of evolution is expressed as [10, 58]:

$$C_i^k = \varphi_0 \cdot C_i^{k-1} + \sum_{j=1}^{n} (\varphi_j^- \cdot C_{i-1,j}^{k-1} + \varphi_j^+ \cdot C_{i+1,j}^{k-1}) \tag{3.4}$$

where: $C_i^k$ – concentration of substance in cell $i$ at time $t_k$, $n$ – number of dimensions ($n = 2$).

The values of the evolutionary coefficients must satisfy the following normalization rule, required by the mass conservation law [10, 58]:

$$\varphi_0 + \sum_{j=1}^{n} (\varphi_j^- + \varphi_j^+) = 1 \tag{3.5}$$

To ensure the stability of the numerical procedure, the relative time step measure should be maximum 0.5 [10, 35, 58]:

$$\frac{\Delta t \cdot D_i}{\Delta x^2} \leq 0.5 \tag{3.6}$$

where: $\Delta t$ – time step, $D_i$ – diffusion coefficient for particular substance and $\Delta x$ – grid dimension.

The diffusion potential of chlorides used in eq. (2.9) is calculated in the 2D cross-section configuration (Fig. 3.3). The Poisson eq. (2.6) is solved using FDM, with central difference expressions. The convergence is achieved by assuming that the maximum error value between two iterations cannot be greater than $10^{-6}$. The convergence condition is assumed as:

$$\frac{\sum_{i,j} \psi_{i,j}^{l} - \sum_{i,j} \psi_{i,j}^{l-1}}{\sum_{i,j} \psi_{i,j}^{l-1}} \leq 10^{-6} \tag{3.7}$$

where: $\sum_{i,j} \psi_{i,j}^{l}$ – sum of chlorides potential values at nodes $i, j$ of cross-section in iteration $l$.

The chlorides and oxygen concentrations are calculated repeatedly in a time loop until the free chloride threshold value is reached (see Fig. 3.1). After reaching the chloride threshold the electric potential distribution is calculated with respect to the current oxygen concentration. The Laplace eq. (2.34) is solved using FEM for a 1D problem with Lagrange shape functions. The distribution is calculated for the section of rebar, between two cathodes, illustrated in Fig. 3.4. The anode is assumed in the middle of the section. Due to symmetry, only half of the section is analyzed, between the anode and a cathode. The boundary conditions for the potential at anode and cathode sites are calculated from eqs. (2.28) and (2.29), assuming that initially the anode and cathode current densities are equal to $i_{oa}$ and $i_{oc}$, respectively. The proposed model does not consider any additional conditions for anode and cathode sites. The cathode and anode areas are not in any relation and they become equal with time. The corrosion current is calculated according to eq. (2.33). The equation is solved using FEM with Lagrange shape functions as well.

The mass of rust and volumetric expansion are calculated according to the analytical expressions presented in Section 2.3. As a result of the first part of calculations a loading programme is achieved. In further analysis the obtained pressure evolution is applied at the steel-concrete interface, to simulate cracking of concrete and reduction of bonding between those two components of RC structural member.

## 3.3 Numerical model of propagation phase

The proposed model of corrosion effects in RC cross-section is focused on the analysis of cracking of concrete, caused by rust expansion. To simulate the influence of corrosion on bonding between steel and concrete, the entire RC structural element needs to be modelled. Two- and three-dimensional models are built using FEM. The simulation of

damage due to corrosion is performed in the Abaqus package. The FE models consider material models available in Abaqus, which are briefly discussed below.

### 3.3.1 Damage-plasticity model

The first constitutive model for concrete behavior used in the calculations is based on the plasticity-damage formulation proposed by Lubliner [33] and modified by Lee and Fenves [29]. The model aims at capturing the effects of irreversible damage associated with the failure mechanisms under low confining pressures.

In the theory summarized below small strains are assumed and Voigt's matrix-vector notation is used. It is well-known that in the theory of small strains the strain rate tensor $\dot{\boldsymbol{\varepsilon}}$ can be decomposed into elastic part $\dot{\boldsymbol{\varepsilon}}^e$ and plastic part $\dot{\boldsymbol{\varepsilon}}^p$:

$$\dot{\boldsymbol{\varepsilon}} = \dot{\boldsymbol{\varepsilon}}^e + \dot{\boldsymbol{\varepsilon}}^p \tag{3.8}$$

The elastic constitutive relation can be expressed as:

$$\dot{\tilde{\boldsymbol{\sigma}}} = \mathbf{D}^e \dot{\boldsymbol{\varepsilon}}^e = \mathbf{D}^e (\dot{\boldsymbol{\varepsilon}} - \dot{\boldsymbol{\varepsilon}}^p) \tag{3.9}$$

where: $\dot{\tilde{\boldsymbol{\sigma}}}$ – effective stress rate tensor and $\mathbf{D}^e$ – elastic moduli tensor.

In the adopted damage-plasticity model the physical configuration (real damaging specimen) and the so-called effective configuration (undamaged "skeleton" of the specimen) are distinguished, and strain equivalence in the two configurations is assumed.

The material degradation associated with cracking of concrete leads to a reduction of the initial elastic stiffness denoted by $\mathbf{D}^e$. According to the simplest concept of isotropic continuum damage, a scalar damage variable $d$ is introduced to relate the degraded secant stiffness operator $\mathbf{D}^e_{sec}$ to the elastic stiffness matrix $\mathbf{D}^e$:

$$\mathbf{D}^e_{sec} = (1 - d)\, \mathbf{D}^e \tag{3.10}$$

The value of scalar degradation variable changes within the range $0 \leq d \leq 1$. This allows one to express the stress in terms of effective stress $\tilde{\boldsymbol{\sigma}}$ acting on the undamaged skeleton of the material:

$$\boldsymbol{\sigma} = (1 - d)\tilde{\boldsymbol{\sigma}} = (1 - d)\mathbf{D}^e(\boldsymbol{\varepsilon} - \boldsymbol{\varepsilon}^p) \tag{3.11}$$

The damage-plasticity model available in Abaqus expresses the yield function as a function of effective stress and hardening variables:

$$F(\tilde{\boldsymbol{\sigma}}, \tilde{\boldsymbol{\varepsilon}}^p) \leq 0 \tag{3.12}$$

For quasi-brittle materials the yield function is a surface in the effective stress space, for which an inelastic or damage state can be determined. Figure 3.6 shows its 2D representation. The plastic flow is governed by a flow potential $\Phi$, defined in the effective stress space, according to nonassociated flow rule:

$$\dot{\boldsymbol{\varepsilon}}^p = \dot{\lambda}\frac{\partial \Phi(\tilde{\boldsymbol{\sigma}})}{\partial \tilde{\boldsymbol{\sigma}}} \tag{3.13}$$

where: $\dot{\lambda}$ – nonnegative plastic multiplier, satisfying Kuhn–Tucker conditions:

$$\dot{\lambda}F = 0 \qquad \dot{\lambda} \geq 0 \qquad F \leq 0 \tag{3.14}$$

The evolution of the degradation variable is governed by a set of hardening variables $\tilde{\boldsymbol{\varepsilon}}^p$ and the effective stress $d(\tilde{\boldsymbol{\sigma}}, \tilde{\boldsymbol{\varepsilon}}^p)$. The responses related to tensile and compressive damage are different in concrete, therefore it is not convincing to represent all damage states by a single parameter [29]. In the model implemented in Abaqus the damage states are characterized independently by two hardening variables $\tilde{\varepsilon}_t^p$ and $\tilde{\varepsilon}_c^p$, which are referred to as equivalent plastic strains in tension $(t)$ and compression $(c)$:

$$\tilde{\boldsymbol{\varepsilon}}^p = \begin{bmatrix} \tilde{\varepsilon}_t^p \\ \tilde{\varepsilon}_c^p \end{bmatrix} \tag{3.15}$$

Microcracking and crushing are represented by increasing values of hardening variables. The variables control the evolution of the yield surface and the degradation of the elastic stiffness. After computing the time derivative of eq. (3.11), since all infinitesimal quantities can be related to the strain rate (both damage and plasticity are strain-driven), the tangent relation between strain and stress rates can be computed:

$$\dot{\boldsymbol{\sigma}} = \mathbf{D}^{dp}\dot{\boldsymbol{\varepsilon}} \tag{3.16}$$

where $\mathbf{D}^{dp}$ denotes the tangent stiffness operator for the damage-plasticity model (in the computational algorithm so-called consistent tangent is used, cf. [7]).

The constitutive relations for the elastic-plastic response are decoupled from the stiffness degradation response. When concrete is unloaded from any point on the strain softening branch, the unloading stiffness is weakened due to damage. To separate the specimen response in tension and compression, two damage variables are assumed to be functions of the equivalent plastic strains:

$$d_t = d_t(\tilde{\varepsilon}_t^p), \qquad d_c = d_c(\tilde{\varepsilon}_c^p) \tag{3.17}$$

It is noted that damage in quasi-brittle materials can be related to the fracture energy $G_f$ which is the amount of energy required to generate micro-cracks. Softening of concrete is partly a structural phenomenon, nevertheless the fracture energy is treated as a material property. It is normalized by the localization zone size $l$ (also referred to as crack band width), which leads to the following expression for specific fracture energies $g_{t/c}$:

$$g_{t/c} = \frac{G_{t/c}}{l} = \int \sigma(\varepsilon^p) d\varepsilon^p \tag{3.18}$$

Thereby separate fracture energies $G_{t/c}$ are postulated for tension $(t)$ and compression $(c)$ [29].

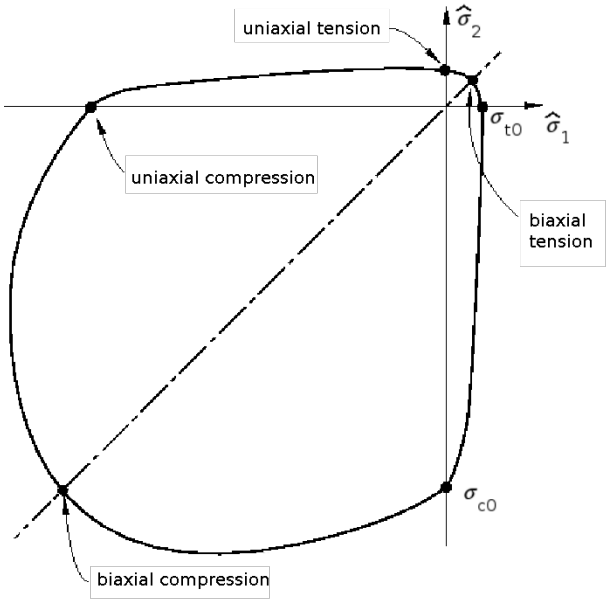


Figure 3.6: Yield function in damage-plasticity model [47]

In uniaxial state the evolution equation for hardening variables can be related to the fracture energies $g_t$ and $g_c$ by:

$$\dot{\tilde{\varepsilon}}_t^p = \frac{1}{g_t} f_t(\tilde{\varepsilon}_t^p)\dot{\varepsilon}^p \ , \qquad \dot{\tilde{\varepsilon}}_c^p = \frac{1}{g_c} f_c(\tilde{\varepsilon}_c^p)\dot{\varepsilon}^p \tag{3.19}$$

where: $f_t$ and $f_c$ – tension and compression "yield" stresses, respectively.

For multiaxial conditions eq. (3.19) involves eigenvalues of stress and plastic strain rate tensors. The matrix $\tilde{\mathbf{h}}(\tilde{\boldsymbol{\sigma}}, \tilde{\boldsymbol{\varepsilon}}^p)$ is related to the fracture energies by:

$$\mathbf{h}(\tilde{\boldsymbol{\sigma}}, \tilde{\boldsymbol{\varepsilon}}^p) = \tilde{\mathbf{h}}(\tilde{\boldsymbol{\sigma}}_{eig}, \tilde{\boldsymbol{\varepsilon}}^p) = \begin{bmatrix} r(\tilde{\boldsymbol{\sigma}}_{eig}) \cdot f_t(\tilde{\varepsilon}_t^p)/g_t & 0 & 0 \\ 0 & 0 & (1 - r(\tilde{\boldsymbol{\sigma}}_{eig})) \cdot f_c(\tilde{\varepsilon}_c^p)/g_c \end{bmatrix} \tag{3.20}$$

where: $\tilde{\boldsymbol{\sigma}}_{eig}$ – effective stress eigenvalues matrix.

The scalar quantity $r(\tilde{\boldsymbol{\sigma}}_{eig})$ is a stress weight factor, with a value ranging $0 \leq r(\tilde{\boldsymbol{\sigma}}_{eig}) \leq 1$. Thus, for multiaxial conditions the evolution of hardening variables can be expressed as:

$$\dot{\tilde{\boldsymbol{\varepsilon}}}^p = \tilde{\mathbf{h}}(\tilde{\boldsymbol{\sigma}}_{eig}, \tilde{\boldsymbol{\varepsilon}}^p) \cdot \dot{\boldsymbol{\varepsilon}}_{eig}^p \tag{3.21}$$

where: $\dot{\boldsymbol{\varepsilon}}_{eig}^p$ – matrix of eigenvalues of plastic strain rate. The eigenvalues are placed in those matrices in algebraic order.

Although tensile and compressive damage variables are defined separately, both responses are described with a single damage variable $d$ defined as:

$$(1-d) = (1-s_c d_t)(1-s_t d_c) \tag{3.22}$$

where: $s_t$ and $s_c$ – functions of stress state that are introduced to represent stiffness recovery effects associated with stress reversals. Their values change within the range $0 \leq s_t, s_c \leq 1$.

The model can be equipped with viscoplastic regularization according to a generalization of the Devaut-Lions approach, in which a viscous upgrade of the plastic strain tensor and hardening variables is derived using an additional viscosity parameter, called relaxation time $\mu$, c.f. [47]. The rate-dependence related to viscosity provides an additional ductility in the model and is an efficient method to overcome the problems of convergence of the cracking simulation algorithm, [41]. The inviscid case is retrieved when $\mu = 0$. Among other approaches the Hoffman plasticity model [56, 57] could be the alternative used for concrete. It allows one for the description of different properties of the material in tension and compression and employs one yield surface within viscoplastic formulation. The Reader interested in the theoretical background and applications of viscoplasticity in the simulations of material failure is referred for instance to the overview work [32].

In the simulations presented in this thesis the damage counterpart of the model is not activated, since monotonically increasing load is only considered. Thus, the yield, plastic potential and hardening functions are used to represent material failure.

### 3.3.2 Cracking model

The second model used in the calculations of RC members is a cracking model for concrete and brittle materials, also available in Abaqus. This model describes the quasi-brittle behavior of concrete. It is assumed the brittle behavior is represented by smeared cracking. "Crack" means a direction in which softening has been detected at calculation material point, however the individual cracks are not tracked. In compression it is assumed that the material is linearly elastic.

In the cracking description three basic crack direction models can be distinguished: fixed direction of orthogonal cracks, rotating cracks and fixed, multidirectional (nonorthogonal) cracks. The fixed orthogonal cracking model assumes that the direction normal to the first crack is aligned with the direction of maximum principal tensile stress, at the time of crack initiation. The model stores this direction and any subsequent cracks can only form orthogonally to the first crack. In the rotating cracks model a single crack can form at any point. The crack direction rotates with the direction of the principal stress axes. The model has no memory of crack directions. The last, multidirectional model allows any number of cracks at the point to form, as the direction of the principal stress axes changes with loading. All crack directions are memorized. In Abaqus the fixed orthogonal cracking model is used [47].

The model assumes that the total mechanical strain rate $\dot{\boldsymbol{\varepsilon}}$ is decomposed into elastic strain rate in uncracked concrete $\dot{\boldsymbol{\varepsilon}}^e$ and cracking strain rate associated with any active cracks, $\dot{\boldsymbol{\varepsilon}}^{ck}$:

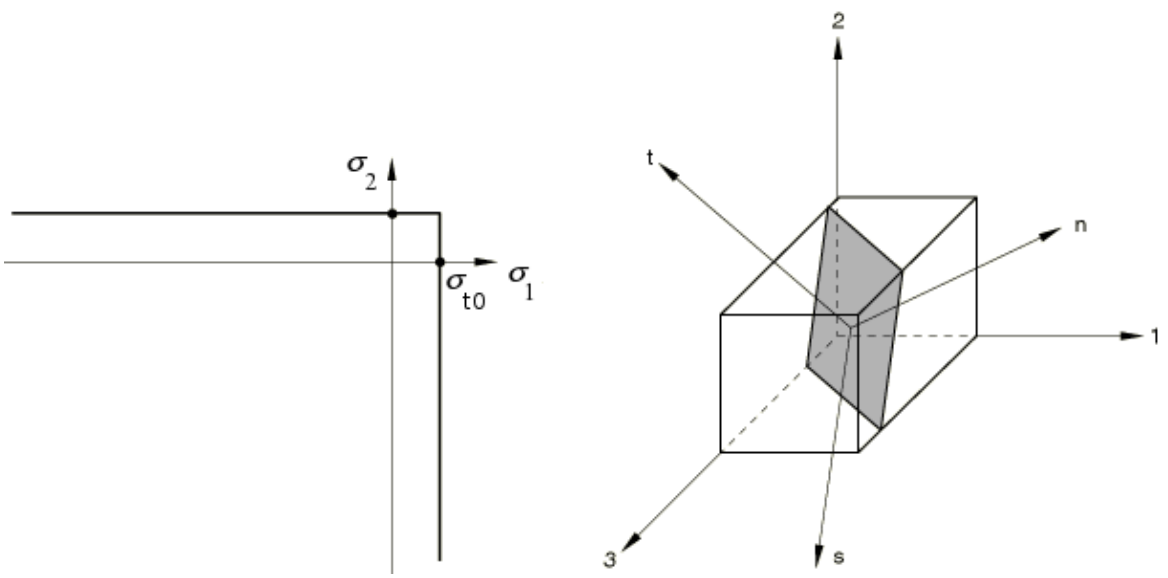


(a) (b)

Figure 3.7: (a) – Rankine criterion in cracking model [47], (b) – Global $(1, 2, 3)$ and local $(n, t, s)$ cracking coordinate system, ($n$ – normal direction, $t, s$ – in-plane directions) [47]

$$\dot{\boldsymbol{\varepsilon}} = \dot{\boldsymbol{\varepsilon}}^{e} + \dot{\boldsymbol{\varepsilon}}^{ck} \tag{3.23}$$

The cracking strains in eq. (3.23) are written in vector form in the local Cartesian coordinate system ($n$, $t$, $s$), shown in Fig. 3.7(b), that is aligned with the crack directions. Thereby, in the global coordinate system strains are denoted by $\boldsymbol{\varepsilon}^{c}$, and in the local system by $\mathbf{e}^{ck}$:

$$\boldsymbol{\varepsilon}^{ck} = [\varepsilon_{11}, \varepsilon_{22}, \varepsilon_{33}, \gamma_{12}, \gamma_{13}, \gamma_{23}] \qquad \mathbf{e}^{ck} = [e_{nn}, e_{tt}, e_{ss}, g_{nt}, g_{ns}, g_{ts}] \tag{3.24}$$

The stress vector is denoted in the global coordinate system by $\boldsymbol{\sigma}$, and in the local system by $\mathbf{t}$:

$$\boldsymbol{\sigma} = [\sigma_{11}, \sigma_{22}, \sigma_{33}, \sigma_{12}, \sigma_{13}, \sigma_{23}] \qquad \mathbf{t} = [t_{nn}, t_{tt}, t_{ss}, t_{nt}, t_{ns}, t_{ts}] \tag{3.25}$$

The relations between strains and stresses in the global and local coordinates can be expressed in matrix form by transformation matrix $\mathbf{T}$:

$$\boldsymbol{\varepsilon}^{ck} = \mathbf{T}\, \mathbf{e}^{ck}, \qquad \mathbf{t} = \mathbf{T}^{T}\, \boldsymbol{\sigma} \tag{3.26}$$

The continuum between cracks is modelled with isotropic, linear elasticity. The orthotropy caused by cracking is introduced in the cracking component. To detect crack initiation, a simple Rankine criterion is used (its 2D version is shown in Fig. 3.7(a)). In the model it is assumed that a crack forms when the maximum principal tensile stress

exceeds the tensile strength of material. Cracking is irrecoverable, but when the stress across the crack becomes compressive, the crack closes completely [47].

The relation between stress rate and cracking strain rate at the crack interface can be expressed by:

$$\dot{\mathbf{t}} = \mathbf{D}^{ck}\ \dot{\mathbf{e}}^{ck} \tag{3.27}$$

where: $\mathbf{D}^c$ – diagonal cracking matrix depending on the state of existing cracks. The diagonal stiffness components are: $(D^I_{nn}, D^I_{tt}, D^I_{ss}, D^{II}_{nt}, D^{II}_{ns}, D^{II}_{ts})$. Two possible states of a crack are considered in the model – an actively opening crack and closing/reopening crack.

The stress rate can be expressed as:

$$\dot{\boldsymbol{\sigma}} = \mathbf{D}^e(\dot{\boldsymbol{\varepsilon}} - \mathbf{T}\ \dot{\mathbf{e}}^{ck}) \tag{3.28}$$

where: $\mathbf{D}^e$ – isotropic elasticity matrix.

Premultiplying eq. (3.28) by $\mathbf{T}^T$ and substituting eq. (3.27), the stress-strain rate equation after transformation can be written in the form:

$$\dot{\sigma} = \left(\mathbf{D}^e - \mathbf{D}^e\ \mathbf{T}\left(\mathbf{D}^{ck} + \mathbf{T}^T\mathbf{D}^e\ \mathbf{T}\right)^{-1}\mathbf{T}^T\mathbf{D}^e\right)\dot{\boldsymbol{\varepsilon}} = \mathbf{D}^{ec}\ \dot{\boldsymbol{\varepsilon}} \tag{3.29}$$

The tension softening behavior is described on the basis of the brittle fracture concept of Hillerborg [21]. The Abaqus model assumes that the fracture energy required to form a unit area of crack surface in Mode I, $G^I_f$, is a material property. The fracture energy value can be related to the tensile stress as a function of the crack-opening displacement:

$$G^I_f = \int \sigma^I_t du_n \tag{3.30}$$

The smeared cracking assumption involves a well-known mesh sensitivity problem. To overcome this difficulty the strain is multiplied by a characteristic length related to the element geometry and formulation:

$$u^{ck}_n = e^{ck}_{nn} \cdot l \tag{3.31}$$

In eq. (3.31) local crack direction $n$ is used as an example.

Crack initiation is based on Mode I fracture only, but postcrack behavior includes both Mode I and Mode II. The Mode II model is based on the observation that the shear behavior is dependent on the crack opening. The cracking conditions for Mode II are activated when cracking has taken place in the associated normal direction. The Abaqus model assumes the postcracking shear stiffness is dependent on the crack opening to prevent the model from a too stiff response. As cracks develop, the shear stress tends to zero. The total shear stress is defined as a function of the total shear strain (directions $n$ and $t$ are used as an example):

$$t_{nt} = D^{II}_{nt} g^{ck}_{nt} \tag{3.32}$$

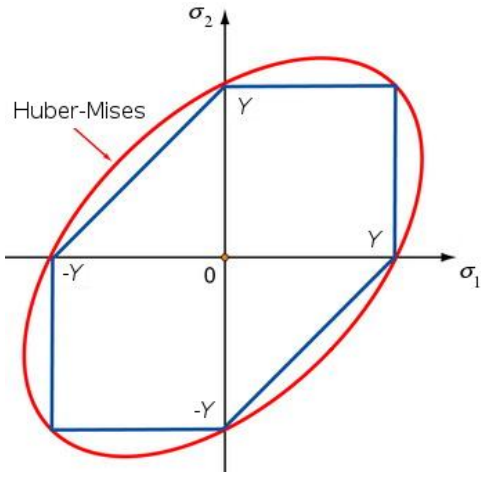


Figure 3.8: Huber-Mises yield surface in classical metal plasticity model

where: $D_{nt}^{II}$ – stiffness that depends on crack opening and can be expressed as:

$$D_{nt}^{II} = \rho(e_{nn}^{ck}, e_{tt}^{ck})G \tag{3.33}$$

where: $G$ – shear modulus of the uncracked concrete and $\rho(e_{nn}^{ck}, e_{tt}^{ck})$ – shear retention factor which has values between one and zero and depends on crack opening.

### 3.3.3 Steel model

Steel is modelled with classical isotropic plasticity model [47]. The model is commonly used for metal plasticity calculations, either as rate-dependent or as rate-independent, and has a particularly simple form. The Huber-Mises yield function with associated flow is assumed. The Huber-Mises yield surface used to define isotropic yielding is presented in Fig. 3.8. It is defined by giving the value of the uniaxial yield stress, as a function of uniaxial equivalent plastic strain.

The total strain is decomposed into elastic and plastic parts:

$$\boldsymbol{\varepsilon} = \boldsymbol{\varepsilon}^e + \boldsymbol{\varepsilon}^p \tag{3.34}$$

The elasticity is linear and isotropic and, therefore, can be written in terms of two material parameters, bulk modulus K and shear modulus G, which can easily be computed from Young's modulus and Poisson's ratio. The elasticity model can be expressed as:

$$p = -K\varepsilon_{vol} \tag{3.35}$$

$$\mathbf{s} = 2G\mathbf{e}^e \tag{3.36}$$

where: $p$ – pressure, $\mathbf{s}$ – deviatoric stress, $\varepsilon_{vol}$ – volume strain, $\mathbf{e}$ – deviatoric strain, defined as:

$$p = -\frac{1}{3}\text{trace}\,(\boldsymbol{\sigma}) \qquad \mathbf{s} = \boldsymbol{\sigma} + p\mathbf{I} \qquad \varepsilon_{vol} = \text{trace}\,(\boldsymbol{\varepsilon}) \qquad \mathbf{e} = \boldsymbol{\varepsilon} - \frac{1}{3}\varepsilon_{vol}\mathbf{I} \tag{3.37}$$

The Abaqus model uses associated plastic flow [47]. Therefore, as material yields, the inelastic deformation rate is in the direction of the normal to the yield surface. In the Huber-Mises model it is purely deviatoric. The flow rule is:

$$\dot{\mathbf{e}}^p = \dot{e}^p\mathbf{n} = \dot{e}^p \cdot \frac{3}{2}\frac{\mathbf{s}}{q} \tag{3.38}$$

where: $\mathbf{n}$ – flow direction, $q$ – Huber-Mises stress, $q = \sqrt{\frac{3}{2}\mathbf{s}\colon\mathbf{s}}$, and $\dot{e}^p$ – equivalent plastic strain rate.

Steel is assumed as rate-independent metal, which leads to yield criterion:

$$q = Y \tag{3.39}$$

where: $Y$ – yield stress.

The model assumes isotropic hardening. This means that yield surface changes size uniformly such that the yield stress increases in all stress directions as plastic straining occurs. In general case the hardening rule can be expressed as:

$$f\,(q, \kappa_i) = 0 \tag{3.40}$$

where: $\kappa_i$ – hardening parameter.

### 3.3.4 Rust model

Rust is modelled as an interface between steel and concrete, whose response is defined in terms of traction versus separation. The traction-separation model assumes initially linear elastic behavior followed by the initiation and evolution of degradation [55]. The elastic behavior is written in terms of elasticity matrix that relates the nominal tractions to the nominal separations across the interface [47]. The nominal traction stress vector consists of three components: the normal component $t_n$, and two shear components $t_s$, $t_t$. The corresponding separations are denoted by $\delta_n$, $\delta_s$ and $\delta_t$. The elastic behavior can be written as:

$$\begin{pmatrix} t_n \\ t_s \\ t_t \end{pmatrix} = \begin{bmatrix} K_{nn} & K_{ns} & K_{nt} \\ K_{sn} & K_{ss} & K_{st} \\ K_{tn} & K_{ts} & K_{tt} \end{bmatrix} \begin{pmatrix} \delta_n \\ \delta_s \\ \delta_t \end{pmatrix} \tag{3.41}$$

In the simulation an uncoupled behavior between the normal and shear components is considered, thus the off-diagonal terms in the elasticity matrix are equal to zero. The traction-separation is linear until reaching the damage initiation criterion. In the presented models the maximum nominal stress criterion is used:

$$\max\left\{\frac{\langle t_n\rangle}{t_n^0}, \frac{t_s}{t_s^0}, \frac{t_t}{t_t^0}\right\} = 1 \tag{3.42}$$

where: $t_n^0, t_s^0, t_t^0$ – maximum peak values of the nominal stress when the deformation is purely normal to the interface or purely in one of the shear directions.

Damage is assumed to initiate when the maximum nominal stress ratio reaches 1, as defined in eq. (3.42). The expression $\langle t_n\rangle$ means that damage will occur only when normal traction is tensile.

In the corrosion simulations the $\frac{\langle t_n\rangle}{t_n^0}$ is defined formally, but practically in favorable circumstances rust can grow constantly with no limit. Since the rust is produced constantly and there is no correlation between normal and shear tractions, there is no limit to normal traction $t_n$. Thus the value $t_n^0$ can be assumed as a high number. Apart from this another reason for neglecting the normal tractions is that the rust layer is assumed to get damaged due to shear tractions.

After reaching the peak value a softening behavior in the traction-separation relation is considered. It is introduced by damage variable $D$, which represents the overall damage in corrosion products and captures the combined effects of all active mechanisms. The traction components are affected by damage according to the following relations:

$$\begin{aligned} t_n &= \begin{cases} (1-D)\cdot\hat{t}_n & \text{for tension} \\ \hat{t}_n & \text{for compression} \end{cases} \\ t_s &= (1-D)\cdot\hat{t}_s \\ t_t &= (1-D)\cdot\hat{t}_t \end{aligned} \tag{3.43}$$

where: $\hat{t}_n$, $\hat{t}_s$, $\hat{t}_t$ – traction components predicted by the elastic relation for the current strains without damage. The damage evolution is described in terms of effective separations:

$$D = \frac{\delta_m^f\left(\delta_m^{max} - \delta_m^0\right)}{\delta_m^{max}\left(\delta_m^f - \delta_m^0\right)} \tag{3.44}$$

where: $\delta_m^f$ – effective separation at complete failure, $\delta_m^0$ – effective separation at damage initiation and $\delta_m^{max}$ – maximum value of effective separation attained during the loading history. The softening behavior is presented in Fig. 3.9.

The effective separations are defined as:

$$\delta_m = \sqrt{\langle\delta_n\rangle^2 + \delta_s^2 + \delta_t^2} \tag{3.45}$$

The mechanical properties of rust are hard to be determined. It is common to assume that rust behaves like water with bulk modulus $K_r$ and Poisson's ratio $\nu_r$ equal to 2 GPa and 0.49, respectively [3, 34]. There were attempts to test rust specimens, cf. [3], but in the model the rust is represented by incompressible material with $K_r$=2 GPa and corrosion is assumed to be uniformly distributed along the reinforcement [17].

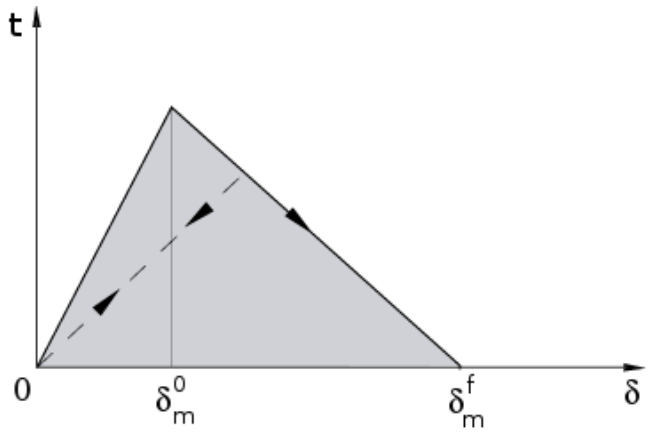


Figure 3.9: Linear softening in traction-separation description [47]

## 3.4 Explicit and implicit time integration method

All the calculations of mechanical aspects of corrosion are performed using Abaqus package, an application based on Finite Element Method, using two available solvers - Abaqus/Standard (A/S) and Abaqus/Explicit (A/E). A/S is a solver using implicit time integration based on the Newton-Raphson method, while A/E uses explicit time integration based on the central difference method. The two algorithms are briefly confronted below on the basis of [7, 11, 47].

### 3.4.1 Explicit time integration method

The explicit time integration method is developed from central difference formulas for velocities and accelerations appearing in the equations of motion. The time of simulation is divided into time steps $\Delta t^i$ ($i$ is a number of current time step). An algorithm presented below is built with a variable time step, which is the outcome of the change of stable time step and the wave speed during the calculations. The equation of motion at the end of time step $\Delta t^i$ can be expressed as:

$$\mathbf{M}\mathbf{a}^i = \mathbf{f}^i = \mathbf{f}_{ext}(\mathbf{d}^i, t^i) - \mathbf{f}_{int}(\mathbf{d}^i, t^i) \tag{3.46}$$

where: $\mathbf{M}$ – lumped mass matrix, $\mathbf{a}^i$ – vector of nodal accelerations, $\mathbf{f}_{ext}(\mathbf{d}^i, t^i)$ – external nodal forces, $\mathbf{f}_{int}(\mathbf{d}^i, t^i)$ – internal nodal forces, $\mathbf{d}^i$ – vector of nodal displacements and $\mathbf{f}^i$ – vector of out-of-balance nodal forces.

By means of the central difference method, the nodal velocities can be expressed as:

$$\mathbf{v}^{i+1/2} = \dot{\mathbf{d}}^{i+1/2} = \frac{\mathbf{d}^{i+1} - \mathbf{d}^i}{t^{i+1} - t^i} = \frac{1}{\Delta t^{i+1/2}} \left( \mathbf{d}^{i+1} - \mathbf{d}^i \right) \tag{3.47}$$

Equation (3.47) can be converted into an integration formula to calculate nodal dis-

placements:

$$\mathbf{d}^{i+1} = \mathbf{d}^i + \Delta t^{i+1/2}\dot{\mathbf{d}}^{i+1/2} \tag{3.48}$$

In a similar way, the difference and integration formulas for nodal accelerations can be written:

$$\mathbf{a}^i = \ddot{\mathbf{d}}^i = \frac{\dot{\mathbf{d}}^{i+1/2} - \dot{\mathbf{d}}^{i-1/2}}{t^{i+1/2} - t^{i-1/2}} = \frac{1}{\Delta t^i}\left(\dot{\mathbf{d}}^{i+1/2} - \dot{\mathbf{d}}^{i-1/2}\right) \tag{3.49}$$

$$\dot{\mathbf{d}}^{i+1/2} = \dot{\mathbf{d}}^{i-1/2} + \Delta t^i \ddot{\mathbf{d}}^i \tag{3.50}$$

The velocities are defined in eq. (3.50) at the midpoints of the time intervals $\Delta t^{i+1/2}$, which is a consequence of using the variable time step. Considering eqs. (3.48) and (3.50) the displacements can be expressed through accelerations. Thus, substituting eq. (3.46), for every time step $\Delta t^i$ the expression for the velocity in eq. (3.50) can be rearranged into:

$$\dot{\mathbf{d}}^{i+1/2} = \dot{\mathbf{d}}^{i-1/2} + \Delta t^i \mathbf{M}^{-1}\mathbf{f}^i \tag{3.51}$$

At any time $t^i$ the nodal displacements $\mathbf{d}^i$ and nodal external forces $\mathbf{f}^i_{ext}$ are known, the nodal forces $\mathbf{f}^i_{int}$ can be calculated using geometric and constitutive equations. The mass matrix is time-independent. Thus, the right-hand side of eq. (3.51) can easily be determined and $\dot{\mathbf{d}}^{i+1/2}$ can be substituted into eq. (3.48) to calculate displacements at time $t^{i+1}$.

Due to the fact that the adopted lumped mass matrix is diagonal, the update of nodal velocities and displacements does not require solving any equations. This is the most important advantage of the explicit method.

The main disadvantage of the explicit integration is the conditional stability of the method. The time step cannot exceed a critical value $\Delta t_{crit}$ given by the Courant stability limit:

$$\Delta t_{crit} = \frac{2}{\omega_{max}} \tag{3.52}$$

where $\omega_{max}$ is the highest frequency of the linearized system. This limit is valid only for systems with no damping. The introduction of damping results in a reduction of the critical time step. For practical application the stable time step can be expressed as:

$$\Delta t = \alpha \Delta t_{crit} \leq \min_e \frac{l_e}{c_e} \tag{3.53}$$

where $l_e$ is the characteristic size of element $e$, $c_e$ is the current wave speed in element $e$ and $\alpha$ is a reduction factor with values within the range $0.8 \leq \alpha \leq 0.98$ [7].

The critical time step decreases with both mesh refinement and increasing stiffness of the material. The time step for a mesh is obtained from time steps calculated for each element, i.e. the minimum element time step is chosen for the mesh time step. The cost of an explicit simulation depends only on the complexity of the model and the number of time steps.

Apart from satisfying condition (3.53), also the energy balance must be checked, cf. [7]. The energy balance allows one to detect instabilities, caused by a nonlinear model, that can lead to overprediction of displacements, despite ensuring that the time step remains stable. Therefore, when performing nonlinear calculations the energy balance must be checked according to:

$$|W_{kin} + W_{int} - W_{ext}| \leq \epsilon \, max(W_{kin}, W_{int}, W_{ext}) \tag{3.54}$$

where $W_{kin}$, $W_{int}$, $W_{ext}$ – kinetic, internal and external energies, $\epsilon$ is a small tolerance (of the order of $10^{-2}$).

Moreover, the explicit simulations can be performed for quasi-static calculations. To ensure that the process remains quasi-static and the inertia forces are negligible it is necessary to check if the kinetic energy of the model does not exceed the value of 5% of the internal energy.

The flowchart for the explicit method is presented in Fig. 3.10, where $\boldsymbol{\sigma}$ is the stress tensor, [15].

### 3.4.2 Implicit time integration method

The implicit time integration scheme is mostly based on Newton's method. For static problems the accelerations in eq. (3.46) are neglected, which, at time $t^{i+1}$, leads to the general expression:

$$\mathbf{r}^{i+1}(\mathbf{d}^{i+1}) = -\mathbf{f}^{i+1} = \mathbf{f}_{int}(\mathbf{d}^{i+1}, t^{i+1}) - \mathbf{f}_{ext}(\mathbf{d}^{i+1}, t^{i+1}) \tag{3.55}$$

where $\mathbf{r}^{i+1}$ is a residual.

The non-zero residuals correspond to out-of-balance forces, so the appropriate limit value for equilibrium solution is $\mathbf{r}^{i+1} = 0$. For rate-independent materials $t$ is not necessarily the real time. It can be replaced by any monotonically increasing parameter.

Newton's method assumes that the nodal displacements at time $t^{i+1}$ are a sum of approximated values $\mathbf{d}_k$ and $\Delta\mathbf{d}$ which is the difference between $\mathbf{d}_k$ and the exact solution ($k$ is iteration number):

$$\mathbf{d}^{i+1} = \mathbf{d}_k + \Delta\mathbf{d} \tag{3.56}$$

The left-hand side of eq. (3.55) can be expanded in a Taylor series about the current approximate solution $\mathbf{d}_k$:

$$\mathbf{r}^{i+1}(\mathbf{d}_k + \Delta\mathbf{d}) = \mathbf{r}^{i+1}(\mathbf{d}_k) + \frac{\partial \mathbf{r}^{i+1}(\mathbf{d}_k)}{\partial \mathbf{d}} \Delta\mathbf{d} + \Phi(\Delta\mathbf{d}^2) \tag{3.57}$$

The terms that are higher order than linear in $\Delta\mathbf{d}$ are dropped, which gives the linear model of nonlinear equations for the static problem:

$$\mathbf{r}^{i+1}(\mathbf{d}_k) + \mathbf{K}\Delta\mathbf{d} = 0 \tag{3.58}$$

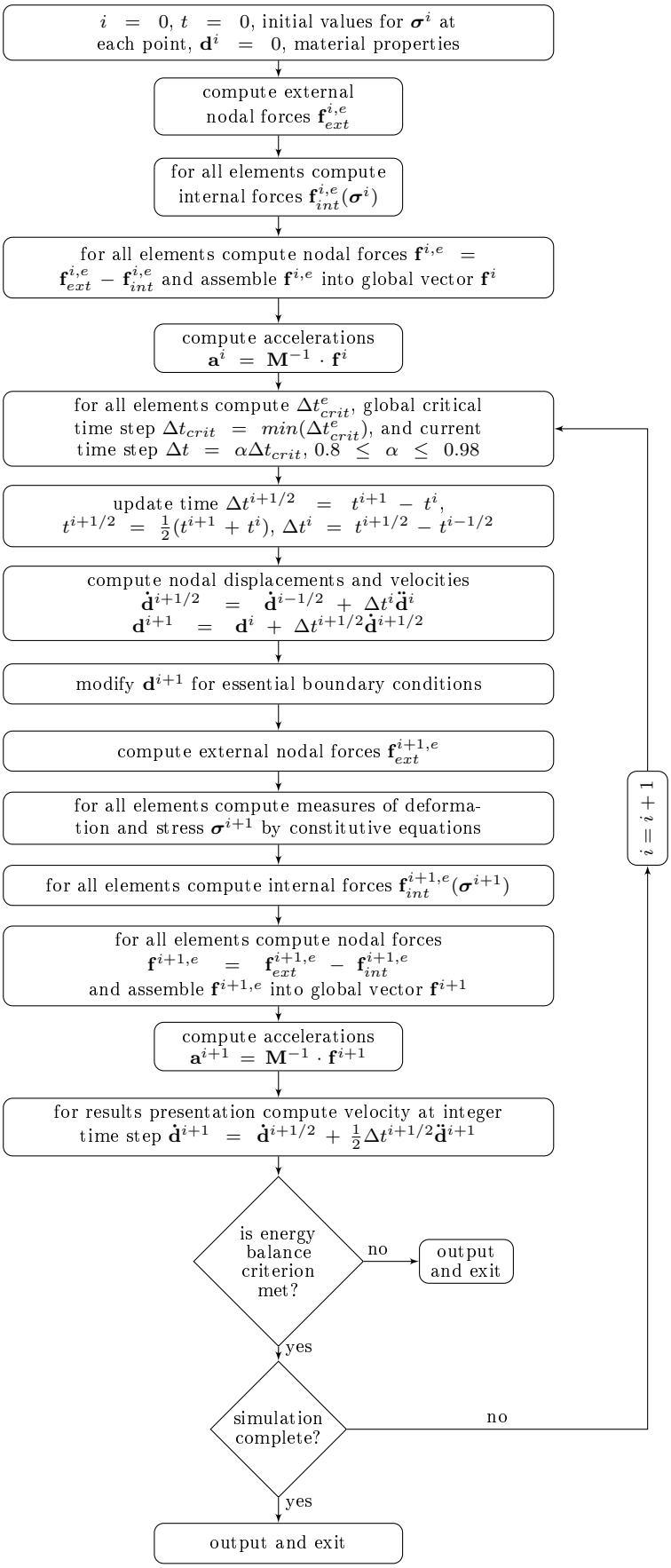


Figure 3.10: Flowchart of explicit integration

where $\mathbf{K}$ is the system Jacobian matrix defined as:

$$\mathbf{K} = \frac{\partial \mathbf{r}^{i+1}(\mathbf{d}_k)}{\partial \mathbf{d}} \tag{3.59}$$

By solving the system of eqs. (3.58), the displacement increments $\Delta\mathbf{d}$ can be obtained and the new displacement approximation at time $t^{i+1}$ is calculated according to:

$$\mathbf{d}_{k+1} = \mathbf{d}_k + \Delta\mathbf{d} \tag{3.60}$$

The $\mathbf{K}$ matrix is also called the effective tangent stiffness matrix and, after substituting eq. (3.55) into (3.59), can be expressed as:

$$\mathbf{K} = \frac{\partial \mathbf{f}_{int}^{i+1}}{\partial \mathbf{d}} - \frac{\partial \mathbf{f}_{ext}^{i+1}}{\partial \mathbf{d}} = \mathbf{K}_{int} - \mathbf{K}_{ext} \tag{3.61}$$

where $\mathbf{K}_{int}$ – tangent stiffness matrix, $\mathbf{K}_{ext}$ – load stiffness matrix, present only for follower loads, cf. [7].

The new displacements $\mathbf{d}_{k+1}$ are checked for convergence. If the convergence criterion is not met, a new linear model is built and the process is repeated for the same time increment. There are three convergence criteria – based on the magnitude of residual $\mathbf{r}$, based on the magnitude of the displacement increments $\Delta\mathbf{d}$ and the energy error criterion [7].

The main advantage of the Newton's method is its quadratic convergence rate when the approximation in iteration $k$ is within the radius of convergence. However, the method is computationally expensive, because the Jacobian matrix needs to be calculated and the problem (3.58) solved in each iteration.

The flowchart for the implicit method is presented in Fig. 3.11, [15].

## 3.5 Finite element model

FE models have been built using Abaqus package, with the material descriptions presented in previous sections. Both algorithms summarized in Section 3.4 are used in the calculations of damage due to corrosion product expansion. In all simulations concrete has been modelled as damage-plasticity material when the implicit algorithm is used and damage-plasticity or cracking material when the explicit algorithm is employed. Steel is modeled as elastic-plastic and rust is represented by traction-separation interface, which opens when corrosion is active. The corrosion interface is shown in Fig. 3.12.

Corrosion products do not generate any pressure on concrete until they fill the porous zone between steel and concrete. This zone is formed by steel consumption in the process and voids in the concrete. It can be found in the literature that the porous zone is approximately 12.5 $\mu$m [20]. In 2D models presented in the thesis the initial thickness of rust is 0.05 mm, however it is assumed that the thickness is a result of steel cross-section loss only. The initial thickness is also applied for a more practical reason, it is useful in mesh generation. In the 3D models the rust interface is initially 0.01 mm thick.

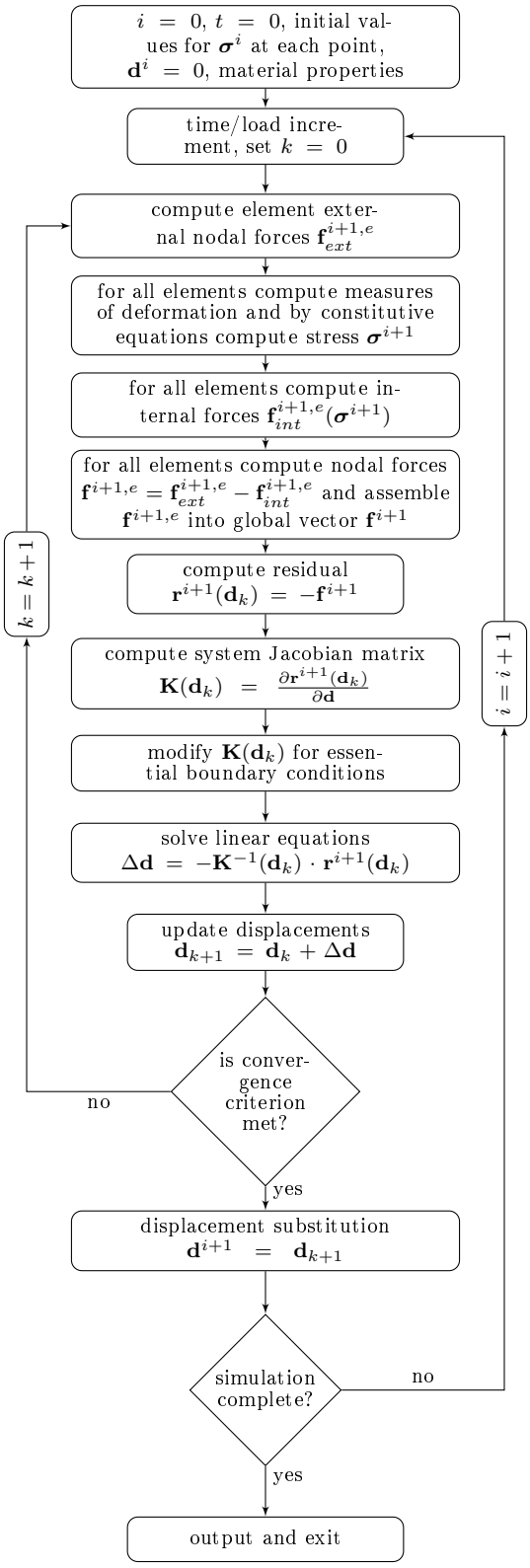


Figure 3.11: Flowchart of implicit integration

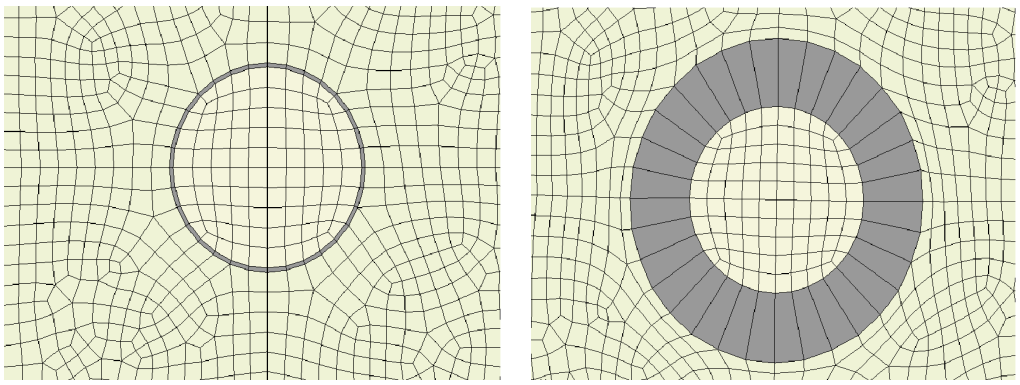

(a) (b)

Figure 3.12: Corrosion interface (a) – closed, (b) – open

The rust expansion is applied as substitute temperature increase, assuming uniformly distributed corrosion. This substitute temperature increase has no physical meaning and should be interpreted only as a numerical trick which allows one to model the increase of the rust layer volume, and can be related to material parameters such as bonding strength. In the thesis the substitute temperature (or volume expansion parameter) is interpreted as corrosion level. The corrosion level $L_{corr}$ is understood as loss of weight related to initial weight of rebar, according to expression [13]:

$$L_{corr} = \frac{G_0 - G}{\rho_s \, A \cdot l} \tag{3.62}$$

where: $G_0$ – initial mass of rebar, $G$ – mass of rebar after corrosion, $A$ – rebar's cross-section area, $l$ – embedment length

A two-dimensional configuration for an RC cross-section analysis is presented in Fig. 3.13. The cross-section has the dimensions 350 x 600 mm, however due to symmetry of the model only half of the configuration is analyzed. The cross-section is reinforced with four 25 mm-diameter bars. The bar spacing is 75 mm. The simulation is performed for two concrete covers – 30 mm and 50 mm [17].

The cross-section is supported at the top edge and along the right edge (symmetry axis). The interface and surrounding continuum elements are connected using tie constraints. The calculations are performed for three mesh densities. For the implicit analysis the mesh is composed in two versions: for 30 mm cover concrete and steel are represented by 4-node plane strain elements and for 50 mm cover by 8-node plane strain elements. For the explicit analysis the mesh is composed of 4-node plane strain elements for both sizes of cover. Rust interface is modelled with 4-node cohesive elements in both implicit and explicit schemes.

The 2D analysis allows one to observe damage of RC cross-section only due to cracking of the concrete around the rebar. To simulate the influence of corrosion on bonding strength, a 3D analysis needs to be performed.

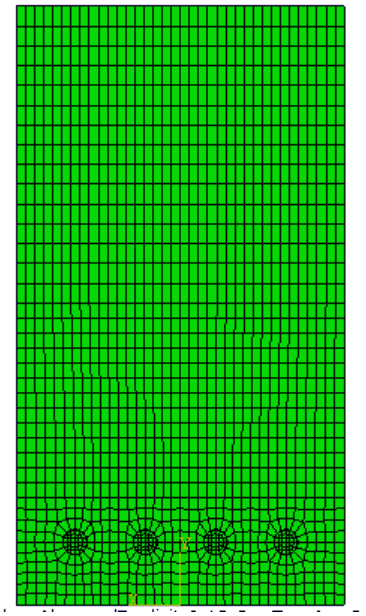

Figure 3.13: Two-dimensional FE model for RC cross-section (coarse mesh)

Due to the fact that rust interface properties, apart from $K_r$ and $\nu_r$, depend on the corrosion level, a single rebar test needs to be performed to calibrate the model parameters. Hence a pullout test is simulated using the 3D configuration presented in Fig. 3.14 [14]. Since double symmetry is noticed, only a quarter of the sample is analyzed.

The simulation is referred to an experiment which has originally been performed by Al Sulaimani et al. [1]. The simulation model assumes 150 x 150 x 40 mm concrete block and 10 mm diameter steel bar placed in the center of the cross-section. The three-dimensional analysis is performed using 8-node solid elements modelling concrete and steel and 8-node cohesive elements modelling the rust layer as interface. However, the rust bond strength and shear stiffness depend on the corrosion level.

Finally, a 3D model for a beam subjected to 3-point bending and corrosion is analyzed, to observe both cracking and bond reduction induced by corrosion and external loading. The 3D model configuration for the beam simulations is presented in Fig. 3.15.

Since the analysis is performed as three-dimensional, the mesh is coarse. What is more, the beam analysis is performed for a quarter of a beam, since double symmetry holds. The mesh is composed of linear brick elements, representing concrete and steel, and 8-node cohesive elements representing the rust interface. The parts are connected using tie constraints. The material models used in the beam simulation are the same as in the pullout analysis, however rust is modelled using the parameters obtained as a result of the pullout calculation.

The model has been prepared in accordance with the experiment performed in [18]. The beam is 5 m long and the cross-section dimensions are 200 x 500 mm. Due to the initial thickness of the interface the steel bars diameters are 31.98 mm and 7.98 mm instead

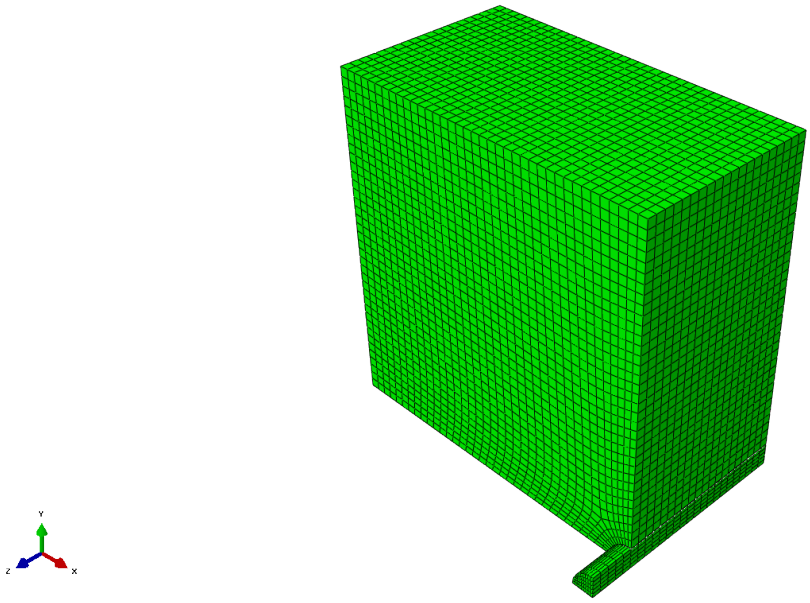

Figure 3.14: Single rebar model – quarter of the sample

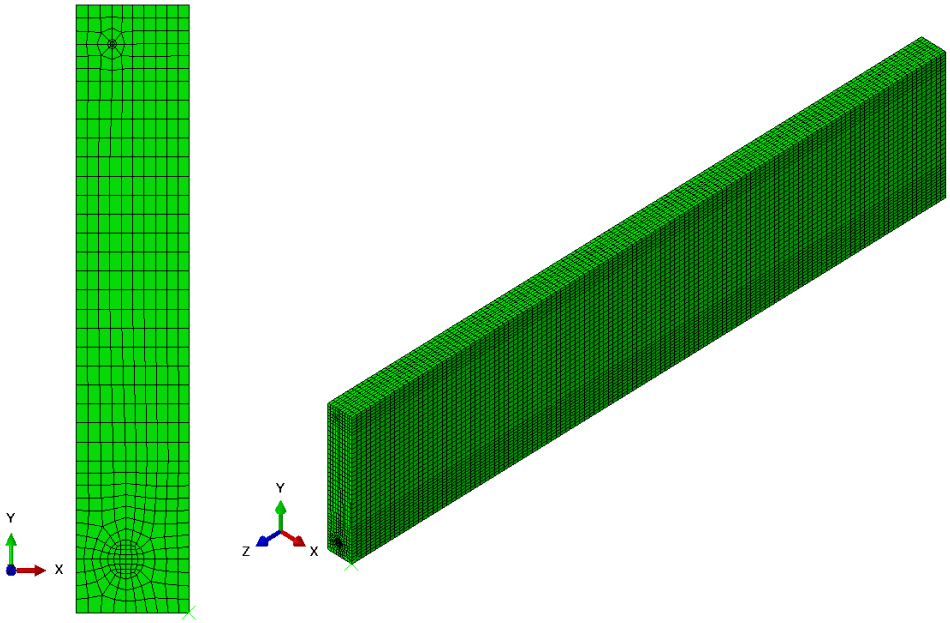


Figure 3.15: Beam model – quarter of the beam

of 32 mm and 8 mm, for bottom and top reinforcements, respectively. The concrete cover is 20 mm. The rust interface properties have been obtained from a single rebar pullout test model, discussed previously and in [14]. The simulation is performed for the beam without transverse steel reinforcement.

# Chapter 4

# Corrosion initiation results

## 4.1 Chlorides concentration analysis

According to the numerical procedure presented in Section 3.2, the chloride and oxygen concentrations are calculated. Concrete is assumed to be uncracked, thus the inflow of detrimental substances is described by eq. (2.9), considering chlorides diffusion and migration. The dimensions of the considered beam cross-section are 350 mm x 600 mm and it is reinforced with four 25 mm diameter bars. The concrete cover is assumed in two variants – 30 mm or 50 mm. The calculations are made with the grid dimension $\Delta x = 0.01$ m and time step $\Delta t = 1$ day.

The model of chloride inflow is confronted with the experimental results available in the literature. First with the data published by Thomas and Bamforth [50], and secondly with results presented by Sandberg [46]. The material parameters and boundary conditions used in simulations of those experiments are presented in Table 4.1. The parameters in Table 4.1 are the result of a calibration process aiming to achieve the best compatibility with the experiment. Hence the diffusion coefficient values and boundary concentrations are slightly different than in [50] or [46].

The total chloride concentrations calculated with the diffusion-migration model and referred to the experimental data presented in [50] are shown in Fig. 4.1. Additionally, in Fig. 4.1, the results are compared with concentrations simulated using the diffusion model. The concentration is expressed as a percentage of concrete mass, as it was in the referred paper [50]. It is assumed that the chloride threshold is 0.5% of mass of concrete. The simulation has been performed using the data for OPC.

The results representing chloride concentrations after 1, 2 and 3 years show that the diffusion-migration model is more accurate, when compared to the experiment. Although initially there is a very slight difference between the models considering the two driving forces and diffusion only, the gap between those two simulations increases in time. Finally, after 6 years and more of concrete exposure to chlorides, the discrepancy between the two simulations is larger and it seems that the experimental results can be simulated better by Fick's law (Fig. 4.2). The model considering the diffusion and migration processes

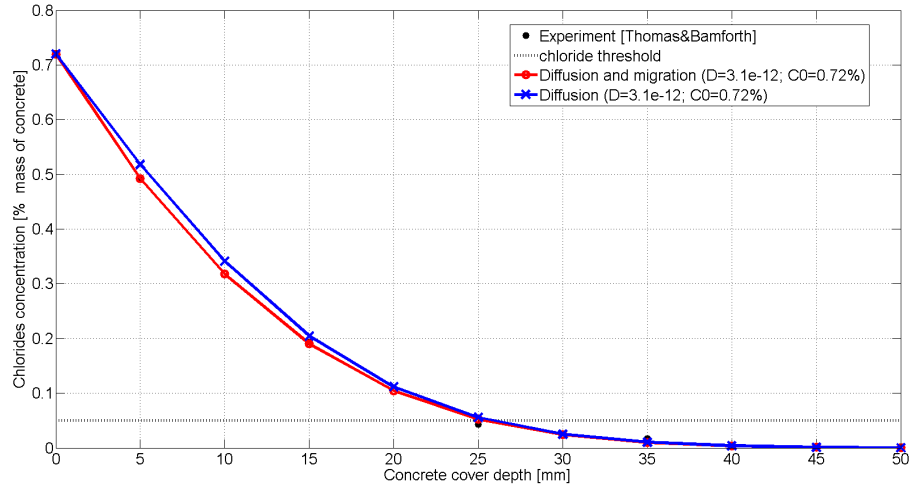


(a)

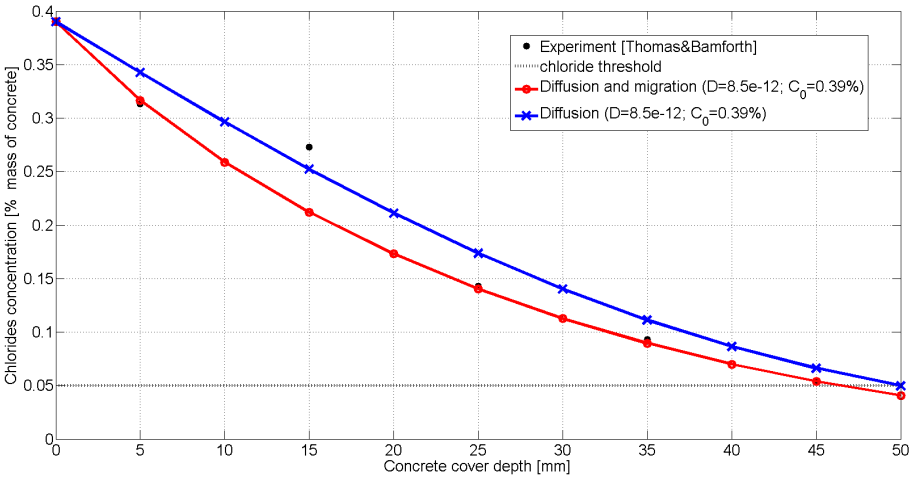


(b)

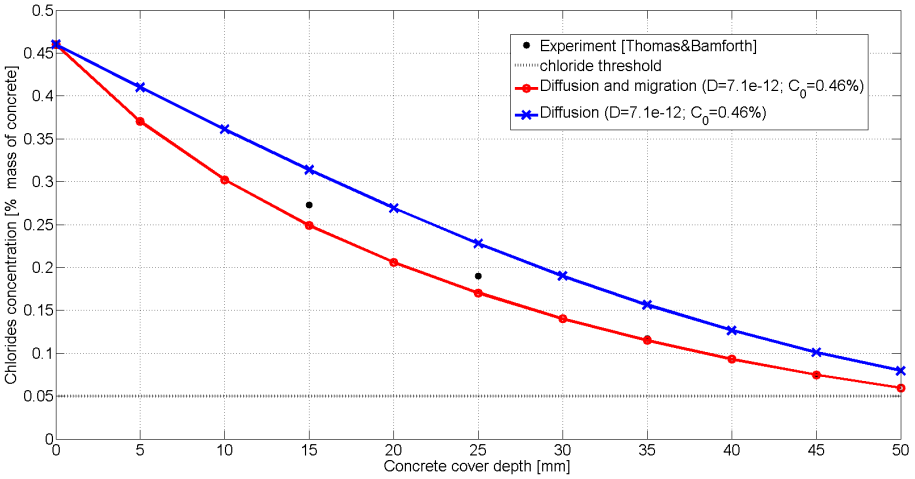


(c)

Figure 4.1: Chloride concentrations calculated with models of diffusion-migration and diffusion itself referred to experimental data [50]. Concentrations after: (a) – 1 year, (b) – 2 years, (c) – 3 years

Table 4.1: Material data used in simulation

Simulation of Thomas & Bamforth [50] experiment (mass of concrete = 2400 kg/m$^3$)

| Age | $D_{cl}$ [x $10^{-12}$m/s$^2$] | Boundary conc. [% mass of concrete] |
|---|---|---|
| 6 months | 9.4 | 0.36 |
| 1 year | 3.1 | 0.72 |
| 2 years | 8.5 | 0.39 |
| 3 years | 7.1 | 0.46 |
| 6 years | 10.0 | 0.30 |
| 8 years | 15.0 | 0.30 |

Simulation of Sandberg [46] experiment (5.1 years, mass of cement = 420 kg/m$^3$ )

| w/c | $D_{cl}$ [x $10^{-12}$m/s$^2$] | Boundary conc. [% mass of cement] |
|---|---|---|
| 0.4 | 4.5 | 5.5 |
| 0.5 | 4.7 | 7.0 |

is in agreement with the experimental results for early years of exposure. However, one must notice that, according to the experiment, the chlorides concentration exceeds the threshold along almost 50 mm of concrete depth after only 2 years of concrete exposure, which is quite fast. During this time the results obtained with the diffusion-migration model are nearly identical to the experiment presented in [50]. The difference between the two models becomes significant in time when concrete is already highly saturated with chlorides. Thus, in the most important aspect of the chloride concentration analysis, which seems to be the time needed to reach the threshold value (i.e. the time to rebar depassivation), the proposed model, considering diffusion and migration, gives accurate results.

In the simulation the material behavior has been modelled only by the diffusion coefficient. What is more, the diffusion coefficient is constant during the calculations as concrete aging is neglected. Unfortunately, there is no unique value of the diffusion coefficient for concrete used in the experiment presented in [50]. Although in [50] it is mentioned that the diffusion coefficient can be estimated from eq. (2.8), it seems that experimental values do not follow the expression proposed in that paper. Taking this into account, it cannot be stated that the simulation presented in the thesis predicts the future concentration in the time scale of for instance 30 years. It shows only the ability to reproduce the experimental results.

The chloride concentration simulation has also been confronted with the experimental results published in [46]. The concentration is expressed as a percentage of cement mass. The simulation has been performed using the the data for sulfate resisting Portland cement with water-to-cement ratio equal to 0.4 or 0.5. The results of simulation are presented in Fig. 4.3.

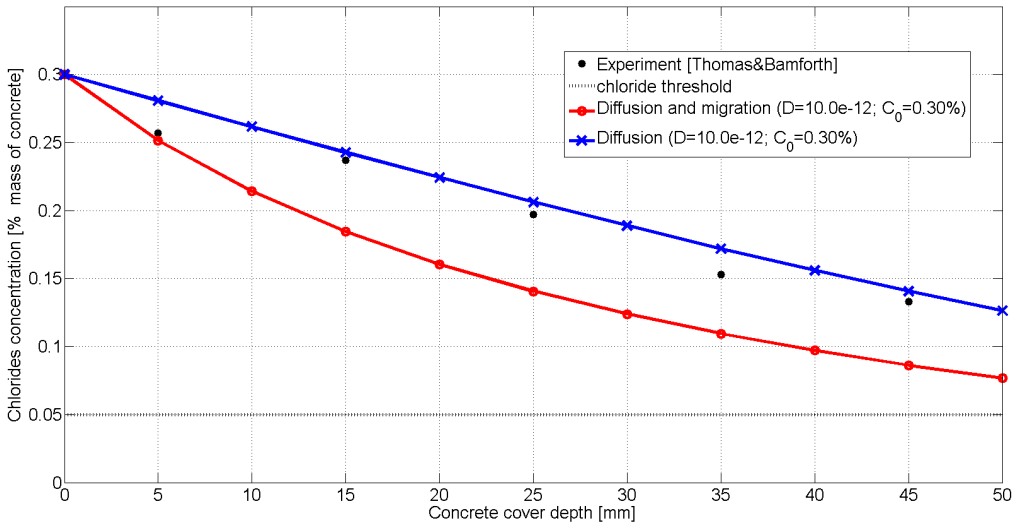


Figure 4.2: Chloride concentrations calculated with models of diffusion-migration and diffusion itself after 6 years of exposure and referred to experimental data [50]

It can be noticed that the chloride concentration calculated using eq. (2.9) is in good accordance with the experimental results. For comparison the concentration calculated with Fick's law is presented. The difference between the two models is visible, and it is easy to notice that the model considering only diffusion does not entirely capture the character of the chloride flux. The material behavior is governed by the diffusion coefficient and there is no other parameter representing concrete composition. The difference in $w/c$ ratio is not included in the model. The diffusion coefficient used in the calculations is time independent. The results presented in Fig. 4.3 are calculated for 5.1 years of exposure to chlorides, however the diffusion coefficient used in calculations is equal to the one published as the coefficient for 0.5 year of exposure [46]. This suggests that knowing the almost initial value of diffusion coefficient it is possible to predict concentration after 5.1 years. Unfortunately, the boundary concentration remains the problem. The boundary concentrations used in the calculations are much higher than the ones reported in [46]. Additionally, in Fig. 4.3(b) it can be noticed that in the experiment the boundary value is smaller than the concentration at 5 mm depth. Hence the concentration at the concrete surface should not be treated as a boundary condition. To establish the boundary condition for chlorides at least one experimental profile should be available. The model described by eq. (2.9) gives reliable results that are in accordance with experiment however the simulation needs to be preceded with experiment to calibrate the model input parameters. Nevertheless, it is possible to obtain the chloride profile after 5.1 years, knowing the data of the experiment after 0.5 year of exposure.

It has been assumed that the binding relation is expressed by Freundlich isotherm, c.f. eq. (2.4). The relation diagram is presented in Fig. 4.4.

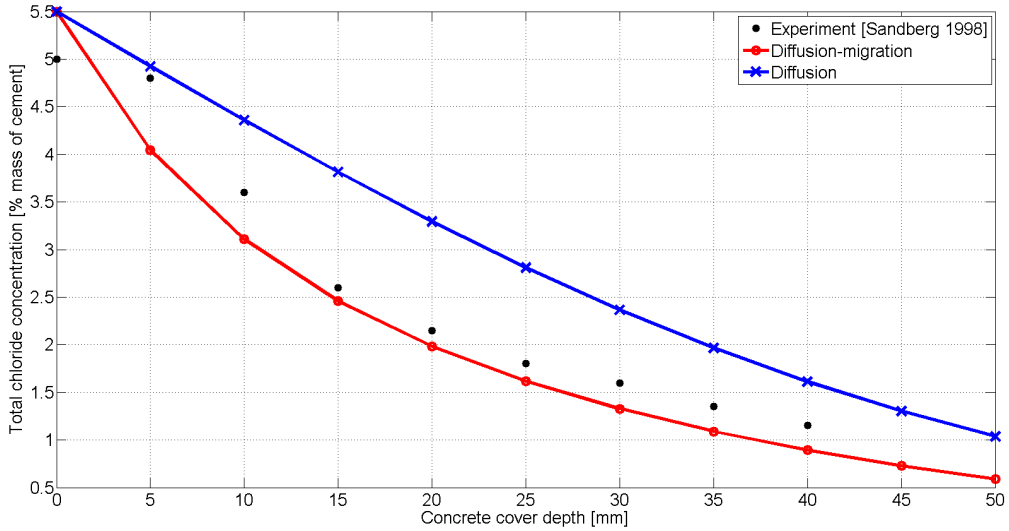


(a)

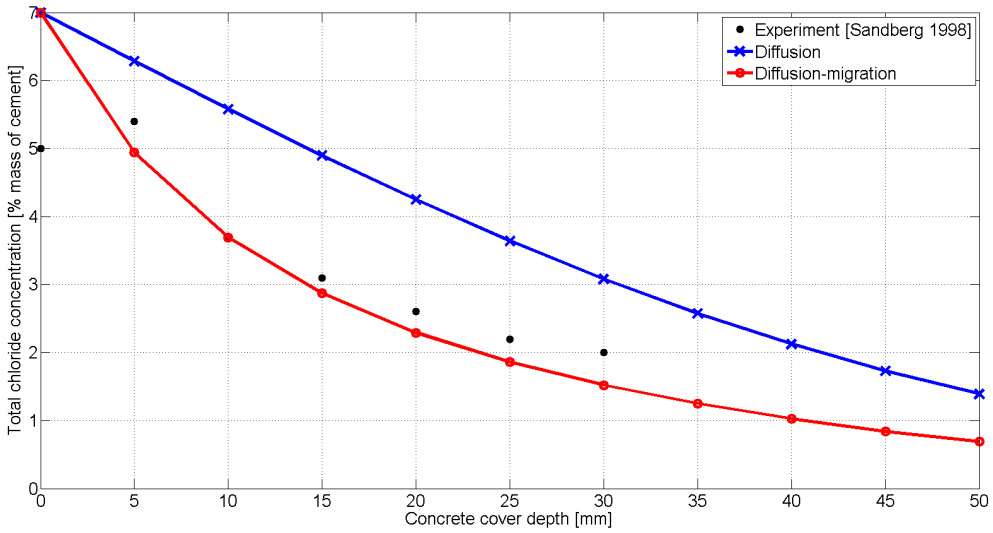


(b)

Figure 4.3: Chloride concentrations calculated after 5.1 years with diffusion-migration and diffusion models, referred to experimental data [46] for SRPC concrete with: (a) – w/c= 0.4, (b) – w/c=0.5

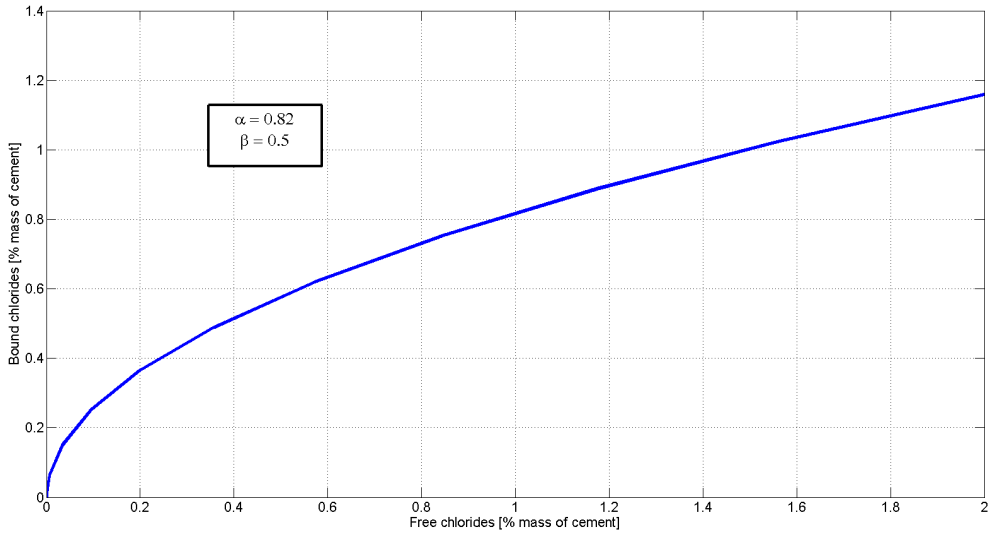


Figure 4.4: Freundlich binding relation

In addition to the simulations of two the experiments, some parametric study has been performed. The calculations of chloride concentration and initiation time have been performed for two different concrete covers – 30 mm and 50 mm. Since there is no universal value of chloride diffusion coefficient, the calculations have been performed for three different values – 2.5, 5.0, $10.0 \times 10^{-12}$ m/s$^2$. The other parameters of concrete used in the calculations are presented in Table 4.2.

The chloride concentration after 3, 6 and 12 years is presented in Fig. 4.5. Three lines represent the concentrations calculated with three different diffusion coefficients. The chloride threshold value is assumed to be 0.4% of cement mass and is marked with the dotted horizontal line. It can be seen in Fig. 4.5 that as time passes the difference between the lines representing $D_{cl} = 5.0 \times 10^{-12}$ m/s$^2$ and $D_{cl} = 10.0 \times 10^{-12}$ m/s$^2$ decreases. Figure 4.6(a) presents the results after 24 years, and it can be clearly noticed that the difference between $D_{cl} = 5.0 \times 10^{-12}$ m/s$^2$ and $D_{cl} = 10.0 \times 10^{-12}$ m/s$^2$ is nearly negligible, while it remains significant in the case of lines $D_{cl} = 2.5 \times 10^{-12}$ m/s$^2$ and $D_{cl} = 5.0 \times 10^{-12}$ m/s$^2$. The explanation is that high diffusion coefficient quickly leads to high chlorides concentration at reinforcement level (i.e. along the whole cover), however as concrete gets saturated with chlorides the flux rate decreases and concentration does not increase considerably.

Figure 4.6(b) presents concentrations after 24 years calculated with different boundary conditions and $D_{cl} = 2.5 \times 10^{-12}$ m/s$^2$. The results show that even a very high boundary concentration ($C_b = 8\%$ cement mass) does not cause high increase of the concentration at the reinforcement level. Although higher boundary concentration causes the higher chlorides concentration at the reinforcement depth, the boundary value seems to be of secondary importance. What is more, the boundary concentration is an environmentally

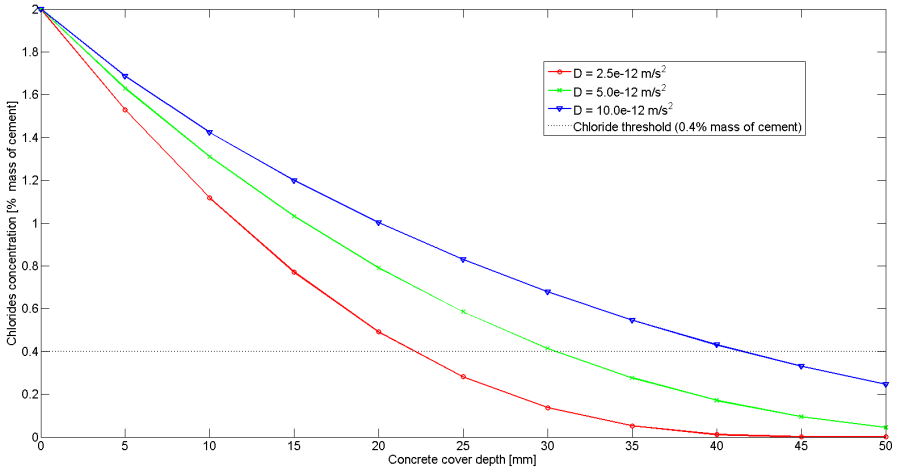


(a)

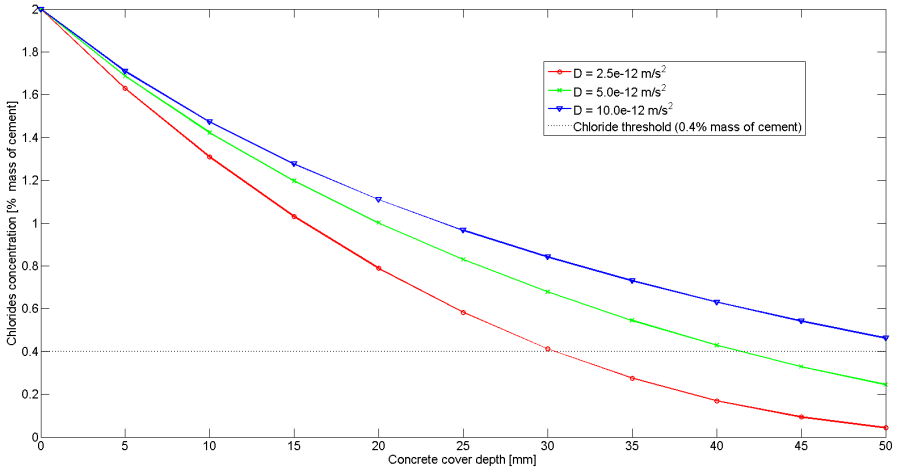


(b)

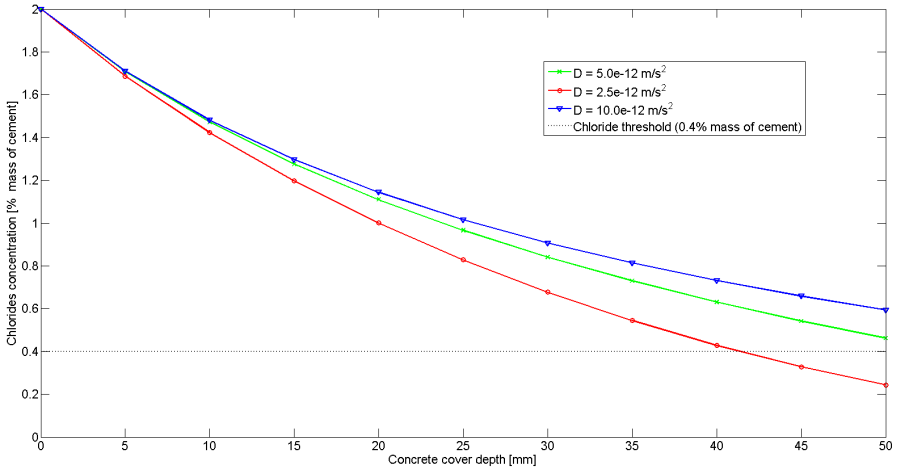


(c)

Figure 4.5: Chloride concentrations simulated with diffusion-migration model. Concentrations after: (a) – 3 years, (b) – 6 years, (c) – 12 years

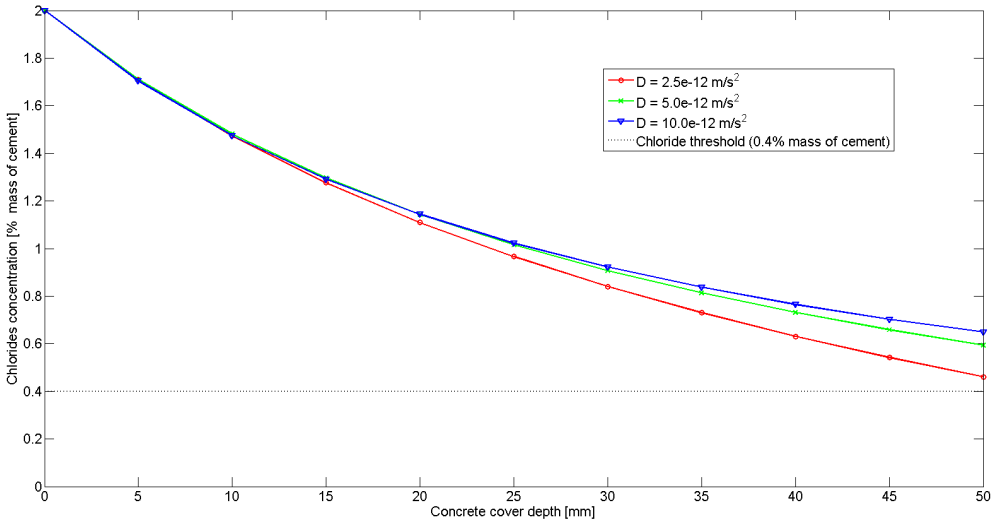


(a)

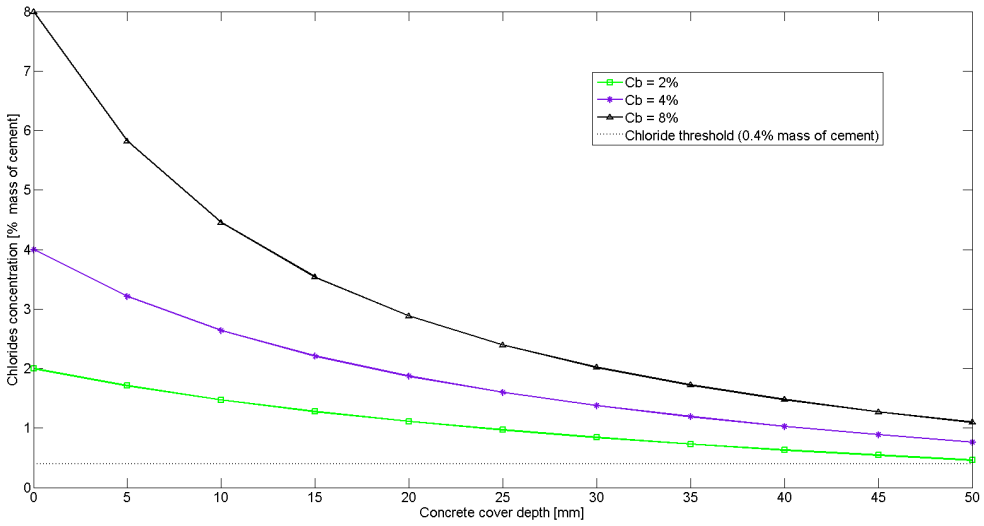


(b)

Figure 4.6: Chloride concentration simulated with diffusion-migration model after 24 years: (a) – different diffusion coefficients, (b) – different chloride boundary concentration

Table 4.2: Material data used in parametric study

Chloride transport

| Parameter | Value |
|---|---|
| $D_{cl}$ [$\times 10^{-12}$ m/s$^2$] | 2.5; 5.0; 10.0 |
| Cement content [kg/m$^3$] | 288 |
| Boundary conc. [% mass of cement] | 2.0; 4.0; 8.0 |
| Binding parameters | $\alpha = 0.82$; $\beta = 0.5$ |
| z | 1 |

Oxygen transport

| Parameter | Value |
|---|---|
| $D_{ox}$ [$\times 10^{-12}$ m/s$^2$] | 1 |
| Initial conc. [$\times 10^{-3}$ kg/m$^3$] | 5.0 |
| Boundary conc. [$\times 10^{-3}$ kg/m$^3$] | 8.576 |

defined parameter, which cannot be freely assumed.

The initiation time is assumed as the time when the chloride concentration at the reinforcement level reaches the chloride threshold value. Table 4.3 presents the initiation time (in days) calculated for 30 mm and 50 mm covers with varying diffusion coefficient, boundary conditions and threshold value. The results are also presented in Figs. 4.7, 4.8 and 4.9, where a nonlinear relationship between the initiation time and the aforementioned parameters can be observed.

Figure 4.7 presents the diagram of the diffusion coefficient vs. the initiation time. The relation is nonlinear and the decrease of the diffusion coefficient is rapid in the case of 30 mm cover, while in the case of 50 mm the slope of the diagram is smaller. The range of initiation time available for 50 mm cover is much wider than for 30 mm, which allows for more flexibility when the concrete mixture is composed. The 30 mm cover assumption results in short initiation time. Increasing the concrete cover to 50 mm leads to a significant extension of the initiation time. For the 50 mm cover the initiation time calculated using $D_{cl} = 10.0 \times 10^{-12}$ m/s$^2$ is only 378 days shorter than for 30 mm cover and calculated using $D_{cl} = 2.5 \times 10^{-12}$ m/s$^2$. This leads to the conclusion that the most significant parameter governing the problem of chloride transport is the depth of the concrete cover. Although the diffusion coefficient is an important parameter, yet improving the concrete diffusivity cannot extend the initiation time so significantly as increasing the concrete cover depth can. Expanding the cover from 30 mm to 50 mm results in time extension from 527 to 1749 days for $D_{cl} = 10.0 \times 10^{-12}$ m/s$^2$ and from 2127 to 7036 days for $D_{cl} = 2.5 \times 10^{-12}$ m/s$^2$.

This observation seems to be confirmed when the dependency of initiation time on the boundary concentration is analyzed. Figure 4.8 presents the nonlinear relation between the boundary concentration and the initiation time for the 30 mm and 50 mm covers. The computations proceed with $D_{cl} = 2.5 \times 10^{-12}$ m/s$^2$. It can be noticed that the lower the boundary concentration, the longer the initiation time. The diagram slope is very strong

Table 4.3: Dependence of chloride initiation time on diffusion coefficient, boundary conditions and chloride threshold

| Diffusion coefficient $\times 10^{-12}$ m/s$^2$ | Initiation time [days] 30 mm cover | 50 mm cover |
|---|---|---|
| 2.5 | 2127 | 7036 |
| 3.75 | 1415 | 4686 |
| 5.0 | 1060 | 3510 |
| 7.5 | 705 | 2337 |
| 10.0 | 527 | 1749 |

| Boundary concentration (% mass of cement) | Initiation time [days] 30 mm cover | 50 mm cover |
|---|---|---|
| 2 | 2127 | 7036 |
| 3 | 1470 | 4666 |
| 4 | 1187 | 3721 |
| 6 | 920 | 2866 |
| 8 | 786 | 2451 |

| Chloride threshold (% mass of cement) | Initiation time [days] 30 mm cover | 50 mm cover |
|---|---|---|
| 0.20 | 650 | 1924 |
| 0.25 | 739 | 2227 |
| 0.30 | 836 | 2576 |
| 0.35 | 942 | 2993 |
| 0.40 | 1060 | 3510 |
| 0.45 | 1194 | 4189 |

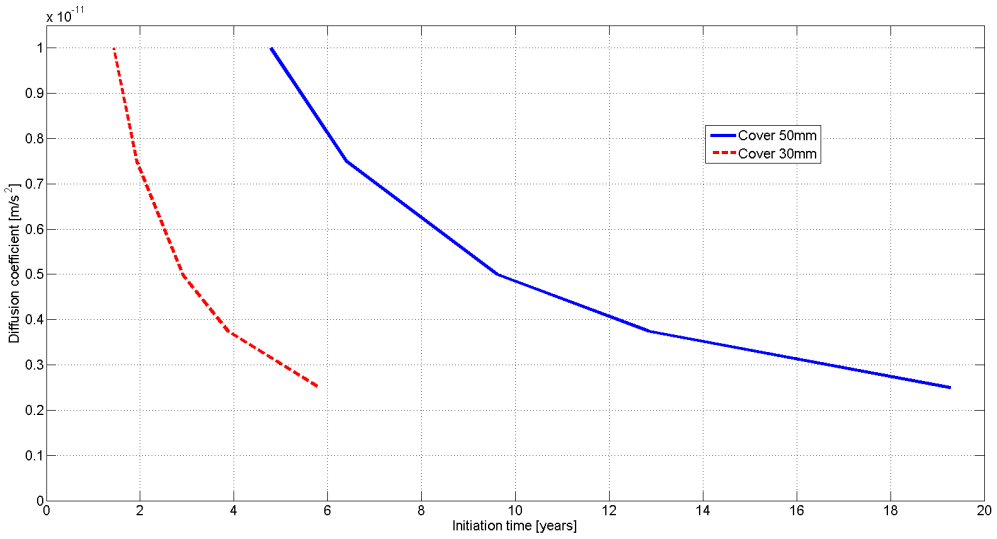


Figure 4.7: Relationship between initiation time and diffusion coefficient

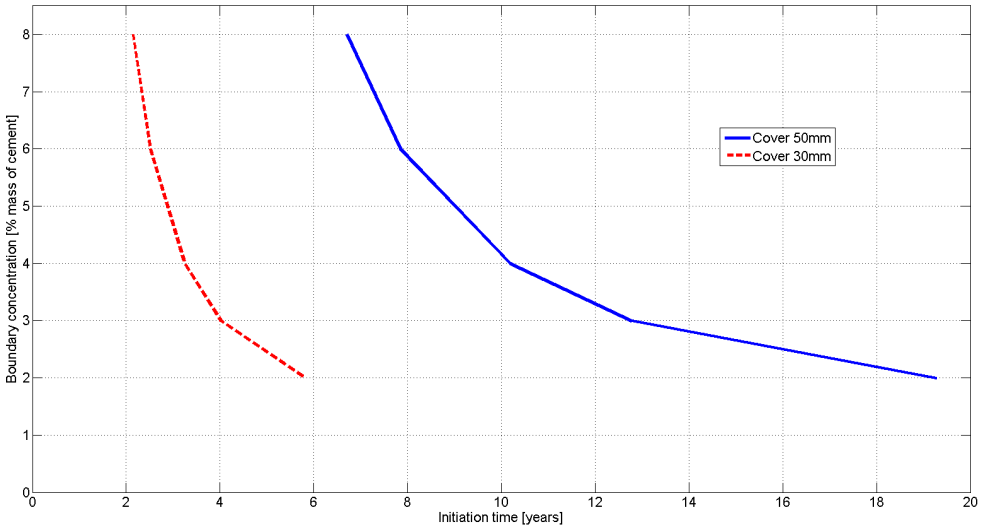


Figure 4.8: Relationship between initiation time and chloride boundary concentration

for 30 mm cover, while the decay is more gradual for 50 mm. Again, the range of initiation times is wider for 50 mm than for 30 mm cover. This could matter when the environmental conditions (i.e. boundary concentration) change. However, a more interesting conclusion is that the initiation time calculated with low boundary concentration and 30 mm cover is even shorter than the initiation time calculated with $C_b = 8\%$ cement mass and 50 mm cover. The increase of the cover results in time extension from 786 to 2451 days for $C_b = 8\%$ and from 2127 to 7036 days for $C_b = 2\%$. Thus, taking into account the boundary concentration it seems to be necessary to assume the concrete cover at least 50 mm thick.

Figure 4.9 presents the chloride threshold level vs. the initiation time diagram for the 30 mm and 50 mm concrete covers. The calculations are performed with $D_{cl} = 5.0 \times 10^{-12}$ m/s$^2$ and $C_b = 2\%$. Again the relationship is nonlinear. Obviously, the higher the chloride threshold, the longer the initiation time. However, there is a huge difference when the results for 30 mm and 50 mm cover are compared. When the dependence of the initiation time on the threshold value is analyzed, the need to increase the cover depth is even more visible than in the previous cases. For the 50 mm cover the initiation time calculated with a very restricted threshold level 0.20% is 730 days longer than for 30 mm cover and a very liberal threshold value of 0.45%. Again, it is clearly visible that the concrete cover depth should not be smaller than 50 mm.

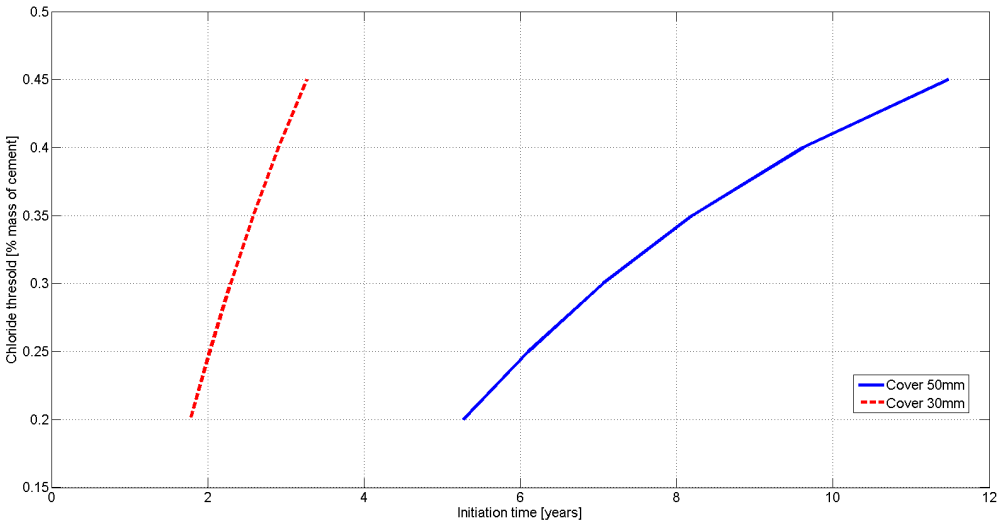


Figure 4.9: Relationship between initiation time and chloride threshold level

## 4.2 Oxygen concentration and corrosion macrocell analysis

Simultaneously with chlorides, oxygen penetrates the concrete cover. Since oxygen occurs as a particle, the concentration in concrete can be calculated using Fick's law, see eq. (2.14). Oxygen concentration distributions for selected time moments are shown in Fig. 4.10. The oxygen concentration is important as it limits the cathodic reaction. It is assumed that all oxygen available in the cross-section is consumed in the reaction. To simplify the model, the dependence of oxygen diffusivity on moisture content is neglected.

As the chloride concentration reaches the chloride threshold value the corrosion macrocell is generated. The passive layer is decomposed and the rebar becomes electric conductor. The distribution of the electric potential generated during the polarization process is presented in Fig. 4.11. It shows the distribution of the electrical potential between cathode (C) and anode (A). The values of the electrical potential calculated at the anode and cathode are similar to those obtained by other researchers [37], although there is a difference in the diagram character, which was assumed in the thesis as linear. The change of electrical potential in time is visible in the first days after depasivation, however within one month it stabilizes.

A similar behavior is visible in Fig. 4.12, presenting the corrosion current density occurring once the rebar's passive layer is broken. The horizontal axis is in logarithmic scale, which allows one to observe the initial change of the current density. After one week from depassivation the current density stabilizes at the level of $3.0 \times 10^{-3}$ A/m$^2$.

The depassivation of steel reinforcement indicates the end of the corrosion initiation phase and the beginning of the corrosion propagation phase. Due to the flow of the

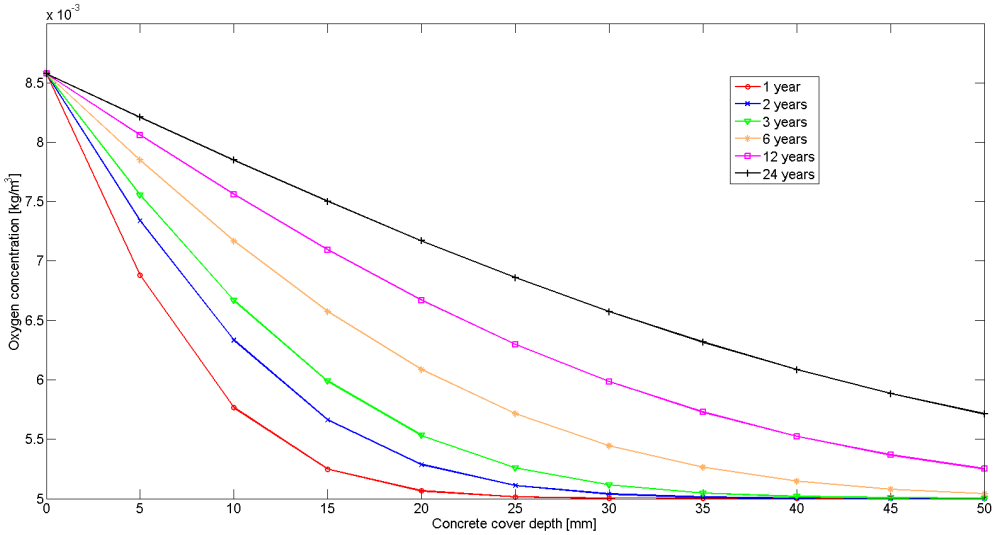


Figure 4.10: Dependence of oxygen concentration on concrete cover

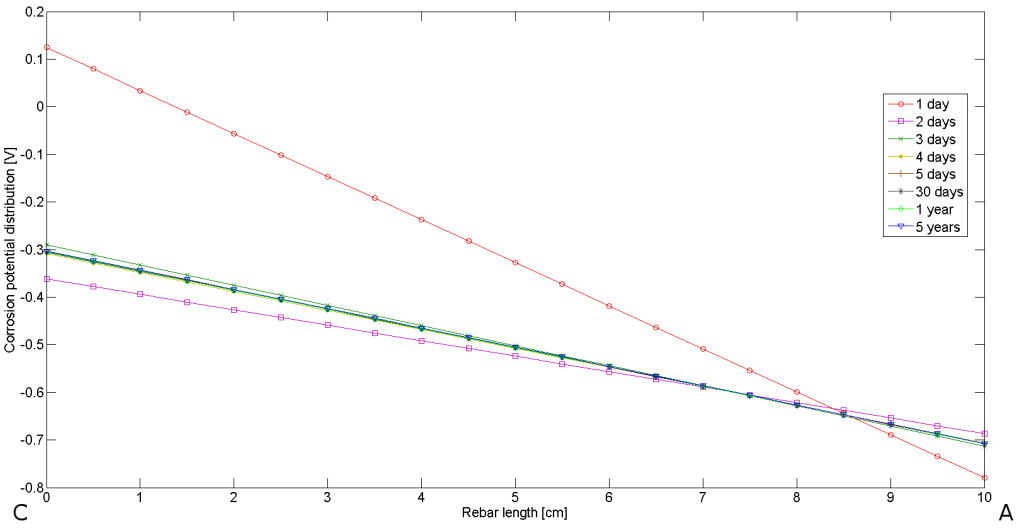


Figure 4.11: Electrical potential distribution along rebar

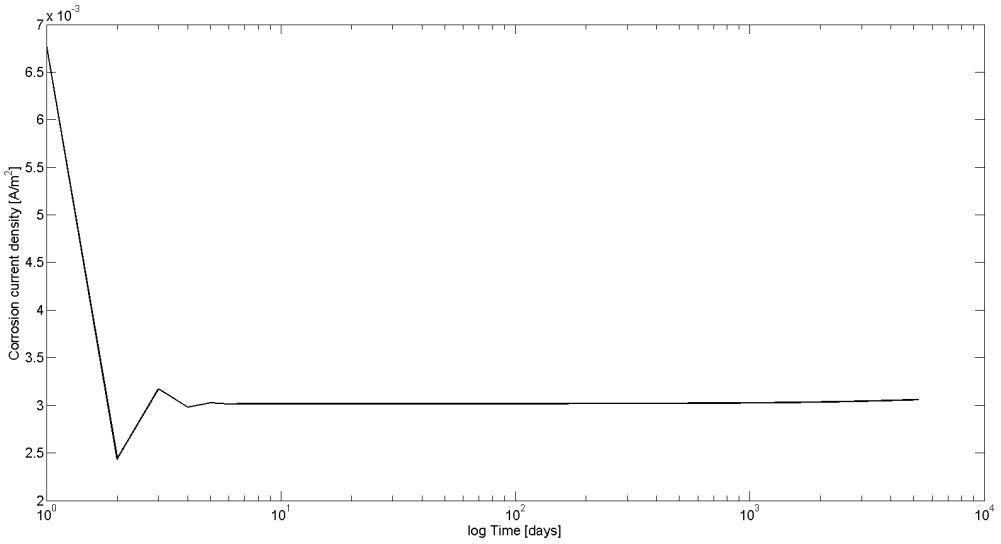


Figure 4.12: Corrosion current versus time

corrosion current rust is produced, generating stresses in concrete. The stress analysis is presented in the following chapter.

# Chapter 5

# Propagation results

## 5.1 Cross-section analysis

According to model configuration presented in Chapter 3.5 the calculations of damage due to corrosion product expansion are performed. The material data used in the analysis are placed in Tables 5.1 and 5.2. Calculations are performed using two values of dilation angle: 5 and 25 degrees. Please notice that the boundary conditions on the right impose symmetry.

The results obtained for the RC cross-section with 30 mm concrete cover using implicit simulations are presented in Figs. 5.1-5.12. The results presented consider simulations with three densities of meshes composed of linear quadrilateral elements. Figure 5.1 shows maximum principal strain (max-in-plane strain in Abaqus terminology) distributions calculated for the RC cross-section with concrete dilation angle 5°, while Fig. 5.2 presents the results of simulation with angle 25°. The strain distributions indicate the zones of damage of concrete, which can be interpreted as cracks. The calculated cracking is at the initial stage and computations diverge prematurely, however the increase of dilation angle results in more advanced cracking. These analysis results seem inconclusive for the cracking progress considerations. The implicit analysis breaks down due to not satisfying the force equilibrium requirement. Despite changing the algorithm parameters

Table 5.1: Material parameters

| Concrete | | Steel | |
|---|---|---|---|
| Parameter | Value | Parameter | Value |
| E [GPa] | 31 | E [GPa] | 210 |
| $\nu$ [-] | 0.2 | $\nu$ [-] | 0.3 |
| Dilation angle $\psi$ [°] | 5; 25 | | |
| Comp. yield stress $f_c$ [MPa] | 25 | | |
| Tens. yield stress $f_t$ [MPa] | 1.8 | | |
| Fracture energy $G_f$ [-] | 0.1 | | |

Table 5.2: Rust interface parameters

| Parameter | Value |
|---|---|
| E [MPa] | 12 |
| $\nu$ [-] | 0.49 |

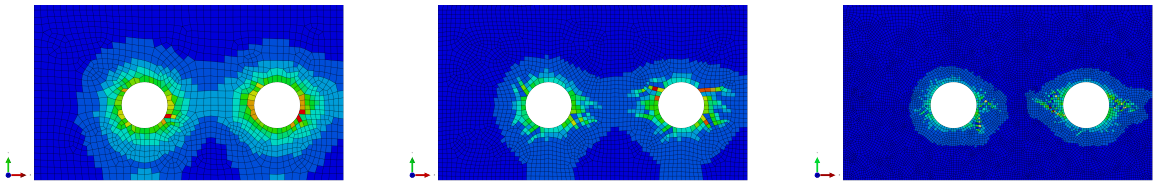

(a) (b) (c)

Figure 5.1: Distribution of max-in-plane strain – Implicit analysis, damage-plasticity model, 30 mm concrete cover and dilation angle 5°: (a) – coarse mesh, (b) – medium mesh, (c) – dense mesh

the simulation aborts at the initial stage and it is not possible to reproduce more advanced stage of cracking.

The size and shape of damage zones are unfortunately mesh-dependent, which would call for some form of regularization. Hence the viscosity parameter $\mu = 0.0001$ has been introduced into the model. The results of simulations performed with different mesh densities, concrete dilation angle 25° and $\mu = 0.0001$ are presented in Fig. 5.3

The viscosity parameter used in the concrete constitutive model allows one to observe the cracking evolution. First, a crack between rebars is formed, which can be observed in Figs. 5.3(a), 5.3(d), 5.3(g). As the calculations proceed, the cracking evolves towards the state presented in Figs. 5.3(b), 5.3(e), 5.3(h). At the final stage of analysis, the crack is formed not only between rebars, but also through the concrete cover, see

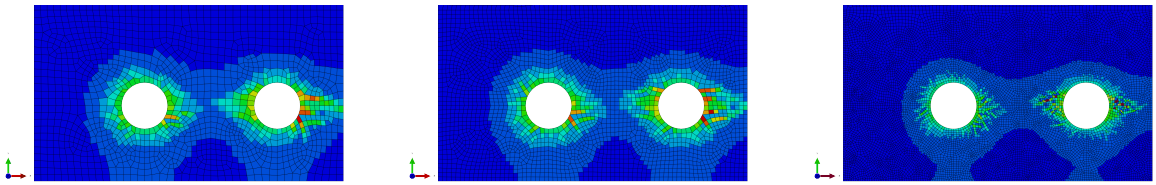

(a) (b) (c)

Figure 5.2: Distribution of max-in-plane strain – Implicit analysis, damage-plasticity model, 30 mm concrete cover and dilation angle 25°: (a) – coarse mesh, (b) – medium mesh, (c) – dense mesh

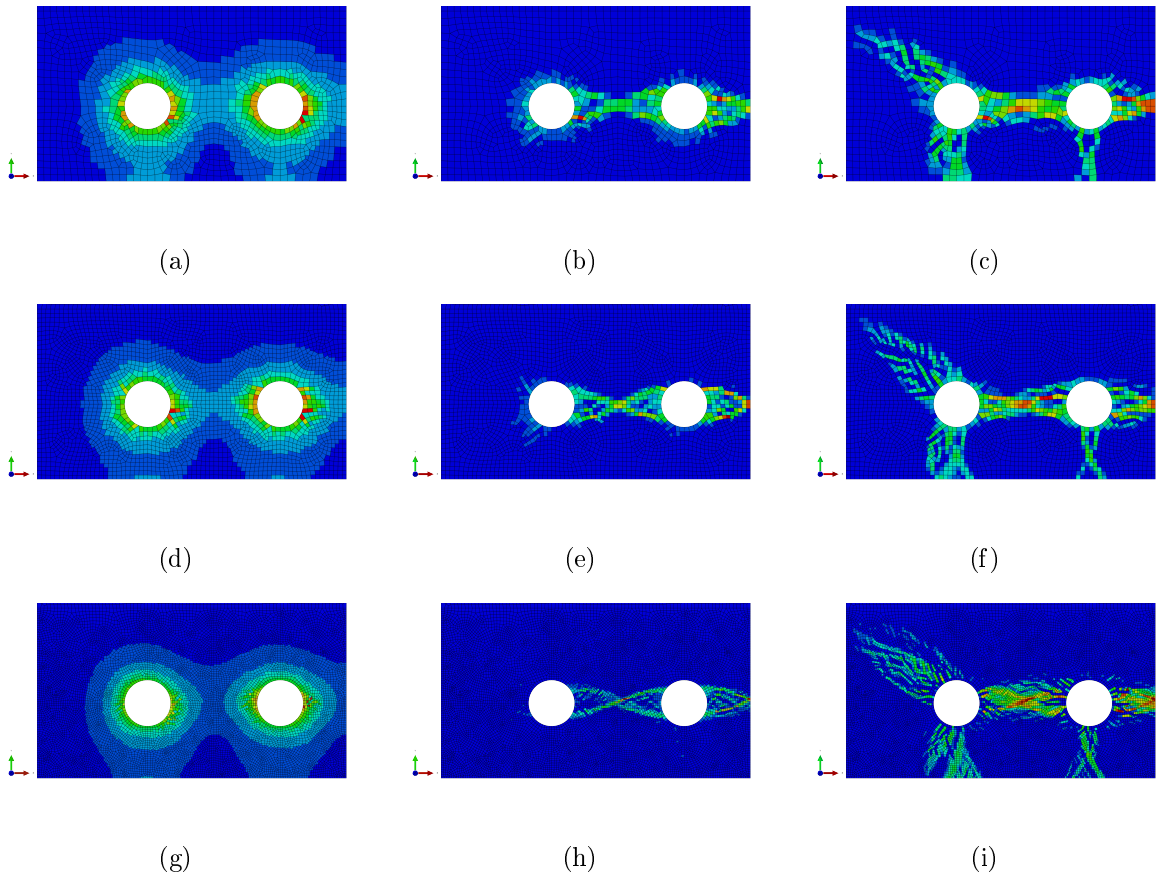

Figure 5.3: Distribution of max-in-plane strain – Implicit analysis, damage-plasticity model, 30 mm concrete cover, $\psi$=25, $\mu$=0.0001. Coarse mesh: (a) – initial cracking, (b) – crack propagation, (c) – final stage of cracking, medium mesh: (d) – initial cracking, (e) – crack propagation, (f) – final stage of cracking, dense mesh: (g) – initial cracking, (h) – crack propagation, (i) – final stage of cracking

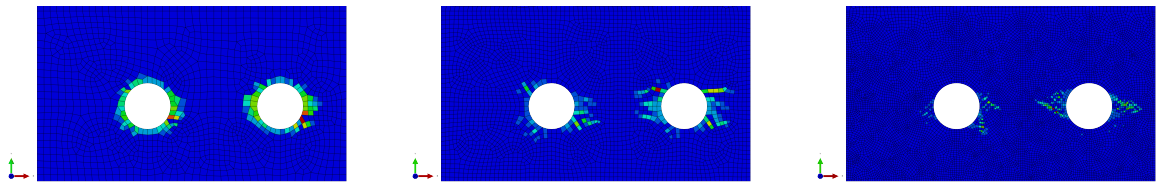

(a) (b) (c)

Figure 5.4: Distribution of PEEQT – Implicit analysis, damage-plasticity model, 30 mm concrete cover and dilation angle 5°: (a) – coarse mesh, (b) – medium mesh, (c) – dense mesh

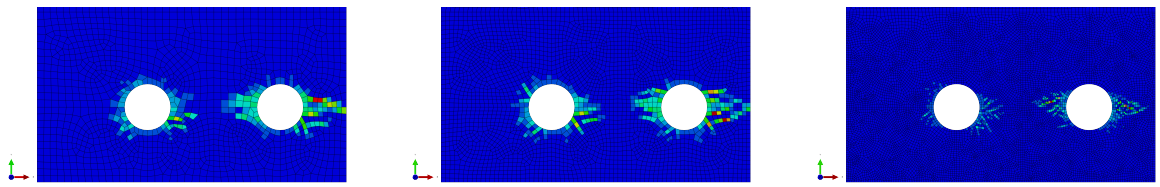

(a) (b) (c)

Figure 5.5: Distribution of PEEQT – Implicit analysis, damage-plasticity model, 30 mm concrete cover and dilation angle 25°: (a) – coarse mesh, (b) – medium mesh, (c) – dense mesh

Figs. 5.3(c), 5.3(f), 5.3(i). Analyzing the cross-section at the macroscale, the important point of the observation is that the first crack is formed between rebars, while the cover is uncracked. Also the cracking pattern is very similar despite the change of mesh density. It suggests that bonding between concrete and steel can be impaired before cracks reveal on the surface of concrete. This may be important when the structural element is subjected to service load. A similar pattern of cracking can also be observed in papers [19, 20, 52].

During the analysis, the PEEQT parameter, which is the tensile plastic equivalent strain, has also been monitored. The results, presented in Figs. 5.4 – 5.6 confirm the observation that plastic strains appear first between rebars and later cross the concrete cover.

Figures 5.7 – 5.9 present the Huber-Mises stress for the implicit analysis, which is a good representative of distortions in the material. In Figs. 5.9(c), 5.9(f), 5.9(i) it is visible that at the places where cracks appear stress relaxation occurs, while redistributed stresses appear in the surrounding concrete.

At the points where maximum strain occurs tensile stress component $\sigma_{nn}$ is calculated ($n$ is a local direction normal to the crack). Figures 5.10 – 5.12 present the simulated relations stress $\sigma_{nn}$ vs. crack mouth opening displacement (CMOD). In the analysis the steel loss is calculated to be 20 $\mu$m. According to [2] such loss causes in a cross-section with the concrete cover 30 mm a visible crack with a width below 0.5 mm. The comparison of the simulation results and experiment performed by Andrade et at. [2]

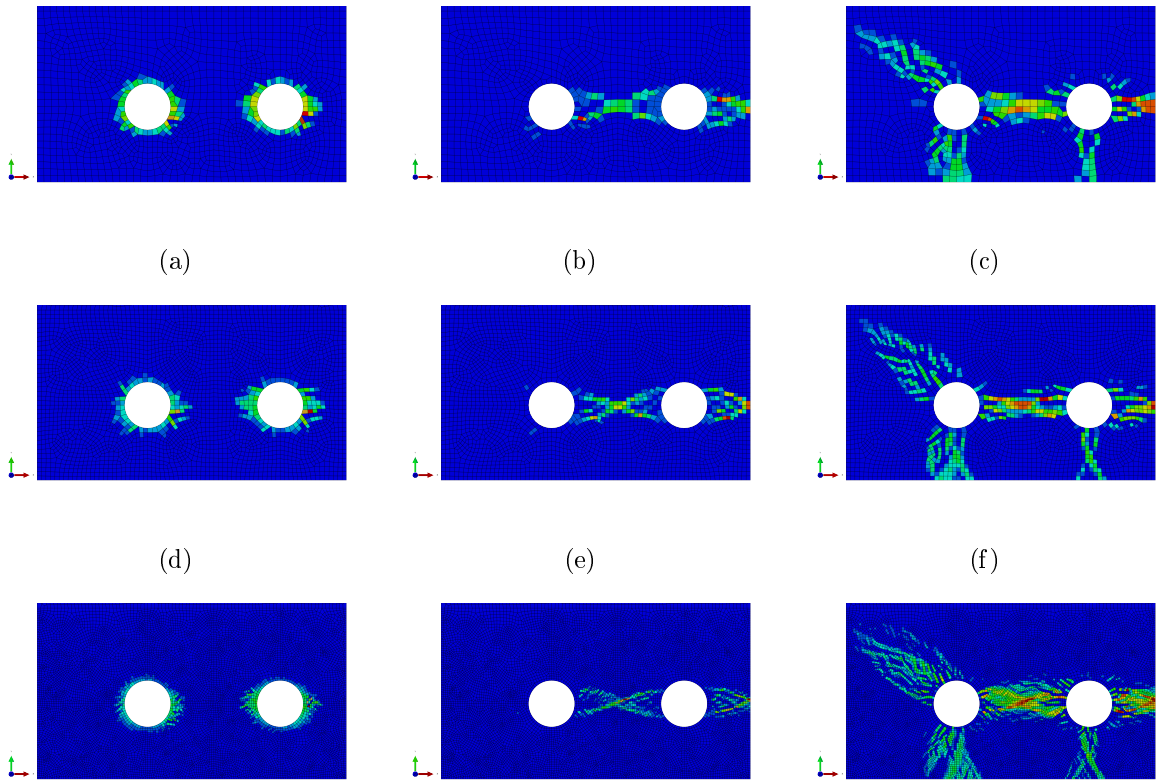

(a) (b) (c)

(d) (e) (f)

(g) (h) (i)

Figure 5.6: Distribution of PEEQT – Implicit analysis, damage-plasticity model, 30 mm concrete cover, $\psi = 25$, $\mu = 0.0001$. Coarse mesh: (a) – initial cracking, (b) – crack propagation, (c) – final stage of cracking, medium mesh: (d) – initial cracking, (e) – crack propagation, (f) – final stage of cracking, dense mesh: (g) – initial cracking, (h) – crack propagation, (i) – final stage of cracking

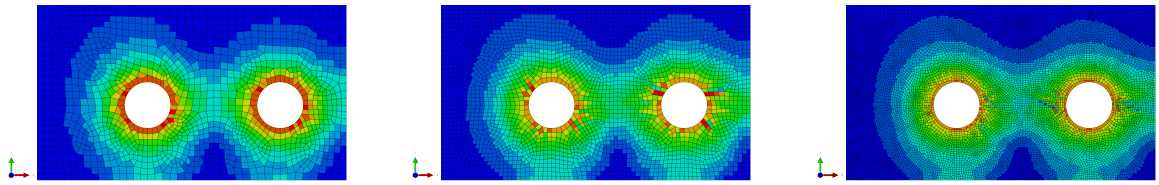

(a) (b) (c)

Figure 5.7: Distribution of Huber-Mises stress – Implicit analysis, damage-plasticity model, 30 mm concrete cover and dilation angle 5°: (a) – coarse mesh, (b) – medium mesh, (c) – dense mesh

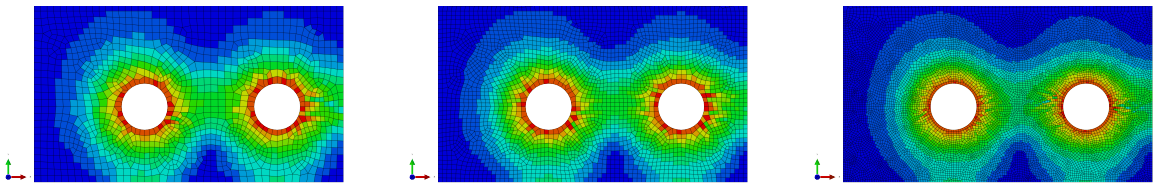

(a) (b) (c)

Figure 5.8: Distribution of Huber-Mises stress – Implicit analysis, damage-plasticity model, 30 mm concrete cover and dilation angle 25°: (a) – coarse mesh, (b) – medium mesh, (c) – dense mesh

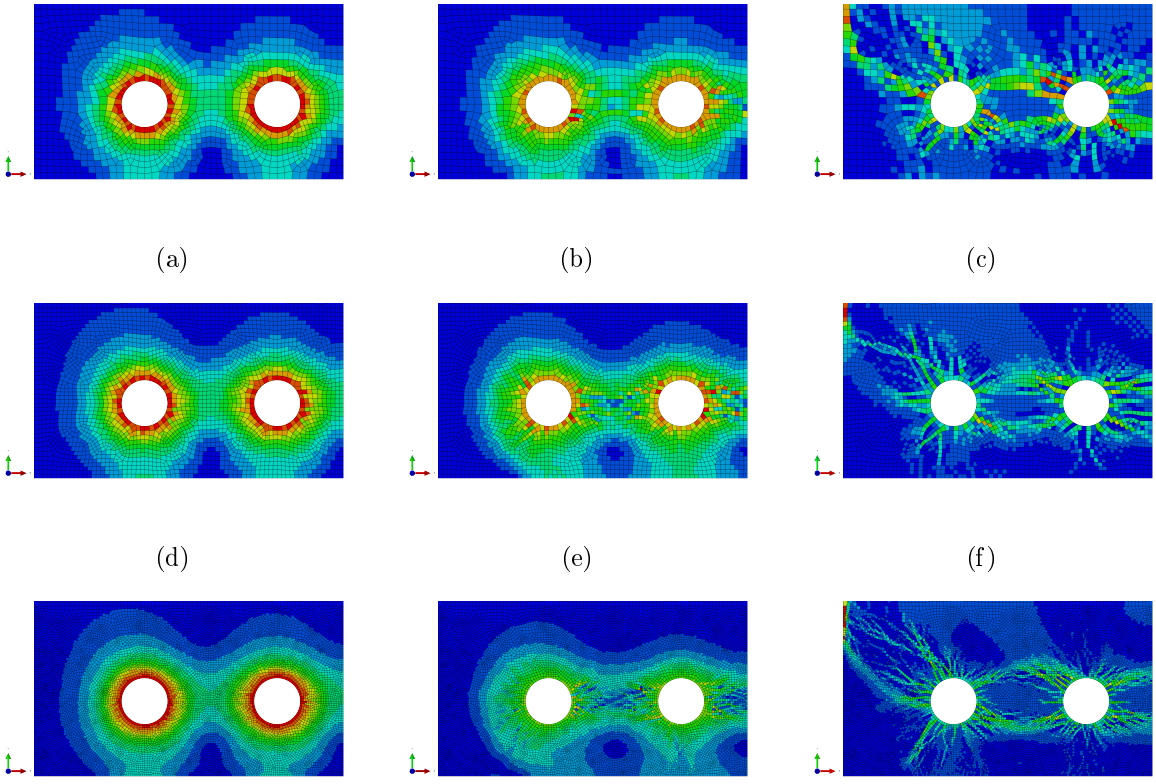

(a) (b) (c)

(d) (e) (f)

(g) (h) (i)

Figure 5.9: Distribution of Huber-Mises stress – Implicit analysis, damage-plasticity model, 30 mm concrete cover, $\psi = 25$, $\mu = 0.0001$. Coarse mesh: (a) – initial cracking, (b) – crack propagation, (c) – final stage of cracking, medium mesh: (d) – initial cracking, (e) – crack propagation, (f) – final stage of cracking, dense mesh: (g) – initial cracking, (h) – crack propagation, (i) – final stage of cracking

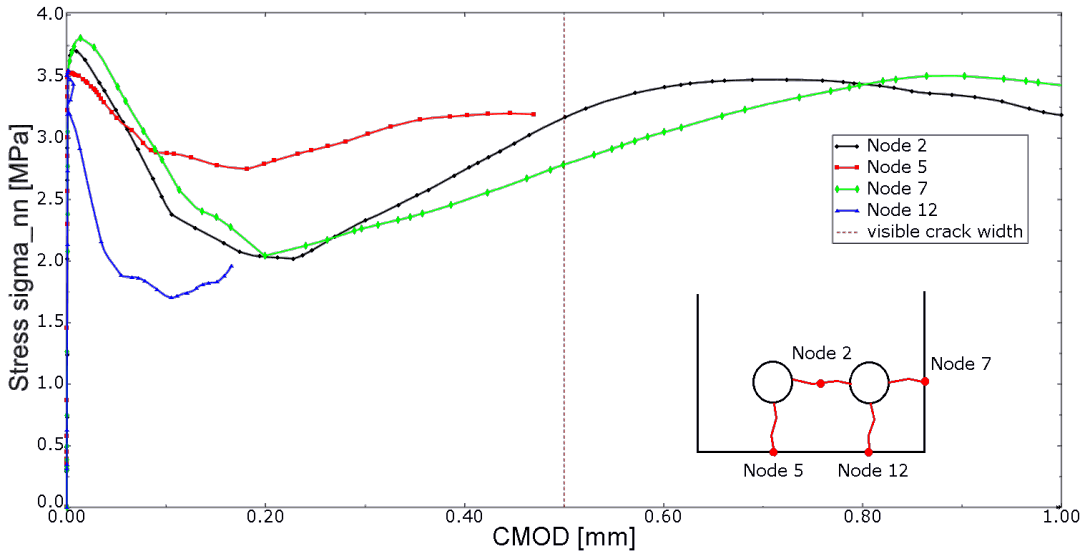


Figure 5.10: Stress $\sigma_{nn}$ vs. CMOD relations at marked points (cf. Fig. 5.3(c)) for RC cross-section analysis with 30 mm cover and coarse mesh

revealed good correlation. It can be observed that at points on the concrete surface the simulated crack width is generally below 0.5 mm, yet not negligible. On the other hand horizontal cracks between rebars are even wider than 1 mm. What is more, in Figs. 5.10 – 5.12 it can be observed that at all nodes, the material exhibits strain softening after reaching the tensile strength. However, one can notice that after stress redistribution a stress hardening occurs. The explanation of this effect can be that the material response observed in Figs. 5.10 – 5.12 is monitored locally at nodes. Since the stress redistribution (visible in Fig. 5.9) occurs, the nodal response also changes as CMOD increases. The presented diagrams respond to the analysis performed with $\mu$=0.0001. It seems to be pointless to present similar diagrams for the calculations with $\mu$=0, since they diverge at the early stage of cracking and no softening can be observed.

For the cross-section analysis it is hard to determine the global measures that could be depicted in a diagram. Admittedly, the pressure load increment could be monitored on the vertical axis, however there does not seem to be one global measure of the cross-section response that could be depicted on the horizontal axis.

For comparison a similar analysis has been performed for a cross-section with the concrete cover of 50 mm. The results of this analysis are presented in Figs. 5.13 – 5.24. The simulation has been performed with concrete dilation angle 5 or 25° and three densities of meshes composed of quadratic quadrilateral elements.

Figures 5.13 – 5.15 present the distributions of maximum principal strains computed with dilation angle 5°or 25°, and viscous parameter 0 or 0.0001. Additionally, in Fig. 5.15 the crack evolution can be observed. The distribution shows that the damage of concrete will take the form of cracking between the rebars. Increasing the cover from 30 mm to 50 mm successfully prevents concrete from cracking through the cover. Although

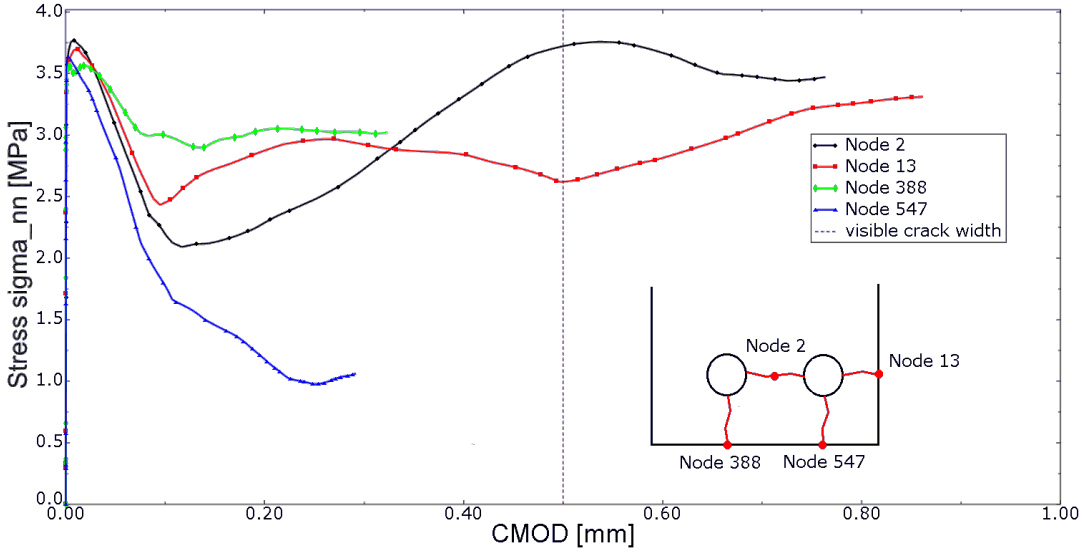


Figure 5.11: Stress $\sigma_{nn}$ vs. CMOD relations at marked points (cf. Fig. 5.3(f)) for RC cross-section analysis with 30 mm cover and medium mesh

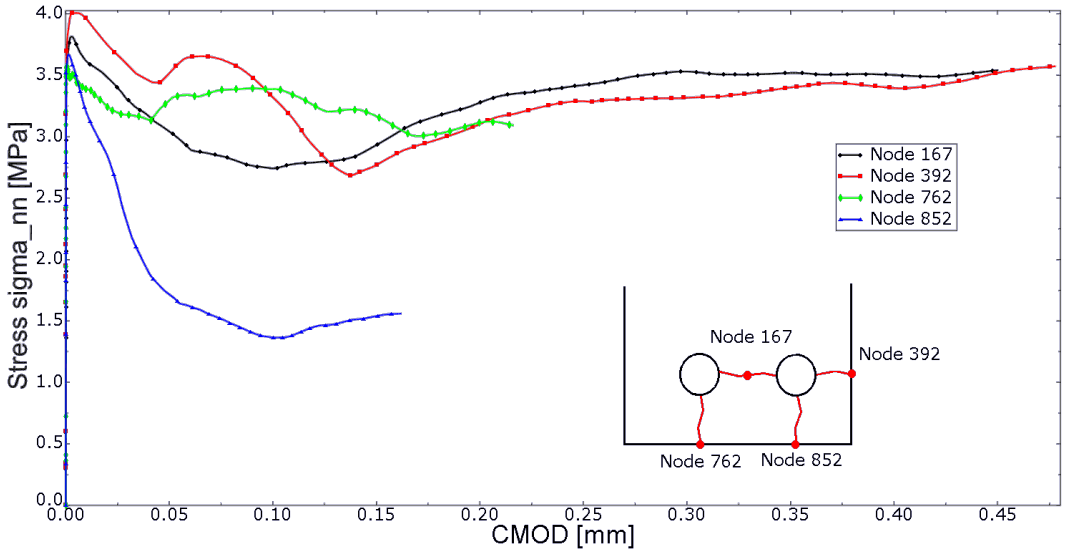


Figure 5.12: Stress $\sigma_{nn}$ vs. CMOD relations at marked points (cf. Fig. 5.3(i)) for RC cross-section analysis with 30 mm cover and dense mesh

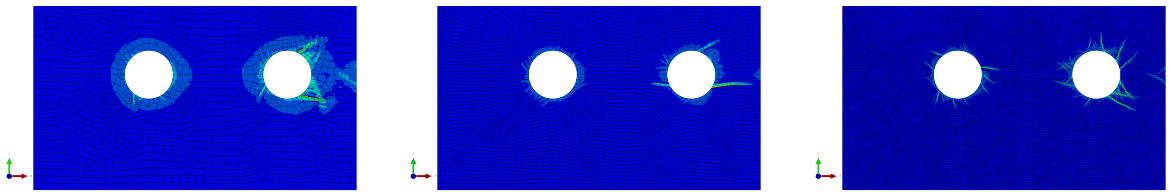

(a) (b) (c)

Figure 5.13: Distribution of max-in-plane strain – Implicit analysis, damage-plasticity model, 50 mm concrete cover and dilation angle 5°: (a) – coarse mesh, (b) – medium mesh, (c) – dense mesh

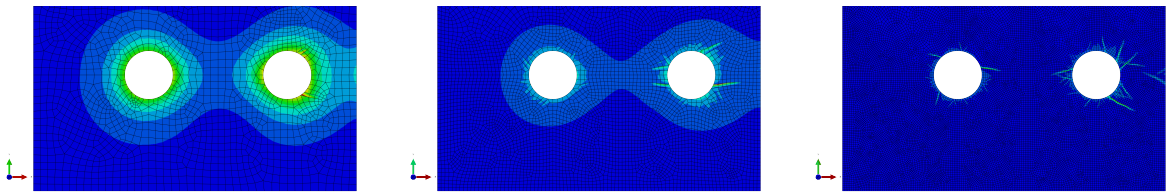

(a) (b) (c)

Figure 5.14: Distribution of max-in-plane strain – Implicit analysis, damage-plasticity model, 50 mm concrete cover and dilation angle 25°: (a) – coarse mesh, (b) – medium mesh, (c) – dense mesh

horizontal cracks between rebars can cause a loss in steel confinement, the cover remains sound and protects reinforcement from a quick inflow of detrimental substances. In the literature one can find $c/d$ ratio which is cover thickness to rebar diameter ratio. In the first simulation $c/d$ is equal to 1.2, after increasing the cover thickness to 50 mm, the $c/d$ ratio reaches the value 2, which seems to be enough to disable cover cracking. One could check numerically whether other size of cover thickness is enough. The normalized thickness $c/d$ together with the concrete tensile strength are the two principal parameters of the mechanical problem of corrosion, cf. [42].

Once again the PEEQT parameter has been monitored, and its distribution is presented in Figs. 5.16 – 5.18. The results confirm the observation that the major crack is formed between rebars, while the cover is uncracked.

Figures 5.19 – 5.21 present the Huber-Mises stress for the simulation of the cross-section with 50 mm cover at the initial and final stages of cracking. The stress relaxation is visible in Figs. 5.21(c), 5.21(f), 5.21(i).

Figures 5.22 – 5.24 present $\sigma_{nn}$ vs. CMOD diagram for points with maximum strains calculated, cf. Figs. 5.18(c), 5.18(f) and 5.18(i).

The maximum calculated crack mouth opening displacement values are around 1.5 mm, however the cracks are horizontal and not visible at the concrete surface. Nevertheless concrete becomes discontinuous. It must be emphasized that cracks formed between re-

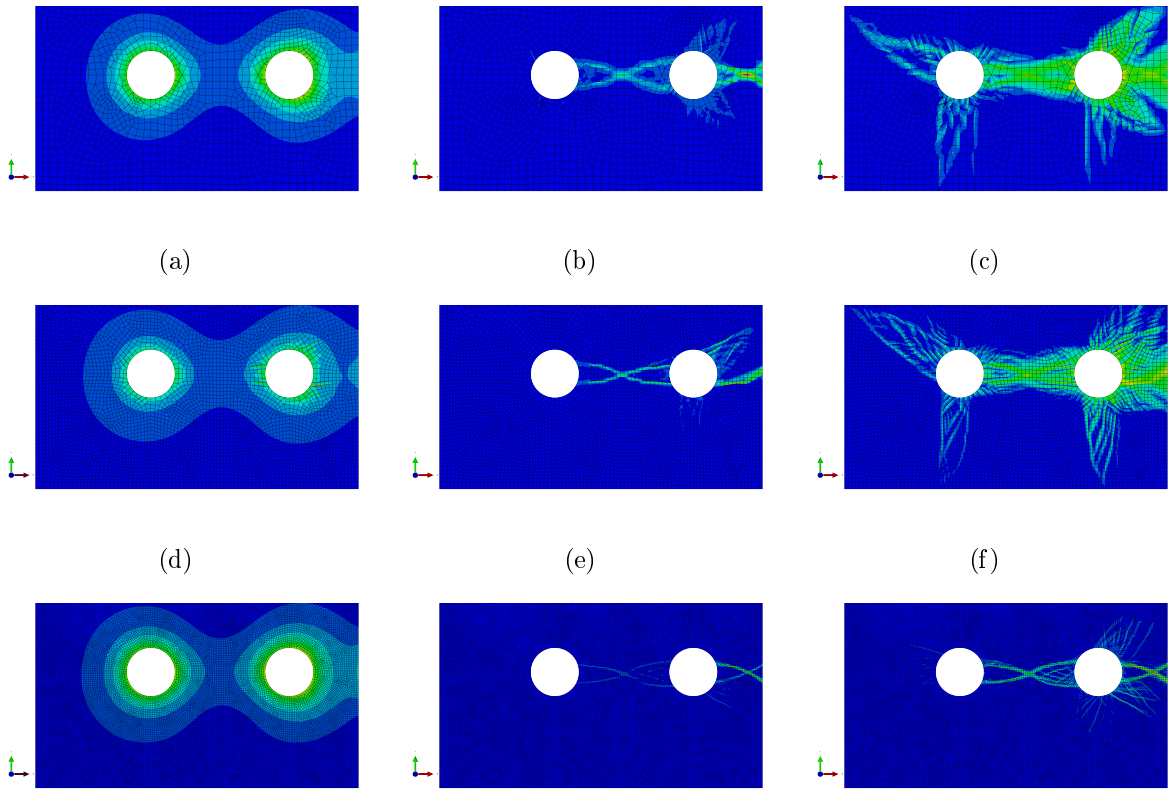

(a) (b) (c)

(d) (e) (f)

(g) (h) (i)

Figure 5.15: Distribution of max-in-plane strain – Implicit analysis, damage-plasticity model, 50 mm concrete cover, $\psi = 25$, $\mu = 0.0001$. Coarse mesh: (a) – initial cracking, (b) – crack propagation, (c) – final stage of cracking, medium mesh: (d) – initial cracking, (e) – crack propagation, (f) – final stage of cracking, dense mesh: (g) – initial cracking, (h) – crack propagation, (i) – final stage of cracking

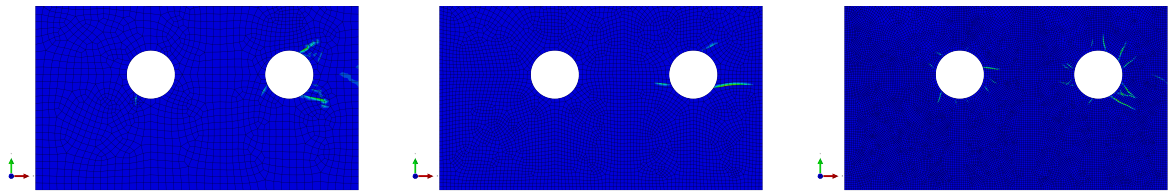

(a) (b) (c)

Figure 5.16: Distribution of PEEQT – Implicit analysis, damage-plasticity model, 50 mm concrete cover and dilation angle 5°: (a) – coarse mesh, (b) – medium mesh, (c) – dense mesh

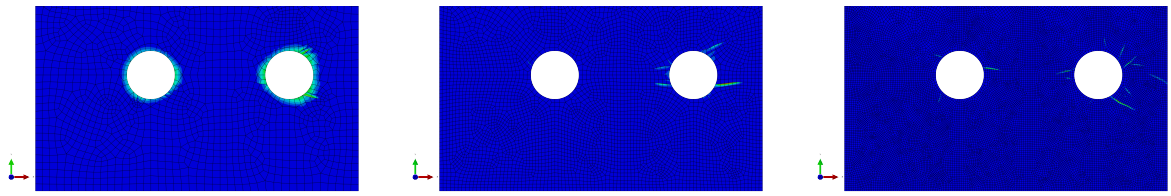

(a) (b) (c)

Figure 5.17: Distribution of PEEQT – Implicit analysis, damage-plasticity model, 50 mm concrete cover and dilation angle 25°: (a) – coarse mesh, (b) – medium mesh, (c) – dense mesh

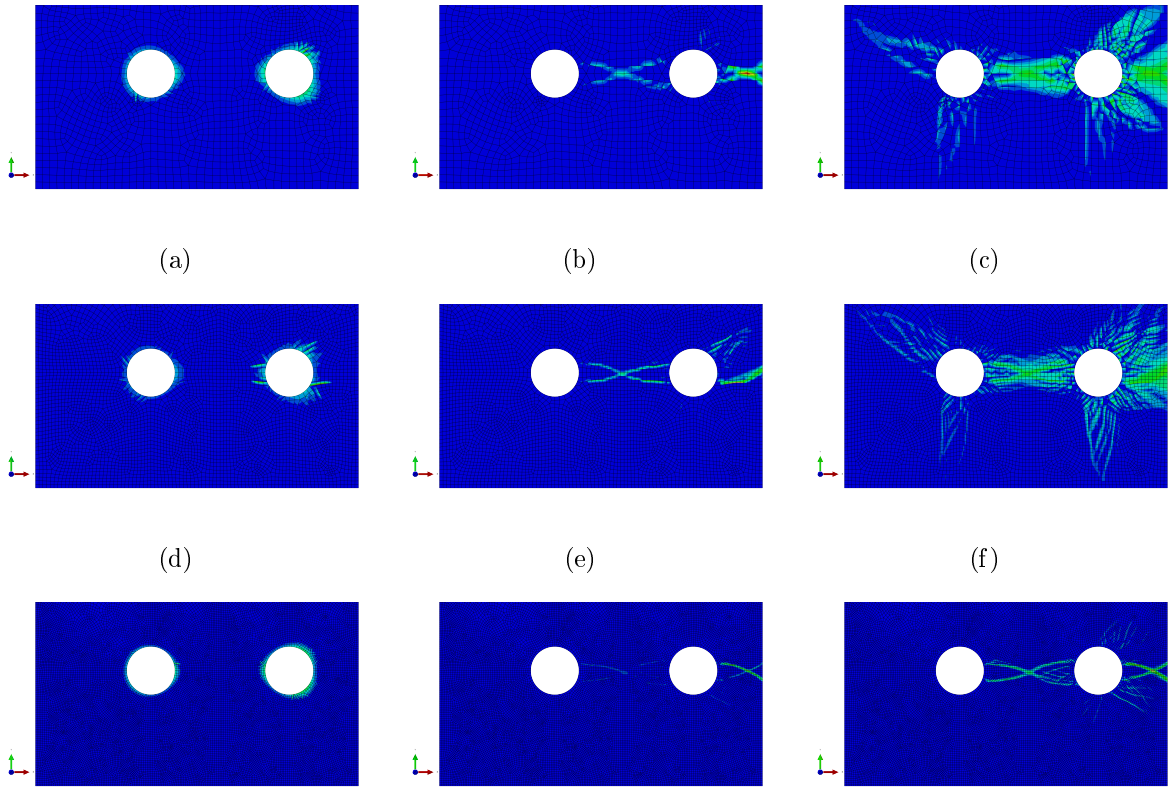

(a) (b) (c)

(d) (e) (f)

(g) (h) (i)

Figure 5.18: Distribution of PEEQT – Implicit analysis, damage-plasticity model, 50 mm concrete cover, $\psi = 25$, $\mu = 0.0001$. Coarse mesh: (a) – initial cracking, (b) – crack propagation, (c) – final stage of cracking, medium mesh: (d) – initial cracking, (e) – crack propagation, (f) – final stage of cracking, dense mesh: (g) – initial cracking, (h) – crack propagation, (i) – final stage of cracking

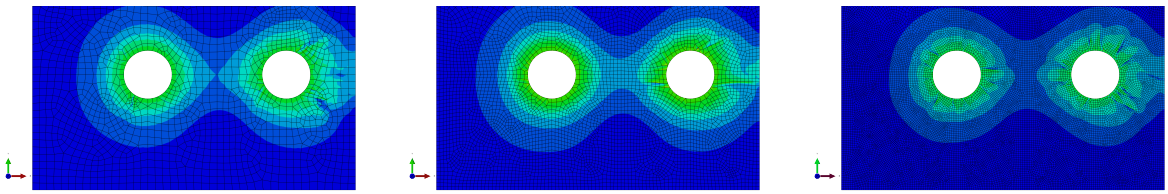

(a) (b) (c)

Figure 5.19: Distribution of Huber-Mises stress – Implicit analysis, damage-plasticity model, 50 mm concrete cover and dilation angle 5°: (a) – coarse mesh, (b) – medium mesh, (c) – dense mesh

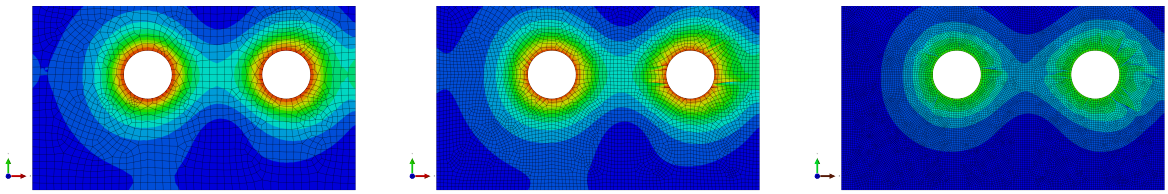

(a) (b) (c)

Figure 5.20: Distribution of Huber-Mises stress – Implicit analysis, damage-plasticity model, 50 mm concrete cover and dilation angle 25°: (a) – coarse mesh, (b) – medium mesh, (c) – dense mesh

bars and through the cover are dangerous for structure durability when the inflow of detrimental substances, such as water, chlorides or sulphates is considered. To illustrate the danger let it be noticed that size of water particle is less than 200 pm, the carbon dioxide molecule is less than 240 pm, the hydrogen molecule is 75 pm and chlorine molecule is 199 pm. The crack with the width of 0.5 mm is enough for water, carbon dioxide, oxygen or chlorides to get into the cross-section, which will result in the progress of corrosion speeding up. The concrete cover has no longer the protective function, which can lead to degradation of the whole structural element. It can be noticed that crack mouth opening displacements of the horizontal cracks have similar values despite the different cover thickness. However, the important point is that increasing the cover thickness prevents it from cracking, which leads to a slower destruction of the RC cross-section due to corrosion and longer service life of the structure.

The cross-section analysis has been also performed using the explicit time integration scheme. The explicit simulation has been performed for dense mesh with dilation angle 25°. The viscous regularization is not available in the explicit analysis. The results obtained from explicit simulation with concrete cover 30 mm and two different concrete models are presented in Figs. 5.25 – 5.28. The results of the simulation performed with damage-plasticity model are presented in Fig. 5.25. In Fig. 5.25(b) the initial horizontal crack is visible. As simulation proceed the cracking pattern gets more complex form, presented at Fig. 5.25(c). Concrete is cracked horizontally between rebars and vertically through the cover, however Fig. 5.25(c) seems to present damage much more developed

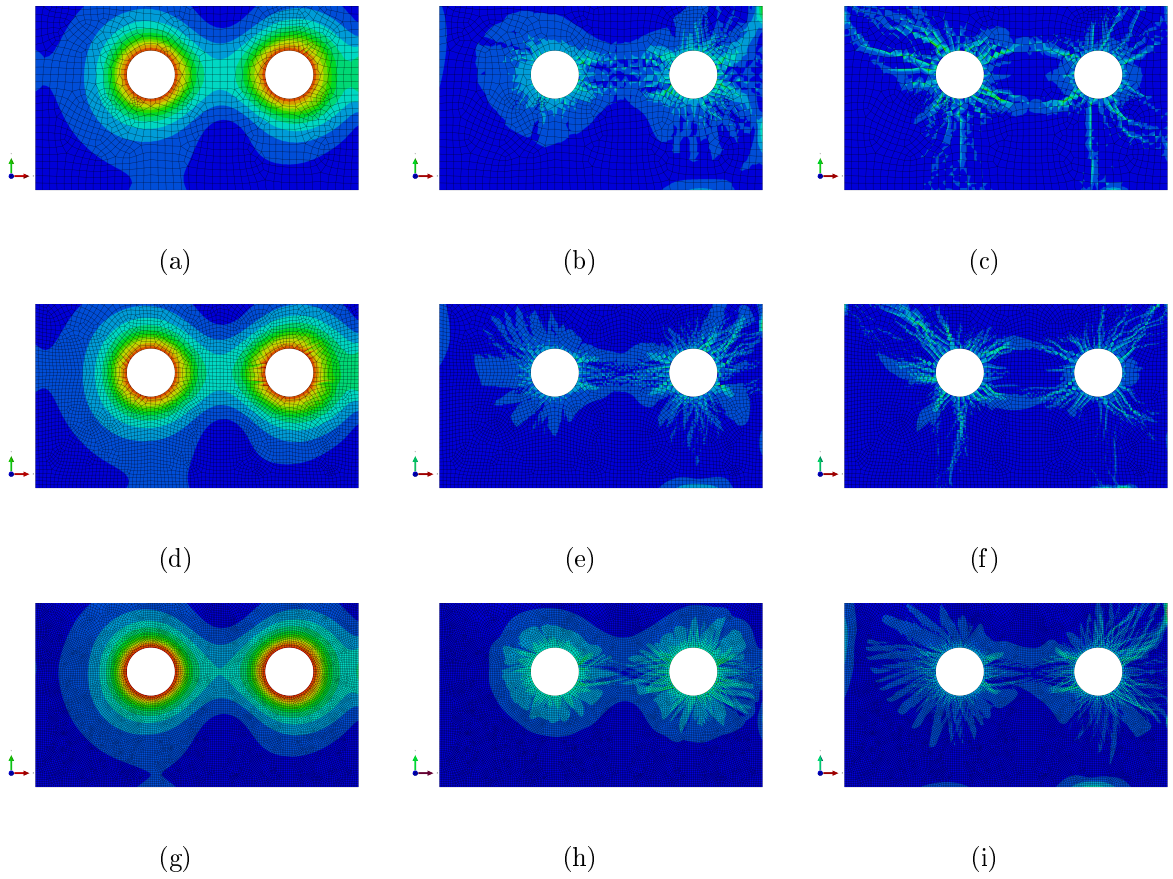


Figure 5.21: Distribution of Huber-Mises stress – Implicit analysis, damage-plasticity model, 50 mm concrete cover, $\psi = 25$, $\mu = 0.0001$: Coarse mesh: (a) – initial cracking, (b) – crack propagation, (c) – final stage of cracking, medium mesh: (d) – initial cracking, (e) – crack propagation, (f) – final stage of cracking, dense mesh: (g) – initial cracking, (h) – crack propagation, (i) – final stage of cracking

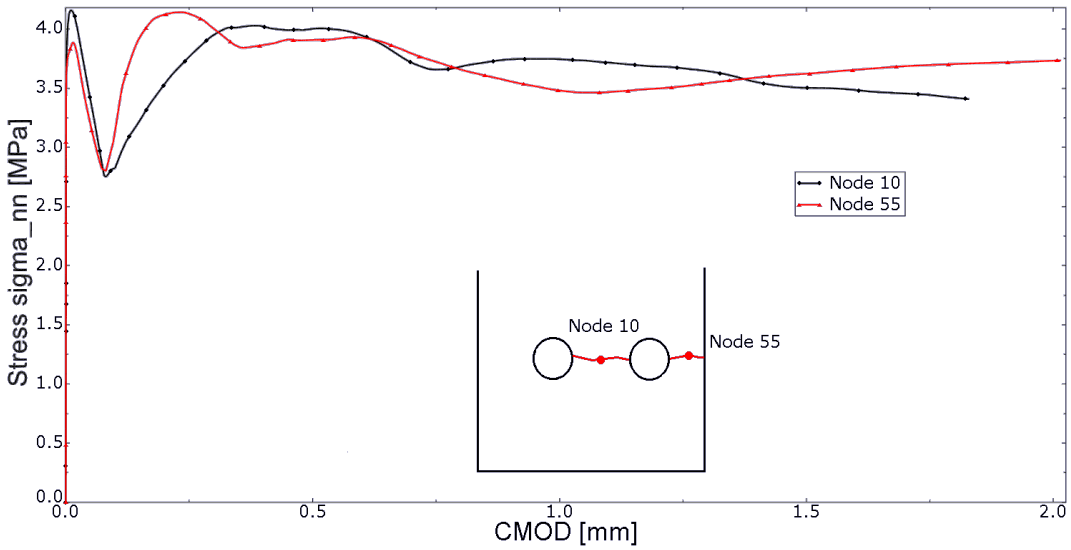


Figure 5.22: Stress $\sigma_{nn}$ vs. CMOD relations at marked points (cf. Fig. 5.18(c)) for RC cross-section analysis with 50 mm cover and coarse mesh

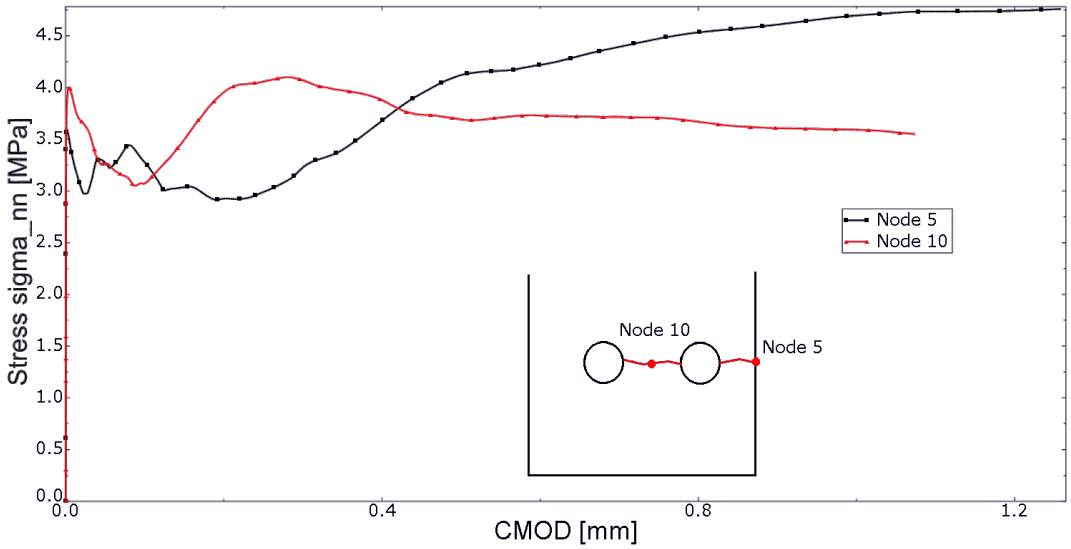


Figure 5.23: Stress $\sigma_{nn}$ vs. CMOD relations at marked points (cf. Fig. 5.18(f)) for RC cross-section analysis with 50 mm cover and medium mesh

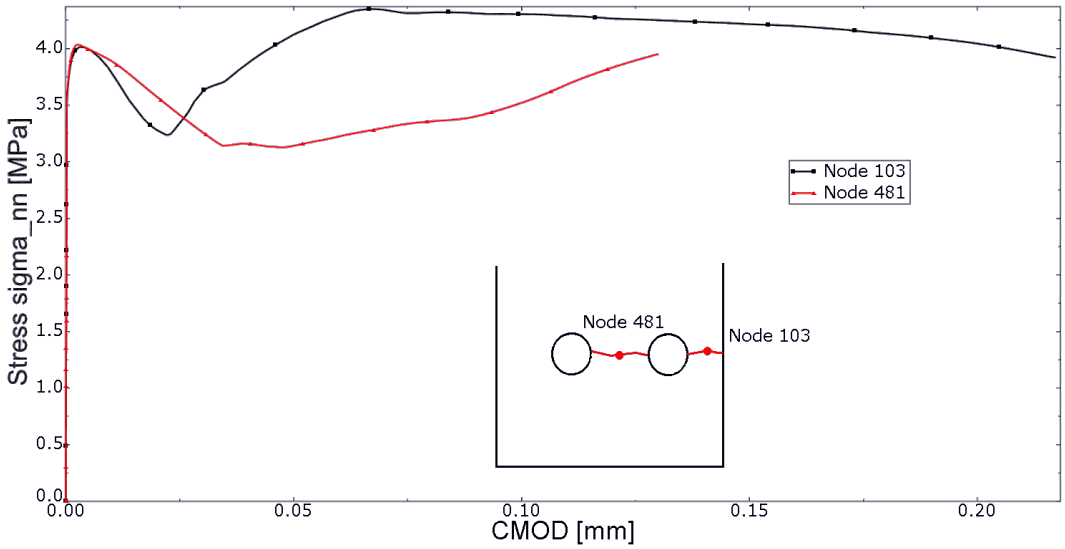


Figure 5.24: Stress $\sigma_{nn}$ vs. CMOD relations at marked points (cf. Fig. 5.18(i)) for RC cross-section analysis with 50 mm cover and dense mesh

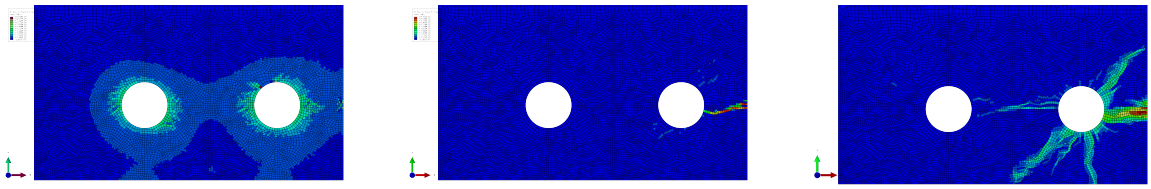

(a) (b) (c)

Figure 5.25: Distribution of max-in-plane strain – Explicit analysis, damage-plasticity model, 30 mm concrete cover and dilation angle 25°

than it was assumed to appear.

In Fig. 5.26 results for the calculations using concrete modelled as brittle cracking material are presented. The initial crack is formed between rebars. Unfortunately the computations abort prematurely, despite changes in analysis parameters, hence only the initial pattern is presented. Nevertheless, for both material models the maximum values of CMOD (similar as in implicit analysis) appear in the middle of the distance of two internal rebars.

In Figs. 5.27 and 5.28 the Huber-Mises stress distribution is presented. The stress relaxation can be observed for both materials.

In Fig. 5.29 the stress $\sigma_{nn}$ vs. CMOD diagrams are presented. CMOD values calculated using the damage-plasticity model are much greater than those obtained with the cracking model. This can be due to the fact that simulation with cracking model diverge prematurely but can also be a result of differences between the two material models.

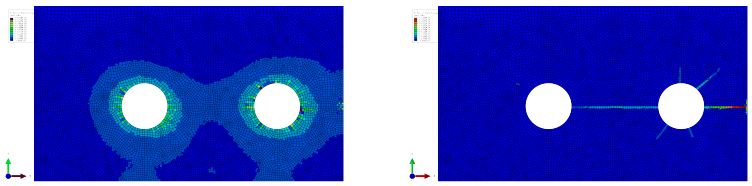

(a) (b)

Figure 5.26: Distribution of max-in-plane strain – Explicit analysis, cracking model, 30 mm concrete cover and dilation angle 25°

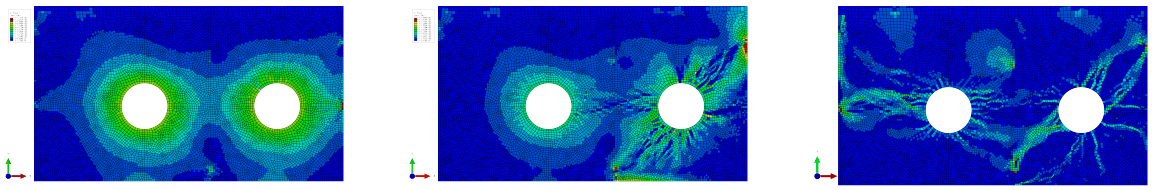

(a) (b) (c)

Figure 5.27: Distribution of Huber-Mises stress – Explicit analysis, damage-plasticity model, 30 mm concrete cover and dilation angle 25°

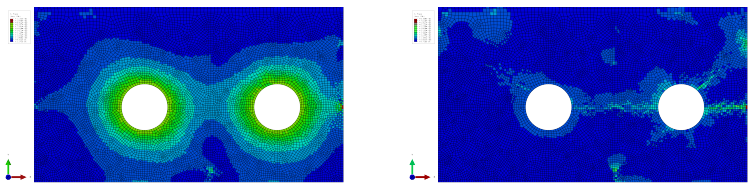

(a) (b)

Figure 5.28: Distribution of Huber-Mises stress – Explicit analysis, cracking model, 30 mm concrete cover and dilation angle 25°

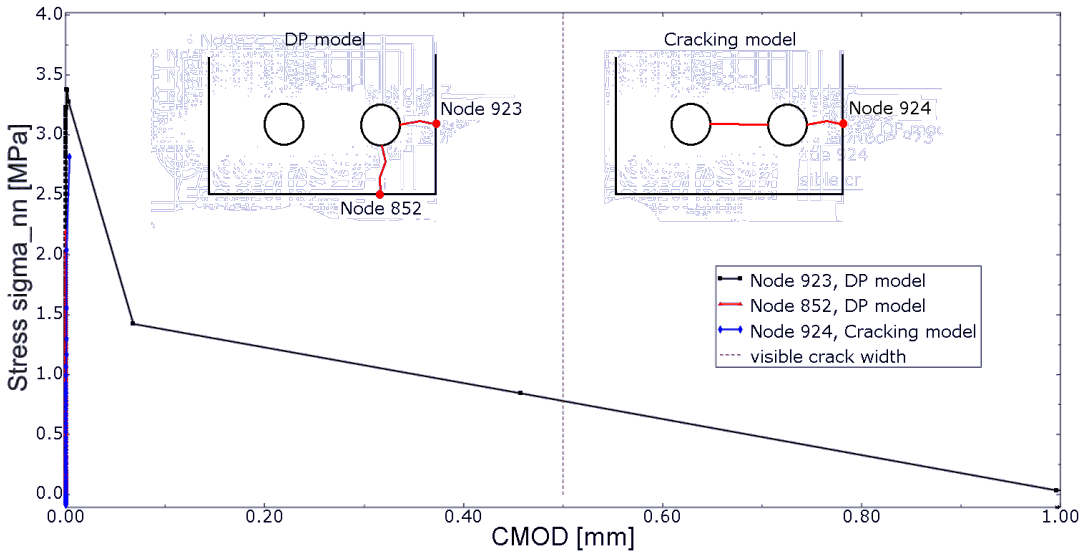


Figure 5.29: Stress $\sigma_{nn}$ vs. CMOD relations at marked points (cf. Figs. 5.25(c) and 5.26(b)) for RC cross-section analysis with 30 mm cover and dense mesh, explicit analysis

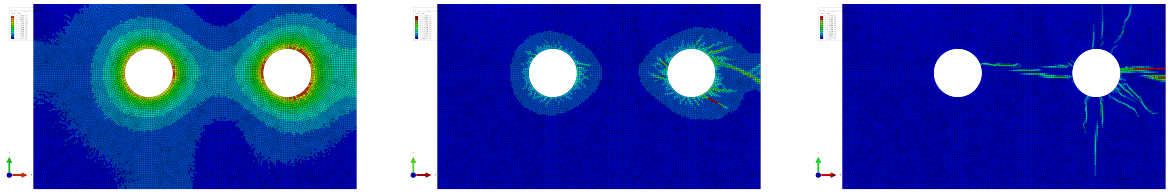

(a) (b) (c)

Figure 5.30: Distribution of max-in-plane strain – Explicit analysis, damage-plasticity model, 50 mm concrete cover and dilation angle 25°

The damage-plasticity and cracking models have also been employed in the explicit analysis of the cross-section with 50 mm cover. The results are presented in Figs. 5.30 – 5.33. Figure 5.30 presents the evolution of max-in-plane strain distribution calculated with the damage-plasticity model, while Fig. 5.31 presents similar evolution calculated with the cracking model. The final cracking patterns presented in Figs. 5.30(c) and 5.31(c) are very similar for both models, although slightly different than in the case of implicit algorithm. The main crack is formed horizontally between rebars, and no crack is visible at the concrete surface. However in explicit analysis a short vertical crack appears, while it is not visible in the implicit analysis performed with the same density of mesh. To be exact, in the implicit analysis a short vertical crack is formed, but only in the calculations performed with coarse and medium meshes.

Nevertheless, regardless what the type of analysis or material model are, the simu-

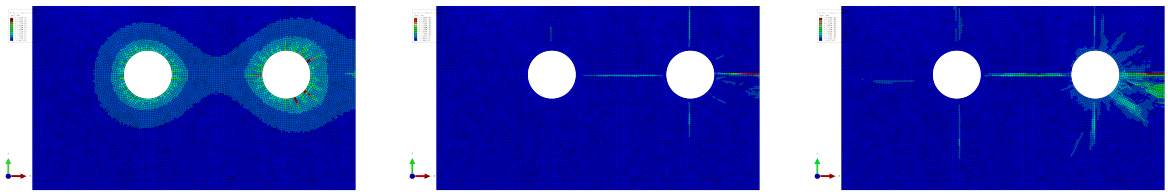

(a) (b) (c)

Figure 5.31: Distribution of max-in-plane strain – Explicit analysis, cracking model, 50 mm concrete cover and dilation angle 25°

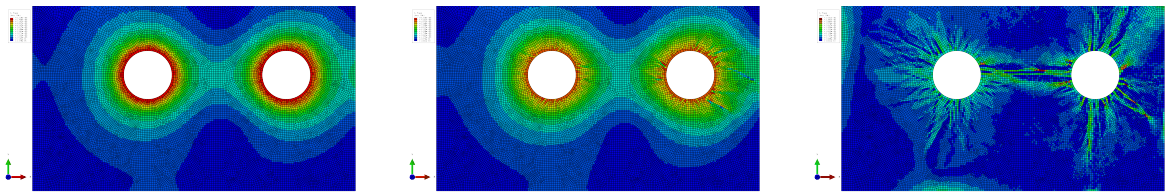

(a) (b) (c)

Figure 5.32: Distribution of Huber-Mises stress – Explicit analysis, damage-plasticity model, 50 mm concrete cover and dilation angle 25°

lations indicate that first crack is formed horizontally, and later the concrete cover is cracked. For 30 mm cover the vertical crack is visible at the concrete surface, while for 50 mm the concrete surface remains continuous.

The evolutions of Huber-Mises stress distribution for damage-plasticity and cracking models are presented in Figs. 5.32 and 5.33. For the damage-plasticity model a stress relaxation is presented in Fig. 5.32. On the other hand, for the cracking model a partly false stress pattern can be observed especially in Fig. 5.33(c). Although there is a difference in stress distribution between Figs. 5.33(b) and 5.33(c) it is hard to point out where the relaxation takes place or to observe the redistribution of stresses. The cracking model is generally less stable than the damage-plasticity model and, what follows, the results obtained with the cracking model are harder to interpret and less reliable.

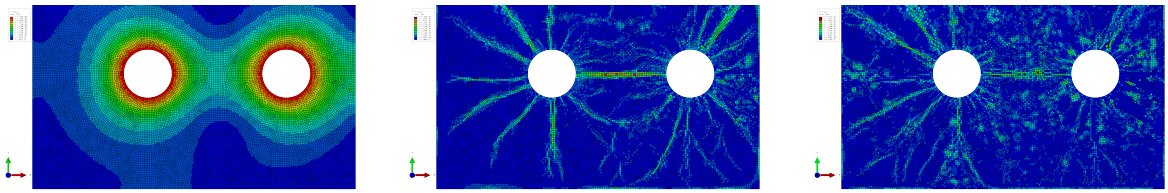

(a) (b) (c)

Figure 5.33: Distribution of Huber-Mises stress – Explicit analysis, cracking model, 50 mm concrete cover and dilation angle 25°

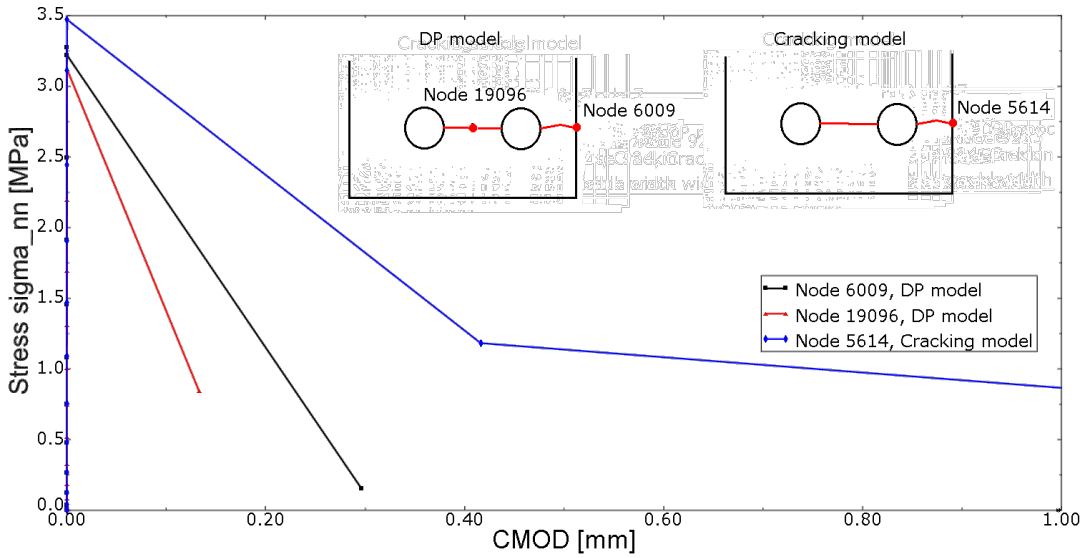


Figure 5.34: Stress $\sigma_{nn}$ vs. CMOD relations at marked points (cf. Figs. 5.30(c) and 5.31(c)) for RC cross-section analysis with 50 mm cover and dense mesh, explicit analysis

Figure 5.34 presents stress $\sigma_{nn}$ vs. CMOD diagrams for the damage-plasticity and cracking models, respectively. For the cracking model it can be observed that CMOD is at least 1 mm and after reaching the peak value strain softening occurs. For the damage-plasticity model CMOD of horizontal cracks is 0.3 mm.

Figure 5.35 presents the distribution of displacement vectors for the final stage of cracking calculated using explicit algorithm. Additionally a cracking pattern has been marked with red line. In both figures the spalling tendency is clearly visible.

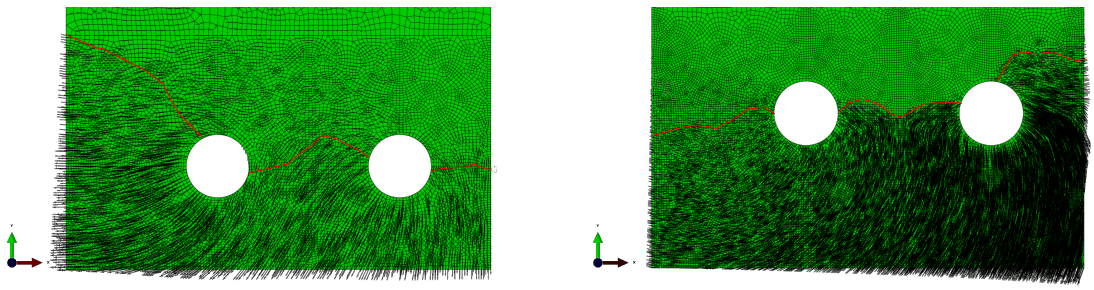

(a) (b)

Figure 5.35: Distribution of displacement vectors for the final stage of cracking, implicit analysis, damage-plasticity model (a) – 30 mm cover (b) – 50 mm cover

Table 5.3: Material parameters – pullout model

| Concrete | | Steel | |
|---|---|---|---|
| Parameter | Value | Parameter | Value |
| E [MPa] | 37 000 | E [MPa] | 206 000 |
| $\nu$ [-] | 0.2 | $\nu$ [-] | 0.3 |
| Stress at comp. peak $f_c$ [MPa] | 30 | Yield stress $\sigma_e$ [MPa] | 450 |
| Strain at comp. peak $\varepsilon_c$ [-] | 0.2% | Plastic tangent stiff. $E_T$ [MPa] | 2 200 |
| Tens. yield stress $f_t$ [MPa] | 4.3 | | |

## 5.2 Pullout test

The material models discussed previously have also been used to simulate a pullout tests, which were originally performed in [1]. In the experimental test the bond behavior was studied in different stages of corrosion: no corrosion, precracking, cracking (defined as appearance of the first visible crack) and postcracking. The experiments were performed on 150 mm cubic concrete specimens with 10, 14 and 20 mm diameter bars, centrally embedded in concrete. The embedment length-to-bar diameter ratio was 4. The steel used had an average yield strength of 450 MPa and concrete had a compressive strength of 30 MPa. This experiment was also the subject of FE analysis conducted in [8].

In the thesis the single rebar pullout simulation is performed to obtain the interface parameters, which are going to be used in the 3D beam model. The simulation model assumes 150 x 150 x 40 mm concrete block and 10 mm diameter steel bar placed in the center of the cross-section. This gives the embedment length-to-bar diameter ratio 4 and $c/d$ equal to 7. The three-dimensional analysis of a quarter configuration is performed using 8-node solid elements modelling concrete and steel and 8-node cohesive elements modelling the rust layer as interface. The material model parameters for concrete and steel have been partly adopted from [8] and are presented in Table 5.3.

Five levels of corrosion are assumed: 0% – no corrosion, 0.87% – precracking, 4.27% – cracking, and finally 6.7% and 7.8% – postcracking. The corrosion is applied first, while in the following steps the displacement of the free end of rebar is applied.

The diagrams showing the bond-slip behavior for the analyzed implicit model compared to the results of the experiment are presented in Fig. 5.36. It can be observed that the results of FE analysis are in good agreement with the experimental results for the case with no corrosion and high levels of corrosion (6.7% and 7.8%). The discrepancies between the model and the experiment for the 0.87% and 4.27% corrosion curves can be a result of corrosion products distribution which is an effect that has been neglected in the analysis. The thin layer of concrete lying around the reinforcement has in fact much weaker properties than the rest of the material. However, whenever rust is produced, it is accumulated around the reinforcement in the empty space generated by steel consumption, but also fills voids in the neighboring weak concrete. The mixture of weak concrete and corrosion products results in an increase of mechanical parameters of this thin layer

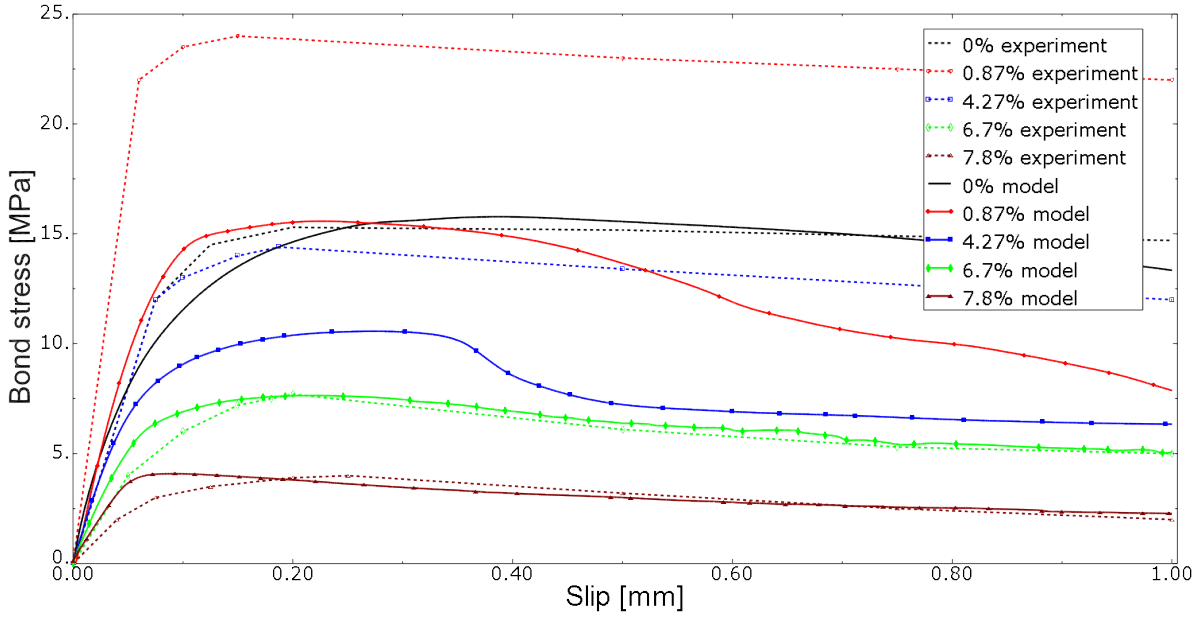


Figure 5.36: Bond stress vs slip of free end

of material, in other words bond gets temporarily stronger. Hence for small amounts of corrosion the bond strength increases. For higher levels of corrosion, the confinement provided by concrete is lost due to cracking and, as rust layer gets thicker, a lubricating effect is introduced into the model, thus the bond strength decreases significantly. Unfortunately, the interface model presented in the thesis simulates well the behavior corresponding with high corrosion levels. The simulation of increase of bond strength due to rust-concrete interaction is almost not represented. The visible non linear decrease of the 4.27% diagram can be related to the fact that at this level of corrosion concrete actively cracks and the total loss of bond is an interaction of damages of the interface and concrete. At the corrosion levels of 6.7% and 7.8% concrete is already cracked at the beginning of the process, so the loss of bond observed in the diagram is mainly related to the damage of the rust interface. The discrepancy observed suggests that the model should be further investigated, focusing on the concrete behavior.

During the analysis, the PEEQT parameter has been monitored for concrete. The results presented in Fig. 5.37 illustrate the distribution of the PEEQT parameter for different values of free end slip (0.2, 0.4 and 0.6 mm) in the model with no corrosion acting, calculated using the implicit algorithm. When no corrosion is applied, the pullout simulation results indicate that PEEQT distribution is nonuniform along the reinforcement. Plastic strains appear mainly in the front part of concrete and no crack propagates through the cover.

Next, the corrosion has been applied and results for 0.87%, 4.27%, 6.7% and 7.8% are presented in Fig. 5.38. For the precracking level of corrosion (0.87% in Figs. 5.38(a) – 5.38(c)) the plastic strains next to the rebar can mainly be observed in the front part

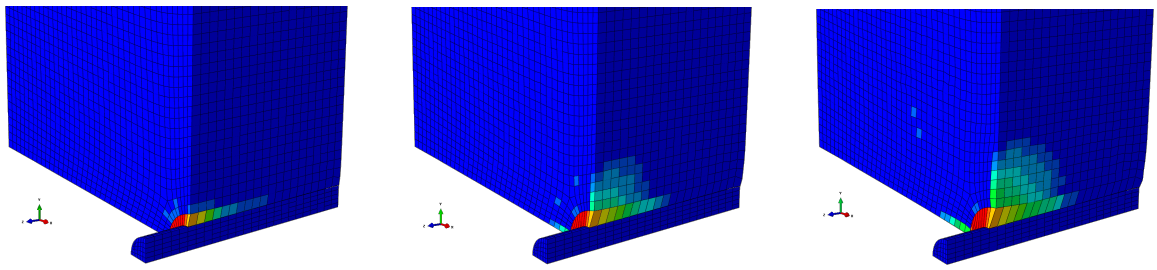

(a) (b) (c)

Figure 5.37: Distribution of equivalent plastic tensile strain (PEEQT) for model with no corrosion and free end slip: (a) – 0.2 mm, (b) – 0.4 mm, (c) – 0.6 mm

of concrete, similar as in case of no corrosion. Additionally, single short cracks begin to form.

As corrosion increases to the cracking level (4.27% in Figs. 5.38(d) – 5.38(f)), the PEEQT distribution gets more uniform along the reinforcement. Thus the whole concrete-rust contact area gets involved in the process. What is more, the cracks penetrate through the concrete, moreover they develop as rebar displacement increases.

For 6.7% corrosion (Figs. 5.38(g) – 5.38(i)) concrete is visibly cracked in the front part, however there is also nonzero PEEQT noticed in the back part of the concrete block. Thus the cracked front part of concrete provides no confinement. The only interlocking force transfer between concrete, rust and steel occurs in the back part along the reinforcement.

For 7.8% corrosion (Figs. 5.38(j) – 5.38(l)) there are clearly visible cracks in the front part of concrete. However, it seems that concrete is severely damaged due to corrosion, thus as steel displacements increase only minor differences in PEEQT distribution along reinforcement can be observed. Hence, the conclusion can be drawn that for high corrosion levels the total bond strength depends strictly on the rust parameters.

The other parameter that has been monitored during the analysis is the scalar damage variable (SDEG). SDEG appears in the interface, whenever the maximum stress criterion is satisfied. The distribution of SDEG in the interface for three values of free end slip and three levels of corrosion is shown in Fig. 5.39. For the precracking level of corrosion no damage in the interface can be observed (this case is not shown). The first damage is noticed for 4.27% of corrosion in the back part of the interface. As the slip of the rebar increases, the damaged area of the interface increases too, as presented in Figs. 5.39(a) – 5.39(c).

For 6.7% of corrosion SDEG is distributed (Figs. 5.39(d) – 5.39(f)) along a large part of the length of reinforcement, while for 7.8% of corrosion (Figs. 5.39(g) – 5.39(i)) almost the whole interface is damaged at the beginning of the simulation. Thus for postcracking level of corrosion interface is mainly responsible for bond strength in the pullout simulation.

Again, the calculations with the same loading application have been repeated using the explicit algorithm and concrete represented by damage-plasticity or cracking model.

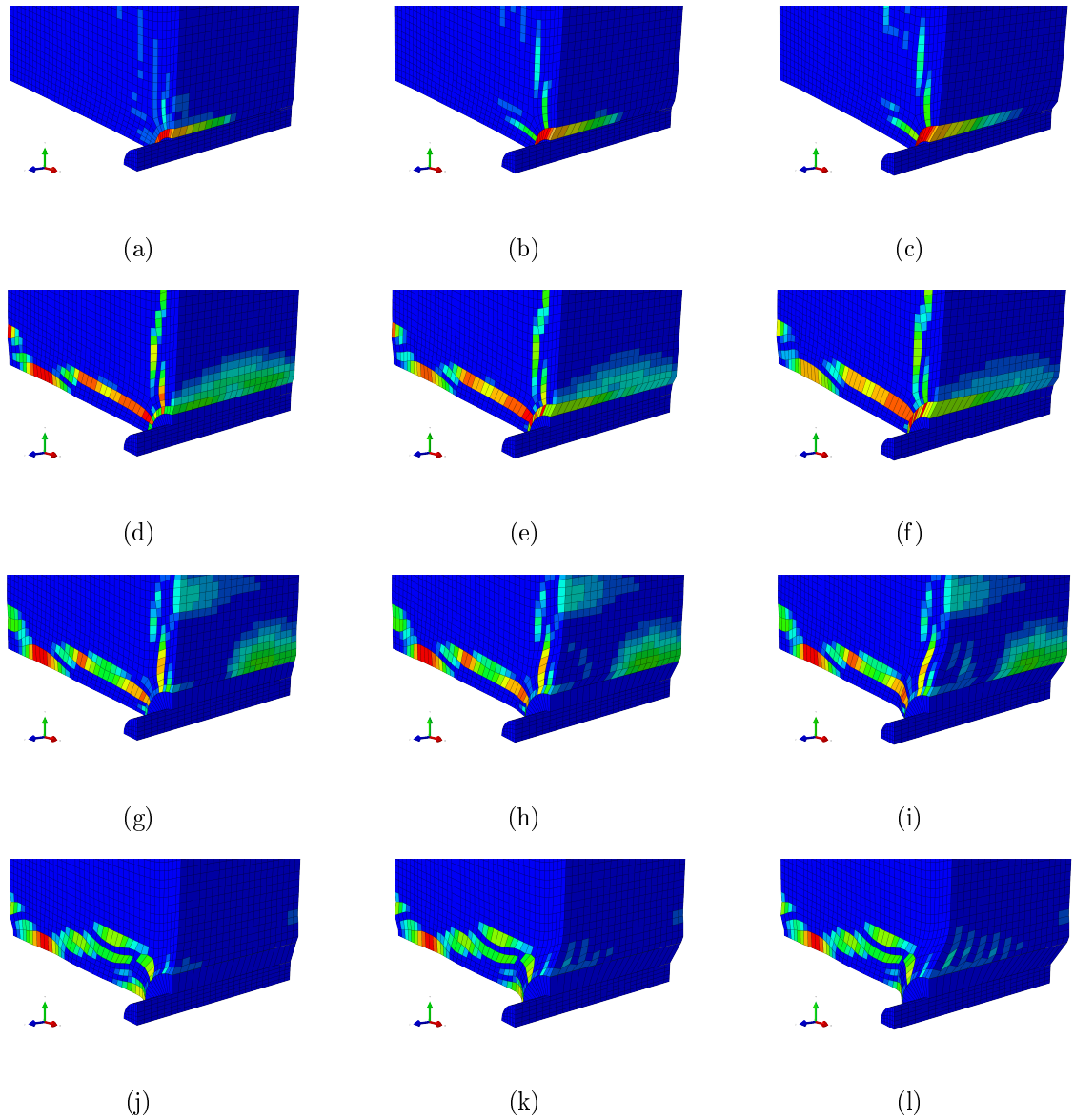


Figure 5.38: Distribution of equivalent plastic tensile strain (PEEQT); 0.87% corrosion, free end slip: (a) – 0.2 mm, (b) – 0.4 mm, (c) – 0.6 mm; 4.27% corrosion, free end slip: (d) – 0.2 mm, (e) – 0.4 mm, (f) – 0.6 mm; 6.7% corrosion, free end slip: (g) – 0.2 mm, (h) – 0.4 mm, (i) – 0.6 mm; 7.8% corrosion, free end slip: (j) – 0.2 mm, (k) – 0.4 mm, (l) – 0.6 mm

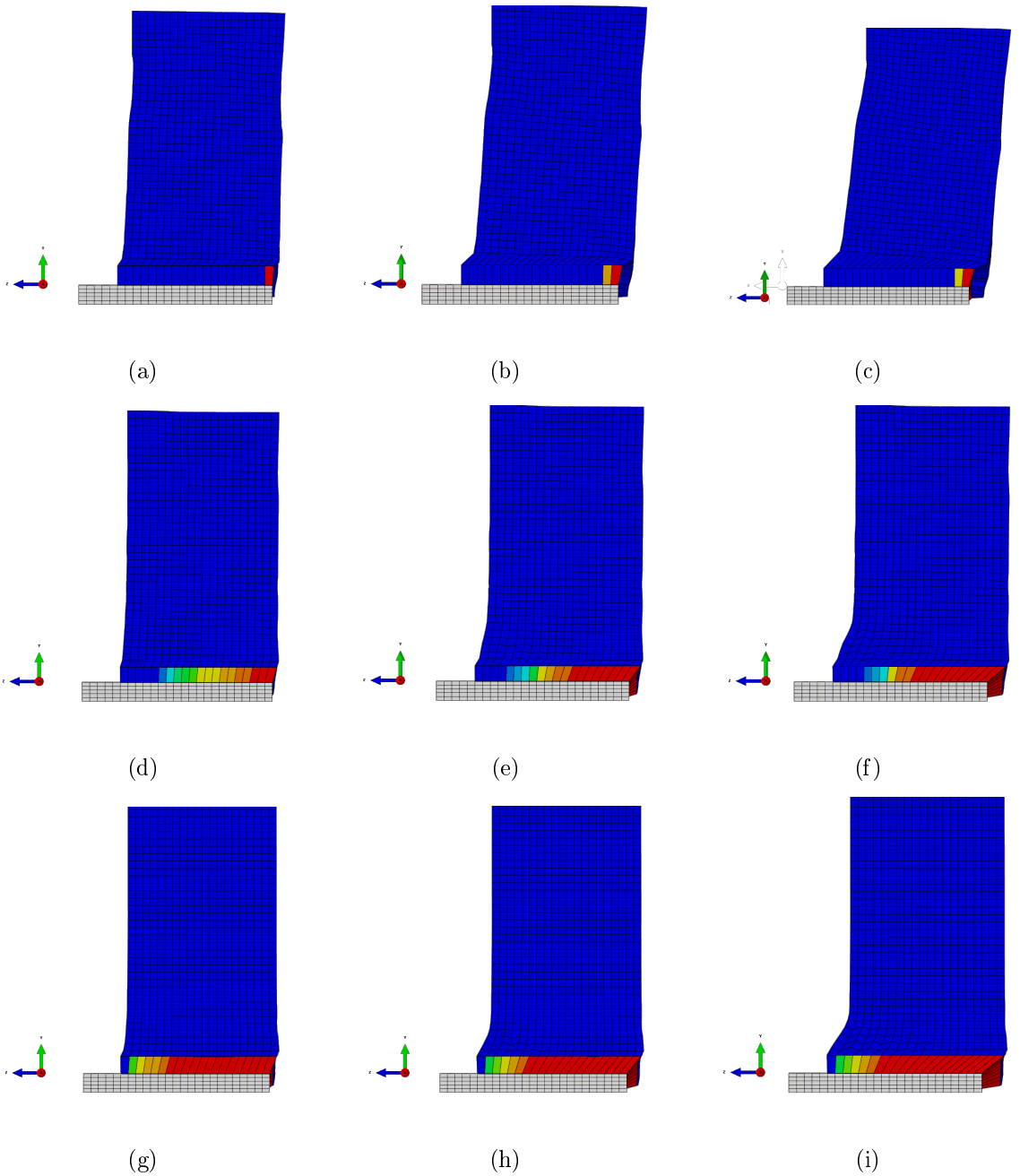


Figure 5.39: Distribution of scalar damage variable (SDEG); 4.27% corrosion, free end slip: (a) – 0.2 mm, (b) – 0.4 mm, (c) – 0.6 mm; 6.7% corrosion, free end slip: (d) – 0.2 mm, (e) – 0.4 mm, (f) – 0.6 mm; 7.8% corrosion, free end slip: (g) – 0.2 mm, (h) – 0.4 mm, (i) – 0.6 mm

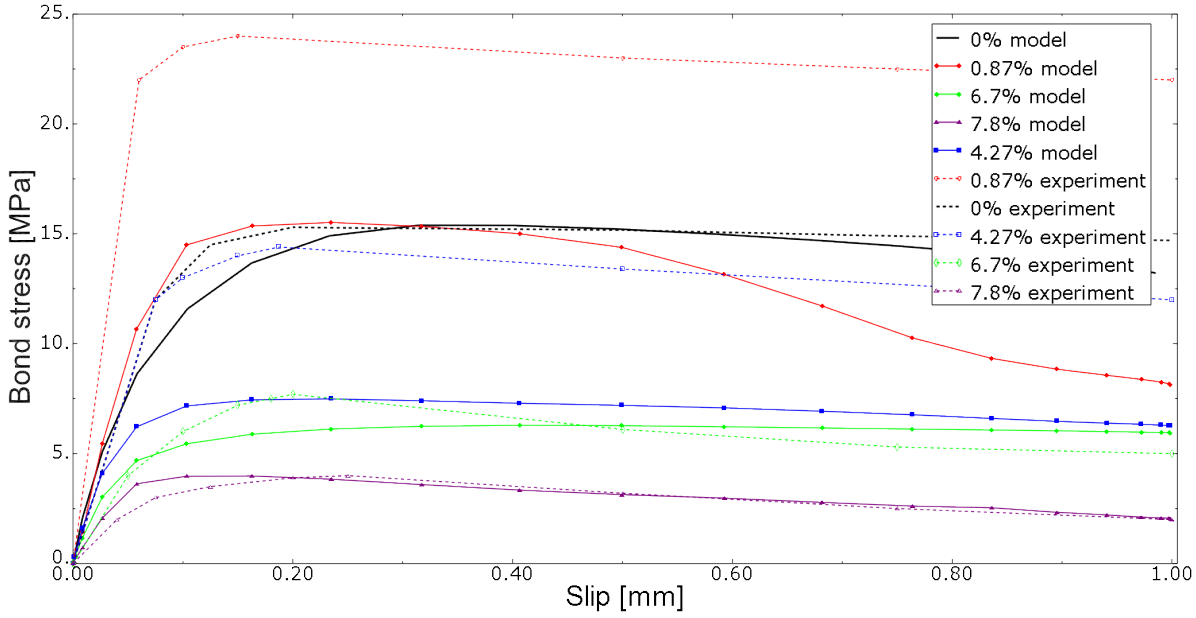


Figure 5.40: Bond stress vs slip of free end for explicit simulation, damage plasticity model

The results of the explicit calculations with damage-plasticity are presented in Figs. 5.40 – 5.43. Figure 5.40 presents bond-slip relations for different levels of corrosion. The correlation of simulation and experiment is slightly worse than in the case of implicit simulation. There is a huge discrepancy between the model and experiment for 0.87% corrosion. For cracking level (4.27%) the difference between the model and experiment is bigger than in the implicit simulation. A similar situation can be observed for 6.7% corrosion. A full agreement between the results and experiment is noticed only for the case of no corrosion and very high level of corrosion.

The distributions of PEEQT for 0.2, 0.4, 0.6 mm free end slip and no corrosion values are presented in Fig. 5.41. They are the same as for the implicit model.

Figure 5.42 presents PEEQT distributions for 0.87%, 4.27%, 6.7% and 7.8% of corrosion. The results of explicit analysis when compared to implicit simulation reveal huge discrepancies, especially in the case of 4.27% and 6.7% of corrosion. Again, for the pre-cracking level of corrosion (0.87% in Figs. 5.42(a) – 5.42(c)) the plastic strains are mainly observed in the front part of concrete, however single short cracks begin to form. The PEEQT distribution is quite similar to the implicit simulation. For 4.27% corrosion (Figs. 5.42(d) – 5.42(f)), the PEEQT distribution gets more uniform along the reinforcement and a single crack is visible, penetrating concrete block. The PEEQT distribution, thus the possible damage as well, differ from the case of implicit algorithm, however in both simulations, the crack penetrating concrete is visible.

For 6.7% corrosion (Figs. 5.42(g) – 5.42(i)) and 7.8% corrosion (Figs. 5.42(j) – 5.42(l)) there is a clearly visible crack in the front part of concrete. In this case the PEEQT

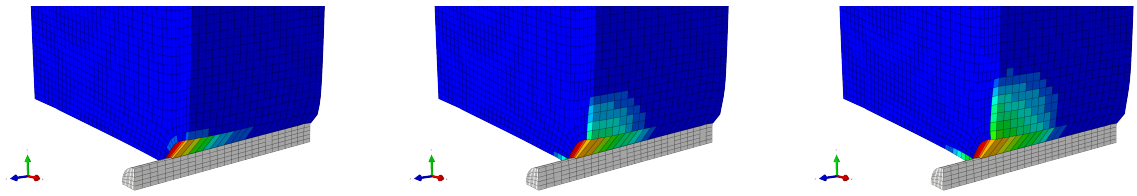

(a) (b) (c)

Figure 5.41: Distribution of equivalent plastic tensile strain (PEEQT) for explicit, damage-plasticity model with no corrosion and free end slip: (a) – 0.2 mm, (b) – 0.4 mm, (c) – 0.6 mm

distribution can be noticed along the front part of reinforcement, while for 7.8% it is nearly negligible. However, for postcracking levels of corrosion almost no difference in PEEQT distribution can be observed as the rebar slip increases. Thus, once again it seems that for high corrosion levels the total bond strength depends mainly on the rust interface parameters.

For the explicit analysis the SDEG parameter has also been monitored. The distribution of SDEG in the interface for three values of free end slip and three levels of corrosion is shown in Fig. 5.43. In contrast to the implicit simulation, in the explicit analysis the first damage in the interface is noticeable in the case of 6.7% of corrosion. For precracking and cracking levels of corrosion no damage in the interface can be observed.

For 6.7% and 7.8% of corrosion SDEG is distributed along reinforcement (Figs. 5.43(d) – 5.43(i)), and the results are similar to those obtained from implicit calculations. However, for the postcracking levels of corrosion the damaged area of the rust interface is smaller than those observed in the implicit analysis. This effect has also been noticed in Fig. 5.40, since the maximum stress values obtained during the explicit analysis are smaller than those obtained in the implicit simulation. Nevertheless, it can again be stated that for postcracking levels of corrosion the bond strength in pullout simulation is governed by interface parameters.

The explicit simulation has also been performed with concrete modelled as cracking material. For the cracking model the value of the tension yield stress presented in Table 5.3 has been decreased to 2.8 MPa to obtain agreement between model and experiment. Unfortunately, the simulation performed with this model provides credible results only in the case of no corrosion. For the models with other levels of corrosion the computations diverge prematurely. The internal energy decreases abruptly when nonlinearities in subsequent finite elements occur. What follows, the kinetic energy is much higher than internal energy, and the process does not remain quasi-static. Thus, the further calculations do not make any sense in the case of static considerations. This effect remains in spite of changes of analysis parameters, incrementation etc.

In Fig. 5.44 the bond-slip relation for the cracking model is presented. The curves representing 0.87%, 4.27%, 6.7% and 7.8% are plotted as long as the results seem to be

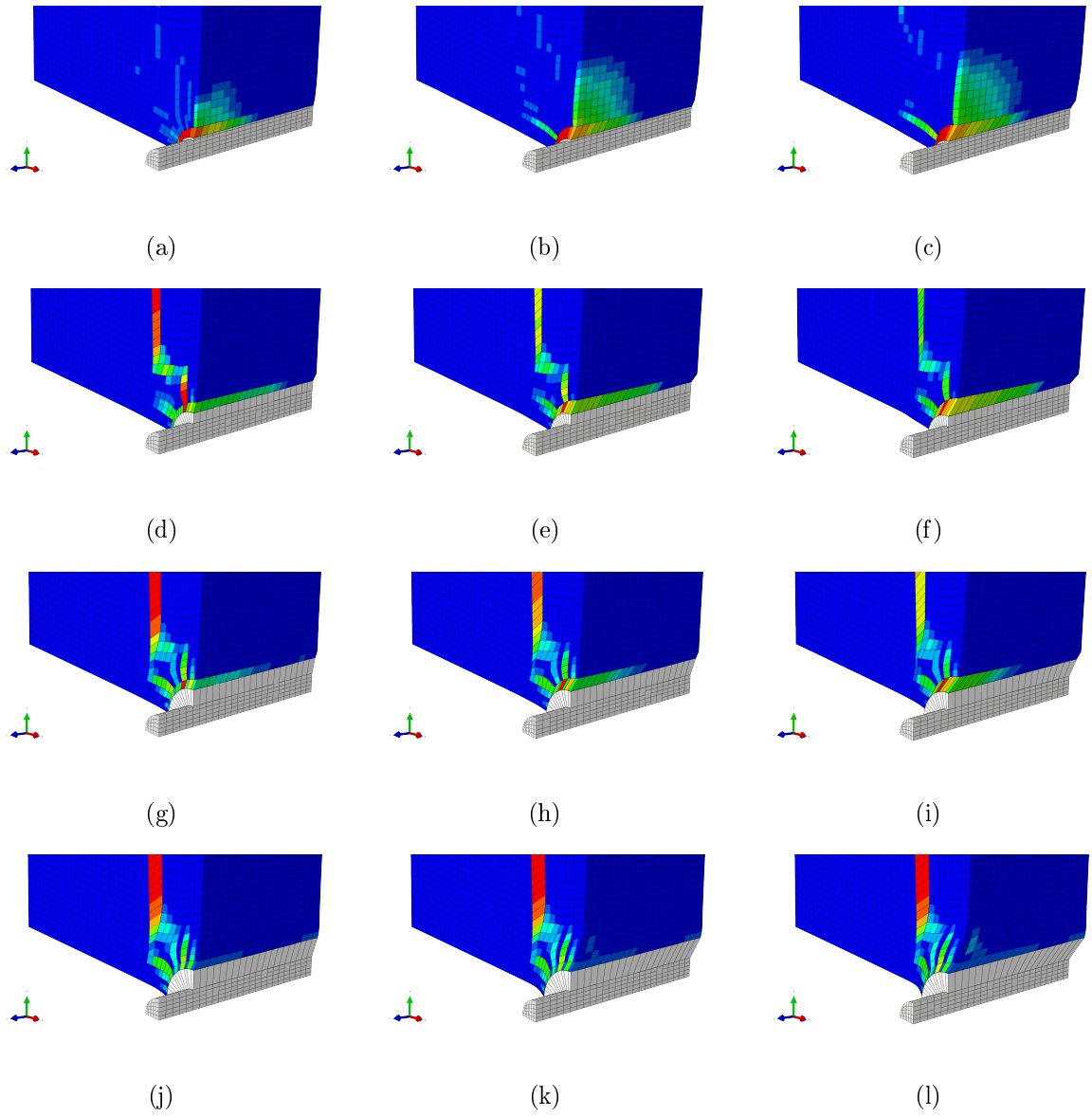


Figure 5.42: Distribution of equivalent plastic tensile strain (PEEQT) for explicit simulation and damage-plasticity model; 0.87% corrosion, free end slip: (a) – 0.2 mm, (b) – 0.4 mm, (c) – 0.6 mm; 4.27% corrosion, free end slip: (d) – 0.2 mm, (e) – 0.4 mm, (f) – 0.6 mm; 6.7% corrosion, free end slip: (g) – 0.2 mm, (h) – 0.4 mm, (i) – 0.6 mm; 7.8% corrosion, free end slip: (j) – 0.2 mm, (k) – 0.4 mm, (l) – 0.6 mm

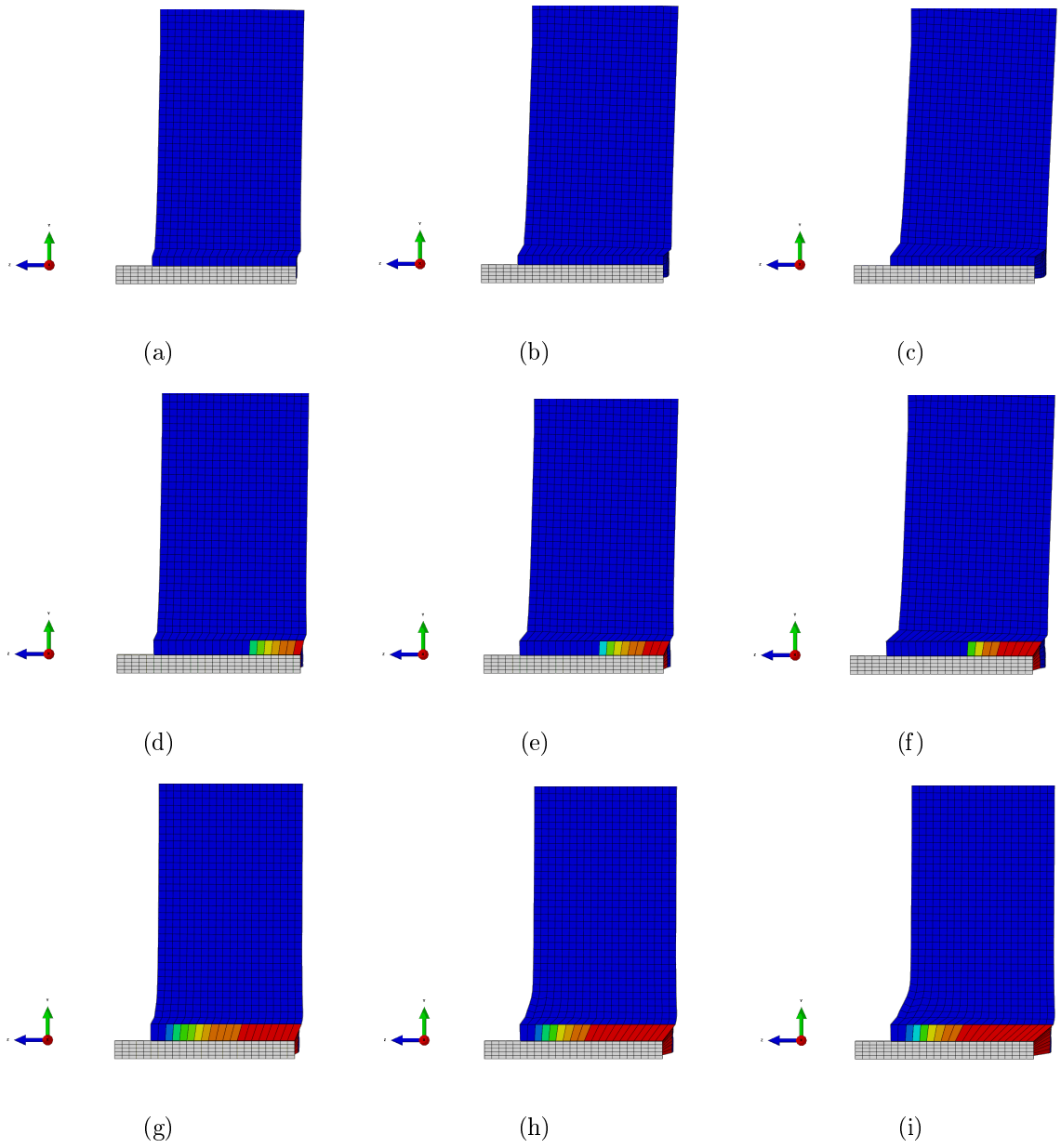


Figure 5.43: Distribution of scalar damage variable (SDEG) for explicit simulation and damage-plasticity model: 4.27% corrosion, free end slip: (a) – 0.2 mm, (b) – 0.4 mm, (c) – 0.6 mm; 6.7% corrosion, free end slip: (d) – 0.2 mm, (e) – 0.4 mm, (f) – 0.6 mm; 7.8% corrosion, free end slip: (g) – 0.2 mm, (h) – 0.4 mm, (i) – 0.6 mm

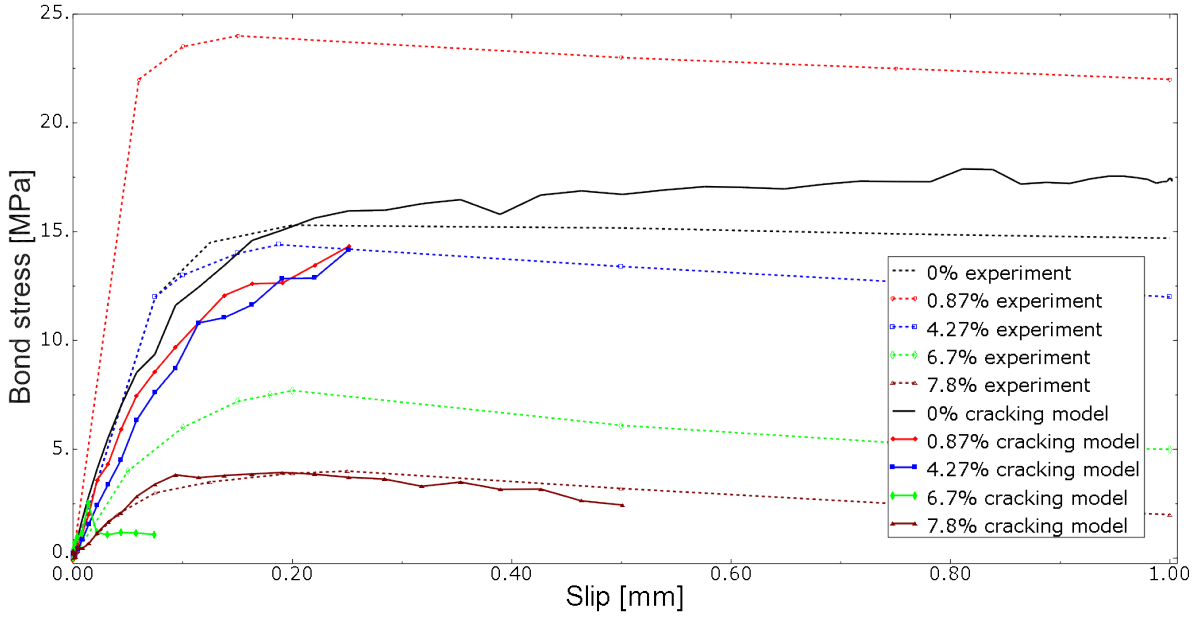


Figure 5.44: Bond stress vs slip of free end for explicit simulation, cracking model

credible for quasi-static analysis, i.e. the kinetic energy of the process does not exceed 5% of the internal energy. The calculation and experimental results are in good correlation only in the case of 7.8% corrosion. Other simulation cases seem to differ significantly from experiment. The 6.7% corrosion model diverges at the beginning of the process, and the obtained results in fact do not exceed the corrosion application. No pullout analysis has been performed for this level of corrosion. For 7.8% of corrosion concrete is severely cracked at the beginning of the pullout process and the bond-slip behavior is related to rust interface parameters only. This explains the agreement between the model and the experiment. However, the overall response of the model leaves the impression that the cracking model is not adequate for both corrosion and pullout simulations. In the case of pullout simulation with no corrosion applied the model seems to be reliable, although the results achieved with damage-plasticity model in the implicit and explicit analyses are more convincing.

The distribution of maximum in-plane strains for 0.2, 0.4, 0.6 mm free end slip and no corrosion are presented in Fig. 5.45. The results of the cracking analysis when compared to the damage-plasticity model reveal huge discrepancies. The strain distribution presented in Fig. 5.45 indicates that the pullout sample is cracked when the rebar slip is only 0.2 mm. During the simulation the cracking pattern does not change significantly.

Figure 5.46 presents maximum in-plane strain distributions for 0.87%, 4.27%, 6.7% and 7.8% of corrosion. The results refer to the steps of analysis when the simulation was quasi-static. Hence, Figs. 5.46(a) and 5.46(b) present the results for 0.87% and 4.27% corrosion and slip 0.2 mm, while in Fig. 5.46(c) a distribution of max-in-plane strains for 6.7% corrosion and no slip can be observed. It can be noticed that the cracks penetrating

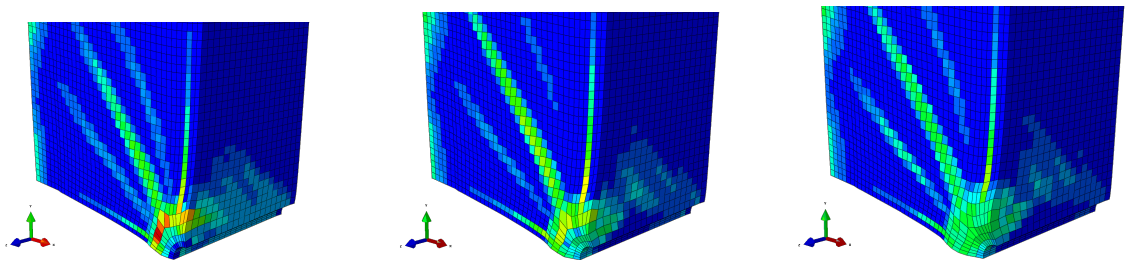

(a) (b) (c)

Figure 5.45: Distribution of max-in-plane strains for explicit, cracking model with no corrosion and free end slip: (a) – 0.2 mm, (b) – 0.4 mm, (c) – 0.6 mm

through the whole block are already formed at the beginning of the pullout simulation. Also the cracking pattern is different than the one obtained with the damage-plasticity model.

For corrosion of 7.8% (Figs. 5.46(d) – 5.46(e)) there is a clearly visible crack for slip value of 0.2 and 0.4 mm. However, there is no visible difference in the maximum in-plane strain distribution as the rebar slip increases, which indicates that the total bond strength depends on the rust interface parameters for high corrosion levels.

For the explicit analysis the SDEG parameter has also been monitored. The distributions of SDEG in the interface and three levels of corrosion are shown in Fig. 5.47. For the precracking level of corrosion no damage in the interface can be observed. Since the calculations diverge prematurely the results for 4.27% corrosion are presented for the slip value of 0.2 mm, for 6.7% when no slip occurs, and for 7.8% for free end slip of 0.2 and 0.4 mm. Unfortunately, the distribution of SDEG presented in Fig. 5.47(b) suggests that when only corrosion acts and no free end slip is applied the model does not give reliable results. This happens in spite of changing analysis parameters. The spurious deformation presented in Fig. 5.47(b) is a result of using the cracking model, which seems to be not stable during the calculations. For 7.8% of corrosion SDEG is distributed (Figs. 5.47(c) – 5.47(d)) along reinforcement similarly to the simulations with the damage-plasticity model.

The simulation brings as a result the interface parameters, which can be used in the beam model. According to the experiment the bond strength and bond stiffness depend on the corrosion level. The FE analysis revealed a similar dependence. In the interface model used, apart from the bond strength and initial stiffness values, the damage evolution also depends on the corrosion level. The determined rust interface parameters are listed in Table 5.4.

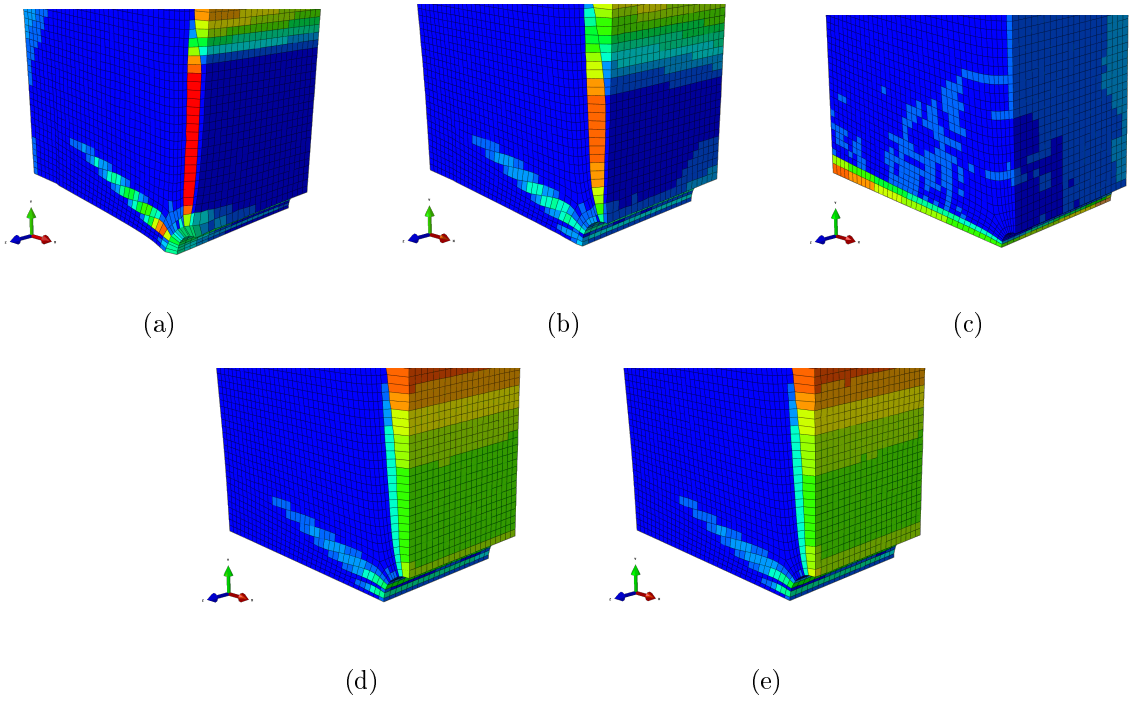


Figure 5.46: Distribution of max-in-plane strains for explicit simulation and cracking model: (a) – 0.87% corrosion, free end slip 0.2 mm, (b) – 4.27% corrosion, free end slip 0.2 mm, (c) – 6.7% corrosion, no free end slip, (d) – 7.8% corrosion, free end slip 0.2 mm, (e) – 7.8% corrosion, free end slip 0.4 mm

Table 5.4: Dependence of rust interface parameters on corrosion levels

| Bond strength | Bond stiffness | $\delta_m^f - \delta_m^0$ | Corrosion |
|---|---|---|---|
| 300 MPa | 1200 N/mm$^3$ | 2.5 | 0% |
| 300 MPa | 3000 N/mm$^3$ | 2.5 | 1% |
| 50 MPa | 700 N/mm$^3$ | 2.5 | 4% |
| 17 MPa | 30 N/mm$^3$ | 0.4 | 6% |
| 6 MPa | 20 N/mm$^3$ | 1.5 | 7% |
| 4 MPa | 5 N/mm$^3$ | 1 | 8% |

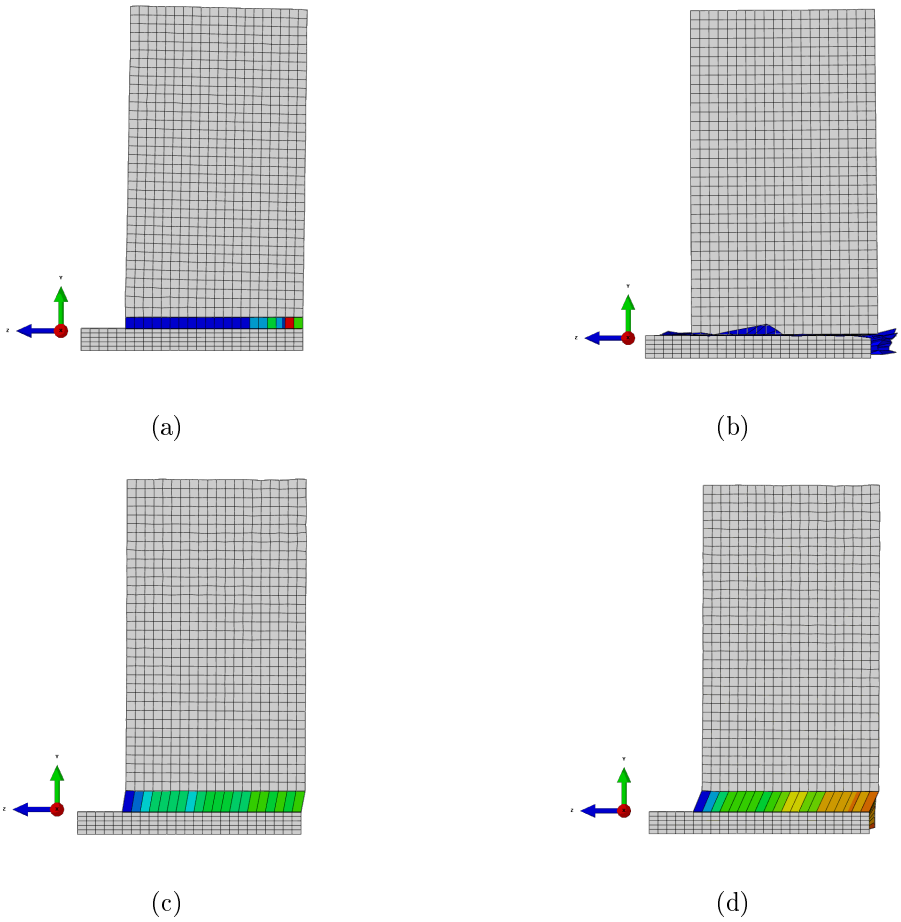

(a) (b)

(c) (d)

Figure 5.47: Distribution of scalar damage variable (SDEG) for explicit simulation and cracking model: (a) – 4.27% corrosion, free end slip 0.2 mm, (b) – 6.7% corrosion, no free end slip, (c) – 7.8% corrosion, free end slip 0.2 mm, (d) – 7.8% corrosion, free end slip 0.4 mm

Table 5.5: Material parameters – beam model

| Concrete | | Steel | |
|---|---|---|---|
| Parameter | Value | Parameter | Value |
| E [MPa] | 20 000 | E [MPa] | 200 000 |
| $\nu$ [-] | 0.2 | $\nu$ [-] | 0.3 |
| Stress at comp. peak $f_c$ [MPa] | 38.3 | Yield stress $\sigma_e$ [MPa] | 350 |
| Strain at comp. peak $\varepsilon_c$ [-] | 0.2% | Plastic tangent stiff. $E_T$ [MPa] | 3 295 |
| Tens. yield stress $f_t$ [MPa] | 2 | | |

## 5.3 3D beam analysis

After the analyses presented in the previous sections, a three-dimensional model of the beam with corrosion and service load applied has been considered. The model has been prepared in accordance with the experiment performed by [18]. The tested beam is subjected to 3-point bending. The beam is 5 m long and the cross-section dimensions are 200 x 500 mm. The total deflection value applied in the middle of the span is 50 mm.

The simulation is performed for a quarter of the beam, since double symmetry holds. Concrete is modelled using the damage-plasticity model. To overcome the mesh-dependency problem, the viscous parameter is used as numerical stabilization measure and not physical phenomenon, since statics is considered. Steel is assumed as elastic-plastic material and rust is introduced as interface with initial thickness 0.01 mm. Due to the initial thickness of the interface the steel bars diameters are 31.98 mm and 7.98 mm instead of 32 mm and 8 mm, for bottom and top reinforcements, respectively. The rust interface properties have been obtained from the single rebar pull out test model, discussed in the previous section and in [14]. The simulation is performed for the beam without transversal steel reinforcement. The implicit algorithm is employed. Since the analysis is performed as three-dimensional, the mesh is quite coarse. The concrete, steel and rust parameters used are shown in Tables 5.4 and 5.5 and the model configuration is presented in Fig. 3.15. The preliminary beam model and its results has been presented in [16].

The analysis considers three cases of corrosion and deflection application. Two cases include the corrosion and forced deflection applied simultaneously. In the first simulation the displacement changes from 0 to 50 mm and corrosion level increases linearly from 0% to 2%, 0% to 4% and 0% to 8%. In the second simulation the different corrosion levels are applied around top and bottom reinforcement. The last case considers different scenarios of load application. The corrosion and external loading are applied in separately in different sequences. Prior to the corrosion analysis the simulation of the beam with no corrosion is performed.

### 5.3.1 Simultaneous increase of corrosion and deflection

Figure 5.48 presents the diagrams of the total force and the evolution of the $\varepsilon_{zz}$ strain in bottom reinforcement, both versus the maximum deflection. The analysis of the beam with no corrosion reveal that the concrete model used is too stiff when compared to the experiment. There is also tension stiffening effect visible. In Fig. 5.48(b) it can be noticed that the reinforcement is under high tension when compared to the experiment. Since the simulated load-carrying capacity is higher than the experiment, also the tension observed in the bottom reinforcement is higher than the tension observed in the experiment. The difference between the model and the experiment in Fig. 5.48(b) is bigger than in Fig. 5.48(a). This can be explained by the fact that Fig. 5.48(b) presents the relation for one bottom rebar, while the diagram presented in Fig. 5.48(a) represents the response of the whole beam.

In the following step of analysis the corrosion is applied to the beam simultaneously with the forced deflection. Three simulations have been performed, with displacement increasing from 0 to 50 mm and corrosion level increasing linearly from 0% to 2%, 0% to 4% and 0% to 8%.

In Fig. 5.48(a) the reduction of load-carrying capacity is observed, however it is not significant. The initial stiffness is the same for all simulations, since they all start with the same conditions – 0% corrosion and no deflection. As corrosion and deflection increases, the total beam strength decreases, and for 8% corrosion the peak force decreases from 250 kN to 210 kN. The influence of corrosion is more visible in Fig. 5.48(b). As the total force decreases the strain in the bottom reinforcement also decreases. The influence of corrosion becomes significant for displacement values from 20 to 30 mm, when the vertical crack in the middle of the span develops. The strain calculated for the model with no corrosion increases abruptly, since it captures all tension forces appearing at the bottom of the beam. However, when corrosion is additionally applied, the strain slope decreases due to fact that concrete is cracked horizontally and a loss of confinement is noticed around the bottom reinforcement. When the displacement is greater than 30 mm there is a switch between 2% corrosion and 4% corrosion curves. This may be explained by the fact that higher corrosion means bigger radial compression, and what follows bigger tension strains. On the other hand, a similar behavior is not observed for the case of 8% corrosion. However, this can be an effect of loss of bond between concrete and steel, which was analyzed in Section 5.2.

Figures 5.49 and 5.50 presents distributions of PEEQT parameter for the beam with 50 mm deflection and different corrosion levels (0, 2, 4 and 8%). The results are presented in isometric view to allow one for the observation of the longitudinal cracks, and also in the mid-span cross-section. For the beam loaded only with imposed deflection the maximum strains appear in the middle of the span, forming a vertical crack (Figs. 5.49(a), 5.49(b)). As corrosion increases, the cross-section corners tend to spall off the beam. In Figs. 5.50(a) – 5.50(c) it can be noticed that when corrosion is 4% or higher the beam corners are spalled off along the whole length of the RC member. Also, for the case of no corrosion or corrosion of 2% or 4% a vertical crack penetrates in the middle of the span. There is some deviation

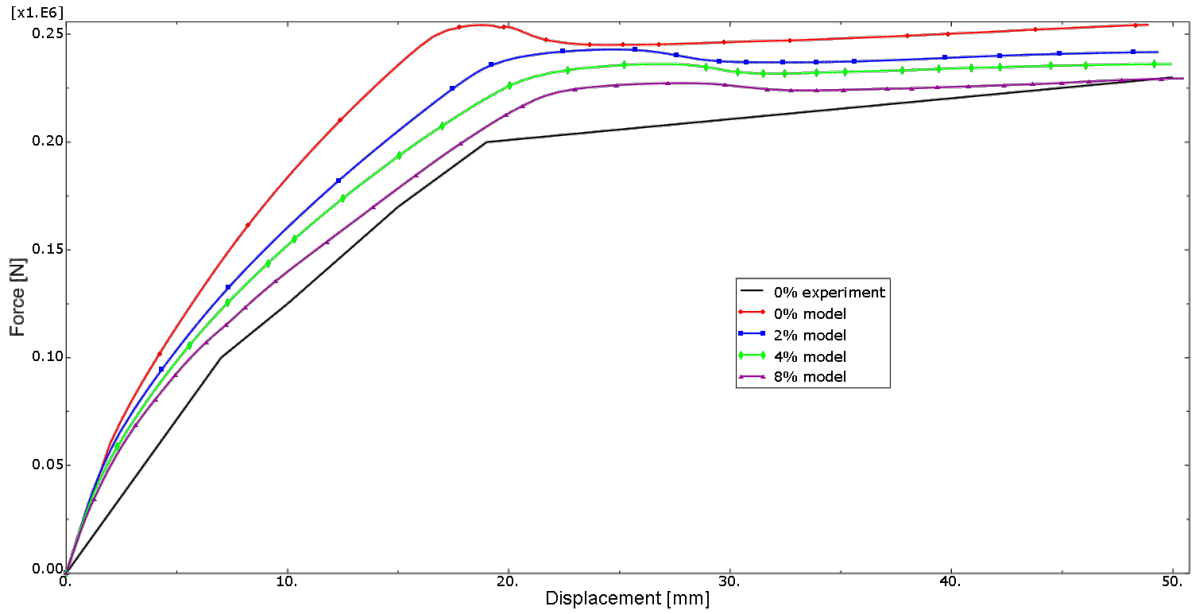


(a)

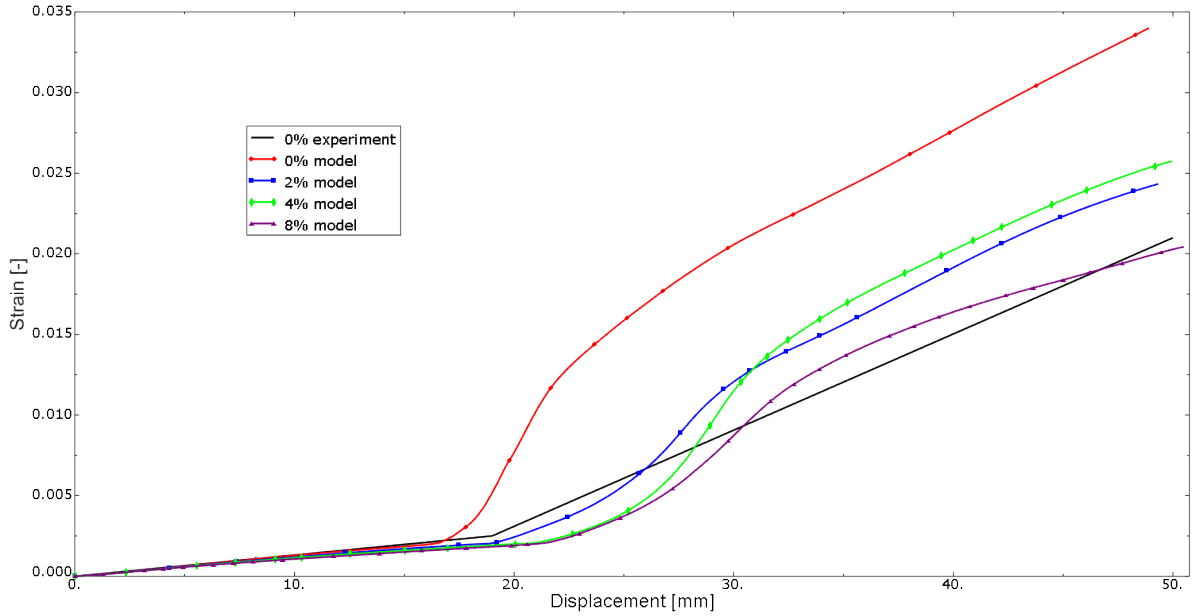


(b)

Figure 5.48: Increasing corrosion applied simultaneously with forced deflection: (a) – Total applied force vs. beam defection, (b) – Evolution of $\varepsilon_{zz}$ strain in bottom reinforcement vs. deflection.

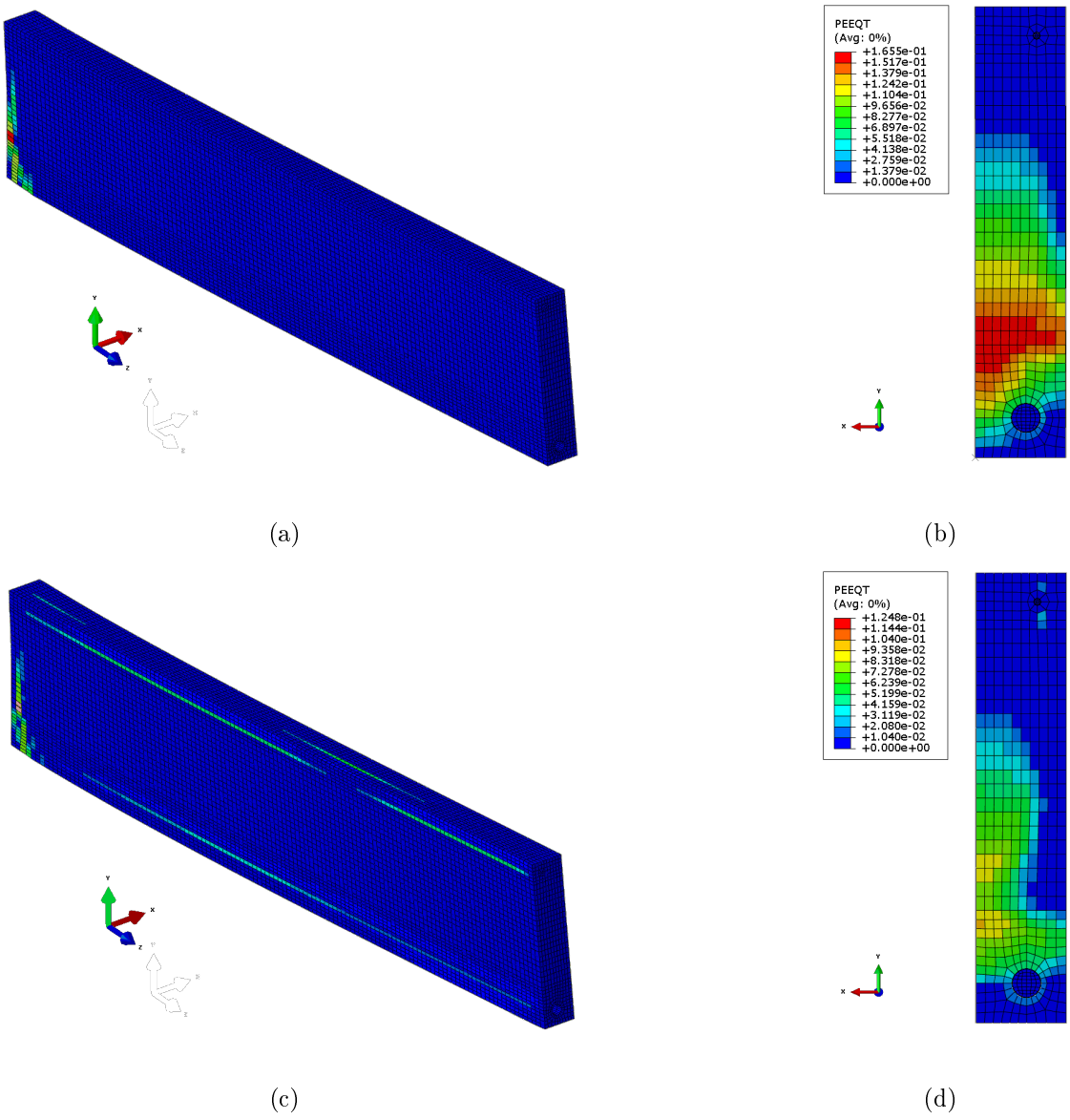


Figure 5.49: Final distribution of PEEQT parameter for beam with 50 mm deflection and increasing corrosion applied simultaneously, presented in isometric and mid-span cross-section views: (a) and (b) – 0.0% corrosion, (c) and (d) – 2.0% corrosion.

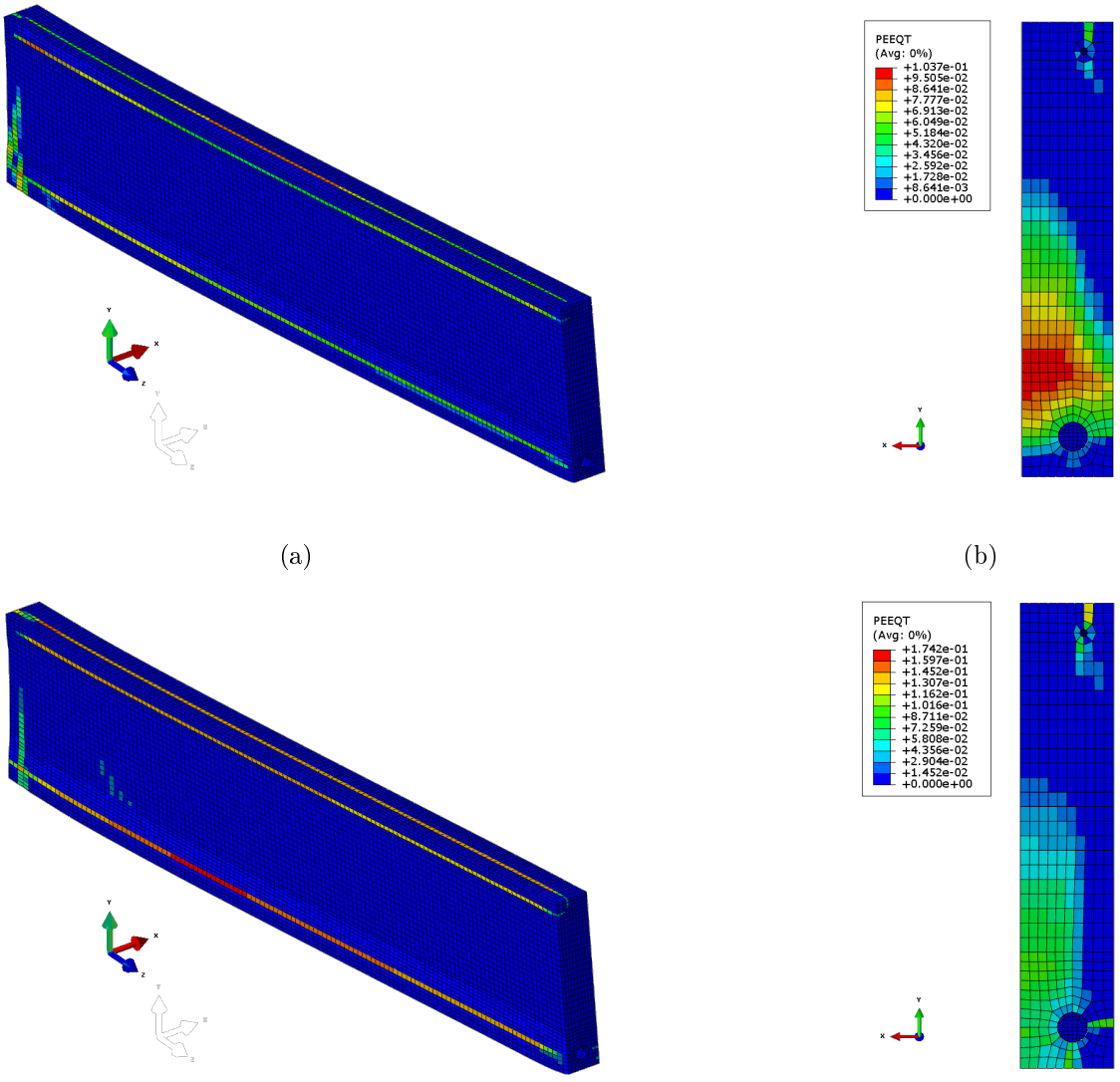


Figure 5.50: Final distribution of PEEQT parameter for beam with 50 mm deflection and increasing corrosion applied simultaneously, presented in isometric and mid-span cross-section views: (a) and (b) – 4.0% corrosion, (c) and (d) – 8.0% corrosion.

form the vertical direction, it seems to be a result of the damage-plasticity description. On the other hand, for corrosion level of 8% (Fig. 5.50(c)), the cracking pattern suggests that corrosion-induced strains dominate. The vertical crack is translated away from the middle of the span, which can be an effect of combination of strains induced by high corrosion and deflection.

In contrast to deflection-caused cracking, the corrosion-induced cracking forms along the whole element and can impair the concrete-reinforcement cooperation. The analysis provided in the thesis considers only statics of the RC structure. The long-time serviceability predictions are not included. However, it must be noted that the developing spalling, presented in Figs. 5.49 and 5.50 can cause in time complete separation of concrete and reinforcement. Thus, although the analysis of the beam with corrosion applied simultaneously with the forced deflection revealed that the reduction of load-carrying capacity due to corrosion is not significant, the corrosion process is of major importance when serviceability limit state is analyzed. Also, since it is responsible for degradation of the whole structure, it is a crucial issue for structural durability estimations.

### 5.3.2 Different corrosion level around top and bottom reinforcement

In the next step of the analysis, the different corrosion levels are applied around top and bottom reinforcement. During simulation deflection increases to 50 mm, while corrosion grows to:

- 2% around bottom and 4% around top,
- 4% around bottom and 2% around top.

In Fig. 5.51 the red curve representing 4% bottom and 2% top corrosion is very similar to the blue dotted line standing for 2% bottom and top. According to diagrams presented in Fig. 5.51(a) the beam seems to be slightly weaker when 4% corrosion is applied around top reinforcement. This is a result of horizontal cracks generated in the top part of concrete which is in compression. Thus, it seems that corrosion influences the overall response of the beam by generating cracks in the compression zone. For displacement values ranging 20-30 mm the strains are smaller when compared to those calculated with model with no corrosion (Fig. 5.48(b)), thus there is a loss of confinement caused by horizontal cracks around the bottom reinforcement. However, in Fig. 5.51(b) slightly different effects can be noticed than the one observed in Fig. 5.48(b). Up to 24 mm displacement the response of 4% bottom and 2% top curve is nearly the same as in the case 2% bottom and top. Next, the red curve exhibits a sudden increase of the strain value. This can be related to increasing corrosion and to concrete strain softening visible as a little drop in corresponding curve in Fig. 5.51(a). As displacement and corrosion increase to the final values the slope of the strain curve decreases, since there is a loss of bonding between steel and concrete.

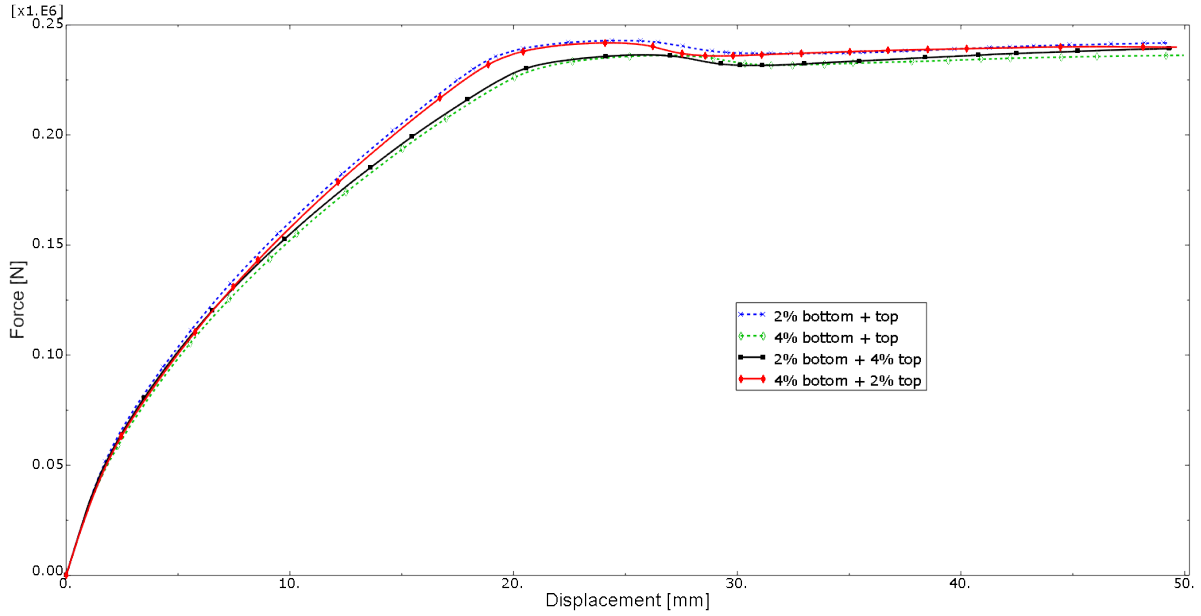


(a)

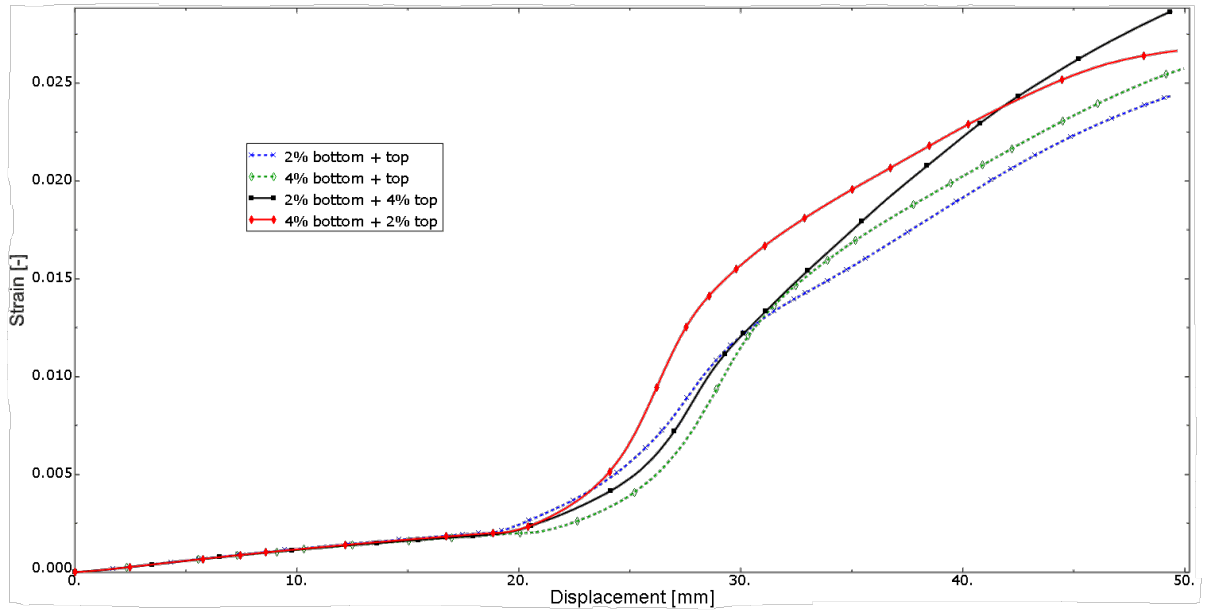


(b)

Figure 5.51: Different corrosion levels applied around top and bottom reinforcement, simultaneously with forced deflection: (a) – Total applied force vs. beam defection, (b) – Evolution of $\varepsilon_{zz}$ strain in bottom reinforcement vs. deflection.

In the case of 2% bottom and 4% top corrosion (represented by the black line in Fig. 5.51 the increase of strains (for displacements 20-30 mm) is not so rapid. As presented in Fig. 5.51(a) the beam is weaker than for the case of 4% bottom and 2% top, so the strains in the bottom reinforcement are smaller.

Although the diagrams presenting strain-displacement relations are not so close to each other as in the case of overall response of the beam in Fig 5.51(a), there are similar tendencies visible in Fig. 5.51(b). The red curve of 4% bottom and 2% top and the blue dotted curve of 2% bottom and top both exhibit rapid increase of strains, followed by nearly linear relation and decrease of the slope of strain diagram for displacements greater than 40 mm. Also it is characteristic for both diagrams that they intersect with black curve of 2% bottom and 4% top and green dotted curve of 4% bottom and top, respectively.

Nevertheless, corrosion is much more influential when strains in a single bottom bar is analyzed. For an overall response of the beam corrosion is not very significant, however it decreases the load-carrying capacity of the beam. It seems important that corrosion around the top reinforcement is more influential than corrosion around the bottom rebar.

Figure 5.52 presents distribution of PEEQT parameter for the beam with 50 mm deflection and simultaneously applied different corrosion levels around the top and bottom reinforcement. Once again, the results are presented in isometric view and in mid-span cross-section. The results presented in cross-section view are quite similar for both cases. The equivalent plastic tensile strains appear in concrete in the bottom part of mid-span cross-section, since they are caused by deflection. The more interesting issue is the influence of corrosion on the cracking pattern. As in the previous simulations, also in the considered cases the horizontal cracks are formed as a result of corrosion. In Fig. 5.52(a), when corrosion around the bottom reinforcement is 2.0% and around top 4.0%, the longitudinal cracks are clearly visible in the top part of the RC member. At the bottom of the beam the horizontal crack is at the beginning of the process of propagation. Thus, the top corners of the beam can spall off the beam.

However, when top corrosion is 2% and the bottom is 4% the cracks can be observed along both reinforcements bars. Although the red curve in Fig. 5.51(a) suggests that this case is advantageous when load-carrying capacity is considered, the cracking pattern in Fig. 5.52(c) indicates that the beam can be more damaged with such corrosion distribution. The effect of not negligible cracking along the bottom reinforcement can also be noticed in Fig. 5.51(b) in strain–displacement relation. Since corrosion increases to 4% the slope of strain curve decreases, due to the loss of confinement and bonding. Thus, from the serviceability point of view the case of 4.0% corrosion around bottom and 2.0% corrosion around top reinforcement is much more dangerous than inverse distribution of corrosion.

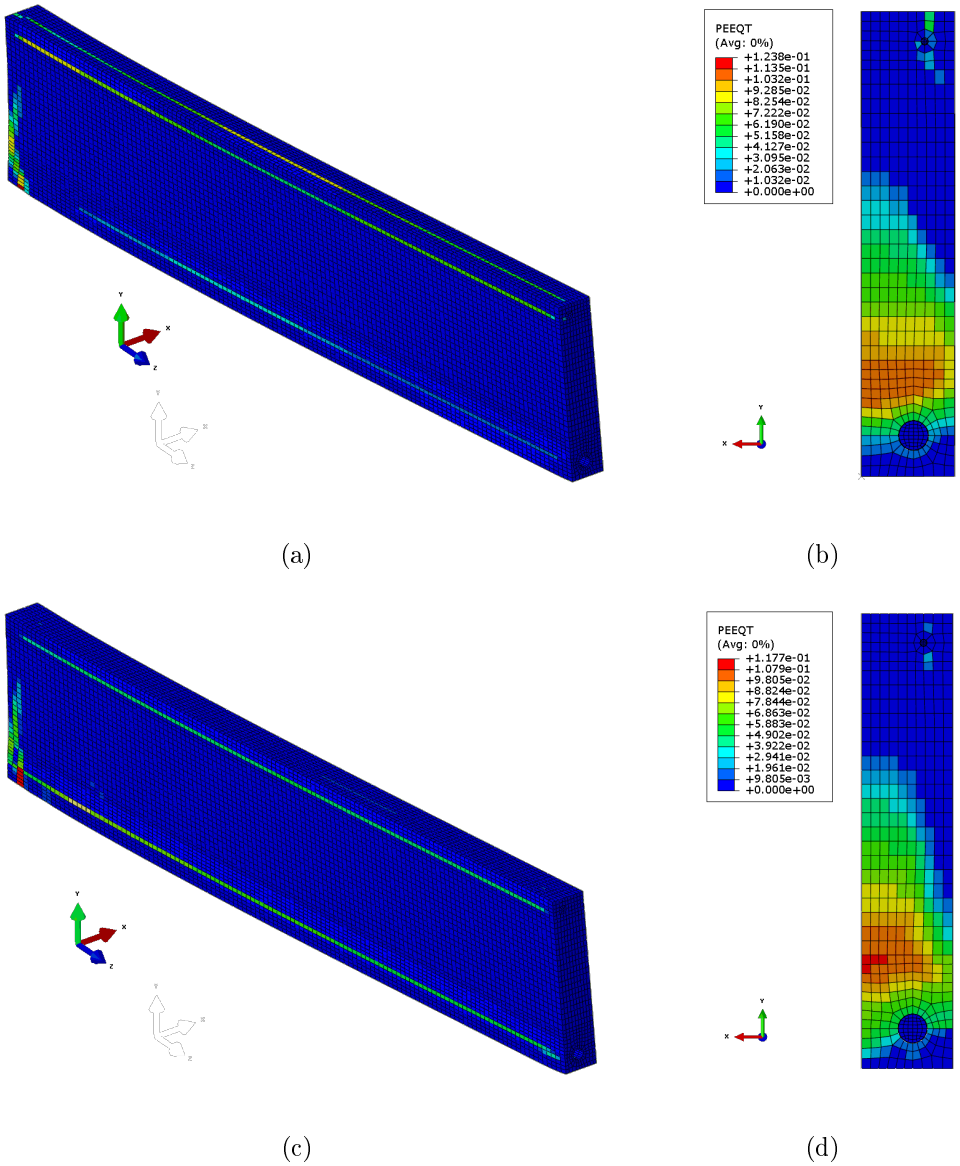


(a) (b)

(c) (d)

Figure 5.52: Final distribution of PEEQT parameter for beam with 50 mm deflection and simultaneously applied different corrosion levels around top and bottom reinforcement: (a) and (b) – 2.0% bottom and 4.0% top, (c) and (d) – 4.0% bottom and 2.0% top.

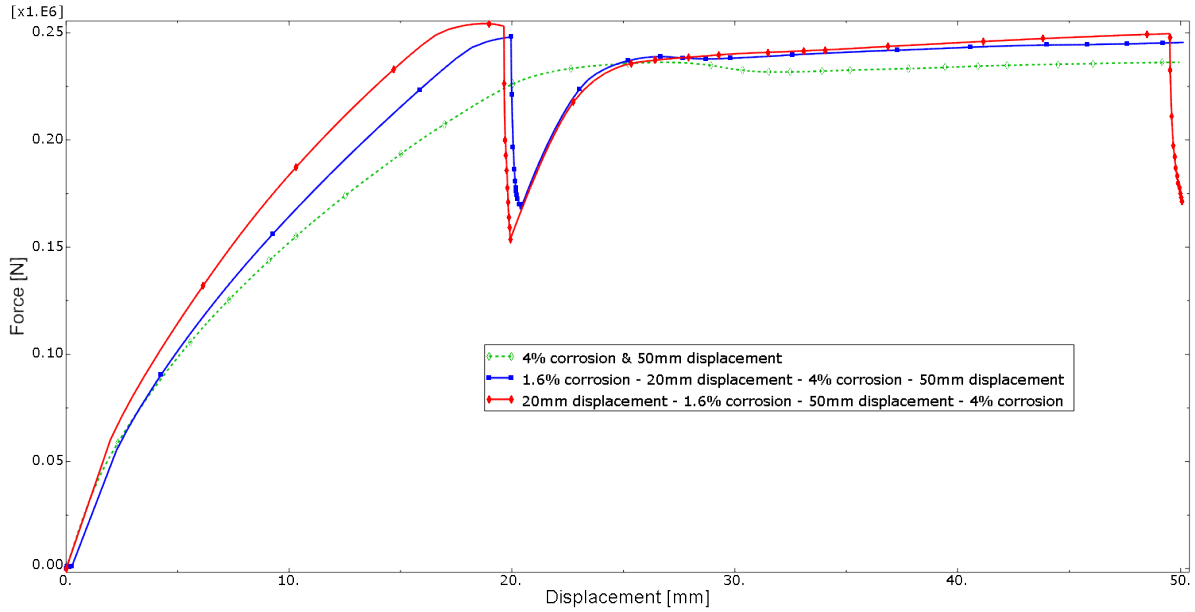


(a)

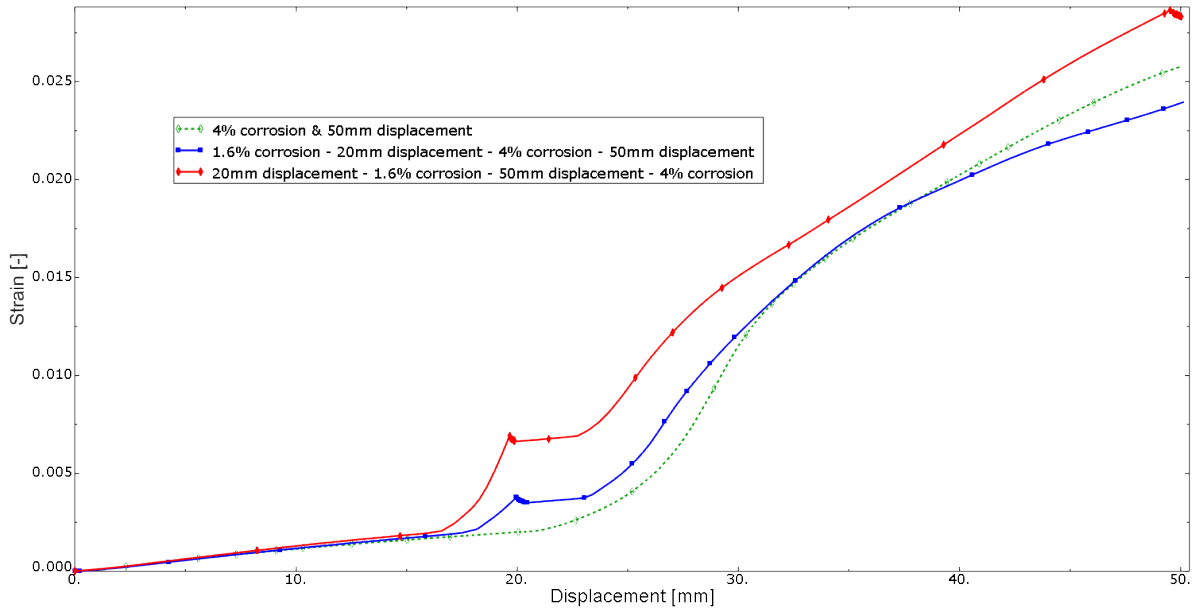


(b)

Figure 5.53: Corrosion and external loading applied in separate steps and in different sequences: (a) – Total applied force vs. beam defection, (b) – Evolution of $\varepsilon_{zz}$ strain in bottom reinforcement vs. deflection.

### 5.3.3 Different sequences of corrosion and deflection application

The last step of considered analysis are different scenarios of load application. The corrosion and external loading are applied in separate steps and in different sequences:

- simulation no. 1: 1.6% corrosion – 20 mm displacement – 4% corrosion – 50 mm displacement,
- simulation no. 2: 20 mm displacement – 1.6% corrosion – 50 mm displacement – 4% corrosion.

The simulation no. 1 is presented in Fig. 5.53 by the blue line and the second loading sequence is represented by the red line. For comparison the case of 4% corrosion and 50 mm displacement applied simultaneously is represented by the green dotted line. For the simulation no. 1 the application of 1.6% corrosion prior to displacement does not influence the load carrying capacity as in case of simultaneous application of corrosion and external loading. When displacement is equal to 20 mm the corrosion of 4% is applied. This generates a sudden and significant drop of force visible in Fig. 5.53(a). The drop is caused by horizontal cracking of the concrete. However, since there is significant drop of strains in the bottom reinforcement (Fig. 5.53(b)) it can be stated that the horizontal cracks due to corrosion are the most significant for the overall behavior of the beam.

Next, the displacement increasing to 50 mm is applied. A redistribution of forces occurs in concrete and the total force increases. However, at the same time strain in bottom reinforcement remains almost constant. When displacement is around 25 mm the load bearing capacity in Fig. 5.53(a) is the same for simulation no. 1 and the green dotted line. At the same time strains in the bottom reinforcement (Fig. 5.53(b)) begin to increase. Thus both components (concrete and reinforcement) have their contribution in the load bearing capacity of corroded beam.

The similar characteristics can be observed for simulation no. 2, when 20 mm displacement is applied first and next 1.6% corrosion. Again, the drop of total force is observed when corrosion is applied. The drop is even greater than in simulation no. 1. Also this drop of force does not influence strains in the bottom reinforcement. When the displacement begins to increase to 50 mm, the force and strains begin to increase too, in a similar way as in simulation no. 1. At the end of red diagram again a drop of force can be noticed since corrosion of 4% is applied.

In Fig. 5.53(a) it can be noticed that corrosion increasing simultaneously with increasing displacements causes decrease of load carrying capacity greater than in the case when corrosion and displacements are applied in separate steps of analysis. It is visible mainly for displacements smaller than 20 mm. However, when the beam is already loaded, additional application of corrosion results in a sudden drop of total force, which may be more dangerous for the structure than in the case of simultaneous application.

Figures 5.54 – 5.57 present the distributions of PEEQT parameter in isometric view and mid-span cross-section for the beam with corrosion and external loading applied in separate steps. Figures 5.54 and 5.55 present the results for simulation no. 1, after each

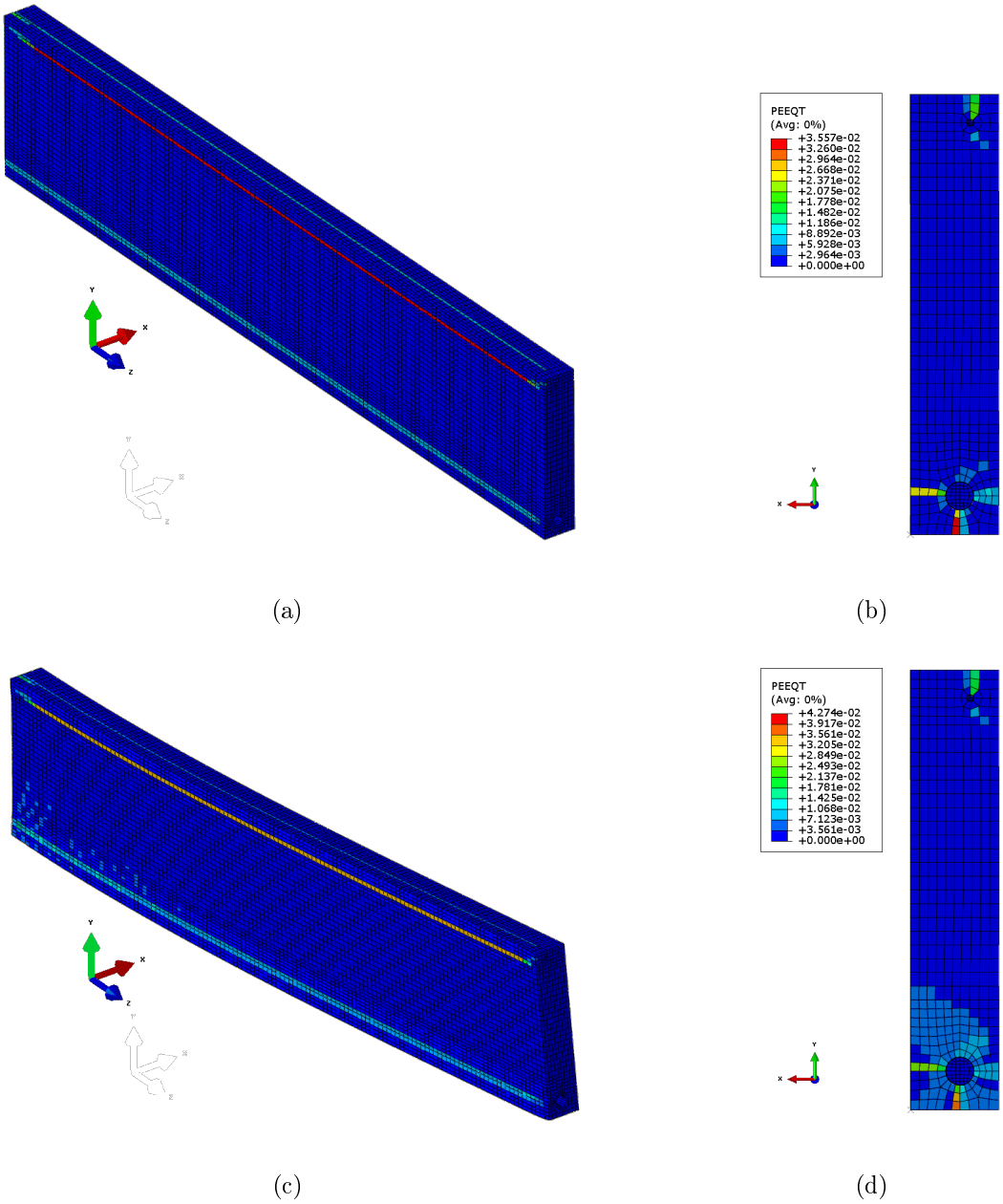


Figure 5.54: Final distribution of PEEQT parameter for beam in simulation no. 1, presented in isometric and mid-span cross-section views: (a) and (b) – 1.6% corrosion, (c) and (d) – 1.6% corrosion – 20 mm displacement.

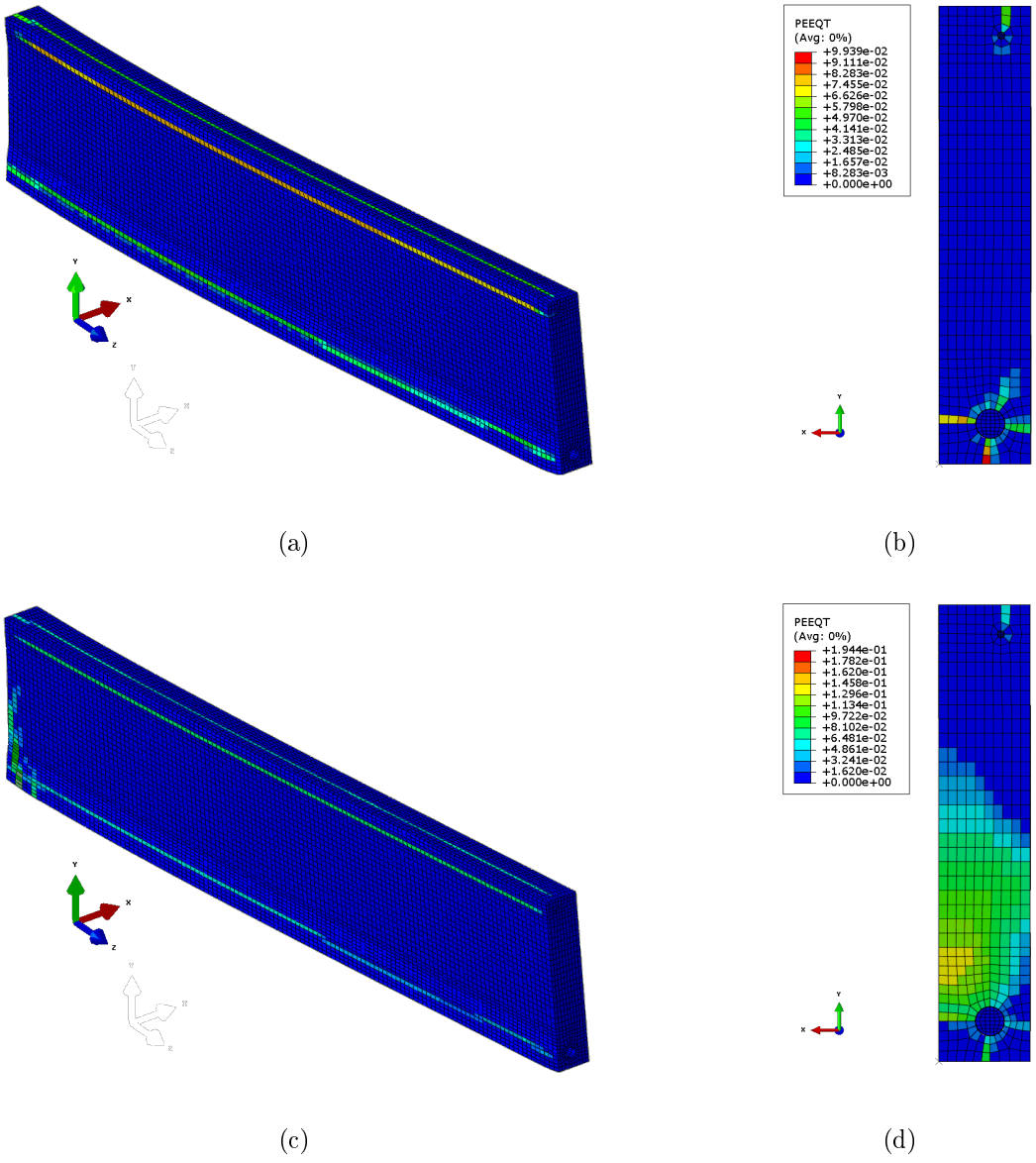


(a) (b)

(c) (d)

Figure 5.55: Final distribution of PEEQT parameter for beam in simulation no. 1, presented in isometric and mid-span cross-section views: (a) and (b) – 1.6% corrosion – 20 mm displacement – 4% corrosion, (c) and (d) – 1.6% corrosion – 20 mm displacement – 4% corrosion – 50 mm displacement.

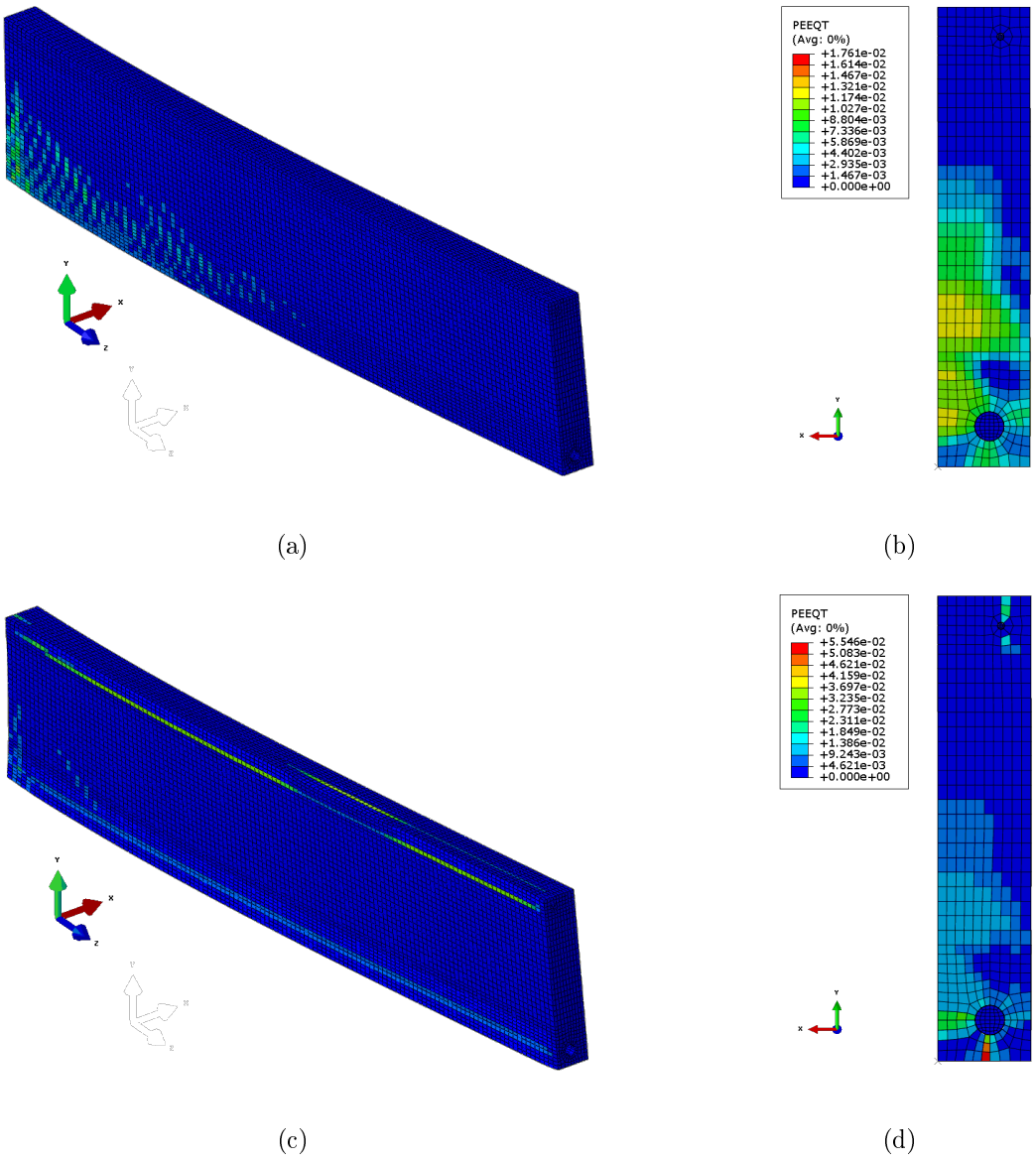


Figure 5.56: Final distribution of PEEQT parameter for beam in simulation no. 2, presented in isometric and mid-span cross-section views: (a) and (b) – 20 mm displacement, (c) and (d) – 20 mm displacement – 1.6% corrosion.

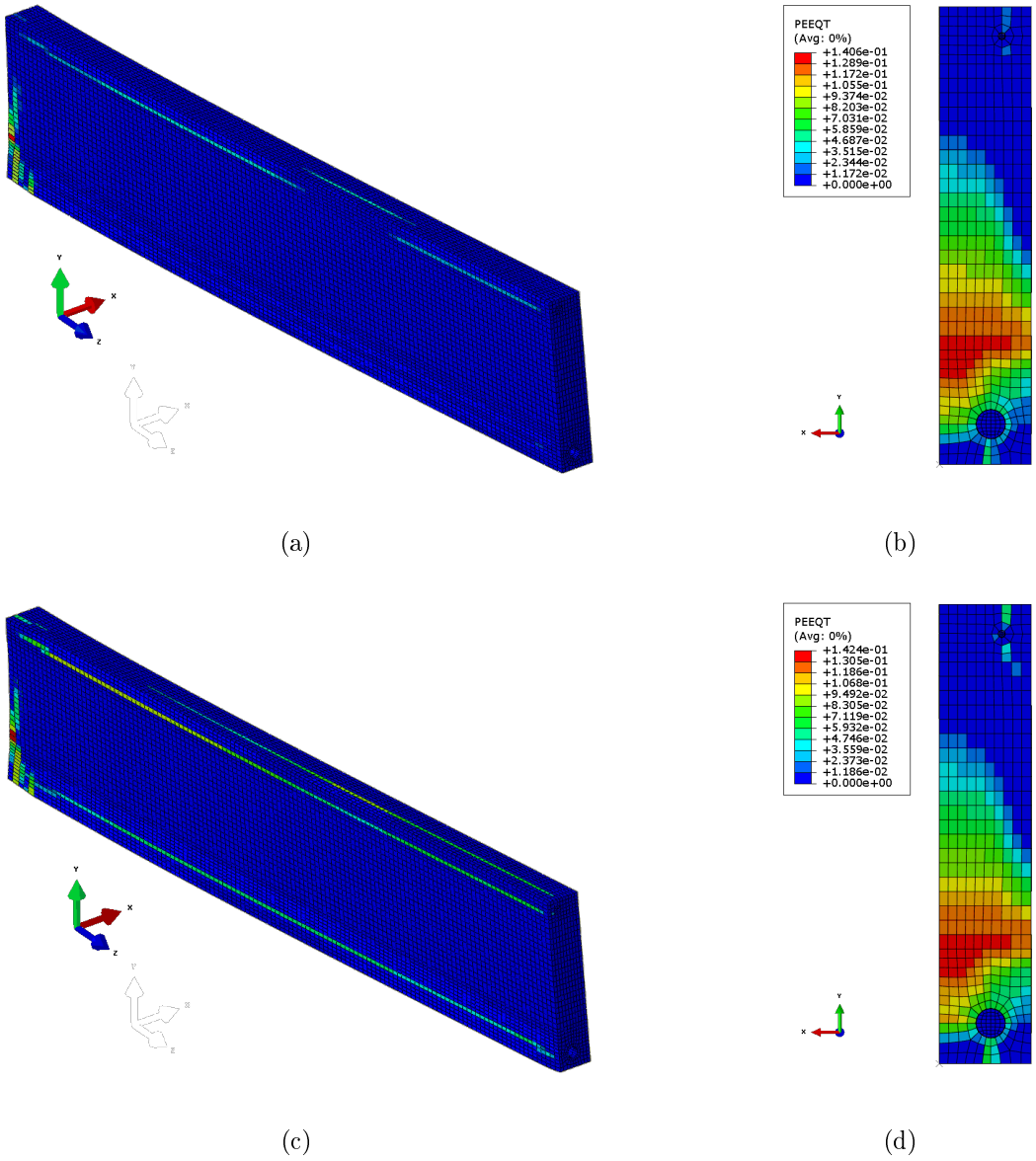


Figure 5.57: Final distribution of PEEQT parameter for beam in simulation no. 2, presented in isometric and mid-span cross-section views: (a) and (b) – 20 mm displacement – 1.6% corrosion – 50 mm displacement, (c) and (d) – 20 mm displacement – 1.6% corrosion – 50 mm displacement – 4% corrosion.

step of loading application (1.6% corrosion – 20 mm displacement – 4% corrosion – 50 mm displacement), and Figs. 5.56 and 5.57 for simulation no. 2 (20 mm displacement – 1.6% corrosion – 50 mm displacement – 4% corrosion).

As can be observed in Fig. 5.54(a) the cross-section corners spall off the beam after the first step of the analysis, i.e. application of 1.6% of corrosion. Application of the following steps of simulation does not change the cracking pattern significantly. The final damage of applying corrosion and displacement in separate steps, presented in Fig. 5.55(c), allows one to observe horizontal cracks caused by corrosion and vertical crack in the mid-span cross-section caused by deflection.

For the beam loaded only with deflection the maximum strains appear in the middle of the span, forming vertical cracks Figs. 5.56(a). In Fig. 5.56(c) it can be noticed that when corrosion is additionally applied the horizontal cracks are formed, however the strain distribution is not as uniform along the whole length of the RC member as in Fig. 5.54(c) presenting the results after the second step of the simulation no. 1. The increase of the deflection to the value of 50 mm causes noticeable change of the cracking pattern. In Fig. 5.57(a) it can be observed that after increasing the deflection the horizontal cracks are at least partly healed. Next, when corrosion increases to 4% both horizontal and vertical cracks are visible again. Nevertheless, in Figs. 5.55(c) and 5.57(c) it can be noticed that the final damage of concrete is similar for both simulations, regardless of what the loading sequence is.

Taking into account Figs. 5.53 – 5.57 it seems that for the RC structure a case when displacement is applied prior to corrosion is more dangerous than the reverse situation. The decrease of the force in Fig. 5.53(a) for simulation no. 2 is bigger than in the case of simulation no. 1. What is more, the strains in the bottom reinforcement in Fig. 5.53(b) are bigger for simulation no. 2. Finally, the cracking pattern depends on the current corrosion level and deflection, while for simulation no. 1 it is more stable during the analysis, which may be helpful for serviceability considerations.

### 5.3.4 Explicit analysis

Again, for comparison the beam model has been calculated with explicit algorithm using two aforementioned material descriptions. Figure 5.58 presents the diagrams of the total force and the evolution of the $\varepsilon_{zz}$ strain in bottom reinforcement, both versus the deflection, calculated using the damage-plasticity model. In Fig. 5.58 it appears that the explicit analysis gives worse results than the implicit simulation, although the kinetic energy condition is satisfied. For the beam with no corrosion the model is overstiff, similarly as in the implicit analysis (Fig. 5.48). However, after reaching the peak value of force the softening takes the fluctuating shape, in spite of changing iteration or other analysis parameters. The diagrams for the beam loaded with corrosion and deflection seem to be unreliable, especially for 4% and 8% of corrosion, see Fig. 5.58(b).

This effect can also be observed in Figs. 5.59 and 5.60 presenting distribution of PEEQT parameter for the beam with deflection and different corrosion levels. The dis-

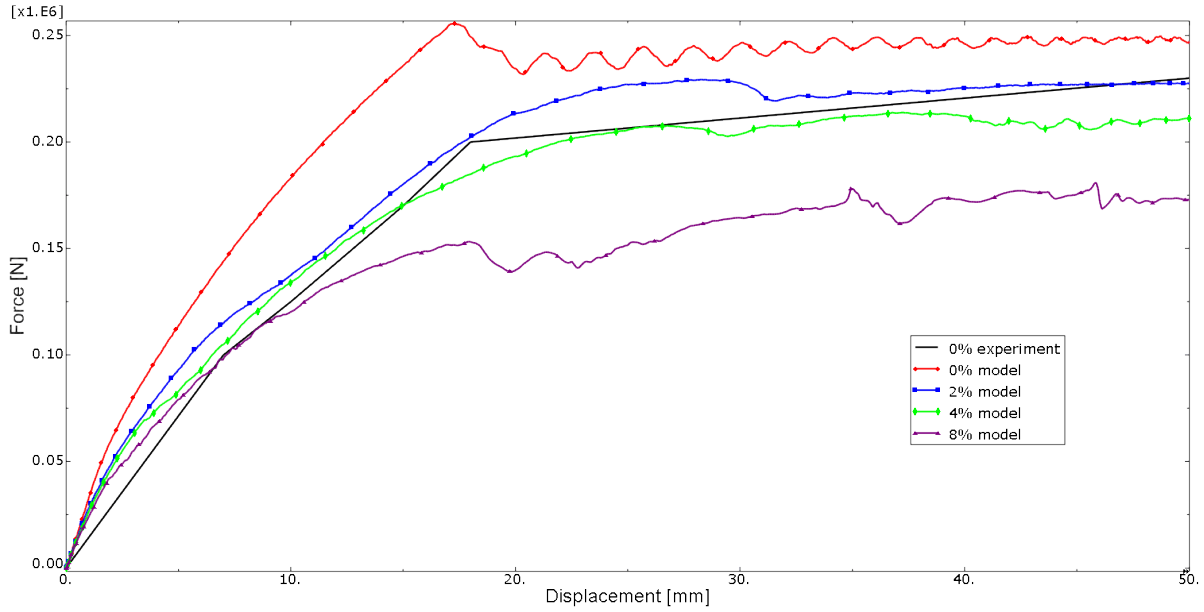


(a)

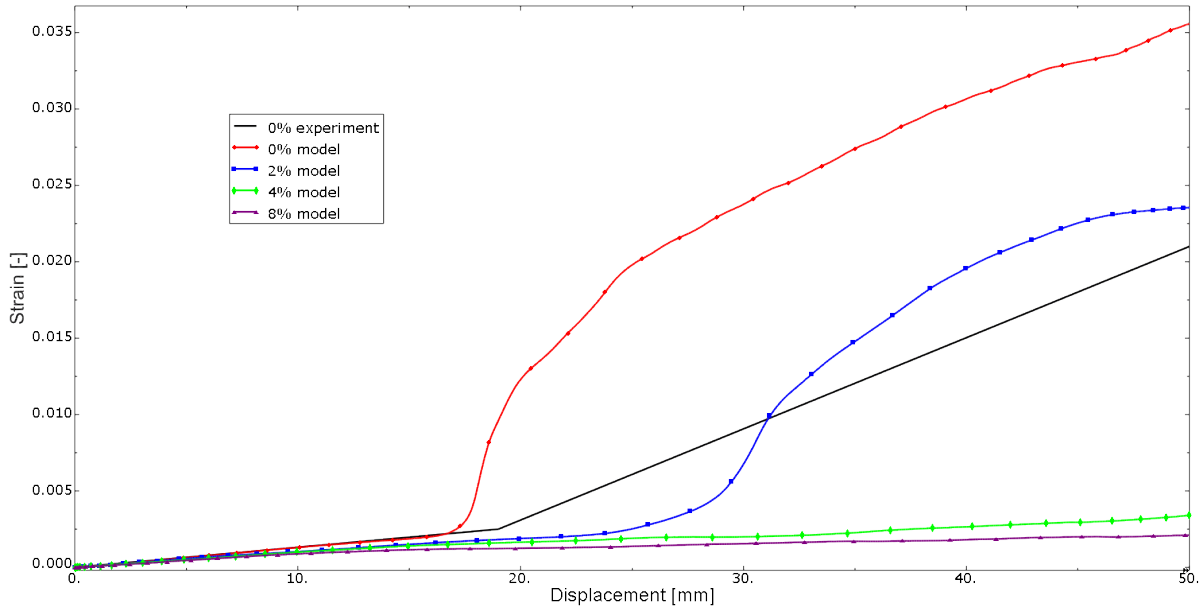


(b)

Figure 5.58: Increasing corrosion applied simultaneously with forced deflection, explicit algorithm, damage-plasticity model: (a) – Total applied force vs. beam defection, (b) – Evolution of $\varepsilon_{zz}$ strain in bottom reinforcement vs. deflection.

placements of the cross-section corners, presented in Figs. 5.60(a) – 5.60(d) are so big that they outweigh the action of deflection. This however, taking into account the cross-section and the implicit beam analyses, must be a strongly exaggerated effect.

In the next step of the analysis, the different corrosion levels are applied around top and bottom reinforcement. Again, it can be noticed in Fig. 5.61 that increasing level of corrosion to 4% gives false results, visible mainly in Fig. 5.61(b), presenting evolution of $\varepsilon_{zz}$ strain in bottom reinforcement vs. deflection.

The distribution of PEEQT parameter, presented in Fig. 5.62, confirms the observation that corrosion-induced displacements in 3D model dominate in the explicit analysis and produce spurious results.

In the last step of analysis the corrosion and external loading is applied in separate steps and in different sequences. The diagrams are presented in Fig. 5.63. As long as corrosion level is 1.6% the diagrams are similar to those obtained from the implicit simulations (Fig. 5.53). The increase of corrosion to 4% results in big and a spurious drop of force. Note that even the change of the force sign is noticed.

The explicit calculations have been repeated with the concrete cracking model (which is unavailable in Abaqus/Implicit). Figure 5.64 presents the diagrams of the total force and the evolution of the $\varepsilon_{zz}$ strain in bottom reinforcement both versus deflection, calculated using cracking model. Note that the displacement grows only to 10 mm.

For beam model with no corrosion applied, the response (presented by red line in Fig. 5.64(a)) is too stiff when compared to the experimental results (black line). The strains observed in the bottom reinforcement are very close to the experiment. Unfortunately, after adding corrosion computations diverge very early. For corrosion level of 2% the calculations diverge at mid-span deflection equal to less than 4 mm. Increasing the corrosion level results in decreasing the possible mid-span deflection even to less than 1.5 mm.

The strains in the bottom reinforcement, presented in Fig. 5.64(b) follow the same path since the analysis is in the elastic state. Both corrosion and displacement are so small that no influence on strain is observed.

Figures 5.65 and 5.66 present the final available distribution of max-in-plane strain for the beam calculated with different corrosion levels (0, 2, 4 and 8%) and increasing deflection. Figures 5.65(a) and 5.65(b) present max-in-plane strain for the case with no corrosion. Tension strains are visible in the bottom part of concrete, however the process is just beginning, thus there is no crack formed in the middle of a span. Addition of 2% corrosion results in forming longitudinal cracks, surrounding reinforcement and presented in Figs. 5.65(c) and 5.65(d). The application of corrosion causes cracking of concrete, although forced displacement is very small. Increasing corrosion to 4% or 8% induces the increase of cracking strains, however the calculations diverge very quickly. What is more, cracking presented in Figs. 5.66(a) – 5.66(d) seems to dominate and govern the calculations convergence when the cracking model is employed.

The analysis with different corrosion levels around top and bottom reinforcement has been also performed with concrete modelled as a cracking material. Again, the results are

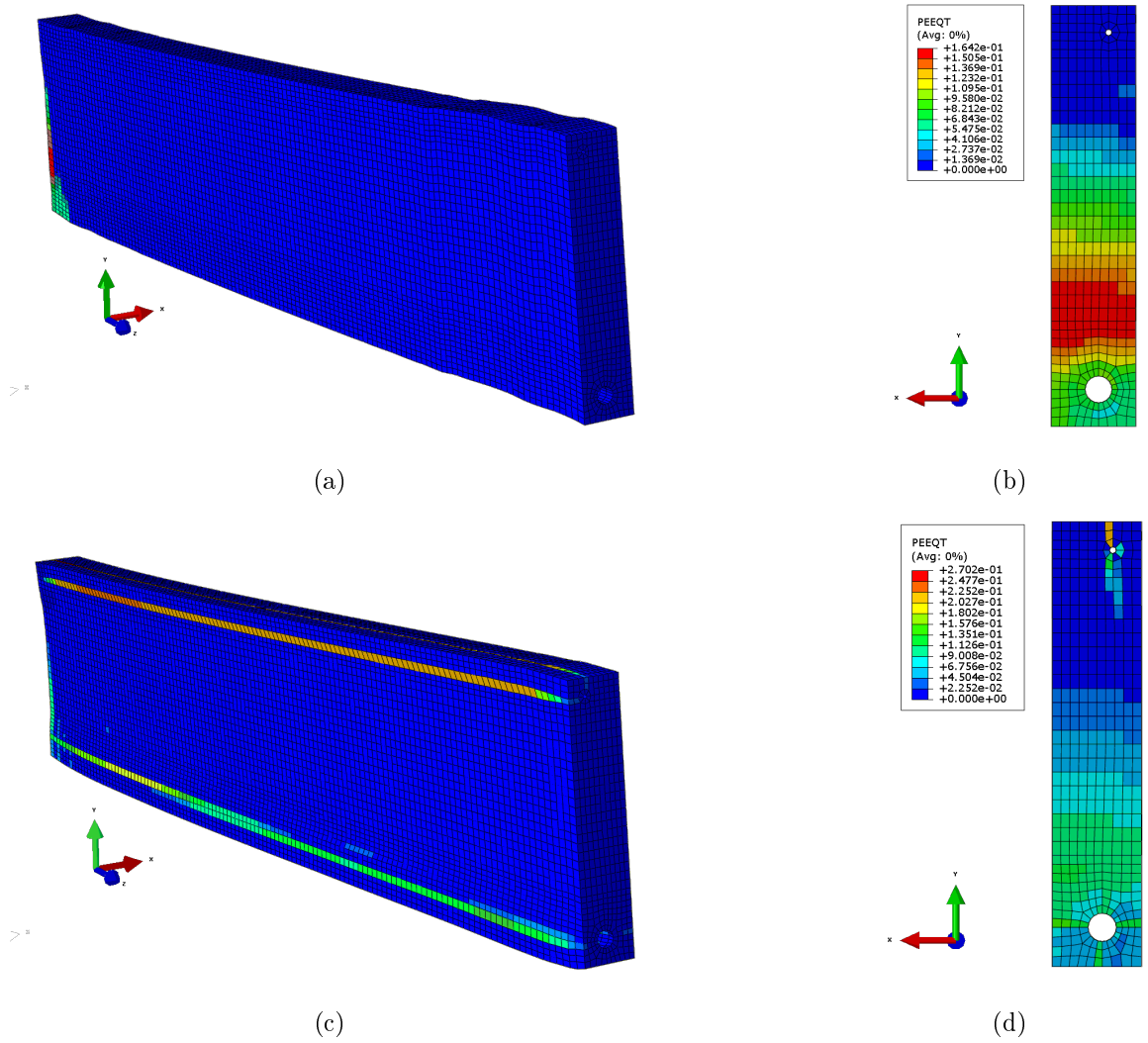


Figure 5.59: Final distribution of PEEQT parameter for beam with 50 mm deflection and increasing corrosion applied simultaneously using explicit algorithm and damage-plasticity model, presented in isometric and mid-span cross-section views: (a) and (b) – 0.0% corrosion, (c) and (d) – 2.0% corrosion.

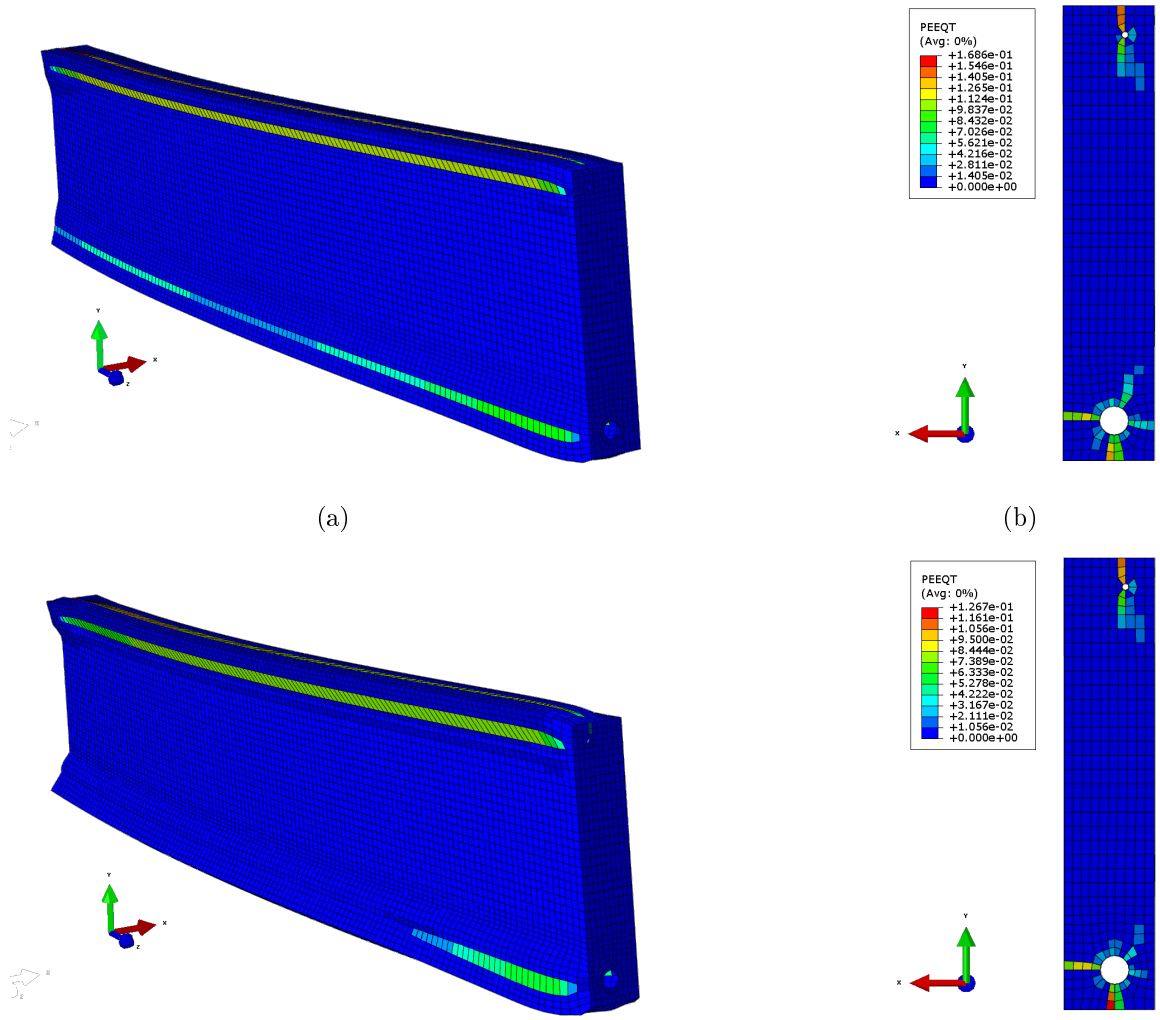


Figure 5.60: Final distribution of PEEQT parameter for beam with 50 mm deflection and increasing corrosion applied simultaneously using explicit algorithm and damage-plasticity model, presented in isometric and mid-span cross-section views: (a) and (b) – 4.0% corrosion, (c) and (d) – 8.0% corrosion.

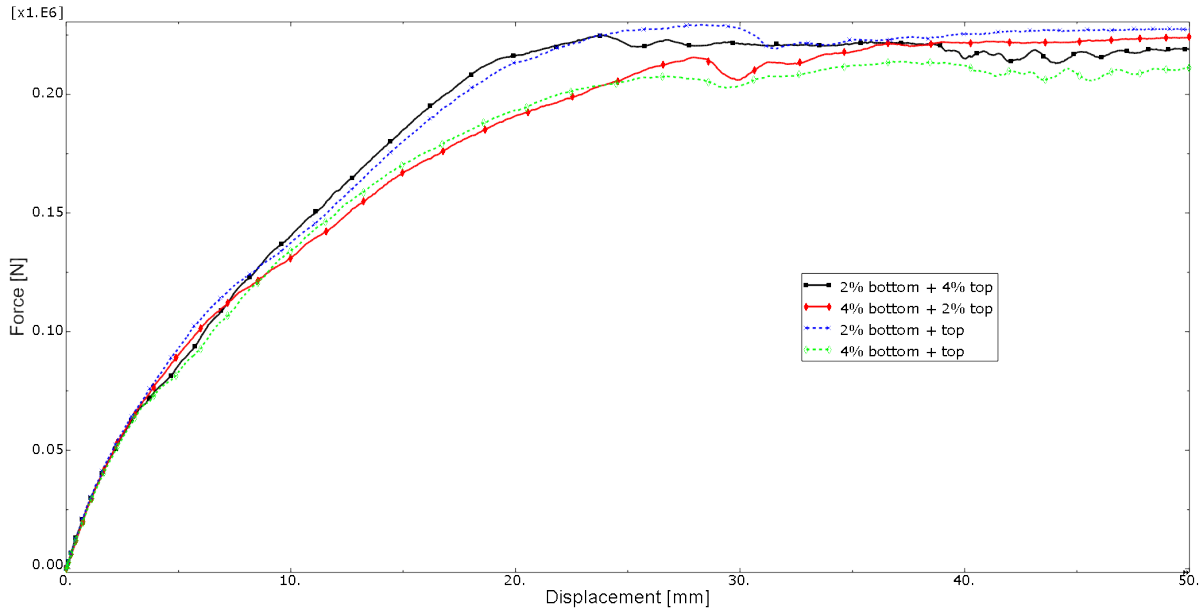


(a)

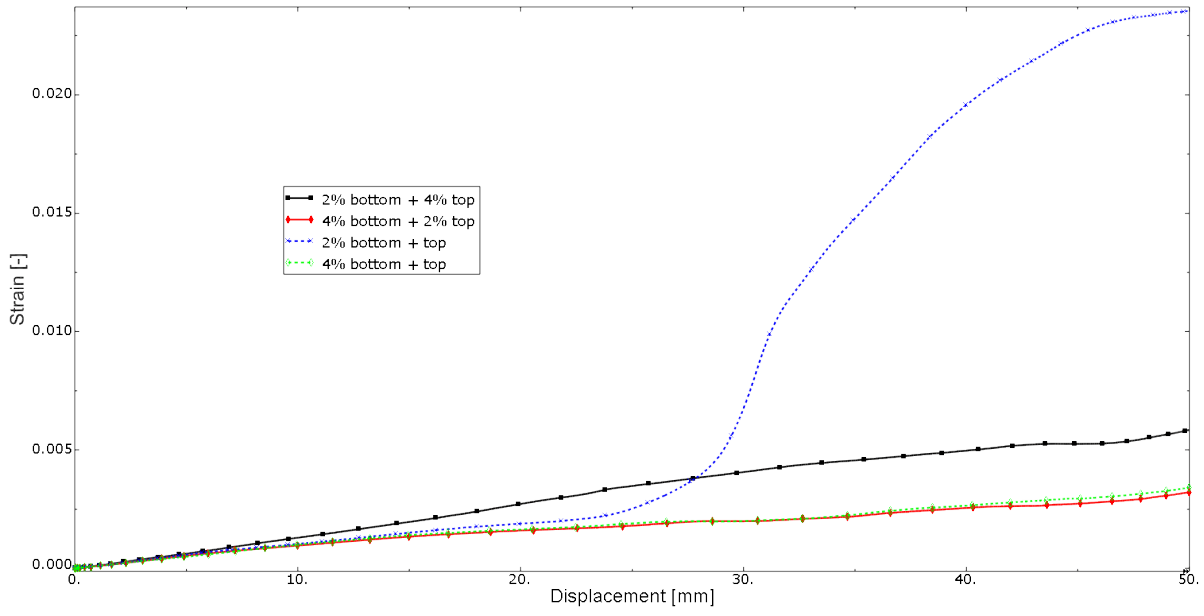


(b)

Figure 5.61: Different corrosion levels applied around top and bottom reinforcement, simultaneously with forced deflection using explicit algorithm and damage-plasticity model: (a) – Total applied force vs. beam defection, (b) – Evolution of $\varepsilon_{zz}$ strain in bottom reinforcement vs. deflection.

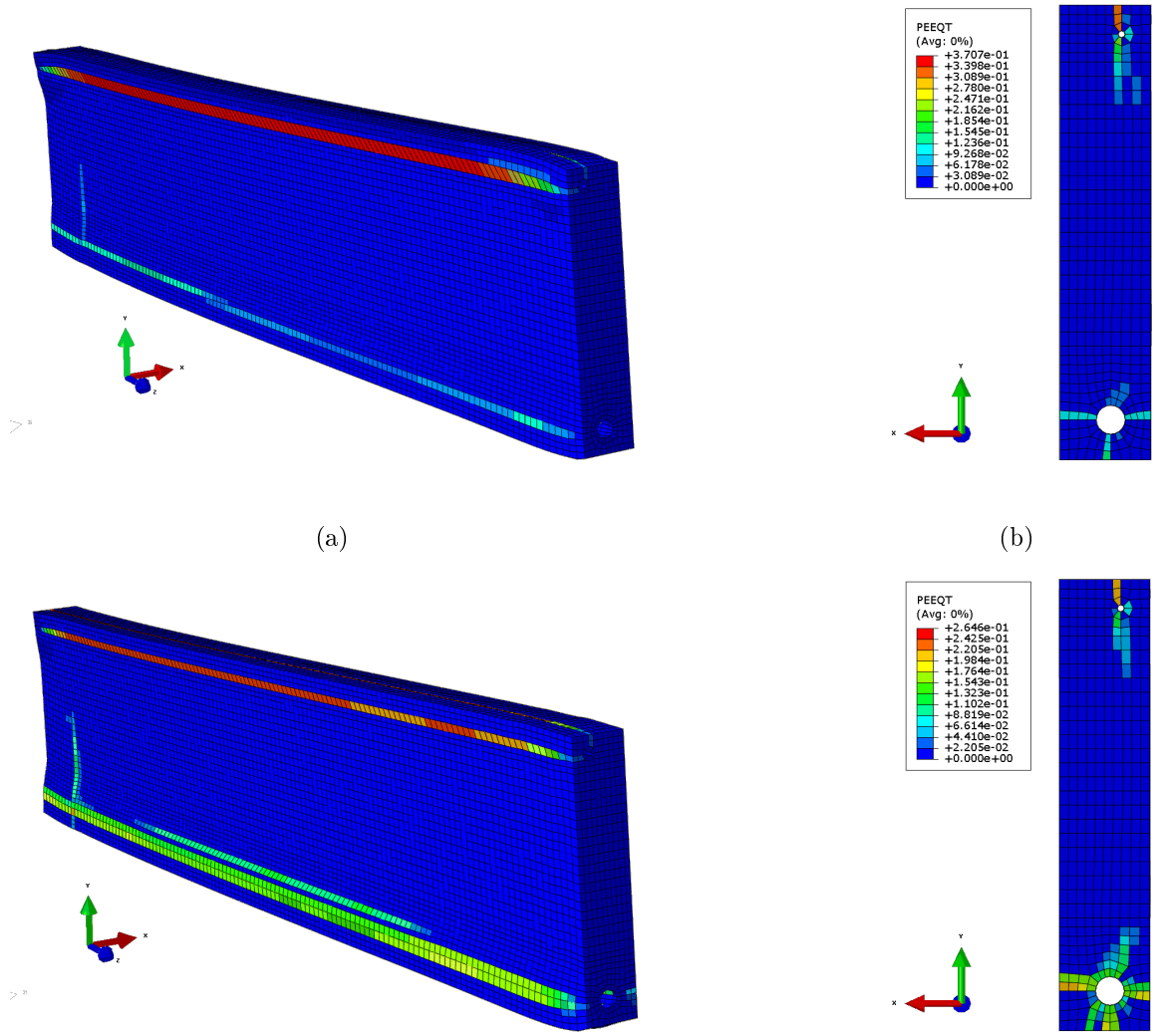


Figure 5.62: Final distribution of PEEQT parameter for beam with 50 mm deflection and simultaneously applied different corrosion levels around top and bottom reinforcement using explicit algorithm and damage-plasticity model: (a) and (b) – 2.0% bottom and 4.0% top, (c) and (d) – 4.0% bottom and 2.0% top.

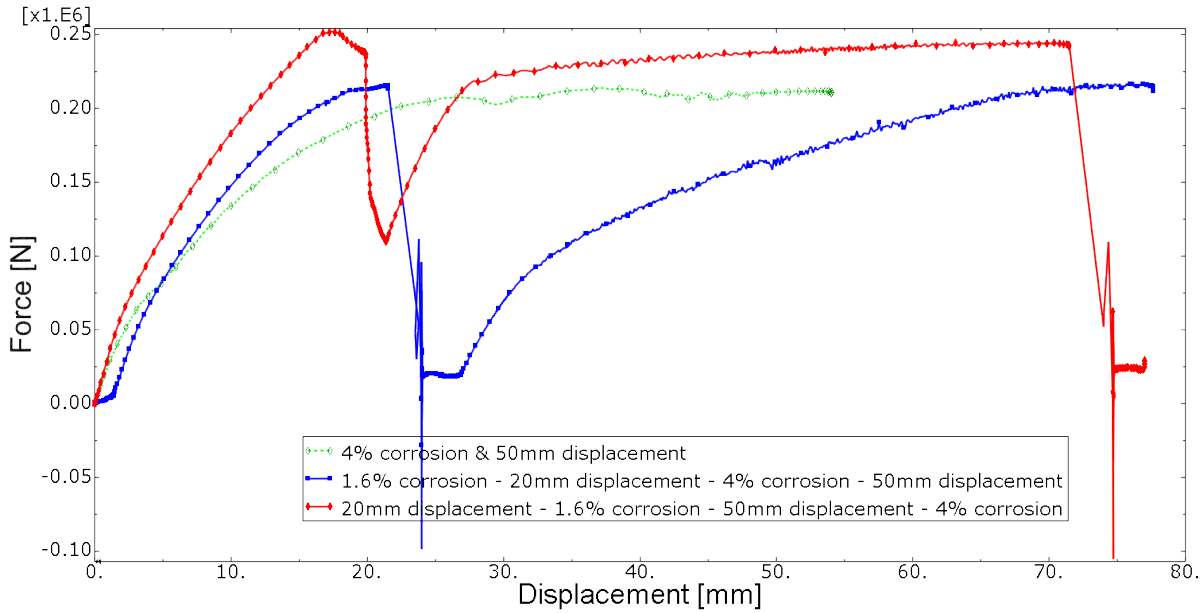


(a)

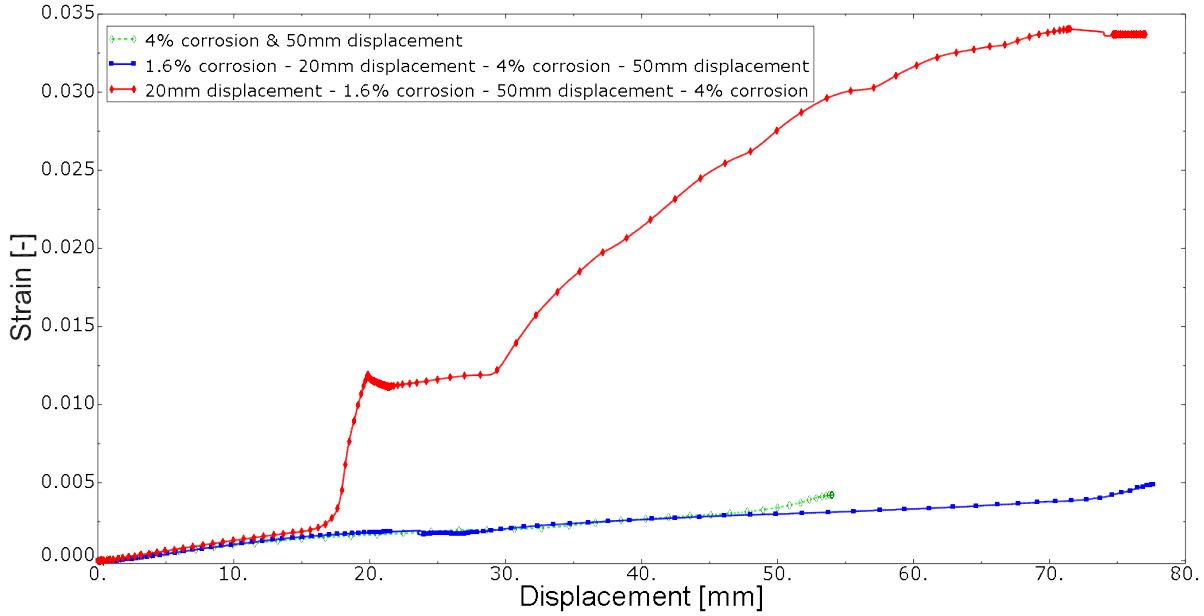


(b)

Figure 5.63: Corrosion and external loading applied in separate steps and in different sequences, explicit algorithm, damage-plasticity model: (a) – Total applied force vs. beam defection, (b) – Evolution of $\varepsilon_{zz}$ strain in bottom reinforcement vs. deflection.

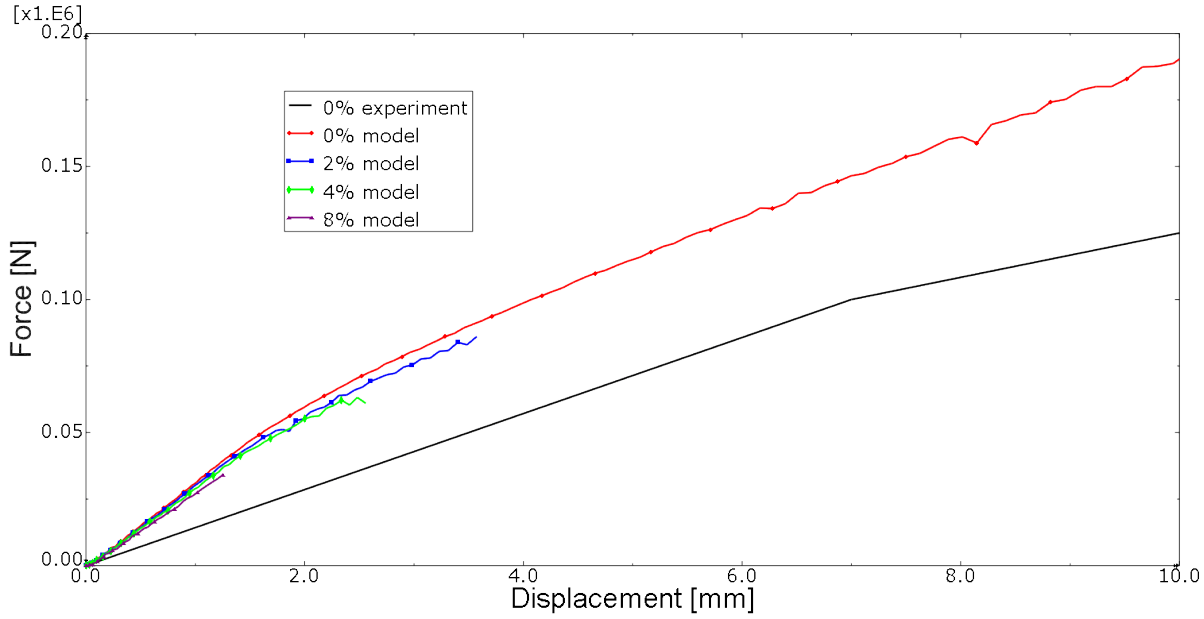


(a)

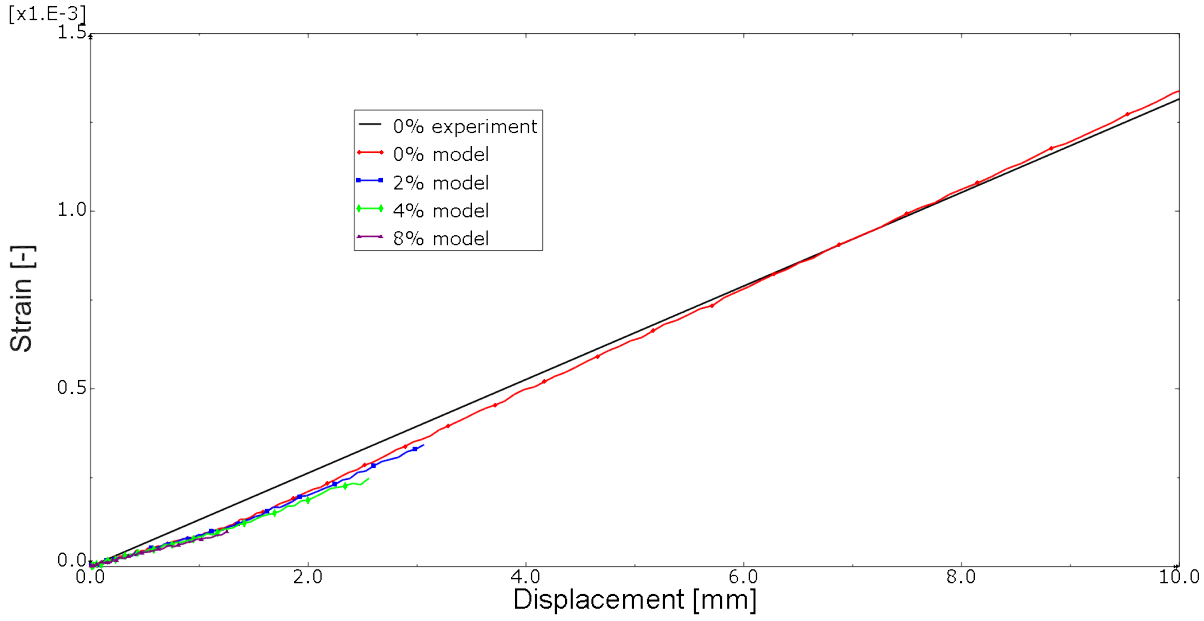


(b)

Figure 5.64: Increasing corrosion applied simultaneously with forced deflection, explicit algorithm, cracking model: (a) – Total applied force vs. beam defection, (b) – Evolution of $\varepsilon_{zz}$ strain in bottom reinforcement vs. deflection.

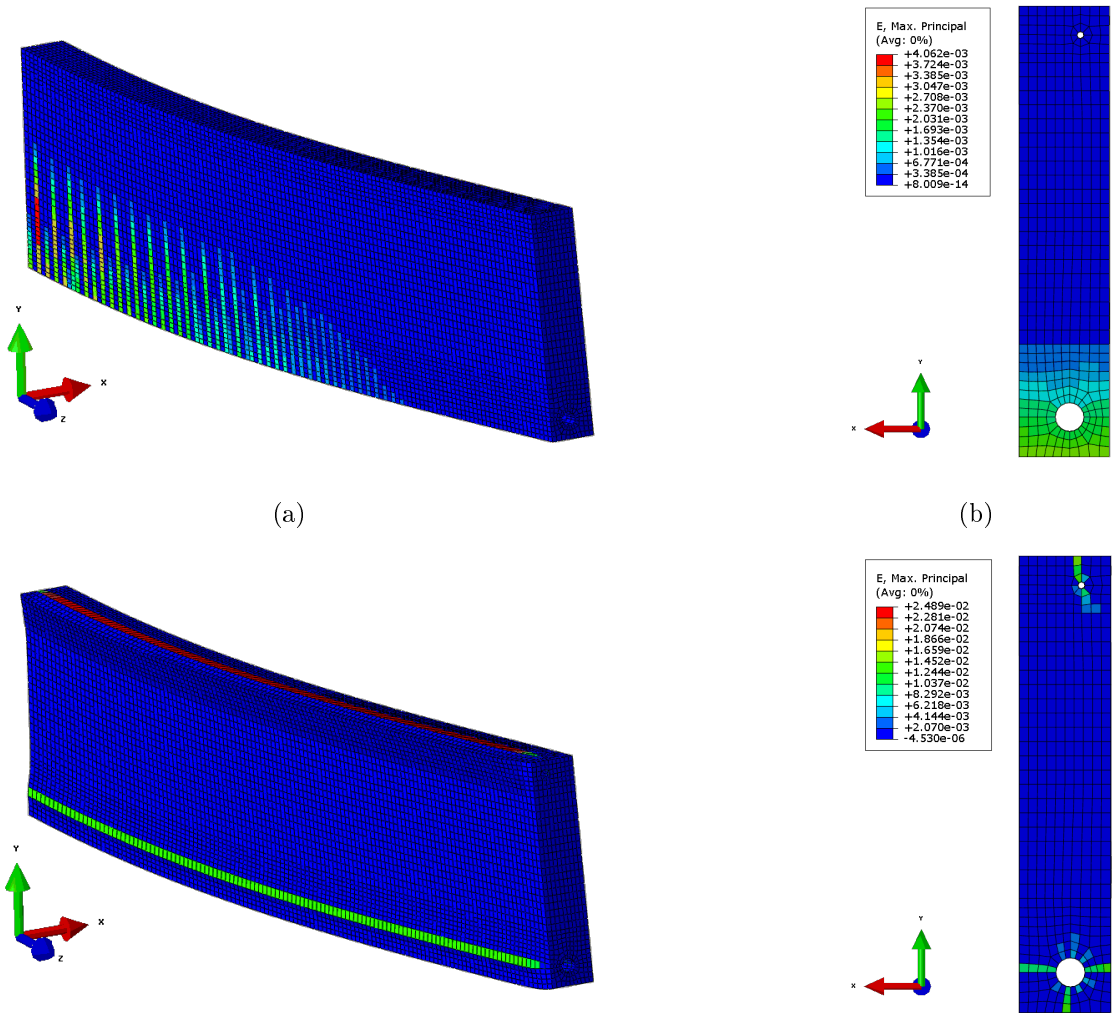


(a) (b)

(c) (d)

Figure 5.65: Final distribution of max-in-plane strain for beam with deflection and increasing corrosion applied simultaneously using explicit algorithm and cracking model, presented in isometric and mid-span cross-section views: (a) and (b) – 0.0% corrosion, (c) and (d) – 2.0% corrosion.

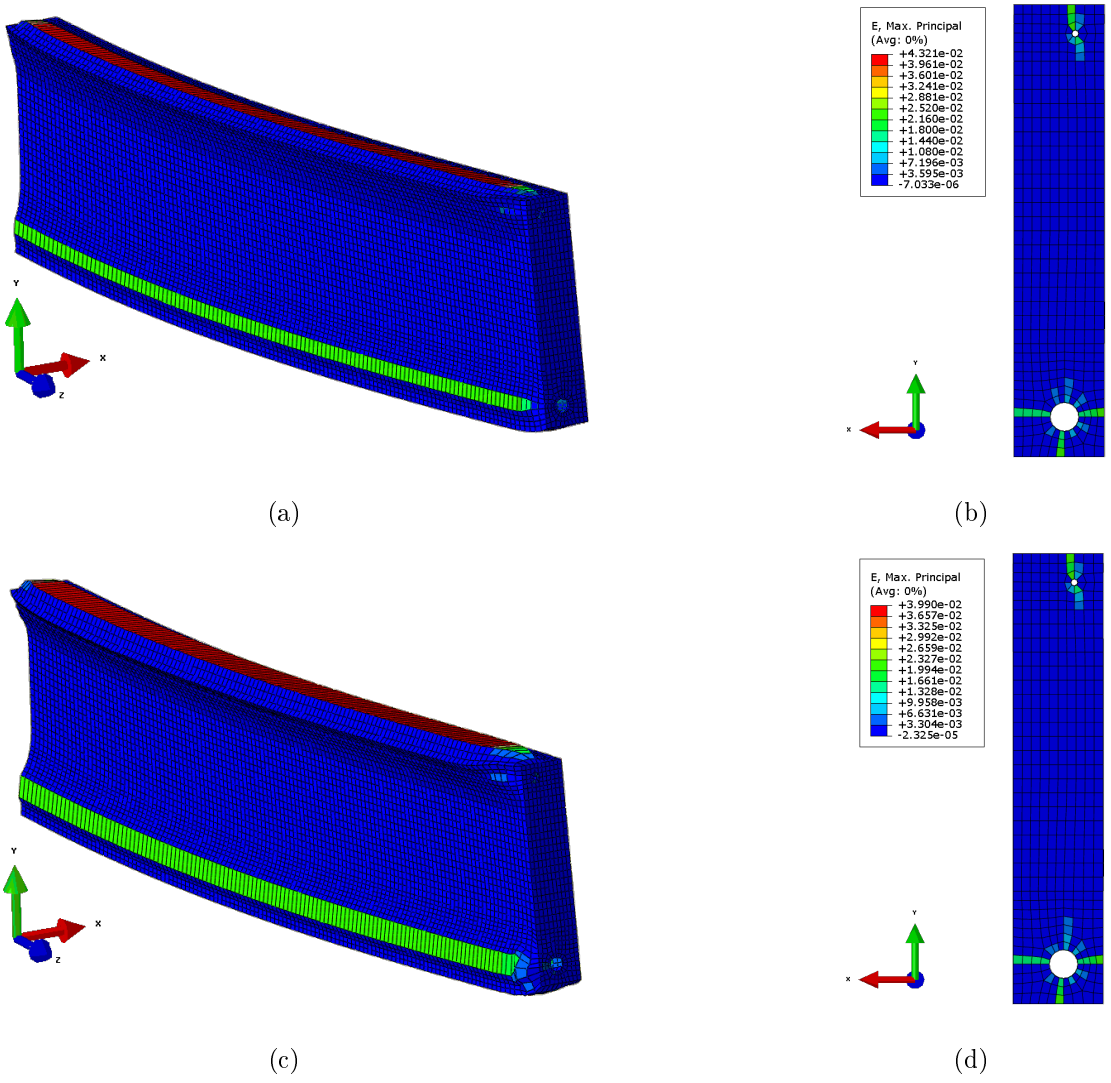


(a) (b)

(c) (d)

Figure 5.66: Final distribution of max-in-plane strain for beam with deflection and increasing corrosion applied simultaneously using explicit algorithm and cracking model, presented in isometric and mid-span cross-section views: (a) and (b) – 4.0% corrosion, (c) and (d) – 8.0% corrosion.

inconclusive, since the calculations diverge prematurely. The computations of both combinations abort at deflections less than 4 mm. All diagrams presented in Fig. 5.67 follow a similar path, because the sample is in the early elastic state. For the corrosion–deflection considerations the calculations performed with the cracking model are inconclusive and diverge soon after the corrosion application.

Figure 5.68 presents the final available distribution of max-in-plane strain for the beam with concrete modelled as a cracking material. The interesting issue is the influence of corrosion on the cracking pattern. As in the previous simulations, also in these cases the horizontal cracks are formed as a result of corrosion. In Fig. 5.68(a), when corrosion around the bottom reinforcement is 2.0% and around the top is 4.0%, the longitudinal cracks are clearly visible in the top part of the RC member. At the bottom of the beam the horizontal crack is less visible. However, when corrosion is applied in the opposite way, the cracks can easily be observed along both reinforcement bars. The cracking pattern in Fig. 5.68(c) indicates that the beam can be more degraded with such corrosion distribution. Another issue is that the brittle cracking model seems to be very sensitive to the loading representing corrosion. The strain distribution, as well as the diagrams presented above reveal that the application of even a small level of corrosion generates high values of strains and brings convergence problems.

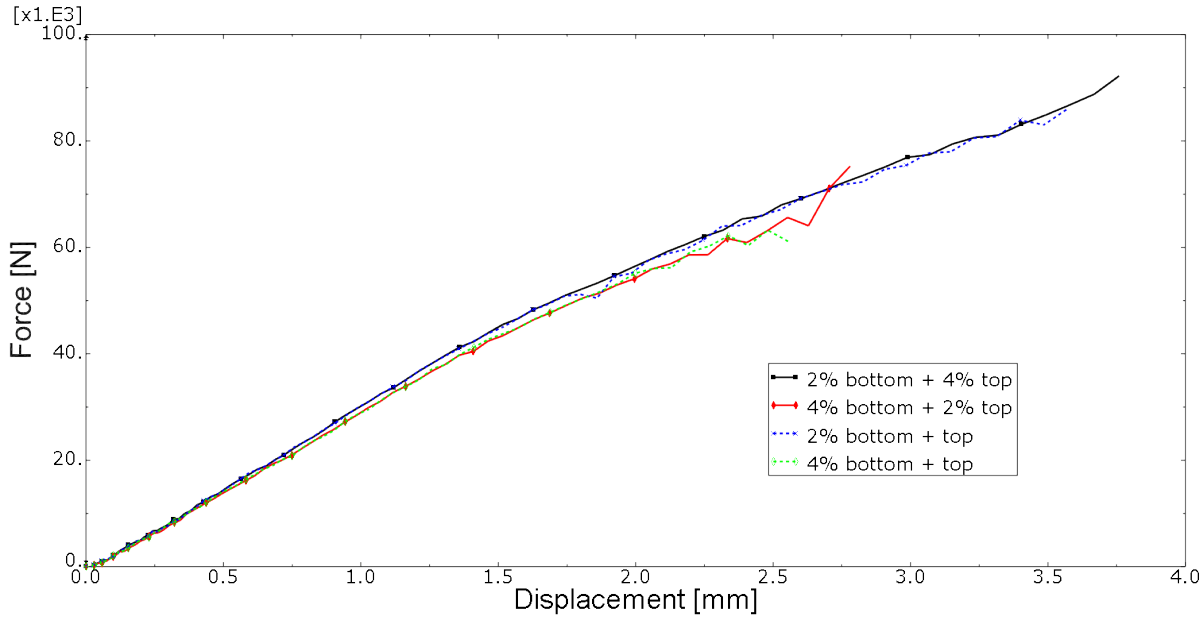


(a)

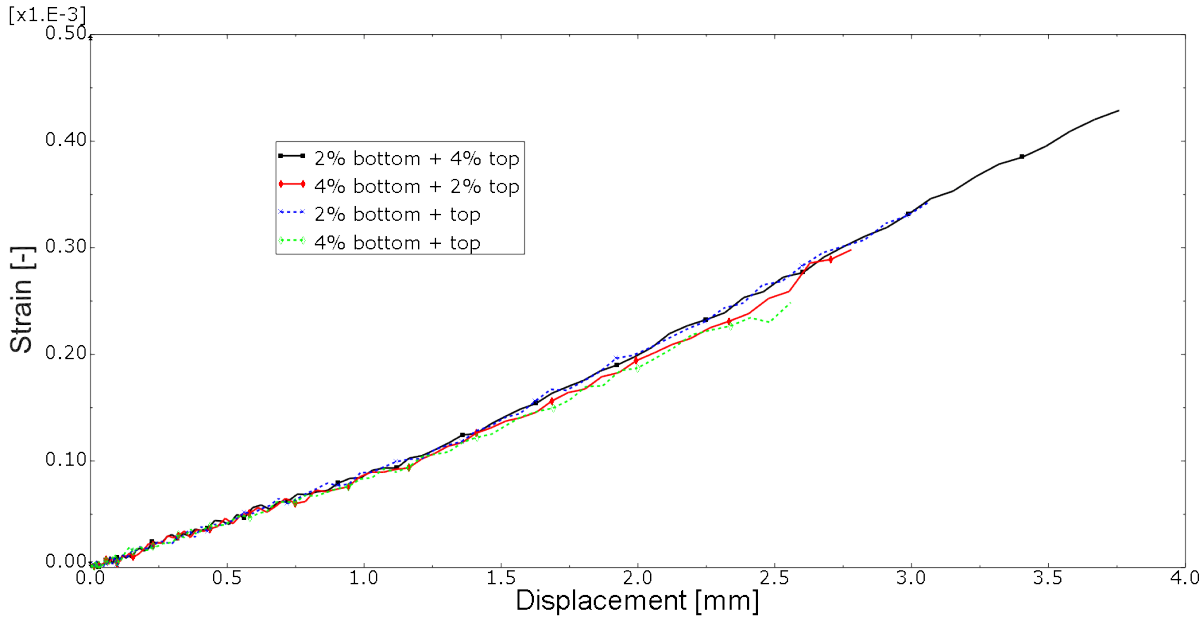


(b)

Figure 5.67: Different corrosion levels applied around top and bottom reinforcement, simultaneously with forced deflection using explicit algorithm and cracking model: (a) – Total applied force vs. beam defection, (b) – Evolution of $\varepsilon_{zz}$ strain in bottom reinforcement vs. deflection.

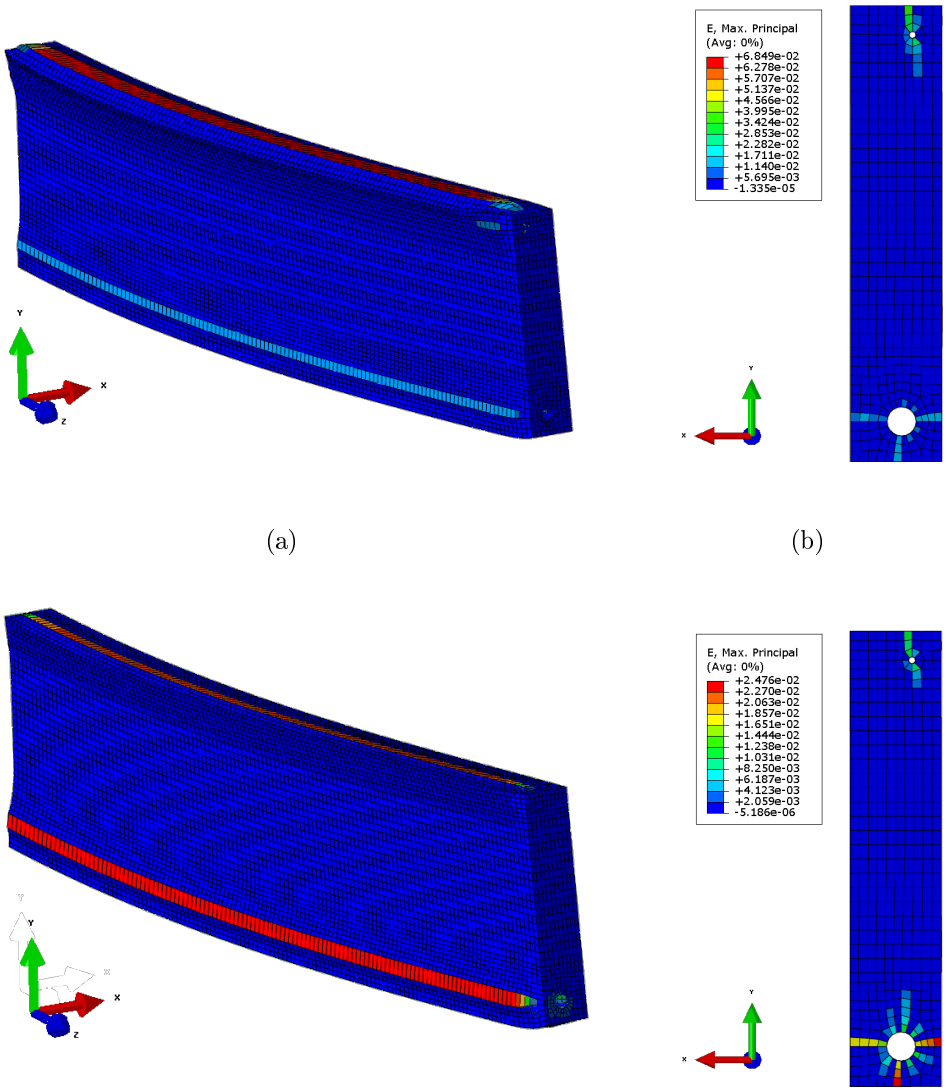


Figure 5.68: Distribution of max-in-plane strain for beam with deflection and simultaneously applied different corrosion levels around top and bottom reinforcement using explicit algorithm and cracking model: (a) and (b) – 2.0% bottom and 4.0% top, (c) and (d) – 4.0% bottom and 2.0% top.

# Chapter 6

# Conclusions and final remarks

## 6.1 Conclusions

The aim of the thesis was to discuss thoroughly the issues related to chloride corrosion of RC element. The mechanism of transport of detrimental substances, generation of corrosion cell as well as cracking analysis have been numerically simulated. The most advanced example presented in the thesis considered 3D model of an RC beam subjected to external load and corrosion. Rust was incorporated as a cohesive interface between steel and concrete. The numerical models used for initiation and propagation phase analyses provided results in good agreement with experiments, although did not capture all of the aspects of the corrosion phenomenon.

The initiation phase of corrosion analysis consisted of: simulation of chlorides and oxygen transport, electrical potential distribution and change of corrosion current in time. The analytical description of chlorides transport considered two driving forces – diffusion and migration, and chloride binding represented by Freundlich isotherm. The numerical model was built using the Cellular Automata. Some additional problems were solved using Finite Difference Method. The obtained numerical results are in agreement with experimental results presented in [50] and [46] in the most crucial aspect, i.e. the time to reach the chloride threshold. For comparison, the concentration was also calculated with Fick's law, which is based only on diffusion. The difference between the two models was visible, and it was easy to notice that the model proposed in the thesis properly represented the data obtained from the experiment. The results also showed that even high boundary concentration of chlorides does not cause high increase of the concentration at the reinforcement level. From this point of view the boundary value seems to be of secondary importance.

The parameter studies revealed that increase of concrete cover is of high importance for corrosion protection. The initiation time was much longer for 50 mm cover when different values of diffusion coefficient, boundary concentration and chloride thresholds are considered than for 30 mm. In all cases the range of initiation time predicted for 50 mm cover was much wider, which allows one for more flexibility when the concrete

mixture is composed. This leads to the conclusion that the most significant parameter governing the problem of chloride transport is the depth of the concrete cover. Although the diffusion coefficient is an important parameter, yet improving the concrete diffusivity did not extend the initiation time so significantly as increasing the concrete cover depth did. This observation was confirmed when the dependence of the initiation time on the boundary concentration was analyzed. Finally, when the dependence of the initiation time on the threshold value was analyzed, the need to increase the cover depth was even more visible than in the previous cases.

The values of the electrical potential calculated at the anode and cathode revealed good accordance with those obtained by other researchers. The change of electrical potential in time was visible in the first days after depasivation, however within one month it stabilized.

The propagation phase was simulated using Abaqus, which is Finite Element Method software. Two kinds of numerical integration algorithm were used - the implicit and the explicit schemes. Concrete was modelled as damaging-plastic material in both schemes, and additionally in the explicit calculations as brittle cracking material. Steel was modelled as elastic-plastic material, and finally rust was incorporated into the model as cohesive interface.

The propagation phase simulations presented in the thesis provided information about the damage in: an RC cross-section under destructive action of corrosion, a pullout test with a corroded bar and a beam subjected to live load and corrosion.

The implicit analysis of the RC cross-section performed with damage-plasticity model without regularization diverged prematurely and the results were inconclusive. Introducing nonzero viscosity parameter allowed one to obtain more advanced patterns of damage.

The cross-section analysis numerically confirmed the observation that corrosion-induced cracks tend to localize in the horizontal plane between rebars. For 30 mm cover thickness the cracks between rebars and through the cover were predicted, which could impair concrete-reinforcement bonding, but also accelerate further corrosion due to easy access of water, chlorides etc. to reinforcement. Finally this could lead to spalling of the whole cover. It was observed that at points on the concrete surface the simulated crack width was generally below 0.5 mm, which correlates well with experimental works [2]. On the other hand, horizontal cracks between rebars were even wider than 1 mm. Increasing the cover from 30 mm to 50 mm successfully prevented concrete from cracking through the cover. Although horizontal cracks between rebars could cause a loss in steel confinement, the cover remained sound and protected reinforcement from a quick inflow of detrimental substances.

The corrosion acting on the cross-section with low cover-to-diameter ($c/d$) ratio caused cracking of the cover, spalling off the corners and could finally lead to a complete loss of bonding between concrete and rebar. It might effectively result in a reduction of structure's service-life. The normalized thickness $c/d$ and the concrete tensile strength are the two principal parameters governing the mechanical problem of corrosion.

The cracking pattern obtained with the explicit simulation and damage-plasticity

model exhibited a more complex form, however, again concrete was at first cracked horizontally between rebars. The explicit calculations using concrete modelled as brittle cracking material aborted prematurely. Nevertheless, for both material models the maximum values of CMOD appeared in the middle of the distance between two internal rebars, similarly as in the implicit analysis.

It is worth noticing that regardless what the type of analysis or material model were, the simulations indicated that the first crack was formed horizontally, and later, depending on concrete cover thickness, the concrete cover was possibly cracked.

To obtain the interface parameters for the 3D simulation of the beam with corroding reinforcement, a 3D pullout simulation needed to be done. The interface model presented in the thesis simulated well the behavior corresponding to the case of no corrosion and high corrosion levels. The discrepancies between the model and the experiment for the precracking and cracking levels of corrosion could be a result of corrosion products distribution, which was an effect that should be further investigated. The pullout simulation revealed that for low levels of corrosion, the loss of bond was an interaction of damages of the interface and concrete. For postcracking levels of corrosion the interface was mainly responsible for the bond strength.

The correlation of the explicit simulation with the damage-plasticity model and experiment was slightly worse than in the case of the implicit simulation, especially for the cases of precracking and cracking levels of corrosion. A full agreement between the results and experiment was noticed only for the case of no corrosion and very high level of corrosion. In fact, the explicit simulation performed with the cracking model provided credible results only for the case of no corrosion. For the models with other levels of corrosion the computations diverged prematurely. This effect remained in spite of changes of analysis parameters, incrementation etc.

The overall response of the model left the impression that the cracking model is not adequate for both corrosion and pullout simulations. The results obtained with the damage-plasticity model in the implicit and explicit analyses were more convincing. The pullout simulation brought as a result the interface parameters, which could be used in the beam model. The FE analysis numerically confirmed the dependence of the bond strength and bond stiffness on the corrosion level.

In the 2D cross-section model it was not possible to include the service load. Therefore, the 3D analysis of corrosion cracking in an RC beam under static loading were performed. The analysis were performed using the same integration algorithms and material models as in pullout simulation. There were three cases of load and corrosion application: corrosion and deflection increasing linearly and simultaneously, different levels of corrosion around top and bottom rebars increasing simultaneously with deflection and finally, corrosion and deflection applied as separate steps in different sequences.

The implicit analysis of the beam with corrosion applied simultaneously with the forced deflection showed that the reduction of load-carrying capacity obtained due to corrosion was not significant. The influence of corrosion was more visible when tension strains in the bottom reinforcement were analyzed. However, the corrosion process is of

major importance when structural durability is assessed and moreover it seems important that corrosion around the top reinforcement was equally influential as corrosion around the bottom rebar.

The results of an analysis when corrosion around the top and bottom reinforcement had different values have shown that when top corrosion was lower than the bottom, the loss of load-carrying capacity was smaller that in the inverse distribution of corrosion. However, the cracking pattern indicated that the beam could be more damaged with such corrosion distribution. Thus, from the serviceability point of view the case of high corrosion around bottom and low corrosion around top reinforcement is much more dangerous than the inverse distribution of corrosion.

Finally, an analysis with different scenarios of load application has been performed. The sequence of corrosion and imposed displacement application has been changed. It turns out that the final damage of concrete was similar regardless of what the loading sequence was. However, the presented results showed that corrosion caused severe damage to the cross-section.

The important observation is that, whenever beam was loaded with deflection and later the corrosion was applied, a sudden and significant drop of load-carrying capacity was noticed, which might be more dangerous for the structure than the simultaneous load and corrosion application. The drop was caused by horizontal cracking of the concrete. However, at the same time there was no noticeable drop or increase of strains observed in the bottom reinforcement. This led to the conclusion that the horizontal cracks are significant for the overall behavior of the beam.

Again, for comparison the explicit simulation was performed with concrete modelled as damage-plasticity and cracking material, however the results for all cases were rather inconclusive. The diagrams for the beam loaded with corrosion and deflection seemed unreliable, especially for high levels of corrosion, in spite of changing analysis parameters. It seems that corrosion-induced displacements in the 3D model govern the explicit analysis and produce spurious results.

The objective of the dissertation was to perform a thorough numerical analysis of the behavior of reinforced concrete elements under the destructive actions of corrosion products and external loading. Any experimental research of corroded structures should be supported with a reliable numerical procedure. The numerical model proposed in the thesis provides a complex simulation from the beginning of the chlorides initiation process through the generation of corrosion macrocell and rust production to the cracking analysis of the 3D beam loaded with imposed deflection and expanding corrosion products. Among many analytical descriptions of the total chloride ions flux, the model proposed in the thesis considers only two driving forces – diffusion and migration.

Although it was a simplification, the simulation of this problem gave as a result the realistic values of the time to reach the chloride threshold. What is more, many authors still use the Fick's diffusion law to calculate the chlorides concentration, which, as it was presented in Chapter 4, gives much worse results. Additionally, one can find the recommendations concerning concrete cover thickness or diffusion coefficient value.

Most authors consider the rust infleunce on the basis of a cross-section analysis. However, considering only the cross-section it is not possible to represent both the corrosion and static load. According to the author's best knowledge, analyses considering simultaneously the corrosion and live load in a 3D model have not been performed so far. Additionally, to reproduce in a possibly precise way all rust properties the 3D simulation of pullout was performed in advance.

The important point of the analysis was to build a proper numerical model for concrete-rust and rust-steel interface, taking into account the volumetric expansion of corrosion products. In the thesis rust was incorporated as a cohesive interface between steel and concrete with the bond strength, stiffness and the evolution of damage depending on the corrosion level. The author found in the literature only a few similar examples of rust representation. In most cases the rust is represented as a substitute pressure acting on concrete.

The analysis of fracture caused by chloride corrosion presented in the thesis can help one to understand the character of the observed damage. At some point, it brings the answer to the question whether the damage is a result of cracking, spalling, the loss of bond between steel and concrete or a combination of all these actions. The results of the simulations can thus be helpful in safety and durability predictions. From the practical point of view the research provides advice for the designer useful in the analysis of the serviceability limit state and as a result to extend the service-life. The corrosion of steel reinforcement in concrete structures exposed to the chlorides is a worldwide problem which consumes large amounts of money every year. Due to its versatility, the model proposed in the thesis can be used when expert opinions are prepared, for structure lifetime predictions or repair cost estimation.

## 6.2 Goals for the future

Although the author did her best to thoroughly discuss the problem of chloride corrosion of reinforcement, there are still issues for further investigation:

- the description of the transport of detrimental substances extended with convection or water transport,
- the incorporation of nonlinear rust production,
- the description of distribution of corrosion products,
- the inclusion of the effect of temporary strengthening of concrete around rebar for low levels of corrosion,
- the 3D analysis of the beam with transversal reinforcement subjected to corrosion and live load,

- the 3D analysis of other structural members, e.g. column or plate, subjected to corrosion and live load,
- the analysis of the influence of the cracking on the corrosion process.

# Bibliography


[1] G.J. Al-Sulaimani, M. Kaleemullah, I.A. Basunbul, and Rasheeduzzafar. Influence of corrosion and cracking on bond behavior and strength of reinforced concrete members. *ACI Structural Journal*, 87:220–231, 1990.

[2] C. Andrade, C. Alonso, and F.J. Molina. Cover cracking as a function of bar corrosion: Part I – experimental test. *Materials and Structures*, 26:453–464, 1993.

[3] I. Balafas and C.J. Burgoyne. Environmental effects on cover cracking due to corrosion. *Cement and Concrete Research*, 40:1429–1440, 2010.

[4] I. Balafas and C.J. Burgoyne. Modeling the structural effects of rust in concrete cover. *Journal of Engineering Mechanics*, 137:175–185, 2011.

[5] Z.P. Bazant. Physical model for steel corrosion in concrete sea structures – application. *Journal of Structural Division*, 105(ST6):1155–1166, 1979.

[6] Z.P. Bazant. Physical model for steel corrosion in concrete sea structures – theory. *Journal of Structural Division*, 105(ST6):1137–1153, 1979.

[7] T. Belytschko, W.K. Liu, and B. Moran. *Nonlinear finite elements for continua and structures*. Wiley, West Sussex, 2000.

[8] L. Berto, P. Simioni, and A. Saetta. Numerical modelling of bond behaviour in RC structures affected by reinforcement corrosion. *Engineering Structures*, 30:1375–1385, 2008.

[9] A.J. Bigaj. *Structural dependence of rotation capacity of plastic hinges in RC beams and slabs*. PhD thesis, Delft University of Technology, 1999.

[10] F. Biondini, F. Bontempi, D.M. Frangopol, and P.G. Malerba. Cellular automata approach to durability analysis of concrete structures in aggressive environments. *Journal of Structural Engineering*, 130(11):1724–1737, 2004.

[11] R.D. Cook, D.S. Malkus, and M.E. Plesha. *Concepts and applications of Finite Elelement Analysis*. John Wiley & Sons, Inc., third edition, 1989.

[12] Y.G. Du, A.H.C. Chan, and L.A. Clark. Finite element analysis of the effects of radial expansion of corroded reinforcement. *Computers and Structures*, (84):917–929, 2006.

[13] C. Fang, K. Lundgren, L. Chen, and C. Zhu. Corrosion influence on bond in reinforced concrete. *Cement and Concrete Research*, 34:2159–2167, 2004.

[14] M. German and J. Pamin. Three-dimensional FE simulation of pullout test of corroded bar from rc specimen. In N. Bicanic et al., editors, *Computational Modelling of Concrete Structures*, pages 967–976. Taylor & Francis, London, 2014.

[15] M. German and J. Pamin. Two-dimensional FE simulation of cracking caused by expansion of corrosion products. In T. Łodygowski, J. Rakowski, and P. Litewka, editors, *Recent Advances in Computational Mechanics, Proceedings of the 20th International Conference on Computer Methods in Mechanics (CMM 2013)*, pages 139–148. CRC Press/Balkema, 2014.

[16] M. German and J. Pamin. FEM simulations of cracking in RC beams due to corrosion progress. *Archives of Civil and Mechanical Engineering*, 15:1160–1172, 2015.

[17] M. German and A. Zaborski. Numerical analysis of chloride corrosion of reinforced concrete. *Technical Transactions*, 3:47–60, 2011.

[18] S. Ghavamian. Three dimensional nonlinear constitutive models of fractured concrete. evaluation – comparison – adaptation. Technical report, MECA Project, EDF RD, 2001.

[19] S. Guzman, J.C. Galvez, and J.M. Sancho. Cover cracking of reinforced concrete due to rebar corrosion induced by chloride penetration. *Cement and Concrete Research*, 41:893–902, 2011.

[20] S. Guzman, J.C. Galvez, and J.M. Sancho. Modelling of corrosion-induced cover cracking in reinforced concrete by an embedded cohesive crack finite element. *Engineering Fracture Mechanics*, 93:92–107, 2012.

[21] A. Hillerborg, M. Modeer, and P. E. Petersson. Analysis of crack formation and crack growth in concrete by means of fracture mechanics and finite elements. *Cement and Concrete Research*, 6:773–782, 1976.

[22] B.S. Jang and B.H. Oh. Effects of non-uniform corrosion on the cracking and service life of reinforced concrete structures. *Cement and Concrete Research*, (40):1441–1450, 2010.

[23] T. Jaśniok. *Identification of corrosion rate of reinforcement due to polarization measurements (in Polish).* Ph.D. dissertation, Faculty of Civil Engineering, Silesian University of Technology, Gliwice, 2004.

[24] M. Jirasek. Nonlocal models for damage and fracture: comparison of approaches. *International Journal of Solids and Structures*, 35:4133–4145, 1998.

[25] O. Klinghoffer, T. Frolund, and E. Poulsen. Rebar corrosion rate measurements for service life estimates. In *ACI Fall Convention 2000, Toronto, Canada, Comitte 365 "Practical Application of Service Life Models"*, 2000.

[26] T. Krykowski. *Modeling of concrete cover damage caused by rebar corrosion in reinforced concrete (in Polish).* Polish Academy of Sciences, Committee on Civil Engineering, Warsaw, 2012.

[27] T. Krykowski and A. Zybura. FEM modelling of concrete degradation caused by rebar corrosion in reinforced concrete. *Architecture Civil Engineering Environment*, 4:71–80, 2009.

[28] A. Łapko. *Design of concrete structures (in Polish).* Arkady, first edition, 2003.

[29] J. Lee and G.L. Fenves. Plastic-damage model for cyclic loading of concrete structures. *Journal of Engineering Mechanics*, 124(8):892–900, 1998.

[30] T. Liu and R.W. Weyers. Modeling the dynamic corrosion process in chloride contaminated concrete structures. *Cement and Concrete Research*, 28(3):365–379, 1998.

[31] Y. Liu. *Modeling the Time-to-Corrosion Cracking of the Cover Concrete in Chloride Contaminated Reinforced Concrete Structures.* PhD thesis, Virginia Polytechnic Institute and State University, October 1996.

[32] T. Łodygowski. Numerical solutions of initial boundary value problems for metals and soils. In P. Perzyna, editor, *Localization and fracture phenomena in inelastic solids*, pages 392–468, Wien - New York, 1998. CISM Course Lecture Notes No. 386, Springer-Verlag.

[33] J. Lubliner, J. Oliver, S. Oller, and E. Oñate. A plastic-damage model for concrete. *International Journal of Solids and Structures*, 25(3):299–326, 1989.

[34] B. Martin-Perez. *Service life modelling of RC highway structures exposed to chlorides.* Ph.D. dissertation, University of Toronto, Toronto, 1992.

[35] E. Nielsen and M.R. Geiker. Chloride diffusion in partially saturated cementitious material. *Cement and Concrete Research*, 33:133–138, 2002.

[36] B.H. Oh and S.Y. Jang. Effects of material and environmental parameters on chloride penetration. *Cement and Concrete Research*, 37:47–53, 2007.

[37] J. Ozbolt, G. Balabanic, and M. Kuster. 3D numerical modelling of steel corrosion in concrete structures. *Corrosion Science*, 53:4166–4177, 2011.

[38] J. Ozbolt, G. Balabanic, G. Periskic, and M. Kuster. Modelling the effect of damage on transport processes in concrete. *Construction and Building Materials*, 24:1638–1648, 2010.

[39] J. Ozbolt, F. Orsanic, and G. Balabanic. Modeling damage in concrete caused by corrosion of reinforcement: coupled 3D FE model. *International Journal of Fracture*, 178(1-2):233–244, 2012.

[40] J. Ozbolt, F. Orsanic, and G. Balabanic. Modeling pull-out resistance of corroded reinforcement in concrete: Coupled three-dimensional finite element model. *Cement and Concrete Research*, 46:41–55, 2014.

[41] J. Pamin. Computational modelling of localized deformations with regularized continuum models. *Mechanics and Control*, 30(1):27–33, 2011.

[42] S.J. Pantazopoulou and K.D. Papoulia. Modelling cover-cracking due to reinforced corrosion in RC structures. *Journal of engineering mechanics*, 4:4133–4145, 2001.

[43] P. Pluciński. *Numerical analysis of mechanical effects of rebar corrosion in concrete structures (in Polish)*. Ph.D. dissertation, Cracow University of Technology, Cracow, 2008.

[44] E. Samson, J. Marchand, and J.J. Beaudoin. Describing ion diffusion mechanisms in cement-based materials using the homogenization technique. *Cement and Concrete Research*, 29:1341–1345, 1999.

[45] E. Samson, J. Marchand, K.A. Snyder, and J.J. Beaudoin. Modeling ion and fluid transport in unsaturated cement systems in isothermal conditions. *Cement and Concrete Research*, 35:141 – 153, 2005.

[46] P. Sandberg. Chloride initiated reinforcement corrosion in marine concrete. Technical report, TVBM-I015, Lund, Sweden, 1998.

[47] SIMULIA. *Abaqus Theory Manual (6.10)*. Dassault Systemes, Providence, RI, USA, 2010.

[48] W. Starosolski. *RC structures according to PN-B-03264:2002 and Eurocode 2 (in Polish)*. Wydawnictwo naukowe PWN, 12 edition.

[49] P. Thoft-Christensen. Modelling of the deterioration of reinforced concrete structures. In *IFIP WG 7.5 Working Conference on Reliability and Optimization of Structural Systems, Ann Arbor, USA*, 2000.

[50] M.D.A. Thomas and P.B. Bamforth. Modelling chloride diffusion in concrete. Effect of fly ash. *Cement and Concrete Research*, 29:487–495, 1999.

[51] P. Virmani. Corrosion costs and preventive strategies in the united states. Technical report, CC Technologies to Federal Highway Administration, Office of Infrastructure Research and Development, FHWA-RD-01-156, 2002.

[52] D. Vorechovska and M. Vorechovsky. Modeling of reinforcement corrosion in concrete. *Proceedings of FraMCoS-7*, pages 929–935, 2010.

[53] X. Wang and X. Liu. Bond strength modeling for corroded reinforcements. *Construction and Building Materials*, 20:177–186, 2006.

[54] W. Węglewski. *Modelling of concrete deterioration caused by sulphur corrosion.* PhD thesis, Institute of Fundamental Technological Research, Polish Academy of Sciences, 2008.

[55] A. Winnicki. *Viscoplastic and internal discontinuity models in analysis of structural concrete.* Series Civil Engineering, Cracow University of Technology, Cracow, 2007.

[56] A. Winnicki, C. J. Pearce, and N. Bićanić. Viscoplastic Hoffman consistency model for concrete. *Computers and Structures*, 79:7–19, 2001.

[57] A. Wosatko, A. Winnicki, and J. Pamin. Numerical analysis of Brazilian split test on concrete cylinder. *Computers and Concrete*, 8(3):243–278, 2011.

[58] A. Zaborski. Concrete elements durability in aggressive environments: cellular automata simulation. *Environmental Effects on Buildings, Structures, Materials and People, Lublin University of Technology*, pages 303–312, 2007.

[59] A. Zybura, M. Jaśniok, and T. Jaśniok. *Diagnostics of reinforced concrete structures (in Polish).* Wydawnictwo Naukowe PWN, Warsaw, 2011.

# Streszczenie

Analiza zaprezentowana w pracy dotyczy elementów żelbetowych poddanych korozji i obciążeniu zewnętrznemu jak również zależnościom między nimi. W szczególności praca dotyczy korozji chlorkowej zbrojenia oraz spowodowanego nią zarysowania betonu.

Zjawisko korozji przyjęto opisywać dwuetapowym modelem Tuuttiego zakładającym fazy inicjacji i propagacji korozji. W fazie inicjacji stężenie chlorków w betonie wzrasta. Gdy wokół zbrojenia stężenie chlorków przekroczy wartość progową następuje całkowita depasywacja zbrojenia. Tworzy się ogniwo korozyjne, w którym woda zawarta w porach betonu pełni rolę elektrolitu, a pręt zbrojeniowy przewodnika. Przepływający prąd elektryczny powoduje powstanie produktów korozji. Rozpoczyna się druga faza korozji – faza propagacji, w której produkowana rdza zwiększa swoją objętość. Efektem jest powstanie wokół korodujących prętów zbrojeniowch wzrastającego ciśnienia. Co za tym idzie, następuje zarysowanie betonu, jego odspojenie, utrata wytrzymałości, a w końcu zniszczenie elementu żelbetowego. Teoretyczne podstawy zjawiska zostały opisane w pracy w rozdziale 2.

Zaprezentowana w pracy analiza numeryczna pozwoli na ustalenie czy uszkodzenie wynika głównie z zarysowania, odspojenia betonu, utraty przyczepności między stalą a betonem lub kombinacji powyższych. Ważnym elementem symulacji jest budowa odpowiedniego interfejsu beton-rdza-stal. Stanowi to dodatkową trudność, wprowadzając do obliczeń problem kontaktu. Kolejnym wyzwaniem jest właściwa reprezentacja ciśnienia wywołanego narastającymi produktami korozji. W ramach pracy zaprezentowane są jedno-, dwu- i trójwymiarowe modele bazujące na Metodzie Elementów Skończonych (MES), Automatów Komórkowych oraz Metodzie Różnic Skończonych (MRS). Analizę przeprowadzono w środowisku Matlab oraz Abaqus. Wszystkie uzyskane wyniki są zestawione z wynikami eksperymentów z zakresu korozji.

W rozdziale 3 opisany został model numeryczny zaproponowany do opisu fazy inicjacji jak i fazy propagacji korozji. W modelu inicjacji założono, że transport chlorków odbywa się w wyniku dwóch zjawisk – dyfuzji i migracji, natomiast transport tlenu tylko w wyniku dyfuzji. Zbudowano dwuwymiarowe modele numeryczne bazujące na Automatach Komórkowych. Do obliczeń potencjału korozyjnego oraz gęstości prądu zbudowano jednowymiarowy model w oparciu o MRS. Masa rdzy jest liniowo zależna od gęstości prądu korozyjnego.

W następnym kroku zbudowano dwu- i trójwymiarowe modele z użyciem MES. Analizę propagacji korozji przeprowadzono przy użyciu pakietu Abaqus, korzystając z kontynualnych modeli materiałów dostępnych w programie. Beton został opisany modelem plastyczności z uszkodzeniem, a stal modelem sprężysto-plastycznym. Rdzę przyjęto jako interfejs między betonem a stalą, którego parametry zależą od poziomu korozji.

Analizę wykonano schematem jawnego i niejawnego całkowania numerycznego. Dla porównania, w schemacie jawnym beton przyjęto również jako materiał kruchy, ulegający zarysowaniu. Przeprowadzano symulację przekroju żelbetowego poddanego działaniu korozji. Dodatkowo zbudowane zostały modele trójwymiarowe, analizujące wpływ rdzy na

próbę wyciągania pręta z bloku betonowego oraz zachowanie belki żelbetowej poddanej trójpunktowemu zginaniu i korozji. Model belki zakładał różne sposoby przykładania obciążenia: jednorodnej korozji zbrojenia działającej równocześnie z ugięciem, różnego rozkładu korozji wokół górnego i dolnego zbrojenia działającej równocześnie z ugięciem oraz korozji i ugięcia przyłożonego oddzielnie w różnych krokach i w różnej kolejności.

Wyniki symulacji fazy inicjacji przedstawiono w rozdziale 4, natomiast fazy propagacji w rozdziale 5. Wszystkie wyniki wykazały zbieżność z eksperymentem potwierdzając poprawność zastosowanych modeli materiałowych oraz obliczeniowych. Przeprowadzone analizy parametryczne pozwoliły na wskazanie kluczowych parametrów materiałowych oraz wrażliwych punktów symulacji. Praca zawiera również pewne zalecenia, które zastosowane w praktyce pozwoliłyby na wydłużenie czasu użytkowalności konstrukcji żelbetowej.

Model numeryczny zaproponowany w pracy zawiera kompletną symulację zjawiska od początku procesu wnikania chlorków, poprzez utworzenie ogniwa korozyjnego i produkcję rdzy, aż po trójwymiarową analizę zarysowania belki obciążonej ugięciem i postępującą korozją. Spośród różnych dostępnych modeli opisu transportu jonów chlorkowych, w pracy założono, że odbywa się on w wyniku dyfuzji i migracji. Jest to pewne uproszczenie, jednak w rezultacie symulacja dała rzeczywiste wartości czasu do osiągnięcia progowego stężenia chlorków. Co więcej, nadal wielu autorów do obliczeń stężenia chlorów posługuje się prawem dyfuzji Fick'a, które, jak pokazano w rozdziale 4, daje zdecydowanie gorsze wyniki.

Większość autorów rozważa wpływ korozji na podstawie analizy przekroju żelbetowego. Niestety, w takiej analizie nie ma możliwości uwzględnienia korozji i obciążenia zewnętrznego. Według najlepszej wiedzy autora, nie ma opisanych w literaturze przypadków trójwymiarowych symulacji jednoczesnego działania korozji i obciążenia. Aby dokonać takiej analizy zbudowano model belki, a wyniki jego obliczeń zaprezentowano w rozprawie w rozdziale 5. Dodatkowo, aby możliwie najdokładniej odwzorować wszyste właściwości rdzy, w pracy zaprezentowano trójwymiarowy model testu wyciągania pręta z betonowego bloku.

Ważnym punktem obliczeń było zbudowanie poprawnego modelu interfejsu między betonem i stalą, uwzględniającego ekspansję objętościową rdzy. W pracy rdza została włączona do obliczeń jako interfejs, którego parametry zależą od stopnia korozji. Autor nie znalazł podobnych przykładów symulacji w literaturze. W większości przypadków rdza reprezentowana jest poprzez zastępcze ciśnienie działające na beton wokół zbrojenia.

Zaprezentowana symulacja ma za zadanie ułatwić oszacowanie czasu użytkowania i trwałości konstrukcji. Korozja jest zjawiskiem powszechnym oraz generującym spore koszty. Oprócz kosztów bezpośrednich, związanych z naprawami zniszczonych elementów występują również znacznie wyższe koszty pośrednie, związane z wyłączeniem danego elementu z użytkowania (np. zatory drogowe i opóźnienia w transporcie spowodowane zamknięciem skorodowanego mostu). Model zaproponowany w pracy może być przydatny przy przygotowywaniu opinii eksperckich i oszacowaniach kosztów napraw.